UNIVERSITY OF SOUTHAMPTON

Advances in Parahydrogen-Enhanced Nuclear Magnetic Resonance

by

James Eills

A thesis submitted in partial fulfillment for the degree of Doctor of Philosophy

in the
Faculty of Engineering and Physical Sciences
School of Chemistry

28/04/2019

UNIVERSITY OF SOUTHAMPTON

ABSTRACT

FACULTY OF ENGINEERING AND PHYSICAL SCIENCES
SCHOOL OF CHEMISTRY

Doctor of Philosophy

by James Eills

Nuclear magnetic resonance is a powerful spectroscopic tool, which has found applications in fields such as chemistry, the life sciences, medical imaging, and even fundamental physics, but is often limited by the low polarization of nuclear spins in ambient conditions. Hyperpolarization techniques are used to increase the spin polarization, which can lead to large signal enhancements. In the context of magnetic resonance imaging, this can allow for *in vivo* observation of metabolites at physiological concentrations, which would otherwise not be possible given current sensitivity limits.

This thesis describes a number of hyperpolarization methods and their applications to *in vivo* imaging, with particular emphasis on parahydrogen-induced hyperpolarization. This technique allows for the production hyperpolarized samples via chemical reaction with a specific spin-isomer of hydrogen gas. Theory and experiments for producing hyperpolarized samples are described that advance this methodology towards eventual clinical application.

Contents

1 Introduction **1**

2 Fundamental NMR Theory **3**
2.1 Classical Description of NMR . . . 3
2.1.1 Spin-1/2 Nuclei as Tiny, Tiny Bar Magnets . . . 3
2.1.2 Precession . . . 5
2.1.3 The Vector Model . . . 5
2.1.4 Fourier Transform NMR . . . 7
2.1.5 The NMR Spectrum . . . 9
2.1.6 Relaxation . . . 10
2.1.6.1 General Principles . . . 10
2.1.6.2 T_1 Measurement Techniques . . . 12
2.2 Quantum Description of NMR . . . 14
2.2.1 Nuclear Spin . . . 14
2.2.2 Spin States and Hilbert Space . . . 14
2.2.3 Operators and Liouville Space . . . 16
2.2.3.1 Superoperators . . . 18
2.2.3.2 The Density Operator . . . 19
2.2.3.3 The Hamiltonian Operator . . . 21

3 Hyperpolarization **24**
3.1 Introduction . . . 24
3.1.1 Basic Principles - Beating the Boltzmann Distribution . . . 24
3.1.2 Hyperpolarization Techniques . . . 25
3.1.3 Hyperpolarized Targets for *in vivo* Medical Imaging . . . 27
3.2 Parahydrogen Induced Hyperpolarization . . . 29
3.2.1 Nuclear Spin States of Molecular Hydrogen . . . 29
3.2.2 Relaxation of Nuclear Singlet States . . . 30
3.2.3 Enrichment of Hydrogen Gas in the Singlet Spin Isomer . . . 31
3.2.4 Chemistry and Reactions . . . 34
3.2.4.1 Irreversible Parahydrogen Addition: Hydrogenative PHIP 35
3.2.4.2 Reversible Parahydrogen Addition: Signal Amplification by Reversible Exchange . . . 36
3.3 Parahydrogen Spin Dynamics . . . 37
3.3.1 Chemical Shift Inequivalence . . . 37
3.3.1.1 PASADENA . . . 39
3.3.1.2 ALTADENA . . . 41

3.3.2 Inequivalent J-couplings to a third spin . . . 42
3.3.2.1 Far from equivalence regime . . . 44
3.3.2.2 Near-equivalence regime . . . 46

4 Singlet Order Manipulation at Ultra-Low Field 52
4.1 Introduction . . . 52
4.2 Theoretical Description of the Field Sweep . . . 53
4.2.1 State Bases and the Spin Hamiltonian . . . 53
4.2.2 Avoided Crossings . . . 56
4.2.3 The Field-Sweep Experiment . . . 58
4.3 Materials and Methods . . . 60
4.4 Results . . . 62
4.4.1 Field-Sweep Hyperpolarization of ^{13}C NMR Signals . . . 62
4.4.2 Reversal of the Field-Sweep Direction . . . 63
4.4.3 Effect of Field-Sweep Duration on Polarization Transfer Efficiency 64
4.4.4 Polarization Enhancement . . . 64
4.5 Conclusions . . . 65

5 Singlet Order Manipulation at High Field 67
5.1 Introduction . . . 67
5.2 Theoretical Description of SLIC and S2hM . . . 69
5.2.1 State Bases and the Spin Hamiltonian . . . 69
5.2.2 S-Spin SLIC . . . 70
5.2.3 S-Spin S2hM . . . 73
5.3 Materials and Methods . . . 77
5.4 Results . . . 77
5.4.1 SLIC Method . . . 79
5.4.2 S2hM Method . . . 80
5.4.3 SLIC Parahydrogen Demonstration . . . 83
5.5 Relayed Polarization Transfer in an AA'MX System . . . 84
5.5.1 Materials and Methods . . . 84
5.5.2 Results and Analysis . . . 85
5.6 Summary . . . 88

6 Hyperpolarized [1-^{13}C]fumarate via Parahydrogen 90
6.1 Introduction . . . 90
6.2 Reaction Chemistry . . . 92
6.3 Materials and Methods . . . 92
6.4 Results and Analysis . . . 92
6.5 Summary . . . 97

7 Preservation of [1-^{13}C]fumarate Spin Order 98
7.1 Introduction . . . 98
7.2 Physicochemical Properties of [1-^{13}C]fumarate . . . 99
7.2.1 Relaxation Properties of [1-^{13}C]Fumarate - Field and Temperature Dependence . . . 99
7.2.2 EPR Measurements on Precipitated Fumarate . . . 101
7.2.2.1 Materials and Methods . . . 102

7.2.2.2 Results and Analysis . . . 102
7.2.3 Crystallinity of Precipitated Fumarate . . . 102
7.2.3.1 Materials and Methods . . . 102
7.2.3.2 Results and Analysis . . . 103
7.3 Thermal Polarization Demonstration . . . 103
7.3.1 Materials and Methods . . . 104
7.3.2 Results and Analysis . . . 106
7.4 Dynamic Nuclear Polarization Demonstration . . . 109
7.4.1 Materials and Methods . . . 109
7.4.2 Results and Analysis . . . 110
7.5 Summary . . . 111

8 Conclusions and Outlook 113

9 Appendix I 115
9.1 Transformation Efficiency . . . 115
9.2 Pulse Sequences . . . 118
9.2.1 SLIC Transfer Sequence . . . 118
9.2.2 S2hM Transfer Sequence . . . 119
9.2.3 Goldman Transfer Sequence . . . 120
9.2.4 Kadlecek 2b Transfer Sequence . . . 121
9.2.5 Refocused INEPT . . . 122
9.2.6 T_{00} Filter . . . 123

10 Appendix II 124

Bibliography 151

List of Figures

2.1 Energy levels of a spin-1/2 particle in a magnetic field 4
2.2 NMR vector model 5
2.3 Example pulse sequence 8
2.4 Relaxation in the vector model 11
2.5 Inversion recovery experiment 12
2.6 Saturation recovery experiment 13
2.7 Magnitude and z-axis projection of a spin-1/2 nucleus 14

3.1 Hyperpolarized ^{3}He and ^{129}Xe lung MR images 27
3.2 Hyperpolarized ^{13}C-labelled pyruvate prostate cancer MR images 28
3.3 Hyperpolarized ^{13}C-labelled dimethyl maleate MR images of a rat 28
3.4 Magnetic field dependence of singlet and triplet state eigenvalues 30
3.5 An illustration of the difference between T_1 and T_S 31
3.6 An illustration of three relaxation mechanisms experienced by a proton pair 32
3.7 Rotational energies and para-enrichment fraction of H_2 gas 33
3.8 Illustration of hydrogenative PHIP and SABRE 34
3.9 Proposed mechanism of Rh-catalysed hydrogenative PHIP 35
3.10 Rh(I) hydrogenation catalysts. 36
3.11 A graphical representation of a molecule in which a pair of J-coupled parahydrogen protons have a chemical shift difference 38
3.12 A graphical representation of the mixing between the singlet-triplet and Zeeman state bases 38
3.13 Thermal equilibrium vs PASADENA state populations and resulting spectra 40
3.14 Eigenvalues of the basis states as a function of magnetic field, for two J-coupled protons with a nonzero chemical shift difference 41
3.15 Thermal equilibrium vs PASADENA state populations and resulting spectra 42
3.16 A graphical representation of a molecule in which a pair of J-coupled parahydrogen protons have identical chemical shifts, but different J-couplings to an X nucleus 43
3.17 A model spin system for a far-from equivalence proton pair 44
3.18 I-spin spectral simulation of a far from equivalence spin system 45
3.19 A model spin system for a near-equivalence proton pair 46
3.20 A matrix plot of $\hat{H}$ in the $\mathbb{STZ}$ basis 47
3.21 Eigenvalues of Hamiltonian $\hat{H}$ basis states as a function of applied field for a near-equivalence spin system 48
3.22 Technique 1; B_0 field manipulations for a simple field cycling experiment . 49
3.23 Technique 2; B_0 field manipulations for an experiment described in the text 49

3.24 Technique 3; Illustration of state populations after hydrogenation a sample as described in the text . . . 50
3.25 Eigenvalues of Hamiltonian $\hat{H}_{\mathrm{drf}}$ basis states as a function of applied rf amplitude for a near-equivalence spin system . . . 51

4.1 Hydrogenation and polarization transfer . . . 53
4.2 Field sweep events sequence . . . 53
4.3 1-^{13}C-maleic acid NMR energy levels and spectra . . . 54
4.4 Eigenvalues as a function of external field . . . 57
4.5 State populations during a field sweep . . . 60
4.6 Experimental apparatus . . . 61
4.7 Demonstration of the field sweep technique . . . 62
4.8 Field-sweep direction reversal results . . . 63
4.9 Field sweeps of varied duration . . . 65
4.10 Field-sweep polarization enhancement results . . . 66

5.1 I-spin singlet order and S-spin polarization during SLIC pulse . . . 72
5.2 S2hM pulse sequence . . . 74
5.3 Density operator evolution during the S2hM pulse sequence . . . 76
5.4 [1-^{13}C]fumaric acid J-couplings and spectra . . . 78
5.5 SLIC and S2hM pulse sequences . . . 79
5.6 SLIC and S2hM pulse sequence optimization plots . . . 81
5.7 Transfer sequence B_1 offset dependence . . . 82
5.8 S2hM polarization enhancement spectra . . . 83
5.9 S2B2M pulse sequence illustration . . . 84
5.10 [1-^{13}C-O-$^{13}C_2$]dimethyl maleate thermal equilibrium ^{13}C NMR spectrum and J-couplings . . . 85
5.11 Rf pulses in the time and frequency domains . . . 87
5.12 S2B2M pulse sequence and optimization plot . . . 88
5.13 S2B2M polarization enhancement spectra . . . 89

6.1 Proposed reaction mechanism for the formation of fumarate via parahydrogen . . . 91
6.2 S2hM pulse sequence and fumarate J-couplings . . . 92
6.3 Fumarate parahydrogen-enhanced ^{1}H NMR spectra . . . 93
6.4 Parahydrogen-enhanced ^{13}C NMR spectra . . . 94
6.5 ^{1}H NMR spectrum showing selectivity of the trans-hydrogenation . . . 95
6.6 Spin-relaxation data and pulse sequences . . . 96

7.1 Magnetic field dependence of the ^{13}C solid-state T_1 in [1-^{13}C-2,3-D_2]fumaric acid . . . 100
7.2 Temperature dependence of the ^{13}C solid-state T_1 in [1-^{13}C-2,3-D_2]fumaric acid . . . 101
7.3 EPR spectra of washed precipitate . . . 103
7.4 Powder XRD spectra of precipitated and stock fumaric acid . . . 104
7.5 Solubility of fumarate in water . . . 104
7.6 Precipitation experimental apparatus . . . 105
7.7 Continuously monitored precipitation experiment . . . 107

7.8 Inversion recovery precipitation experiments 108
7.9 Pictures of fumarate precipitation procedure on the glass sinter 110
7.10 Precipitation-DNP results 111

9.1 Pulse sequences for calibration of the conversion amplitude of the ^{13}C SLIC pulse 116
9.2 SLIC optimization pulse sequence 118
9.3 S2hM optimization pulse sequence 119
9.4 'Goldman' optimization pulse sequence 120
9.5 'Kadlecek 2b' optimization pulse sequence 121
9.6 Refocused INEPT block 122
9.7 Graphical depiction of the T_{00} filter 123

List of Tables

3.1 Exchange-symmetry of Ψ^{tot} . . . 32

4.1 $\hat{H}_0$ eigenstate energies . . . 56
4.2 Mixing terms at avoided crossings . . . 57

6.1 [1-^{13}C]fumarate spin relaxation data . . . 95

7.1 [1-^{13}C-2,3-D_2]fumaric acid solution-state T_1 data . . . 100

9.1 SLIC pulse sequence phase cycle . . . 118
9.2 S2hM pulse sequence phase cycle . . . 119
9.3 'Goldman' pulse sequence phase cycle . . . 120
9.4 'Kadlecek 2b' pulse sequence phase cycle . . . 121
9.5 T_{00} filter parameters . . . 123

Abbreviations

Acronym	Definition
CSA	Chemical Shift Anisotropy
DC	Direct Current
dDNP	dissolution Dynamic Nuclear Polarization
DNP	Dynamic Nuclear Polarization
EPR	Electron Paramagnetic Resonance
FID	Free Induction Decay
FT	Fourier Transform
INEPT	Insensitive Nuclei Enhanced by Polarization Transfer
LLS	Long-Lived State
M2S	Magnetization-to-Singlet
MAS	Magic Angle Spinning
MR	Magnetic Resonance
MRI	Magnetic Resonance Imaging
NMR	Nuclear Magnetic Resonance
PEEK	PolyEther Ether Ketone
PHIP	ParaHydrogen Induced Polarization
ppm	Parts Per Million
PTFE	PolyTetraFluoroEthylene
PXRD	Powder X-Ray Diffraction
rf	Radio Frequency
S2B2M	Singlet-to-Bridge-to-Magnetization
S2hM	Singlet-to-Heteronuclear-Magnetization
S2M	Singlet-to-Magnetization
SABRE	Signal Amplification By Reversible Exchange
SEM	Scanning Electron Microscopy
SEOP	Spin-Exchange Optical Pumping
SLIC	Spin-Lock Induced Crossing
$\mathbb{STZ}$	Singlet-Triplet-Zeeman
TEMPO	(2,2,6,6-tetramethylpiperidin-1-yl)oxyl
TTL	Transistor-Transistor Logic
ZULF	Zero and UltraLow Field

Declaration of Authorship

This thesis is the result of work done wholly while I was in registered candidature for a Ph.D. degree at the University of Southampton. The material presented here is based on work mostly done by myself. Where the work was carried out jointly with others, a substantial part is my own original work and co-workers and their roles have been clearly indicated. The material contained herein has not been submitted by the author for a degree at any other institution.

Signed: 28/04/2019

Acknowledgements

I am grateful to a large number of people who have made this work, and my journey in academia so far, a wonderful experience.

Foremost, I would like to thank my advisers Malcolm Levitt and Marcel Utz for their continual guidance throughout my Ph.D.

I am overwhelmingly grateful for Malcolm's input relating to the work in this thesis, for which he has been a seemingly limitless source of knowledge. Perhaps more importantly, he has taught me a great deal about the fundamental principles of carrying out and communicating scientific research. Most important of all, he has fostered a wonderful working environment, which made my time at Southampton great fun.

In his role as my secondary supervisor, Marcel has helped me develop throughout my time in Southampton. I have yet to find an area of science Marcel is not well versed in, and his breadth of knowledge has helped to open my eyes to other areas of science outside the relatively narrow field of work in this thesis.

Additionally, I would like to thank Dima Budker, who has also provided fantastic advice and mentoring in numerous aspects of my research, both before and during my Ph.D.

I would also like to thank the people directly involved in the research that contributed to this thesis. In something close to chronological order, I am indebted to: William Hale, Laura Jowett, Stephanie Chapman, James Emsley, Stefan Glöggler, Gabriele Stevanato, Christian Bengs, Giuseppe Pileio, Stuart Elliott, Javier Alonso-Valdesueiro, Marina Carravetta, Shamim Alom, Hana Kouřilová, Aliki Moysiadi, John Blanchard, Teng Wu, Julia Hollenbach, Weidong Gong, Benno Meier, Karel Kouril, George Bacanu, Mohammed Sabba, Barbara Ripka, Manvendra Sharma, Matheus Rossetto, Gabriel Rossetto, and Sylwia Ostrowska.

Specific acknowledgements are owed to; Gabriele Stevanato, Christian Bengs, Giuseppe Pileio, and Stuart Elliott for help developing the SLIC and S2hM theory; Christian Bengs for writing SpinDynamica scripts; Stefan Glöggler and Hana Kouřilová for construction of the parahydrogen generator; John Blanchard and Teng Wu for construction of the zero-field apparatus; Benno Meier, Karel Kouril, and Hana Kouřilová for construction of the DNP apparatus.

I am particularly grateful to the whole Budker group, and in particular Anne Fabricant, for making me feel so welcomed on my various trips to Mainz; Román Picazo Frutos, Kirill Sheberstov, and Anjusha Sreeja for their helpful advice on the writing-up of this work; Shamim Alom for his reliable lack of help with this work; Ruth Werzlau and Barbara Ripka for keeping me going when I needed it the most; and William Hale,

Christian Bengs, Aliki Moysiadi, and Stuart Elliott for their ceaseless support through my Ph.D.!

Finally, I am greatly indebted to my family for all their support over the years. None of this would have been possible without them.

Chapter 1

Introduction

Magnetic resonance spectroscopy and magnetic resonance imaging (MRI) are widely applied spectroscopic techniques, but are often limited by the low polarization of nuclear spins at ambient temperature, even in the highest available magnetic fields. There are a number of hyperpolarization techniques that overcome this limitation by strongly polarizing the nuclear spins [1–5].

The two hyperpolarization techniques used for this work are parahydrogen induced polarization (PHIP) [6], and dissolution dynamic nuclear polarization (dDNP) [7]. In PHIP, nuclear spin polarization is engendered from the nuclear spin-singlet ($I = 0$) *para* isomer of hydrogen gas. Para-H_2 molecules are bound (reversibly, or irreversibly) to a substrate molecule, to produce a ^{1}H-polarized product. In dDNP, nuclear spin polarization of a target molecule is engendered from a polarized electron bath. Electrons have naturally higher spin polarization, and this can be converted into nuclear spin polarization [8].

One significant motivation for the production of hyperpolarized substances is for *in vivo* imaging experiments [5, 9, 10]. There is a marked difference in the metabolism of biomolecules in healthy cells as compared to tumorous or necrotic cells, and this can provide contrast for magnetic resonance imaging [11].

A number of metabolites are currently under investigation for this purpose, including [1-^{13}C]pyruvate [11–13], [1,4-$^{13}C_2$]fumarate [14–18], [1-^{13}C]glutamate [19, 20], and [1-^{13}C]succinate [21–24], to name a few. The typical procedure is to produce a solution containing a ^{13}C-hyperpolarized metabolite, and inject the solution into a subject. The molecules are metabolised (i.e. converted into different molecules in a metabolic pathway), and by measuring the rate of metabolism, an inference can be made about the type/health of cells in a particular region of the body.

After production of the hyperpolarized molecules, the whole procedure to the point of MRI signal acquisition should take no more than approximately one minute,

because the nuclear spins relax from the hyperpolarized state to the thermal equilibrium polarization state.

This is part of the reason ^{13}C is the nucleus of choice in the aforementioned molecules [5], rather than ^{1}H; carbon-13 spins typically relax slower. The second reason for the use of ^{13}C is the lack of background signal in the body. The natural abundance of carbon-13 is just 1.1%, whereas protons are hugely abundant in the body because humans are ∼60% water!

This thesis describes techniques for converting parahydrogen proton polarization into ^{13}C polarization, which is necessary for producing ^{13}C-polarized metabolites for *in vivo* use via PHIP. This thesis also describes a method to extend the hyperpolarization lifetime in the metabolite fumarate, after DNP hyperpolarization.

Chapter 2

Fundamental NMR Theory

Nuclear magnetic resonance (NMR) theory can, broadly speaking, be described using two distinct approaches:

1. Classically, where the nuclear spins are approximated to behave as tiny bar magnets which transform (e.g. rotate) in space. Although not rigorously correct, many experiments can be described by considering the net magnetization of the sample as a vector in 3D space.
2. Quantum mechanically, where the individual nuclear spins are in distinct, quantized states, and an operator describes the state of the spin ensemble. Most experiments can be described by propagating this operator in a higher dimensional Liouville space.

For much of the work presented here it will be necessary to have an understanding of the quantum theory. Unfortunately, many millenia of human evolution hunting lions on the African savannah has left us rather poorly equipped for this task. For this reason, the classical approach is also included, which is dramatically more intuitive, and turns out to be sufficient for describing many of the experiments in this thesis.

This chapter is mostly based on theory described in Refs [25, 26], and should provide the reader with sufficient knowledge to understand the later chapters.

2.1 Classical Description of NMR

2.1.1 Spin-1/2 Nuclei as Tiny, Tiny Bar Magnets

Matter - or at least the kind of consequence to the average person - for the most part, is made up of atoms. These atoms each contain a nucleus. This nucleus can possess a special property; spin.

Nuclear spin is an intrinsic property of each atomic nucleus, and can take half-integer or whole-integer values. For the purpose of this work we are only interested in spin-1/2 nuclei; specifically the proton, ^{1}H, and an isotope of carbon, ^{13}C, which occurs at ∼1% natural abundance (with spin-0 ^{12}C occurring at ∼99% natural abundance). Neglecting the dynamics of nuclei with spin >1/2 allows us to avoid the rather complicated field of quadrupolar NMR.

Spin¿1/2 nuclei have a magnetic dipole moment, and can be considered to behave - to an approximation - as tiny bar magnets: when placed in an external magnetic field, they have a tendency to align along the direction of the magnetic field. This external field will be called B_0, and is assumed to be oriented along the $+z$-axis.

For the classical description of NMR, we need to take just one lesson from quantum mechanics.

When placed in a magnetic field, a spin-1/2 nucleus has two energy levels, with an energy separation that depends linearly on magnetic field. This is illustrated in Fig. 2.1. We will label these two levels α and β for now, and the reason for this will become clear in section 2.2. In a truly quantum mechanical way, if the magnetization

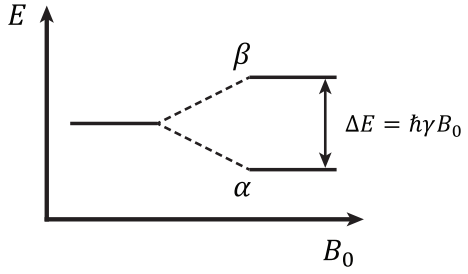

FIGURE 2.1: The energy levels of a spin-1/2 particle in a magnetic field.

of a spin-1/2 nucleus is observed, it will be found to be in one of these two energy levels. When measuring an ensemble of spins, each spin can exist in either state α or β, and overall the nuclei have a preference to exist in the lower energy state, α. The difference in populations of the two energy levels at *thermal equilibrium* is dictated by the Boltzmann distribution:

$$\frac{\mathrm{P}_\beta}{\mathrm{P}_\alpha} = e^{-\Delta E/k_\mathrm{B}T}, \tag{2.1}$$

where $\mathrm{P}_\beta/\mathrm{P}_\alpha$ is the population ratio between the corresponding states, k_B is the Boltzmann constant, and T is the temperature of the system. The polarization level of an ensemble of spin-1/2 nuclei is given by:

$$p = \frac{\mathrm{P}_\alpha - \mathrm{P}_\beta}{\mathrm{P}_\alpha + \mathrm{P}_\beta}. \tag{2.2}$$

For the nuclei in a typical NMR experiment, which operates at ∼298 K, and a field of up to 20 T, this polarization level is in the order of 10^{-5}, which is to say the spins are

weakly aligned along the direction of the magnetic field; the polarization is small. It is this small degree of spin polarization that leads to the famously low sensitivity of the NMR experiment.

We can now return to a classical description of NMR, and study the net magnetic moment of the entire spin ensemble.

2.1.2 Precession

The nuclei will precess around the magnetic field axis at a frequency known as the Larmor frequency, which is given by:

$$\omega_j^0 = -\gamma_j B_0, \tag{2.3}$$

with j a spin label that corresponds to a specific nuclear isotope, and γ the gyromagnetic ratio, a property intrinsic to each nuclear isotope type.

γ is in the order of $10^9\,\mathrm{rad\,s^{-1}\,T^{-1}}$ for ^{1}H and ^{13}C nuclei, which corresponds to Larmor frequencies of hundreds of megahertz for a typical high-field NMR experiment.

2.1.3 The Vector Model

The net magnetic moment of the spin ensemble can be modelled as a vector that rotates in real 3D space. This 'vector model' of NMR is illustrated in Fig. 2.2 for an arbitrary sequence of events. The magnetization vector is initially oriented along the z-axis, which corresponds to *longitudinal* magnetization. It is then rotated into the xy-plane, which corresponds to *transverse* magnetization, and then freely precesses around the magnetic field axis.

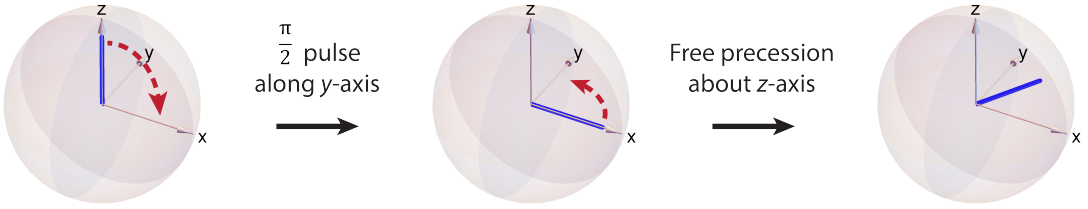

FIGURE 2.2: The vector model. The net magnetization vector is shown in blue. The sequence shown is an imagined scenario of a $\pi/2$ pulse rotating the magnetization vector around the y-axis, followed by free precession of the spins around the z-axis.

The rotation of magnetization vectors in NMR can be described by the Bloch equations [27]. This system of linear differential equations describes the time evolution

of magnetization along an axis in the presence of orthogonal magnetic fields.

$$\begin{aligned}\frac{dM_x(t)}{dt} &= \gamma(B_z(t)M_y(t) - B_y(t)M_z(t)),\\ \frac{dM_y(t)}{dt} &= \gamma(B_x(t)M_z(t) - B_z(t)M_x(t)),\\ \frac{dM_z(t)}{dt} &= \gamma(B_y(t)M_x(t) - B_x(t)M_y(t)).\end{aligned} \tag{2.4}$$

M_k is the magnetization vector component along the k-axis, B_k is the magnetic field along the k-axis, and γ is the gyromagnetic ratio of the nuclear spin. This form of the Bloch equations neglects relaxation (see section 2.1.6).

If we take the case of precessing magnetization around a static magnetic field along the z-axis (B_0), we can write the Bloch equations as follows:

$$\begin{aligned}\frac{dM_x(t)}{dt} &= \gamma B_0 M_y(t),\\ \frac{dM_y(t)}{dt} &= -\gamma B_0 M_x(t),\\ \frac{dM_z(t)}{dt} &= 0,\end{aligned} \tag{2.5}$$

which again neglects relaxation. These equations have the solution

$$\begin{aligned}\frac{dM_x(t)}{dt} &= \cos(\omega^0 t)M_x(0) + \sin(\omega^0 t)M_y(0),\\ \frac{dM_y(t)}{dt} &= \cos(\omega^0 t)M_y(0) + \sin(\omega^0 t)M_x(0),\\ \frac{dM_z(t)}{dt} &= 0,\end{aligned} \tag{2.6}$$

where $\omega^0 = -\gamma B_0$. For the case of precession in the xy-plane, one obtains $M_z(t) = 0$.

In a typical NMR experiment, the B_0 field might be many tesla, and the precession frequency of spin-1/2 nuclei is in the order of hundreds of megahertz. This corresponds to radio frequencies in the electromagnetic spectrum. When considering precessing spins, it can be helpful to make a transformation from a static frame of reference, to a 'rotating frame'. For a spin precessing at an arbitrary frequency ω, the precession frequency in the *rotating frame* is given by:

$$\Omega = \omega - \omega_{\text{ref}}. \tag{2.7}$$

Ω is the 'offset', and ω_{ref} the precession frequency of the rotating frame. We can define an apparent field along the z-axis in the rotating frame, as

$$B_0^{\text{apparent}} = \frac{\Omega}{\gamma}. \tag{2.8}$$

'Pulses' are used in NMR experiments to manipulate the magnetization. A pulse

is a magnetic field oscillating at the frequency of the rotating frame, applied (typically) in the xy-plane to induce precession of the magnetization around an axis other than z. The magnetic field of the pulse is labelled B_1, and is usually many orders of magnitude smaller than the B_0 field amplitude.

The magnetization is precessing around B_0 at the Larmor frequency, and so a weak B_1 field applied along the x-axis would do little to perturb the magnetization. The effective magnetic field experienced by the spins is given by:

$$B_0^{\text{eff}} = \sqrt{(B_1)^2 + \left(B_0^{\text{apparent}}\right)^2}. \tag{2.9}$$

If the B_1 field is applied in the rotating frame (i.e. made to oscillate at the Larmor frequency), $B_0^{\text{apparent}} \to 0$. Hence, the effective field experienced by the spins is then the B_1 field, as desired. The term 'rf pulses' (Radio Frequency) is often used since the typical B_1 fields applied will oscillate at radio frequencies.

This technique is particularly powerful because pulses can address spins at a specific frequency. A clear example of this is an rf pulse being applied to the ^{1}H or ^{13}C 'channel'. We know ^{1}H and ^{13}C spins have different Larmor frequencies (see Eq. 2.3), and so by applying an rf pulse at the ^{1}H Larmor frequency, or *on resonance* with the ^{1}H spins, it has almost no effect on the ^{13}C spins because it is off-resonance with the ^{13}C spins.

2.1.4 Fourier Transform NMR

We will now examine how one can produce an NMR spectrum from the nuclear spin magnetization of a sample of uncoupled nuclear spins in a magnetic field.

We describe an experiment using a *pulse sequence*, shown in Fig. 2.3. The pulse sequence in this case is simply a $\pi/2$ pulse along the y-axis, followed by signal acquisition. The pulse tips the magnetization vector into the xy-plane, and we will assume the pulse duration is much less than the precession period (and hence there is no spin precession during the pulse). The spins then precess freely around the magnetic-field axis with a frequency ω_0 until they relax back to thermal equilibrium. Relaxation will be discussed further in section 2.1.6.

In an inductively-detected NMR experiment, the oscillation of the spins induces a current in coils around the sample, which is detected. The resulting signal is referred to as a *free induction decay* (FID), and is typically an exponentially decaying sinusoidal function. The signal produced from oscillating magnetization in the sample can be written as

$$S(t) = S_0\, e^{i\,\omega_0\, t}\, e^{-t/T_R} = S_0(\cos{(\omega_0\, t)} + i\, \sin{(\omega_0\, t)})\, e^{-t/T_R}, \tag{2.10}$$

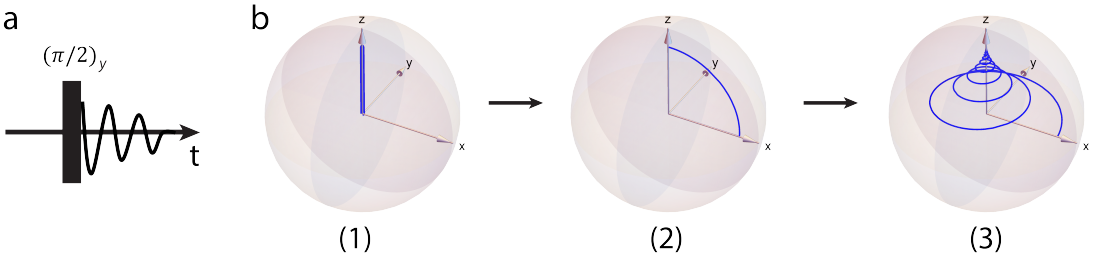

FIGURE 2.3: a) A pulse sequence diagram. b) (1) The sample's magnetization starts at thermal equilibrium along the z-axis; (2) The $(\pi/2)_y$ pulse rotates the magnetization vector around the y-axis; (3) the magnetization vector precesses in the xy-plane around the z-axis and eventually returns to the thermal equilibrium position along the z-axis. Images were generated using the SpinDynamica package for Mathematica [28], and the code is given in Appendix II.

where S_0 is the magnetization projection in the xy-plane immediately following the excitation pulse, and the factor e^{-t/T_R} describes the decay of the detectable signal (i.e. magnetization in the xy-plane) with a time-constant T_R. The conversion from exponential to trigonometric form is performed using Euler's formula: $e^{ix} = \cos x + i \sin x$.

$S(t)$ is relatively simple to interpret if the sample contains spins that precess at the same frequency, but if spins in the sample precess at different frequencies, the FID rapidly becomes uninterpretable.

The solution is to perform a Fourier transform (FT) of the FID, which converts the time-domain data into the frequency-domain. The explicit form of the Fourier transform is

$$f(\omega) = \int_{-\infty}^{\infty} f(t) e^{-i\omega t} dt, \tag{2.11}$$

which can be written more concisely as

$$f(\omega) = \mathcal{F}\{f(t)\}(\omega),$$

where $f(t)$ is a signal in the time domain (which in this case could be the FID), and $f(\omega)$ is the signal in the frequency domain.

The Fourier transform of the FID from Eq. 2.10 is

$$\mathcal{F}\{S(t)\}(\omega) = S_0 \sqrt{\frac{2}{\pi}} \frac{T_R}{1 + (\omega + \omega_0)^2 T_R^2}, \tag{2.12}$$

which is a Lorentzian function centred at $-\omega_0$, with a width proportional to the inverse of the exponential decay rate constant T_R. This is made more clear by examining two distinct Fourier transforms:

$$\mathcal{F}\{e^{i\omega_0 t}\}(\omega) = \sqrt{2\pi}\, \delta(\omega + \omega_0), \tag{2.13}$$

where $\delta(\omega + \omega_0)$ is a delta function at a frequency $-\omega_0$, and

$$\mathcal{F}\{e^{-|t|/T_R}\}(\omega) = \sqrt{\frac{2}{\pi}}\frac{T_R}{1+\omega^2 T_R^2}, \tag{2.14}$$

is a Lorentzian function.

The NMR signal represented in the frequency domain is a spectrum. If a sample contains many spins with different precession frequencies, the spectrum will contain multiple peaks centred at these frequencies. So far we have only seen Larmor frequency differences between spins of different isotopic type. Now we will examine two effects, chemical shift and J-coupling, which are responsible for the appearance of the spectra in this thesis.

2.1.5 The NMR Spectrum

Nuclear spins in a molecule are surrounded by "clouds" of electrons, which can act to either shield or deshield the effect of the external B_0 field on the nuclear spins.

A *chemical shielding factor* σ can be defined, which shifts the resonance frequency of a nuclear spin. We can include this factor in Eq. 2.3:

$$\omega_j = -\gamma_j B_0(1-\sigma), \tag{2.15}$$

The shielding factor is specific to each nucleus in a molecule, although it is possible for multiple nuclei to have the same shielding factor. In this instance we refer to them as *chemically equivalent*.

The shielding factor is often in the order of 10^{-6} for ^{1}H, and 10^{-4} for ^{13}C. When examining spectra, it is inconvenient to use absolute frequencies, which are in the order of hundreds of MHz, but with variations between peaks of perhaps kHz. The *chemical shift* is therefore introduced, as a relative frequency scale. The chemical shift of a nucleus is defined:

$$\delta = \frac{\omega_j - \omega_j^{\text{ref}}}{\omega_j^{\text{ref}}}, \tag{2.16}$$

where ω_j is the precession frequency of the nucleus of interest, and ω_j^{ref} is the precession frequency of a reference compound. δ is a dimensionless quantity, and independent of magnetic field. It is often a small number, and is therefore commonly expressed in parts per million (ppm).

In addition to "seeing" the external B_0 field, the nuclear spins can also see magnetic fields produced by neighbouring nuclear spins mediated by the chemical bonds.

This spin-spin *coupling* is called J-coupling, and gives rise to peak splittings in spectra. J-couplings are typically in the order of 1-100 Hz. The J-coupling interaction is discussed in more detail in section 2.2.3.3.

Both the shielding factor σ and J-coupling are tensor quantities, meaning they depend on molecular and spin orientation with respect to the external magnetic field. However, in solution-state NMR, small molecules typically isotropically tumble rapidly compared to the timescale of an NMR experiment. This isotropically averages the interaction tensors, resulting in a scalar quantity for each.

There are additional electromagnetic effects that nuclear spins experience, e.g. through-space spin-spin coupling (dipole-dipole coupling), and quadrupole coupling for spin>1/2 nuclei [29]. However, aside from their contribution to relaxation effects, these interactions are not relevant in the context of this work.

2.1.6 Relaxation

2.1.6.1 General Principles

Relaxation in NMR is the process by which a nuclear spin system returns to its thermal equilibrium state. In the context of uncoupled spin-1/2 nuclei in a magnetic field, thermal equilibrium corresponds to the bulk magnetization vector pointing along the B_0 field axis, z (see Fig. 2.3(1)).

There are two types of relaxation in this system: T_1, the 'longitudinal' relaxation time, and T_2, the 'transverse' relaxation time. The difference between them is illustrated in Fig. 2.4. T_1 is the rate constant that governs return of the magnetization vector to its equilibrium position in the z-axis, and T_2 is the rate constant that governs return of the magnetization vector to its equilibrium position in the xy-plane. It is more correct to say T_1 and T_2 are the relaxation rate constants for populations, and coherences in the *density operator* (see section 2.2.3.2), respectively, but this does not fit into a classical description of NMR.

From the simple picture in Fig. 2.4, T_1 is defined as

$$M_z(t) = M_{z,\mathrm{eq}} - (M_{z,\mathrm{eq}} - M_z(0))e^{-t/T_1}, \tag{2.17}$$

where $M_{z,\mathrm{eq}}$ is the magnetization vector along the z-axis at thermal equilibrium, and $M_z(t)$ the z-magnetization at time t. T_2 can be defined as

$$M_{xy}(t) = M_{xy}(0)e^{-t/T_2}, \tag{2.18}$$

which assumes $M_{xy,\mathrm{eq}} = 0$.

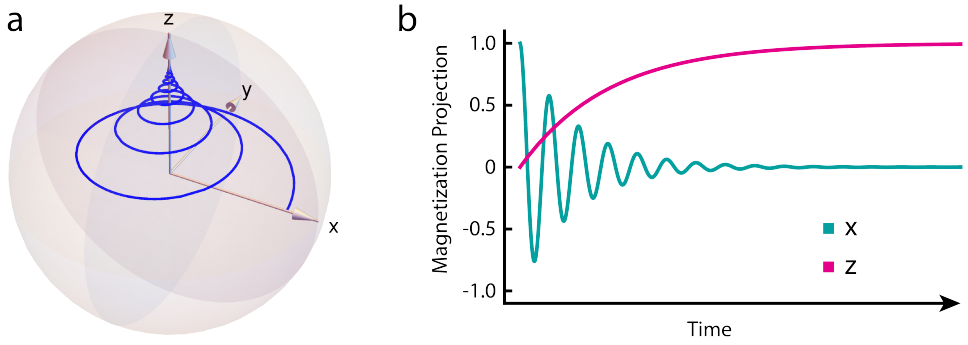

FIGURE 2.4: a) A magnetization vector precesses in the xy-plane around the z-axis and eventually returns to the thermal equilibrium position. b) A plot of the magnetization vector projection along the z-axis (pink), and x-axis (cobalt). Images were generated using the SpinDynamica package for Mathematica [28], and the code is given in Appendix II.

With these definitions, relaxation can be introduced into the Bloch equations from Eq. 2.4, and they can be rewritten as

$$\begin{aligned}
\frac{dM_x(t)}{dt} &= \gamma(B_z(t)M_y(t) - B_y(t)M_z(t)) - \frac{M_x(t)}{T_2}, \\
\frac{dM_y(t)}{dt} &= \gamma(B_x(t)M_z(t) - B_z(t)M_x(t)) - \frac{M_y(t)}{T_2}, \\
\frac{dM_z(t)}{dt} &= \gamma(B_y(t)M_x(t) - B_x(t)M_y(t)) - \frac{M_z(t) - M_z(0)}{T_1}.
\end{aligned} \tag{2.19}$$

For relaxation to occur, the spins need to exchange energy with their surroundings. This process is most efficient when local magnetic fields (usually arising from the molecular environment) fluctuate at - or near - the Larmor frequency of the relaxaing spins. These fluctuating local fields can be thought of as a pulse acting on a spin, but importantly these "pulses" are incoherent and lead to effectively random rotations of the nuclear spins. After sufficient time, this random redistribution of the nuclear spin orientations leads to the thermal equilibrium state being restored.

As a general rule of thumb for solution-state relaxation at high field, rotational motion and molecular tumbling are often efficient relaxation processes, whereas vibrational and electronic transitions are higher frequency and inefficient.

An additional relaxation rate constant T_2^* should also be introduced. T_2^* describes the rate at which precessing nuclear spins coherently dephase in the xy-plane. If a spin system is subject to a magnetic field gradient, the spins will see a different B_0 field and precess at different frequencies. This can lead to rapid dephasing (and hence loss) of transverse magnetization. Note that T_2^* is not the same as T_2: T_2^* is a coherent dephasing of spins, and one can use a *spin echo* [30] to rephase the spins to recover the transverse magnetization, but T_2 relaxation is an incoherent process and cannot be reversed. The relaxation constant introduced as T_R in Eq. 2.10 is T_2^*.

2.1.6.2 T_1 Measurement Techniques

In this thesis, two measurement techniques are employed to measure the T_1 of a sample. Both are presented here.

The *inversion recovery* method [31] is shown in Fig. 2.5. The principle behind this pulse sequence is to invert the thermal equilibrium z-magnetization with a π pulse, and observe the signal after a variable recovery time.

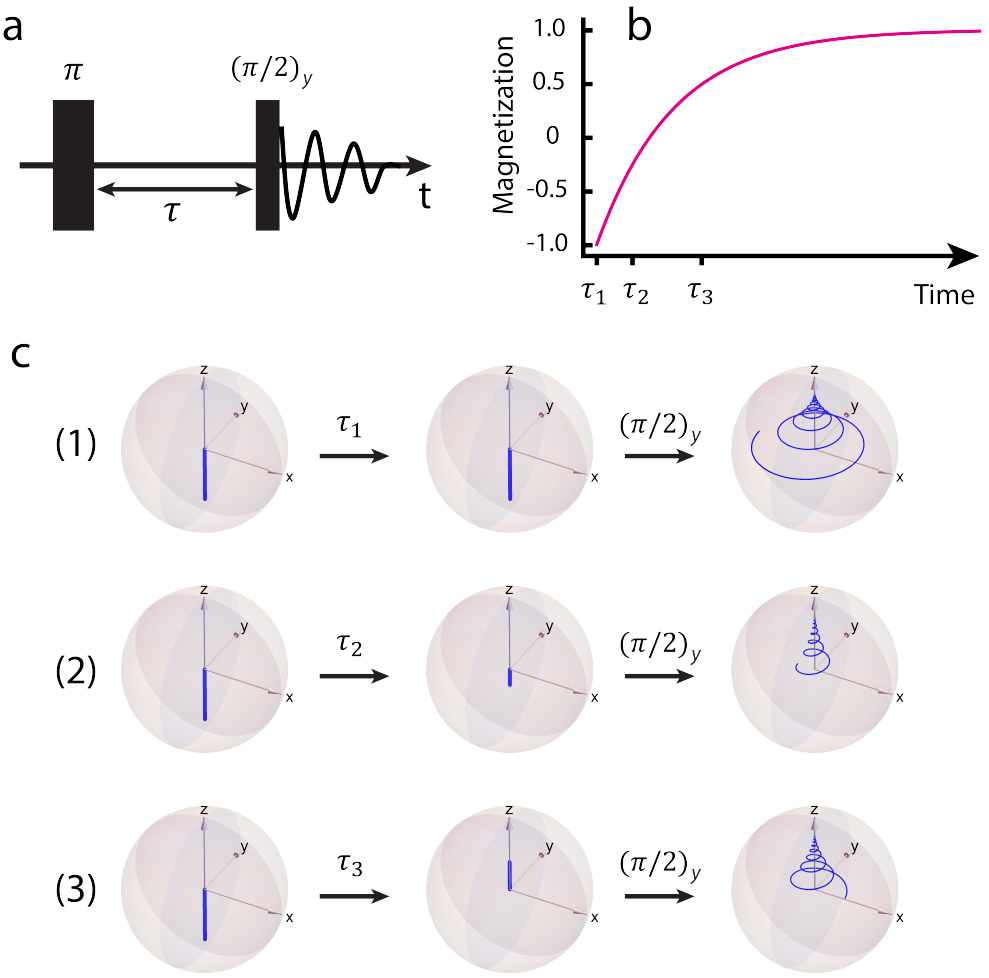

FIGURE 2.5: a) An inversion recovery pulse sequence. b) A plot of the expected signal acquired by varying τ. c) Illustrations of the magnetization vector throughout the pulse sequence, for three different values of τ. The first image in each sequence is the magnetization immediately following the π pulse. The second image is the magnetization after a chosen τ delay. The final image in each sequence shows the FID following a $(\pi/2)_y$ pulse. Note the difference in phase of the FIDs. Images were generated using the SpinDynamica package for Mathematica [28], and the code is given in Appendix II.

The *saturation recovery* method [32] is shown in Fig. 2.6. The principle behind this pulse sequence is to saturate (destroy) the thermal equilibrium z-magnetization with a train of pulses, and observe the signal after a variable recovery time.

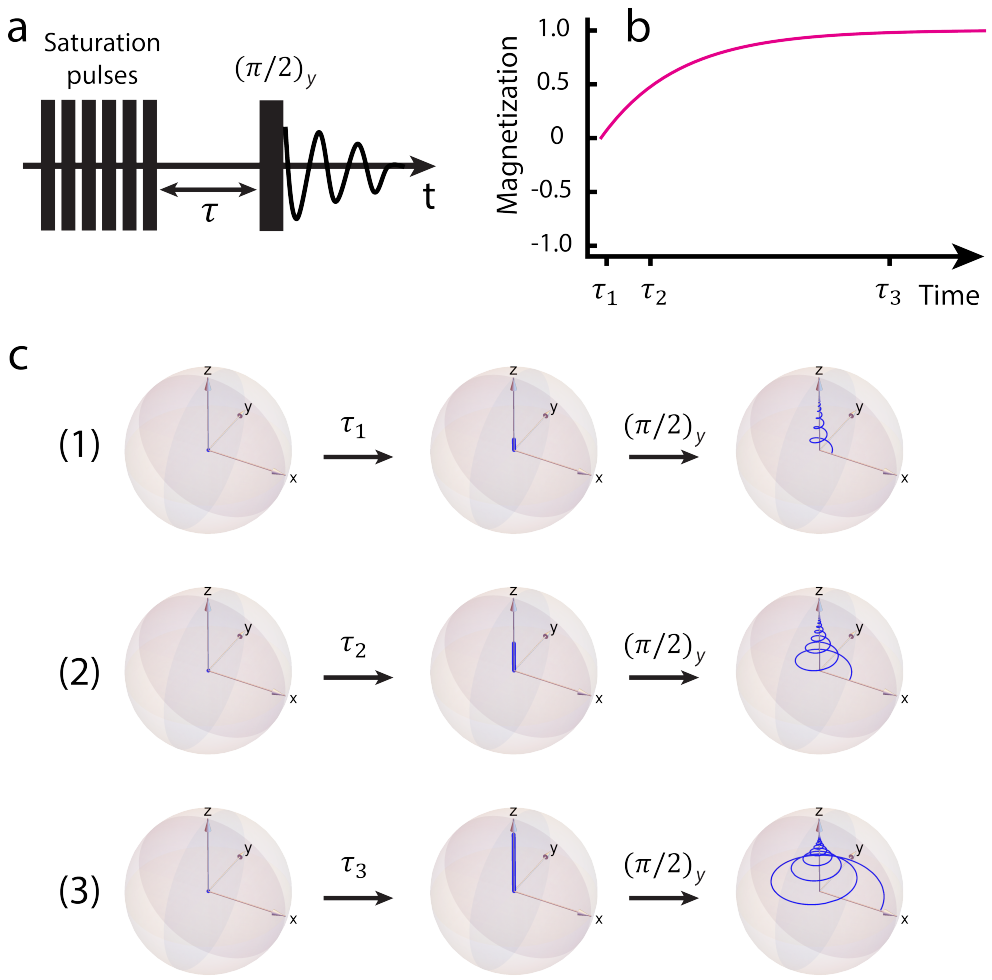

FIGURE 2.6: a) A saturation recovery pulse sequence. b) A plot of the expected signal acquired by varying τ. c) Illustrations of the magnetization vector throughout the pulse sequence, for three different values of τ. The first image in each sequence is the magnetization immediately following the saturation pulses (it has been destroyed). The second image is the magnetization after a chosen τ delay. The final image in each sequence shows the FID following a $(\pi/2)_y$ pulse. Images were generated using the SpinDynamica package for Mathematica [28], and the code is given in Appendix II.

Saturation recovery is the preferred technique in the case of samples with a long T_1, because one does not need to wait for the sample magnetization to recover to thermal equilibrium between experiments. Inversion recovery is preferred in samples with a feasibly short T_1, because the data acquired has a larger dynamic range.

2.2 Quantum Description of NMR

2.2.1 Nuclear Spin

Nuclear spin ($\hat{I}$) is a type of angular momentum. Analogous to the angular momentum of a car wheel, it can be described by a magnitude, $|\hat{I}|$, and direction, m_I. Unfortunately, this is where the similarity ends. The magnitude is given by

$$|\hat{I}| = \hbar\sqrt{I(I+1)}, \tag{2.20}$$

where $\hbar$ is the reduced Planck constant. The projection of $\hat{I}$ along the z-axis (which in many cases is defined by an external magnetic field), is given by

$$\hat{I}_z = m_I\hbar. \tag{2.21}$$

m_I can take values in integer steps from $-I$ to $+I$, and this is shown in Fig. 2.7.

For the case of a spin-1/2 nucleus, $I = 1/2$, and so $m_I = \pm 1/2$. This means if we measure the value of $\hat{I}_z$, we will get value of $\pm m_I\hbar$ with some probability, depending on the 'state' of the system.

We will now examine what it means for the system to be in a state.

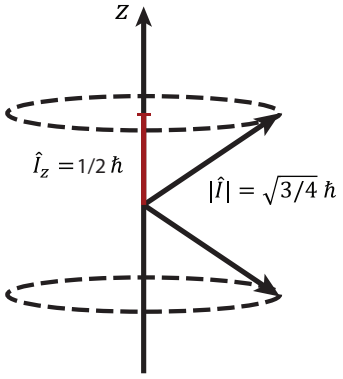

FIGURE 2.7: An illustration of the magnitude ($|\hat{I}|$) and z-axis projection ($\hat{I}_z$) of a spin-1/2 particle in a magnetic field. Note the value of $\hat{I}_z$ depends on the state of the system, and can take values in integer steps from $-I$ to $+I$.

2.2.2 Spin States and Hilbert Space

A spin-1/2 nucleus in a magnetic field can exist in two states; $|I, m_I\rangle$, with $m_I = \pm 1/2$. The I is dropped for brevity, which gives $|m_I\rangle$, which we will henceforth call $|\alpha\rangle$ and $|\beta\rangle$. If the spin is in the $|\alpha\rangle$ state, we colloquially call it 'spin up', and if the spin is in the $|\beta\rangle$ state, we call it 'spin down'. This is a two-level system, and the spin can be in any linear combination of the two states. By *measuring* the spin's projection along z,

we can only get a value of m_I, corresponding to the spin being in $|\alpha\rangle$ or $|\beta\rangle$. Just like Prof. Schrödinger's cat - when the box is opened, the cat can only be observed in one of two states: alive or dead.

In Dirac notation, a quantum state is written as a 'ket', $|\psi\rangle$, and corresponds to a vector in a complex N-dimensional Hilbert space, $\mathcal{H}_N$. The basis vectors ($|\mathrm{r}\rangle$) of this Hilbert space are $|\alpha\rangle$ and $|\beta\rangle$, which are called the *Zeeman basis* states, and take the form

$$|\alpha\rangle = \begin{pmatrix} 1 \\ 0 \end{pmatrix} \qquad |\beta\rangle = \begin{pmatrix} 0 \\ 1 \end{pmatrix}. \tag{2.22}$$

A set of 'bras' can also be defined by taking the conjugate transpose of the corresponding ket, i.e. $|\alpha\rangle^\dagger = \langle\alpha|$, such that

$$\langle\alpha| = \begin{pmatrix} 1 & 0 \end{pmatrix} \qquad \langle\beta| = \begin{pmatrix} 0 & 1 \end{pmatrix}. \tag{2.23}$$

The state $|\psi\rangle$ of a two level system can be completely described in the Zeeman basis as linear combinations of the basis vector states:

$$|\psi\rangle = \mathrm{c}_1 |\alpha\rangle + \mathrm{c}_2 |\beta\rangle = \begin{pmatrix} \mathrm{c}_1 \\ \mathrm{c}_2 \end{pmatrix}, \tag{2.24}$$

and

$$\langle\psi| = \mathrm{c}_1^* \langle\alpha| + \mathrm{c}_2^* \langle\beta| = \begin{pmatrix} \mathrm{c}_1^* & \mathrm{c}_2^* \end{pmatrix}. \tag{2.25}$$

The states are normalised such that $\mathrm{c}_1^2 + \mathrm{c}_2^2 = 1$.

To form a complete Hilbert space, the basis states $|\mathrm{r}\rangle$ must be orthonormal. For orthonormality, the following condition must be satisfied for the inner product of the basis states $|\mathrm{r_i}\rangle$ and $|\mathrm{r_j}\rangle$:

$$\langle \mathrm{r_i} | \mathrm{r_j} \rangle = \delta_{\mathrm{ij}}, \tag{2.26}$$

where the Kronecker Delta is defined as

$$\delta_{\mathrm{ij}} = \begin{cases} 1 & \text{if } \mathrm{i} = \mathrm{j} \\ 0 & \text{if } \mathrm{i} \neq \mathrm{j} \end{cases}, \tag{2.27}$$

and the notation for the inner product $\langle \mathrm{r_i} | \mathrm{r_j} \rangle$ indicates taking the dot product of the two vectors $|\mathrm{r_i}\rangle$ and $|\mathrm{r_j}\rangle$.

For orthonormality, the following condition must be satisfied for the outer product of the basis states $|\mathrm{r_n}\rangle$ and $|\mathrm{r_n}\rangle$ for an N-spin system.

$$\sum_{\mathrm{n}=1}^{\mathrm{N}} |\mathrm{r_n}\rangle \langle \mathrm{r_n}| = \mathbb{1}, \tag{2.28}$$

where $\mathbb{1}$ is the identity matrix.

The inner product is also used to quantify the projection of one state along another. For example, by taking our definition of $|\psi\rangle$ from Eq. 2.24, we can construct the following inner products to determine the projection of $|\psi\rangle$ on $|\alpha\rangle$ and $|\beta\rangle$.

$$\langle\alpha|\psi\rangle = \mathrm{c}_1 \quad \langle\beta|\psi\rangle = \mathrm{c}_2, \tag{2.29}$$

If a second spin is introduced to the system, the Hilbert space is extended to accommodate the additional spin states by taking the tensor product of the component basis spin states:

$$\begin{aligned} |\alpha_1\alpha_2\rangle = |\alpha_1\rangle \otimes |\alpha_2\rangle = \begin{pmatrix} 1 \\ 0 \\ 0 \\ 0 \end{pmatrix} \quad |\alpha_1\beta_2\rangle = |\alpha_1\rangle \otimes |\beta_2\rangle = \begin{pmatrix} 0 \\ 1 \\ 0 \\ 0 \end{pmatrix} \\ |\beta_1\alpha_2\rangle = |\beta_1\rangle \otimes |\alpha_2\rangle = \begin{pmatrix} 0 \\ 0 \\ 1 \\ 0 \end{pmatrix} \quad |\beta_1\beta_2\rangle = |\beta_1\rangle \otimes |\beta_2\rangle = \begin{pmatrix} 0 \\ 0 \\ 0 \\ 1 \end{pmatrix}. \end{aligned} \tag{2.30}$$

The subscripts indicate the spin label, e.g. $|\alpha_1\beta_2\rangle$ means spin 1 is in the α state, and spin 2 is in the β state.

In summary, we can describe the spin state of an N-spin system using the Zeeman basis states. This is unfortunately of little consequence without the ability to act on the states. For this purpose, we will now examine *operators*.

2.2.3 Operators and Liouville Space

Let us consider an operator $\hat{A}$, with eigenstates $|\alpha\rangle$ and $|\beta\rangle$. The action of an operator (which will be denoted by a single hat) on one of its eigenstates is

$$\hat{A}\,|\alpha\rangle = a\,|\alpha\rangle\,, \tag{2.31}$$

i.e. the same state is returned, but multiplied by a, which is the eigenvalue of $|\alpha\rangle$ in the operator basis of A.

The 'expectation value' of an operator can be found by the following operation:

$$\langle\hat{A}\rangle = \langle\alpha|\,\hat{A}\,|\alpha\rangle = a\,\langle\alpha|\alpha\rangle = a, \tag{2.32}$$

which returns the pure eigenvalue.

For a two-level system, the Hilbert space $\mathcal{H}_2$ in which states exist is spanned by the basis vectors $|\alpha\rangle$ and $|\beta\rangle$. In the same way, for a two-level system, four operators are needed to span the four-dimensional (N^2) Liouville space $\mathcal{L}_4$ in which operators exist.

In NMR these are often the three angular momentum operators $\hat{I}_x$, $\hat{I}_y$, and $\hat{I}_z$ defined by the Pauli spin matrices multiplied by $\hbar/2$, and the identity operator $\hat{\mathbb{1}}$.

$$\hat{I}_x = \frac{\hbar}{2}\begin{pmatrix} 0 & 1 \\ 1 & 0 \end{pmatrix} \quad \hat{I}_y = \frac{\hbar}{2i}\begin{pmatrix} 0 & 1 \\ -1 & 0 \end{pmatrix} \quad \hat{I}_z = \frac{\hbar}{2}\begin{pmatrix} 1 & 0 \\ 0 & -1 \end{pmatrix} \quad \hat{\mathbb{1}} = \begin{pmatrix} 1 & 0 \\ 0 & 1 \end{pmatrix}. \tag{2.33}$$

To take a real example drawing on what we have already covered, for our spin-1/2 particle in a magnetic field, we now examine the projection of the $|\alpha\rangle$ state along the z-axis.

$$\hat{I}_z |\alpha\rangle = \frac{\hbar}{2}\begin{pmatrix} 1 & 0 \\ 0 & -1 \end{pmatrix}\begin{pmatrix} 1 \\ 0 \end{pmatrix} = \frac{\hbar}{2}\begin{pmatrix} 1 \\ 0 \end{pmatrix} = \frac{\hbar}{2}|\alpha\rangle. \tag{2.34}$$

Hence, $\pm\hbar/2$ are the eigenvalues of $|\alpha\rangle$ and $|\beta\rangle$, respectively, for the operator $\hat{I}_z$. For convenience, we will henceforth set $\hbar = 1$.

Three additional operators are introduced:

$$\begin{aligned} \hat{I}^2 &= \hat{I}_x^2 + \hat{I}_y^2 + \hat{I}_z^2, \\ \hat{I}^+ &= \hat{I}_x + i\hat{I}_y, \\ \hat{I}^- &= \hat{I}_x - i\hat{I}_y, \end{aligned} \tag{2.35}$$

the *total square angular momentum* operator, and two *shift* operators. These act in the following way:

$$\begin{aligned} \hat{I}^2 |I, m_I\rangle &= I(I+1)\,|I, m_I\rangle \\ \hat{I}^+ |I, m_I\rangle &= -\sqrt{(I(I+1) - m(m+1))}\,|I, m_{I+1}\rangle \\ \hat{I}^- |I, m_I\rangle &= +\sqrt{(I(I+1) - m(m-1))}\,|I, m_{I-1}\rangle. \end{aligned} \tag{2.36}$$

The shift operators shift the spin state either "up", or "down". Using the spin-1/2 particle in a magnetic field as an example,

$$\begin{aligned} \hat{I}^+ |\alpha\rangle = 0 \qquad \hat{I}^+ |\beta\rangle = |\alpha\rangle \\ \hat{I}^- |\alpha\rangle = |\beta\rangle \qquad \hat{I}^- |\beta\rangle = 0. \end{aligned} \tag{2.37}$$

The commutator of two operators is defined as

$$\left[\hat{A}, \hat{B}\right] = \hat{A}\hat{B} - \hat{B}\hat{A}. \tag{2.38}$$

If $\left[\hat{A}, \hat{B}\right] = 0$, the operators commute. The $\hat{I}_x$, $\hat{I}_y$, and $\hat{I}_z$ operators follow cyclic commutation rules:

$$\begin{aligned}\left[\hat{I}_x, \hat{I}_y\right] &= i\hat{I}_z \\ \left[\hat{I}_y, \hat{I}_z\right] &= i\hat{I}_x \\ \left[\hat{I}_z, \hat{I}_x\right] &= i\hat{I}_y\end{aligned} \tag{2.39}$$

This is of great import in NMR, as it imparts rules for the rotations of spins, as is examined below.

2.2.3.1 Superoperators

Just as states are transformed in Hilbert space by operators, so can operators be transformed in Liouville space by *superoperators* (which will be denoted by a double hat).

A simple example of this is the commutation superoperator, $\hat{\hat{A}}$, defined as follows:

$$\hat{\hat{A}}\hat{B} = \left[\hat{A}, \hat{B}\right] = \hat{A}\hat{B} - \hat{B}\hat{A}. \tag{2.40}$$

Applying the commutation superoperator $\hat{\hat{A}}$ to an operator $\hat{B}$ results in the commutator between $\hat{A}$ and $\hat{B}$.

Three rotation superoperators can be defined from commutation superoperators of the angular momentum operators in Eq. 2.33.

$$\hat{\hat{R}}_x(\theta) = \exp\{-i\hat{\hat{I}}_x\theta\} \qquad \hat{\hat{R}}_y(\theta) = \exp\{-i\hat{\hat{I}}_y\theta\} \qquad \hat{\hat{R}}_z(\theta) = \exp\{-i\hat{\hat{I}}_z\theta\}. \tag{2.41}$$

These can be applied to the angular momentum operators using the 'sandwich' formula:

$$\hat{\hat{R}}_z(\theta)\hat{I}_x = \exp\{-i\hat{\hat{I}}_z\theta\}\ \hat{I}_x\ \exp\{+i\hat{\hat{I}}_z\theta\}. \tag{2.42}$$

The result is a rotation of $\hat{I}_x$ by an angle θ around the z-axis of the system:

$$\hat{\hat{R}}_z(\theta)\hat{I}_x = \cos(\theta)\hat{I}_x + \sin(\theta)\hat{I}_y. \tag{2.43}$$

The sense of rotational direction (i.e. the sign of $\sin(\theta)$) is that of a right-handed coordinate system, as defined in Eq. 2.39.

In the following section, the full potential of these operator transformations in describing the dynamics of a spin system will become clear.

2.2.3.2 The Density Operator

The density operator provides information regarding the state of an ensemble of spins in a system. The ability to address a spin ensemble is hugely important considering the number of spins involved in an NMR experiment, which can easily be $\sim 10^{22}$.

Let us consider an isolated spin-1/2 particle in a magnetic field. $|\psi\rangle$ is a superposition state in the two-level system, and $\langle\psi|$ is the corresponding bra:

$$\begin{aligned} |\psi\rangle &= \begin{pmatrix} c_1 \\ c_2 \end{pmatrix} = c_1 |\alpha\rangle + c_2 |\beta\rangle \\ \langle\psi| &= \begin{pmatrix} c_1^* & c_2^* \end{pmatrix} = c_1^* \langle\alpha| + c_2^* \langle\beta| . \end{aligned} \tag{2.44}$$

The density operator $\hat{\rho}$ has the form

$$\hat{\rho} = |\psi\rangle\langle\psi| = \begin{array}{c} \\ \langle\alpha| \\ \langle\beta| \end{array} \begin{array}{c} \begin{array}{cc} |\alpha\rangle & |\beta\rangle \end{array} \\ \begin{pmatrix} c_1^* c_1 & c_2^* c_1 \\ c_1^* c_2 & c_2^* c_2 \end{pmatrix} \end{array}. \tag{2.45}$$

If the number of spins is increased, the density operator has the same form, but now provides information on the ensemble average of the spin states. The 'population' of a given state can be determined from the expectation value of the density operator, as in Eq. 2.32. For example, the population of state $|\alpha\rangle$ is given by

$$\langle\alpha|\hat{\rho}|\alpha\rangle = \langle\alpha|\psi\rangle\langle\psi|\alpha\rangle = c_1^* c_1. \tag{2.46}$$

Hence, the diagonal elements of $\hat{\rho}$ are state populations.

The off-diagonal elements are 'coherences' between states. The coherences are complex numbers, and the two coherences between the same pair of states are complex conjugates of each other. For example:

$$\langle\alpha|\hat{\rho}|\beta\rangle = (\langle\beta|\hat{\rho}|\alpha\rangle)^* = c_1 c_2^* = (c_1^* c_2)^*. \tag{2.47}$$

The *coherence order* between two states in a magnetic field is defined as the difference in angular-momentum projection along z. Recall from Eq. 2.34 (and letting $\hbar = 1$) that

$$\begin{aligned} \hat{I}_z |\alpha\rangle &= m_\alpha |\alpha\rangle = +\frac{1}{2} |\alpha\rangle , \\ \hat{I}_z |\beta\rangle &= m_\beta |\beta\rangle = -\frac{1}{2} |\beta\rangle . \end{aligned} \tag{2.48}$$

We can therefore calculate the coherence order of the coherence $\langle\alpha|\hat{\rho}|\beta\rangle$ as

$$m_\alpha - m_\beta = +1, \tag{2.49}$$

and the coherence order of $\langle\beta|\,\hat{\rho}\,|\alpha\rangle$ as

$$m_\beta - m_\alpha = -1. \tag{2.50}$$

These are known as *single-quantum coherences*, and give rise to conventional NMR signals.

Let us now consider the relationship between the density operator and the three spin operators defined in Eq. 2.33, and draw a connection to the classical description of NMR given in section 2.1.

Recalling from Eq. 2.1, there is only a small population difference between states $|\alpha\rangle$ and $|\beta\rangle$, and hence only a small fraction of the total number of spins in a sample contribute to the net magnetization. If we imagine a sample containing ^{1}H spins in a magnetic field of 3 T at room temperature, $(P_\alpha - P_\beta)/(P_\alpha + P_\beta) \approx 10^{-5}$. We can write the density operator as:

$$\hat{\rho} = \frac{1}{2}\begin{pmatrix} 1+10^{-5} & 0 \\ 0 & 1-10^{-5} \end{pmatrix}, \tag{2.51}$$

Recalling the definitions of $\hat{\mathbb{1}}$ and $\hat{I}_z$ from Eq. 2.33 (and letting $\hbar = 1$), $\hat{\rho}$ can be rewritten as

$$\hat{\rho} = \frac{1}{2}\hat{\mathbb{1}} + 10^{-5}\hat{I}_z. \tag{2.52}$$

Note that $\hat{\mathbb{1}}$ corresponds to an equal number of spins in the $|\alpha\rangle$ and $|\beta\rangle$ states, and $\hat{I}_z$ corresponds to a population difference between the $|\alpha\rangle$ and $|\beta\rangle$ states.

Since $\hat{\mathbb{1}}$ is invariant to rotations, it can be ignored in the context of NMR, and we are left with

$$\hat{\rho} = 10^{-5}\hat{I}_z, \tag{2.53}$$

to describe the thermal equilibrium z-magnetization of the sample.

We can use the density operator formalism to describe the evolution of the spin system under some operations. The sequence illustrated in Fig. 2.3 provides a good example. We know from section 2.1.3 that a $(\pi/2)_y$ rf pulse will rotate the bulk magnetization vector into the x-axis. This is equivalent to *propagating* the density operator under the rotation superoperator $\hat{\hat{R}}_y(\pi/2)$:

$$\hat{\rho}_1 = \hat{\hat{R}}_y\left(\frac{\pi}{2}\right)\hat{\rho}_0 = e^{-i\left(\frac{\pi}{2}\right)\hat{I}_y}\ \hat{I}_z\ e^{+i\left(\frac{\pi}{2}\right)\hat{I}_y} = \hat{I}_x. \tag{2.54}$$

After this, the magnetization will begin to precess around the z-axis, which is equivalent to propagating the density operator under $\hat{\hat{R}}_z(\omega\, t)$:

$$\begin{aligned} \hat{\rho}_2 = \hat{\hat{R}}_z(\omega\, t)\hat{\rho}_1 &= e^{-i\,\omega\, t\,\hat{I}_z}\ \hat{I}_x\ e^{+i\,\omega\, t\,\hat{I}_z} \\ &= \cos(\omega\, t)\hat{I}_x + \sin(\omega\, t)\hat{I}_y, \end{aligned} \tag{2.55}$$

where ω is the Larmor frequency, and t is time.

The term $\exp\{-i\,\omega\,t\,\hat{I}_z\}$ is called a *propagator*, because it propagates the density operator in time. But why does this propagator exist, and furthermore, why do the spins precess in a magnetic field?

The answer is that the system is subject at all times to a *Hamiltonian*, the energy operator, which describes how the system evolves in time.

2.2.3.3 The Hamiltonian Operator

The Hamiltonian operator provides information about the energies of states in a system.

If $|\psi_1\rangle$ and $|\psi_2\rangle$ are eigenstates of the Hamiltonian $\hat{H}$, then

$$\begin{aligned}\hat{H}\,|\psi_1\rangle &= E_1\,|\psi_1\rangle \\ \hat{H}\,|\psi_2\rangle &= E_2\,|\psi_2\rangle\,,\end{aligned} \tag{2.56}$$

where E_1 is the energy of state $|\psi_1\rangle$, and E_2 is the energy of state $|\psi_2\rangle$.

The Hamiltonian can be written in matrix form:

$$\hat{H} = \begin{array}{c} \\ \langle\psi_1| \\ \langle\psi_2| \end{array} \begin{array}{c} \begin{array}{cc} |\psi_1\rangle & |\psi_2\rangle \end{array} \\ \begin{pmatrix} E_1 & 0 \\ 0 & E_2 \end{pmatrix} \end{array}. \tag{2.57}$$

If the Hamiltonian is written in the eigenbasis of the system, it is diagonal (i.e. has no off-diagonal elements), and the diagonal elements are state energies.

The evolution of a quantum system is described by the Schrödinger equation:

$$i\frac{\partial}{\partial t}\,|\psi\rangle = \hat{H}\,|\psi\rangle\,, \tag{2.58}$$

In NMR it is usually more convenient to describe the dynamics of a spin system by considering the evolution of the density operator, rather than states. Using the two expressions

$$\begin{aligned}\frac{\partial}{\partial t}\,|\psi\rangle &= -i\hat{H}\,|\psi\rangle\,, \\ \frac{\partial}{\partial t}\,\langle\psi| &= i\,|\psi\rangle\,\hat{H},\end{aligned}$$

we can then make the following derivation [33]:

$$\begin{aligned}\frac{\partial}{\partial t}\hat{\rho} &= \frac{\partial}{\partial t}\Big[\,|\psi\rangle\langle\psi|\,\Big] \\ &= \left[\frac{\partial}{\partial t}|\psi\rangle\right]\langle\psi| + |\psi\rangle\left[\frac{\partial}{\partial t}\langle\psi|\right] \\ &= -i\hat{H}\,|\psi\rangle\langle\psi| + i\,|\psi\rangle\langle\psi|\,\hat{H}\end{aligned}$$

to give

$$\frac{\partial}{\partial t}\hat{\rho} = -i\big[\hat{H},\hat{\rho}\big]. \tag{2.59}$$

This is known as the Liouville-von Neumann equation.

Let us again consider an isolated spin-1/2 particle in a magnetic field. The Hamiltonian is proportional to the z-angular momentum operator from Eq. 2.33:

$$\hat{H} = \omega\hat{I}_z, \tag{2.60}$$

where $\omega = -\gamma B_0$. In matrix form in the Zeeman basis, this is

$$\hat{H} = \begin{matrix}\\ \langle\alpha| \\ \langle\beta|\end{matrix}\begin{matrix}\begin{matrix}|\alpha\rangle & |\beta\rangle\end{matrix}\\ \begin{pmatrix} +\frac{\omega}{2} & 0 \\ 0 & -\frac{\omega}{2}\end{pmatrix}\end{matrix}. \tag{2.61}$$

and hence

$$\hat{H}\,|\alpha\rangle = +\frac{\omega}{2}\,|\alpha\rangle \tag{2.62}$$

The density operator evolves under a Hamiltonian as follows:

$$\hat{\rho}(t) = e^{-i\,\hat{H}\,t}\;\hat{\rho}(0)\;e^{+i\,\hat{H}\,t}, \tag{2.63}$$

In Eq. 2.55 we wrote free precession of a spin-1/2 particle in a magnetic field as a rotation around the z-axis using the rotation superoperator $\hat{\hat{R}}_z(\omega\,t)$. We now know that for this system $\hat{H} = \omega\hat{I}_z$, which amounts to the same thing.

If the density operator commutes with the Hamiltonian (see Eq. 2.59), there is no evolution of the system. This can be shown using propagators. We let $\hat{H} = \omega\hat{I}_z$, and $\hat{\rho}(0) = \hat{I}_z$:

$$\hat{\rho}(t) = e^{-i\,\omega\,t\,\hat{I}_z}\;\hat{I}_z\;e^{+i\,\omega\,t\,\hat{I}_z} = \hat{I}_z. \tag{2.64}$$

If the density operator does not commute with the Hamiltonian, i.e. $\big[\hat{H},\hat{\rho}\big] \neq 0$, the density operator will evolve. For this case, we let $\hat{H} = \omega\hat{I}_z$, and $\hat{\rho}(0) = \hat{I}_x$:

$$\hat{\rho}(t) = e^{-i\,\omega\,t\,\hat{I}_z}\;\hat{I}_x\;e^{+i\,\omega\,t\,\hat{I}_z} = \cos(\omega\,t)\hat{I}_x + \sin(\omega\,t)\hat{I}_y. \tag{2.65}$$

The Hamiltonian for a multi-spin system is more complicated. Consider a two spin-1/2 system of heteronuclear spins (I and S) in a molecule, which have a J-coupling, J_{IS}. The Hamiltonian is

$$\hat{H} = \omega_{\mathrm{I}}\hat{I}_z + \omega_{\mathrm{S}}\hat{S}_z + 2\pi J_{\mathrm{IS}}\,\hat{\mathbf{I}}.\hat{\mathbf{S}}, \tag{2.66}$$

where $\hat{\mathbf{I}}.\hat{\mathbf{S}} = \hat{I}_x\hat{S}_x + \hat{I}_y\hat{S}_y + \hat{I}_z\hat{S}_z$. In matrix form in the Zeeman basis, this is

$$\hat{H} = \frac{1}{2}\begin{array}{c} \\ \langle\alpha\alpha| \\ \langle\alpha\beta| \\ \langle\beta\alpha| \\ \langle\beta\beta| \end{array}\begin{array}{c} \begin{array}{cccc} |\alpha\alpha\rangle & |\alpha\beta\rangle & |\beta\alpha\rangle & |\beta\beta\rangle \end{array} \\ \begin{pmatrix} +\omega_{\mathrm{I}} + \omega_{\mathrm{S}} + \pi J_{\mathrm{IS}} & 0 & 0 & 0 \\ 0 & +\omega_{\mathrm{I}} - \omega_{\mathrm{S}} - \pi J_{\mathrm{IS}} & 2\pi J_{\mathrm{IS}} & 0 \\ 0 & 2\pi J_{\mathrm{IS}} & -\omega_{\mathrm{I}} + \omega_{\mathrm{S}} - \pi J_{\mathrm{IS}} & 0 \\ 0 & 0 & 0 & -\omega_{\mathrm{I}} - \omega_{\mathrm{S}} + \pi J_{\mathrm{IS}} \end{pmatrix} \end{array}. \tag{2.67}$$

The Zeeman basis is no longer the eigenbasis of this Hamiltonian because the J-coupling introduces off-diagonal elements. For practical purposes, these off-diagonal elements can be ignored when $|\omega_{\mathrm{I}} - \omega_{\mathrm{S}}| \gg 2\pi J_{\mathrm{IS}}$, because the Zeeman basis is approximately the eigenbasis of the Hamiltonian. This is typically the case at high-field, where I and S precess at different Larmor frequencies, which are in the order of 10^8 Hz, compared to J_{IS}, which typically has a magnitude on the order of $1 - 1000$ Hz.

When the Hamiltonian is approximately diagonal in the Zeeman basis, it approximately commutes with z-operators. This means if $\rho \propto \hat{I}_z + \hat{S}_z$, then $-i\big[\hat{H}, \hat{\rho}\big] \approx 0$, and the system does not evolve.

If the magnetic field is set such that the two central diagonal components become degenerate (i.e. at $B_0 = 0$), the Zeeman basis is no longer the eigenbasis. If $\rho \propto \hat{I}_z + \hat{S}_z$, then $-i\big[\hat{H}, \hat{\rho}\big] \neq 0$, and the system will evolve. Specifically, oscillatory transitions will occur between states $|\alpha\beta\rangle$ and $|\beta\alpha\rangle$, with a frequency of J_{IS}.

This idea of inducing population transitions between J-coupled spin states by equalizing diagonal elements of the Hamiltonian is important in later chapters.

From this point forward, the hat will be dropped from the spin operators (i.e. I_z) for simplicity.

Chapter 3

Hyperpolarization

3.1 Introduction

3.1.1 Basic Principles - Beating the Boltzmann Distribution

As discussed in section 2.1.1, the polarization of nuclear spins in a magnetic field is governed by the Boltzmann distribution. The polarization level of nuclear spins at room temperature is 3.4×10^{-6} per tesla for protons, and 8.6×10^{-7} per tesla for carbon-13. The signal in an NMR experiment is proportional to the polarization level of the nuclei under observation, which means that sensitivity of the NMR experiment is limited. At the time of writing, the highest commercially available NMR magnets operate at 1.2 GHz (this number corresponds to the proton Larmor frequency), which is ∼28 T. The polarization level of protons at this field is $\sim 10^{-4}$. Without a paradigm shift in magnet technologies, achieving spin polarization approaching unity by increasing the B_0 magnetic field is not a viable route forward, and comes at huge cost.

The alternative is *hyperpolarization*, which is a general term for a number of techniques that enhance nuclear spin polarization levels beyond that of thermal equilibrium. Hyperpolarized substabces have applications in the fields of medical imaging [5, 9, 11, 12, 34–36], biomolecular interactions [37–41], materials science [42–48], biomolecular structure elucidation [49–52], drug discovery [53–55], and reaction monitoring [56–60], to name a few.

Recall from section 2.1.6 that relaxation phenomena lead to a system returning to its thermal equilibrium state. This means that if a sample is hyperpolarized, the hyperpolarized spin order will be lost with a characteristic relaxation time constant, typically T_1. This is an important consideration in this field of research; many hyperpolarized samples have lifetimes in the order of seconds or minutes, which greatly limits how they can be used.

3.1.2 Hyperpolarization Techniques

There are a number of distinct hyperpolarization methods, of which a few are discussed below.

Brute Force

The simplest hyperpolarization technique is the "brute force" approach, in which hyperpolarization is achieved by simply cooling the sample to cryogenic temperatures (typically a few Kelvin) in the presence of a high magnetic field [61, 62]. The Boltzmann polarization under these conditions for ^{1}H nuclei approaches 1%, and after sufficient time for polarization build-up, thermal mixing schemes can be employed to transfer the proton polarization to ^{13}C nuclei. The sample is rapidly dissolved with a warm solvent (often water) in a dissolution procedure, which liberates the hyperpolarized agent as a solution.

One drawback to this technique is the long ^{1}H T_1 times for many compounds at cryogenic temperatures, which means long times are needed for polarization to build up. Solutions include the use of methyl protons, which can have shorter T_1 times, and special sample preparation procedures [62].

Perhaps the biggest drawback to the brute force approach is the limit of achievable proton polarization at the level of 10^{-2} at feasible magnetic fields and temperatures, which currently precludes use *in vivo*. However, the generality of the technique might lead to other applications.

Optical Pumping

Spin-exchange optical pumping (SEOP) is a method of polarizing the nuclear spins of noble gas atoms (^{3}He or ^{129}Xe) via the unpaired electron spins in an alkali metal vapour [63]. A vapour cell containing an alkali metal (typically Rb) is placed in a magnetic field, and heated to vaporize the metal atoms. A circularly polarized laser is used to spin-selectively optically polarize the alkali metal atoms, which leads to Zeeman polarization of the electron spins. The electron spin polarization is transferred to the noble gas nuclei during collisions. A buffer gas (usually N_2) is included to reduce radiation trapping from spontaneous emission of the alkali metal atoms, which would lead to depolarization.

The ability of optical pumping to produce ^{3}He and ^{129}Xe at polarization levels of >50% at flow rates of >1 litre/hour [64] has been revolutionary for MRI of the lungs. Hyperpolarized gases have also been used for fundamental physics research [65, 66].

The limitation of SEOP is in the choice of polarized targets, which is currently limited to a small number of substances.

Dissolution Dynamic Nuclear Polarization

There are a number of different types of dynamic nuclear polarization (DNP), including solution-state DNP [67], DNP in the solid-state on rotating samples [51], and static solid-state DNP with the goal of sample dissolution for solution-state signal observation [7]. The latter is colloquially referred to as dissolution-DNP, and is discussed here because it is relevant to the results presented in chapter 7.

DNP is a method of polarizing nuclei via thermal equilibrium electron spin polarization. In this sense it is different to optical pumping, because the electrons are not hyperpolarized themselves. Unity electron polarization can be achieved by cooling to temperatures <2 K at 7 T or higher static field strengths. The electron polarization is then transferred to nearby nuclear spins by saturating a microwave-frequency transition.

These requirements mean for dissolution-DNP, a sample is held in a liquid helium cryostat in a high-field magnet (which does not need to be homogeneous), with a nearby microwave source for irradiation. The cryostat is then operated under vacuum to lower the pressure, and hence temperature.

"Free radicals" are molecules with an unpaired electron spin, and these are homogeneously dispersed within the sample. For homogeneous dispersion, the sample should form a glass upon freezing, as opposed to being crystalline. The sample is then rapidly cooled, and held in a cryostat which is at (typically) 1.2-1.5 K. The electrons have a relatively short T_1, in contrast to nuclear spins, as mentioned in the discussion of the brute force method. The sample is irradiated with microwaves to induce polarization transfer from the electron spins to nearby nuclei. The depolarized electrons then rapidly repolarize due to the short T_1, whereas the nuclear spins retain nonequilibrium polarization. This nonequilibrium polarization diffuses through the sample, and after some time (typically tens of minutes), the nuclear spins in the sample are sufficiently polarized (in the order of 0.1). At this point the sample is rapidly dissolved with a pressurized hot solvent, and ejected from the cryostat.

This technique is general, and has been used to produce solutions of metabolites with ^{13}C polarization levels of more than 40% [68].

The large, heavy polarization equipment makes dissolution-DNP a nontransportable hyperpolarization modality. On top of that, the liquid helium coolant and superconducting magnets required to achieve high magnetic fields are expensive. Polarization build-up times are in the order of tens of minutes, although progress has been made to reduce this through the use of cross polarization [68].

A proposed solution to these drawbacks is parahydrogen induced hyperpolarization, which will be discussed in detail in Sections 3.2 and 3.3.

3.1.3 Hyperpolarized Targets for *in vivo* Medical Imaging

The first medical imaging experiments with hyperpolarized samples were performed in the mid-1990s with the optically polarized noble gases ^{3}He [34, 69], and ^{129}Xe [36, 70, 71]. This solved a significant problem in medical imaging; the lungs are a difficult organ to image due to the low density of proton nuclei. Imaging of a gas is inherently difficult due to the low concentration of nuclear spins, but hyperpolarizing the spins overcomes this problem by offering signal enhancements in the order of 10^5.

^{3}He was originally preferred because higher polarization levels could be achieved, and the gyromagnetic ratio is ∼3 times higher than that of ^{129}Xe, leading to higher detection sensitivity. The diminishing world supply of helium has lead to an increasing use of ^{129}Xe for imaging. Additionally, the low solubility of ^{3}He in blood precludes its use as a contrast agent in tissues or blood, but the same is not true for ^{129}Xe. ^{129}Xe is lipophilic, and has a T_1 in the order of 10 s in blood, which has allowed for *in vivo* tissue imaging [72, 73]. Emerging techniques might even allow for *in vivo* biosensing, using ^{129}Xe trapped in molecular cages and observing binding events to targeted biomolecules [37, 74, 75].

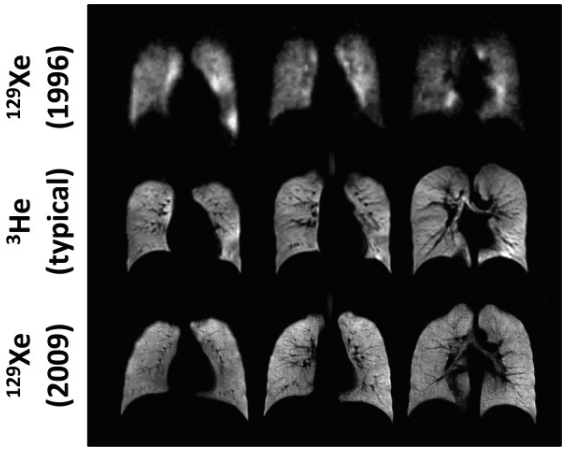

FIGURE 3.1: A comparison between magnetic resonance (MR) images of the lungs using hyperpolarized ^{3}He and ^{129}Xe. Image adapted from Ref. [36]. Copyright 2019 John Wiley and Sons. Adapted with permission.

The next significant advance in hyperpolarized *in vivo* imaging came in the early 2000s with the advent of dissolution-DNP [7], which allows for the production of room temperature solutions of metabolites with signal enhancements in the order of 10^4. This hyperpolarization technique is much more general than optical pumping (which only works for noble gases), because it can be used to polarize any nucleus and is applicable to a wide variety of molecules [2].

Without hyperpolarization, it is possible to acquire high-resolution MR images of the protons from water molecules, which are present at ∼110 M concentration in tissues. Metabolites on the other hand are present at $10^3 - 10^7$ times lower concentrations,

which means images of metabolic flux are not possible, even in high magnetic fields. Dissolution-DNP has overcome this problem by allowing for the production of metabolite solutions at polarization levels of >10%, and since then, numerous *in vivo* studies have been performed using hyperpolarized pyruvate [11–13], glucose [76, 77], ascorbate and dehydroascorbate [78–80], and fumarate [14–18].

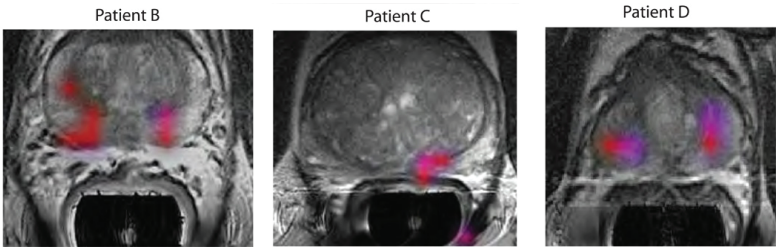

FIGURE 3.2: Images of prostate cancer tumours acquired after injecting patients with dissolution-DNP hyperpolarized ^{13}C-labelled pyruvate. Colour indicates regions of abnormally high lactate/pyruvate concentration, which is indicative of tumour cells. Image adapted from Ref. [11]. Copyright 2019 The American Association for the Advancement of Science. Adapted with permission.

The drawback to dissolution-DNP is the requirement for expensive and nontransportable equipment, which must be located close to the point-of-use due to the short lifetime of hyperpolarized spin order in molecules. A new modality for the production of hyperpolarized metabolites is the use of hydrogenative PHIP, in which hyperpolarization is delivered to a substrate molecule by the addition of para-enriched hydrogen gas. This method is somewhat chemically specific, as the product molecules must be hydrogenation products. The molecules dimethyl maleate [81], 2-hydroxyethylpropionate [82, 83], 2-hydroxyethylacrylate [84], and succinate [21, 23, 24] fit this constraint, and have been studied as *in vivo* contrast agents. Chapter 6 of this thesis describes a novel method to produce hyperpolarized fumarate via parahydrogen [85].

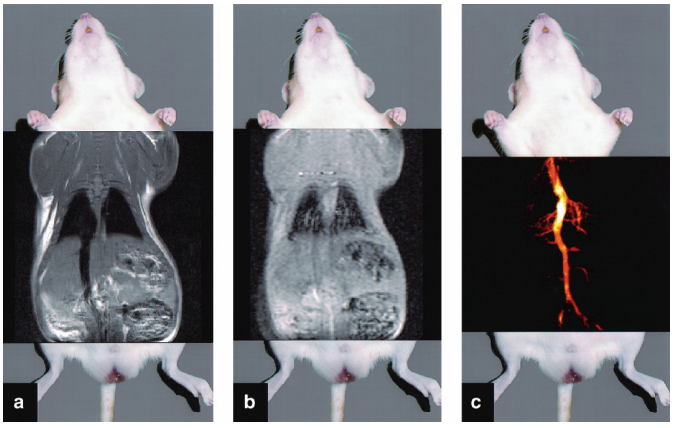

FIGURE 3.3: MR images of a rat, showing (a,b) ^{1}H MRI scans, and (c) a hyperpolarized ^{13}C MRI scan after injection with PHIP-polarized dimethyl maleate. Image adapted from Ref. [81]. Copyright 2019 John Wiley and Sons. Adapted with permission.

The advent of *side-arm hydrogenation* [86, 87], or PHIP-SAH, has expanded the catalogue of PHIP-polarizable molecules. In PHIP-SAH, a hydrogenable side-arm moiety

is chemically bonded to a biomolecule of interest, and (1) the side-arm is parahydrogenated, (2) the proton hyperpolarization is transferred to the biomolecule, and (3) the side-arm is chemically cleaved to liberate the desired product. This has lead to the *in vivo* study of PHIP-polarized pyruvate [88].

Recently, a nonhydrogenative PHIP modality has emerged called SABRE (Signal Amplification By Reversible Exchange), which allows for molecules to be hyperpolarized without chemical addition of the parahydrogen [89–91]. This might provide another path to the formation of hyperpolarized contrast agents for application *in vivo*.

In the majority of hyperpolarized contrast agents (excluding ^{3}He and ^{129}Xe), a ^{13}C spin is polarized. There are three main reasons for this; (1) the T_1 is typically longer than that of ^{1}H spins, which is vital given the transient nature of the hyperpolarized species in the body, (2) due to the 1% natural abundance and lower gyromagnetic ratio of ^{13}C over ^{1}H, there is less background signal, and (3) the chemical shift range of ^{13}C is larger than that of ^{1}H. For this reason, for PHIP-polarized agents, schemes are needed to transfer the proton polarization to ^{13}C spins, which is an important theme in this thesis.

3.2 Parahydrogen Induced Hyperpolarization

3.2.1 Nuclear Spin States of Molecular Hydrogen

Molecular hydrogen is composed of two spin-1/2 particles, which are magnetically equivalent, and coupled through the J-coupling interaction. The two protons can therefore exist in two nuclear spin isomer forms: *ortho* or *para*. The ortho spin isomer has a total spin angular momentum $I = 1$ and is called the 'triplet' isomer, because the angular momentum projection along the z-axis can take three values; $m_I = -1, 0, 1$. The para spin isomer has a total spin angular momentum $I = 0$, and is called the 'singlet' isomer because $m_I = 0$.

These four states of the system can be written as linear combinations of Zeeman basis states:

$$\begin{aligned} |S_0\rangle &= \frac{1}{\sqrt{2}}(|\alpha\beta\rangle - |\beta\alpha\rangle), \\ |T_{+1}\rangle &= |\alpha\alpha\rangle\,, \\ |T_0\rangle &= \frac{1}{\sqrt{2}}(|\alpha\beta\rangle + |\beta\alpha\rangle), \\ |T_{-1}\rangle &= |\beta\beta\rangle\,, \end{aligned} \tag{3.1}$$

where S and T stand for singlet and triplet, and the subscript indicates the state's angular momentum projection along the z-axis, i.e. $I_z\,|S_0\rangle = 0\,|S_0\rangle$, and $I_z\,|T_{+1}\rangle =$

$+1\,|T_{+1}\rangle$. For the two spin-1/2 protons in a molecule of hydrogen, the eigenbasis of the Hamiltonian is the singlet-triplet basis, and the state energies are shown as a function of external magnetic field in Fig. 3.4.

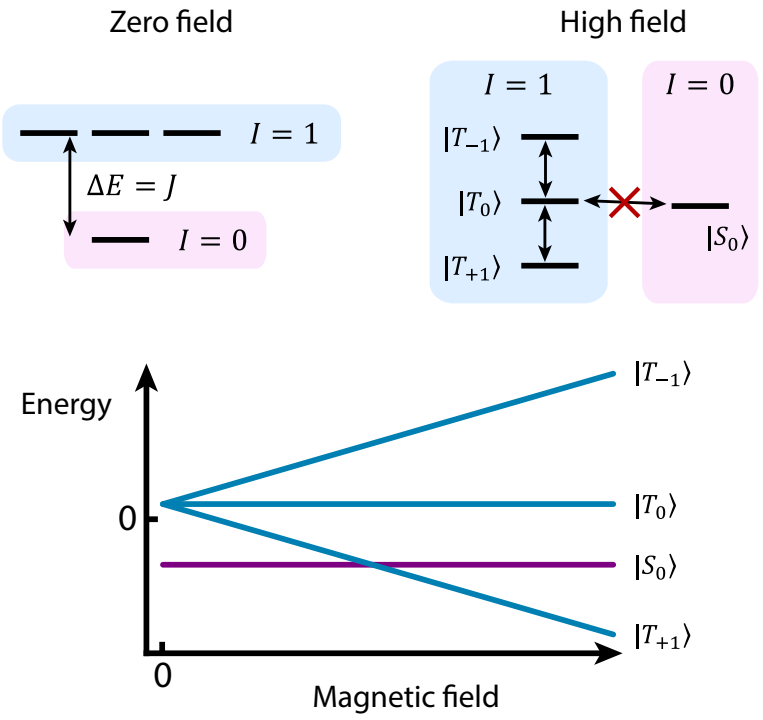

FIGURE 3.4: Energies of the singlet and triplet states of molecular H_2 under the influence of an external magnetic field. The energies of the $|S_0\rangle$ and $|T_0\rangle$ states at zero-field are $-3J/4$ and $+J/4$, respectively, where J is the proton-proton J-coupling.

With respect to spin-exchange operations, the singlet state is antisymmetric, and the triplet states are symmetric. The singlet state is nonmagnetic, meaning the energy of the para isomer of hydrogen gas does not depend on the external magnetic field, and is NMR silent. If nothing breaks the symmetry of the protons, the singlet-triplet basis is an exact eigenbasis, and transitions cannot occur between the singlet and triplet manifolds (see Fig. 3.4).

3.2.2 Relaxation of Nuclear Singlet States

Nuclear spin relaxation between state populations was described in section 2.1.6 using the symbol T_1, and this is the relevant time constant for relaxation between the three triplet states. However, since population movement between the singlet and triplet manifolds is forbidden for symmetry reasons [92], this form of relaxation needs a different time constant, which is called T_S. This is illustrated in Fig. 3.5.

Dipole-dipole relaxation is caused by fluctuations of the through-space dipolar coupling between spins. The fluctuating dipolar fields induced by each spin at the site of the other are correlated [92, 93], meaning the interaction does not break the symmetry

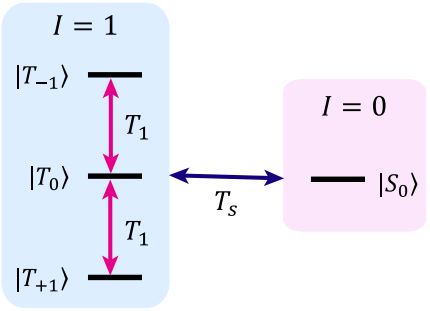

FIGURE 3.5: An illustration of the difference between T_1 and T_S relaxation.

of the two nuclei, and transitions from the $I = 0$ to $I = 1$ manifold remain forbidden. The singlet state is therefore immune to intra-pair dipole-dipole relaxation. However, this mechanism does allow transitions between the triplet states in the $I = 1$ manifold, and is often an efficient T_1 relaxation mechanism.

Spin-rotation relaxation is caused by nuclear spins in a molecule interacting with the magnetic fields produced by fluctuating rotational angular momentum of the molecule [94]. For the symmetric H_2 molecule, spin-rotation cannot induce T_S relaxation, but contributes to T_1 relaxation. In systems with lower symmetry than H_2, the spin-rotation mechanism *can* cause T_S relaxation, but it can still be long-lived with respect to T_1 [95].

Chemical shift anisotropy (CSA) relaxation is caused by fluctuations in the anisotropic chemical shift interaction experienced by each spin, due to motion. This mechanism cannot induce singlet relaxation for a spin pair with a centrosymmetric local molecular geometry (i.e. a molecular inversion centre between them) [96], and hence this is not a T_S mechanism for the H_2 molecule. However, CSA is always a T_1 mechanism, and can induce T_S relaxation for molecules with lower symmetry.

Since the singlet state of H_2 is immune to all three of the above relaxation mechanisms, in the absence of external relaxation mechanisms (i.e. paramagnetic oxygen or wall collisions), parahydrogen can be extremely long-lived (i.e. have a T_S in the order of months) in the gaseous state [97]. However, all of these mechanisms can cause T_1 relaxation, meaning that for a sample of hydrogen gas enriched in a single triplet state the population would be rapidly redistributed between the triplet states with the time constant T_1. An illustration of the mechanisms and the type of relaxation they can induce is shown in Fig. 3.6.

3.2.3 Enrichment of Hydrogen Gas in the Singlet Spin Isomer

The total wave function of molecular hydrogen contains electronic, vibrational, rotational, and spin components, and can be written as:

$$\Psi^{\text{tot}} = \Psi^{\text{elec}}\,\Psi^{\text{vib}}\,\Psi^{\text{rot}}\,\Psi^{\text{spin}}. \tag{3.2}$$

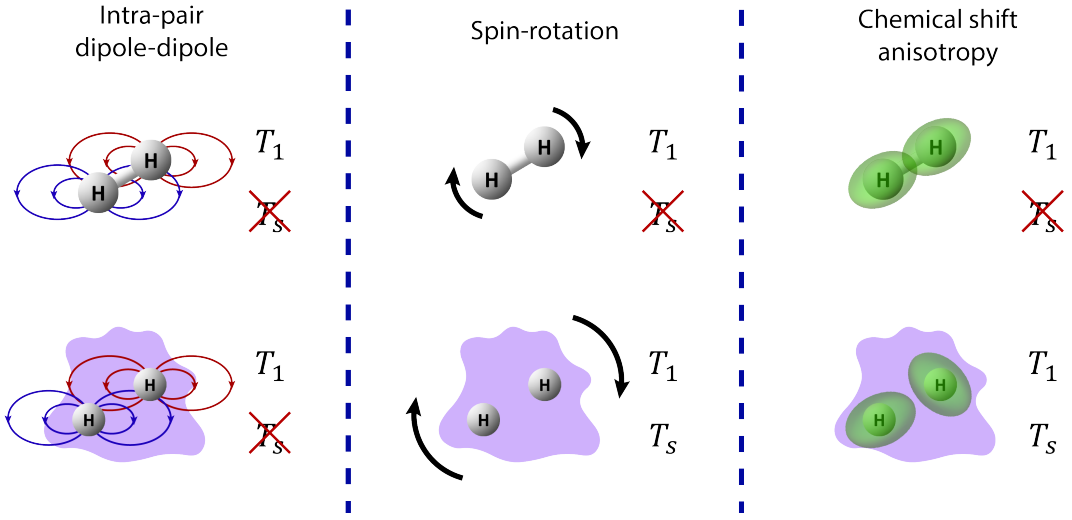

FIGURE 3.6: An illustration of three relaxation mechanisms experienced by the proton pair. The green ellipsoids represent an anisotropic chemical shift tensor. The top row of molecules are H_2, and the bottom row represents the proton singlet pair in a molecule with low symmetry. The red cross through T_S in each molecular case indicates singlet relaxation cannot occur through the given mechanism. For all shown cases T_1 relaxation can occur. The black arrows represent molecular angular momentum, and this should not be confused with general molecular motion, which is required for all relaxation mechanisms.

Since the two protons are fermions, the Pauli exclusion principle applies, which dictates that: the total wave function must remain antisymmetric with respect to exchange of the two protons, i.e.

$$\Psi^{\text{tot}}(x_1, s_1; x_2, s_2) = -\Psi^{\text{tot}}(x_2, s_2; x_1, s_1), \tag{3.3}$$

with x and s the spatial and spin parts of the wave function. The electronic and vibrational ground states are exchange-symmetric, and we will assume only the ground states are populated.

For rotational wave functions: $\Psi^{\text{rot}}_{J=0,2..}$ are exchange-symmetric (even), and $\Psi^{\text{rot}}_{J=1,3..}$ are exchange antisymmetric (odd) states. The opposite is true for the spin wave functions: $\Psi^{\text{spin}}_{J=0,2..}$ are odd, and $\Psi^{\text{rot}}_{J=1,3..}$ are even. We can therefore construct the following table for the overall symmetry of Ψ^{tot}:

	$\Psi^{\text{rot}}_{J=0,2..}$	$\Psi^{\text{rot}}_{J=1,3..}$
$\Psi^{\text{spin}}_{I=0}$	odd	even
$\Psi^{\text{spin}}_{I=1}$	even	odd

TABLE 3.1: Exchange-symmetry of Ψ^{tot}.

Since Ψ^{tot} must remain odd, each rotational state is coupled to a specific spin state. This is illustrated in Fig. 3.7. The rotational state energies are given by $E = BJ(J+1)$, with $B = \hbar^2/2I$. I is the moment of inertia of the diatomic, and is given by $I = \mu l^2$, where μ is the reduced mass, and l is the internuclear distance.

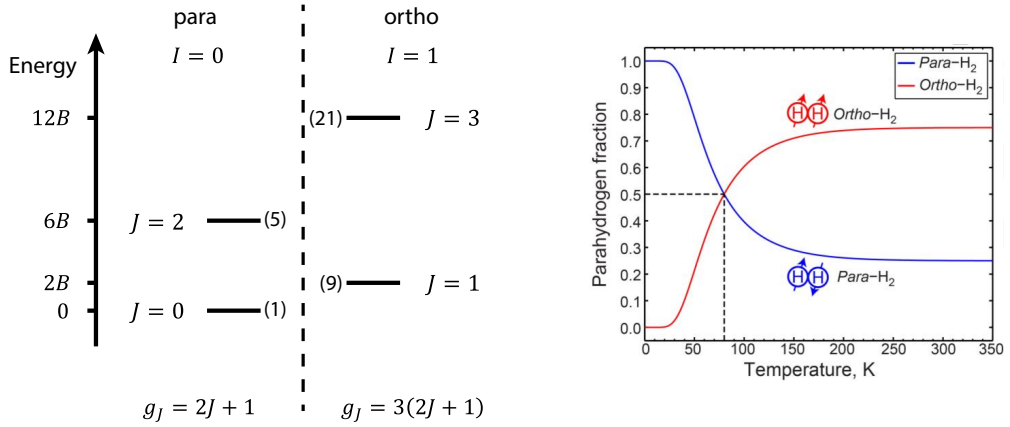

FIGURE 3.7: Left: The rotational energy levels for a two spin-1/2 diatomic molecule. The state energies are shown in terms of B. The rotational states are grouped by their corresponding nuclear spin state. g_J is the degeneracy of each energy level, and g_J is shown in brackets next to each level. Right: The equilibrium parahydrogen fraction of H_2 gas as a function of temperature. The dotted line shows the 50% para-enrichment level achieved by cooling to 77 K with liquid nitrogen. Image modified from Ref [98].

Para-enriched hydrogen gas can be generated by cooling the system. Recalling the Boltzmann distribution discussed in section 2.1.1, the lowest energy rotational state ($J = 0$) becomes more likely if the system is cooled. This means the $I = 0$ nuclear spin singlet state is also populated. Fig. 3.7 shows the relative fraction of the para-isomer as a function of temperature. At room temperature the ortho:para ratio is 3:1.

This cooling procedure only works because the energy separation between the rotational states is so large. For the lowest rotational energy levels, $E_{J=1} - E_{J=0} \approx 171\,\text{K}$ [99]. Recall from Fig. 3.4 that the energy separation between the $I = 0$ and $I = 1$ nuclear spin states alone is equal to the J-coupling. This is in the order of $10^{-8}\,\text{K}$.

It is important to understand that by cooling H_2 gas alone, the ortho/para ratio would remain 3:1, and the $J = 0$ and $J = 1$ states would be populated. To transfer the $J = 1$ population to the $J = 0$ state requires a nuclear spin flip which is disallowed because it would not conserve angular momentum. Spontaneous transitions from $J = 1$ to $J = 0$ are referred to as *homogeneous conversion*, and have an expected transition frequency in the order of $10^{-10}\,\text{Hz}$ [100], which is to say they do not occur on any reasonable timescale.

To populate the ground rotational state, a catalyst is required to temporarily break the proton symmetry. This is known as *heterogeneous conversion*, and is possible because H_2 molecules that approach the surface of a catalyst (which is typically charcoal,

or iron (III) oxide) experience a magnetic field gradient. This induces a difference in spin precession frequency, and this temporary symmetry-breaking interaction allows spin state transitions.

3.2.4 Chemistry and Reactions

Parahydrogen is of little interest to NMR by itself, because despite being in a hyperpolarized nuclear spin state, it is NMR silent. However, after chemical addition to another molecule/substrate, the hyperpolarized proton NMR signals can be released, and result in dramatic signal enhancements.

In solution-state NMR the parahydrogen addition to a substrate can be reversible as in SABRE [89], or irreversible as in hydrogenative PHIP [6]. Examples are shown in Fig. 3.8.

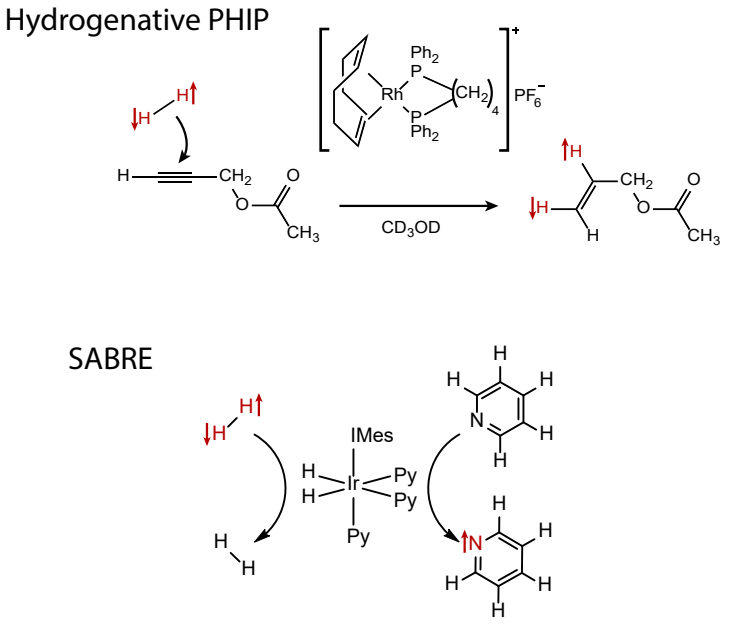

FIGURE 3.8: Top: an example of a hydrogenative PHIP reaction, in which propargyl acetate is parahydrogenated in solution using an Rh(I) catalyst to form allyl acetate. Bottom: an example of a SABRE reaction, in which parahydrogen and pyridine reversibly bind to an iridium catalyst, and the proton polarization is transferred to the pyridine substrate.

In the case of hydrogenative PHIP, a catalyst is required to increase the rate of chemical reaction. All parahydrogen hydrogenation catalysts add the H_2 molecule *pairwise* to the substrate, meaning the two protons remain coupled throughout the reaction, and are added to the same molecule. This is important, because if the proton coupling is lost, the hyperpolarized singlet order is also lost.

The catalysts used are often toxic to humans. Therefore, it is necessary to devise methods to remove the catalyst from solution, keeping in mind the eventual goal of *in vivo* injection of the hyperpolarized substances.

3.2.4.1 Irreversible Parahydrogen Addition: Hydrogenative PHIP

The original PHIP experiments were performed using Wilkinson's catalyst [6], $RhCl(PPh_3)_3$ **(1)**. This catalyst adds H_2 reversibly to the substrate [101], and so a number of rhodium- and palladium-based catalysts have since been used for irreversible pairwise parahydrogen addition [102, 103]. To date, the most widely used of these is $[Rh(cod)(dppb)]BF_4$ (dppb = 1,4-bis(diphenylphosphino)butane], cod = 1,5-cyclooctadiene) **(2)**, due to the relatively high solubility in organic solvents, and high catalytic ability. A reaction mechanism scheme is shown in Fig. 3.9, and the catalysts are shown in Fig. 3.10.

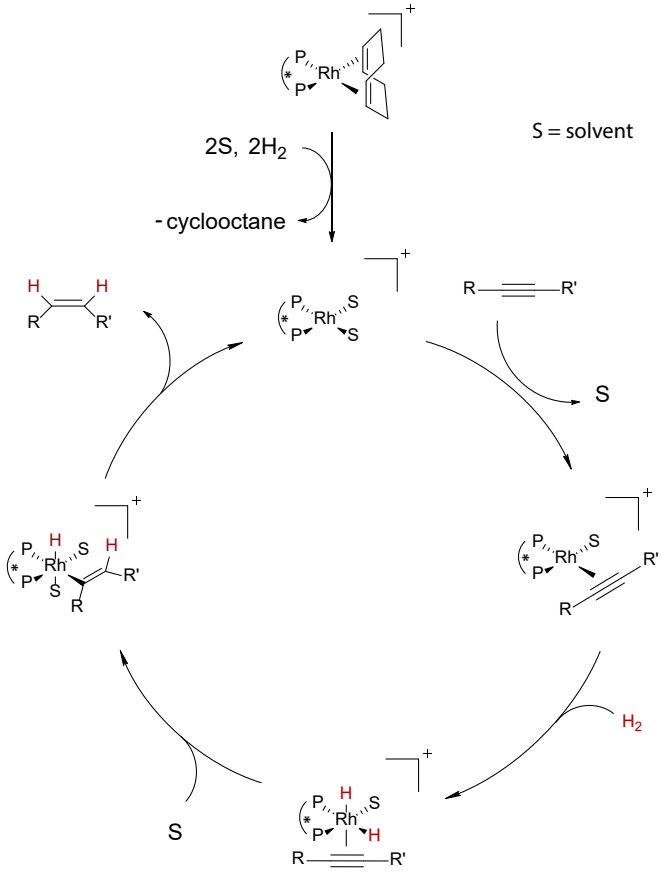

FIGURE 3.9: Proposed mechanism for H_2 *cis*-addition across an unsaturated chemical bond [104].

A number of water-soluble hydrogenation catalysts have also been identified. These are Rh(I) complexes, but with hydrophilic phosphine ligands. Examples are $[Rh(I)(nbd)(pppb)]Na_2$ (pspb = 1,4-bis[(phenyl-3-propanesulfonate)phosphine]butane)

(3), and $[Rh(I)(nbd)(THP)_2]BF_4$ (THP = tris(hydroxymethyl)-phosphine) **(4)** [105, 106], and are shown in Fig. 3.10.

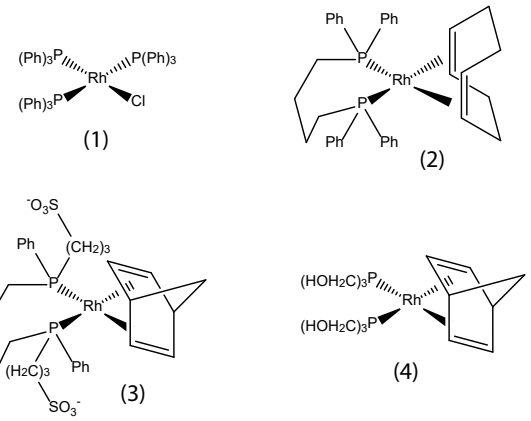

FIGURE 3.10: Rh(I) hydrogenation catalysts.

To remove these homogeneous catalysts from the solutions, a phase extraction can be performed. For the case of hydrogenation in an organic solvent, an aqueous phase can be used to extract the hyperpolarized product molecules as a pure solution [107].

To avoid the problem of catalyst removal from solution, a number of heterogeneous PHIP catalysts have also been developed. One type involves attaching Rh(I) catalysts to the surface of an SiO_2 support via an alkyl chain linker, which has been shown to hydrogenate precursor molecules in both solution and gaseous phase [108]. This can also work for other transition metal complexes [109]. Additionally, supported metals, pure metals, and metal oxides have been shown to work [43, 110, 111]. Heterogenous catalysis has also been shown to work in water solutions using capped Pt nanoparticles [112, 113].

All catalysts discussed so far induce *cis* addition of the hydrogen atoms across a bond. A small number of catalysts have been developed that cause *trans* hydrogenation [114–117], and this is concept forms the basis of chapter 6.

3.2.4.2 Reversible Parahydrogen Addition: Signal Amplification by Reversible Exchange

SABRE reactions employ an iridium-based catalyst to which a parahydrogen and substrate molecule(s) can bind reversibly. This reversible reaction occurs continuously in solution, and the sample is subjected to an rf or B_0 matching field condition, which induces polarization transfer from the parahydrogen to the substrate molecule. In this way, significant substrate polarizaiton can be built up [90, 91, 118, 119].

The most popular SABRE catalyst to date is [Ir(IMes)(cod)Cl] (IMes = 1,3-bis-(2,4,6-trimethylphenyl)-imidazol-2-ylidene). To activate the catalyst, the cod group is hydrogenated and replaced by solvent molecules. IMes is an N-heterocyclic carbene

(NHC) moiety that affects the reaction chemistry through electronic and steric effects. A variety of other NHC ligands have been investigated [120] in SABRE catalysts.

In water, [Ir(IMes)(cod)Cl] is quite insoluble, and therefore produces only modest signal enhancements [121]. For higher efficiency SABRE reactions in water, catalysts have been developed with phosphine ligands that help solubilise the catalyst [122].

3.3 Parahydrogen Spin Dynamics

In this section, the dynamics of a parahydrogen proton pair will be examined for a few important 2- and 3-spin systems, to help frame the discussions encountered in later chapters.

The initial density operator in a parahydrogen reaction is singlet order between the protons (I_1 and I_2). For the two spin-1/2 system, this is represented by the density operator

$$\hat{\rho}_{\text{ini}} = \frac{1}{4}\mathbb{1} - \mathbf{I}_1.\mathbf{I}_2. \tag{3.4}$$

In matrix form in the singlet-triplet basis defined in Eq. 3.1, this is

$$\hat{\rho}_{\text{ini}} = \begin{array}{c} \\ \langle S_0| \\ \langle T_{+1}| \\ \langle T_0| \\ \langle T_{-1}| \end{array} \begin{array}{c} \begin{array}{cccc} |S_0\rangle & |T_{+1}\rangle & |T_0\rangle & |T_{-1}\rangle \end{array} \\ \begin{pmatrix} 1 & 0 & 0 & 0 \\ 0 & 0 & 0 & 0 \\ 0 & 0 & 0 & 0 \\ 0 & 0 & 0 & 0 \end{pmatrix} \end{array}. \tag{3.5}$$

The two protons in a molecule of H_2 have a J-coupling, but after addition to a substrate molecule the protons might experience additional spin interactions. In the next sections, the cases of chemical shift inequivalence between the protons, and inequivalent J-couplings to a third spin, are examined.

3.3.1 Chemical Shift Inequivalence

If the parahydrogen protons are added to *chemically inequivalent* positions on a product molecule with no additional spins, the spin Hamiltonian is

$$\hat{H} = \omega_1 I_{1z} + \omega_2 I_{2z} + \omega_{\text{II}}^J \mathbf{I}_1.\mathbf{I}_2, \tag{3.6}$$

where ω_j is the precession frequency of spin j. A graphical representation of this molecular system is shown in Fig. 3.11.

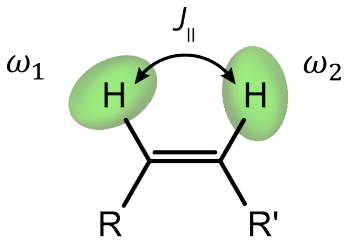

FIGURE 3.11: A graphical representation of a molecule in which a pair of J-coupled parahydrogen protons have a chemical shift difference $(\omega_2 - \omega_1)$. The green ellipsoids represent unequal chemical shift tensors, with different trace.

The new eigenbasis is given by

$$\begin{aligned} |1\rangle &= \cos\left(\frac{\theta}{2}\right)|\alpha\beta\rangle - \sin\left(\frac{\theta}{2}\right)|\beta\alpha\rangle\,, \\ |2\rangle &= |\alpha\alpha\rangle\,, \\ |3\rangle &= \sin\left(\frac{\theta}{2}\right)|\alpha\beta\rangle + \cos\left(\frac{\theta}{2}\right)|\beta\alpha\rangle\,, \\ |4\rangle &= |\beta\beta\rangle\,, \end{aligned} \tag{3.7}$$

where $\theta = \arctan(\omega_{\mathrm{II}}^{J}/\Delta\omega)$, and $\Delta\omega = \omega_2 - \omega_1$. The meaning of θ is represented graphically in Fig. 3.12.

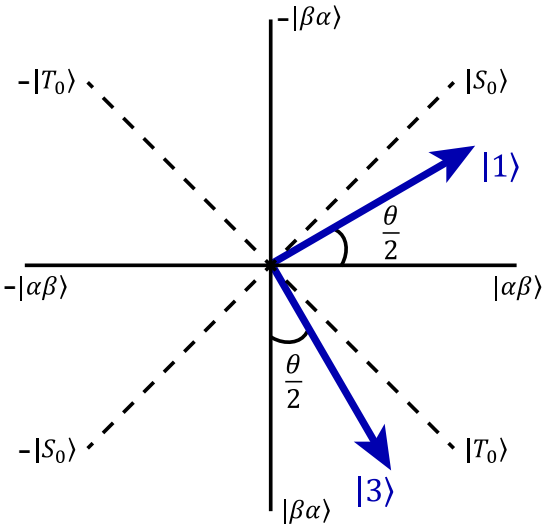

FIGURE 3.12: A graphical representation of states $|1\rangle$ and $|3\rangle$, which illustrates the meaning of θ.

The state energies are given by

$$\begin{aligned} E_1 &= -\frac{1}{2}\sqrt{(\Delta\omega)^2 + (\omega_{\mathrm{II}}^J)^2} - \frac{\omega_{\mathrm{II}}^J}{4}, \\ E_2 &= \frac{1}{2}(\omega_1 + \omega_2) + \frac{\omega_{\mathrm{II}}^J}{4}, \\ E_3 &= \frac{1}{2}\sqrt{(\Delta\omega)^2 + (\omega_{\mathrm{II}}^J)^2} - \frac{\omega_{\mathrm{II}}^J}{4}, \\ E_4 &= -\frac{1}{2}(\omega_1 + \omega_2) + \frac{\omega_{\mathrm{II}}^J}{4}, \end{aligned} \tag{3.8}$$

where E_1 is the energy of state $|1\rangle$.

3.3.1.1 PASADENA

In the case of a PASADENA (Parahydrogen And Synthesis Allow Dramatically Enhanced Nuclear Alignment) experiment [6], $|\Delta\omega| \gg |\omega_{\mathrm{II}}^J|$, and the parahydrogen protons form an AX spin system. This is commonly the case for hydrogenation product molecules at high magnetic fields, because the ${}^3J_{\mathrm{II}}$ coupling of the parahydrogen protons is typically ~10 Hz, but $|\Delta\omega|$ can easily be much larger. For this discussion we take $\Delta\omega \gg \omega_{\mathrm{II}}^J$, and the eigenbasis will be close to the Zeeman basis.

When a molecule of parahydrogen is added to the substrate, the density operator $\hat{\rho}_{\mathrm{ini}}$ is projected onto the new eigenbasis. For simplicity this will be taken as the Zeeman basis:

$$\hat{\rho}_{\mathrm{ini}} = \begin{array}{c} \\ \langle\alpha\beta| \\ \langle\alpha\alpha| \\ \langle\beta\alpha| \\ \langle\beta\beta| \end{array} \begin{array}{c} \begin{array}{cccc} |\alpha\beta\rangle & |\alpha\alpha\rangle & |\beta\alpha\rangle & |\beta\beta\rangle \end{array} \\ \begin{pmatrix} \frac{1}{2} & 0 & -\frac{1}{2} & 0 \\ 0 & 0 & 0 & 0 \\ -\frac{1}{2} & 0 & \frac{1}{2} & 0 \\ 0 & 0 & 0 & 0 \end{pmatrix} \end{array}. \tag{3.9}$$

The populations (diagonal elements) do not evolve in time because these components of the density operator commute with the Hamiltonian. The coherences evolve at a rate approximately given by $\Delta\omega$.

The resulting density operator after hydrogenating an ensemble of molecules at different time points may be expressed as follows:

$$\hat{\rho}_0 = \frac{1}{T}\int_0^T e^{-i\,\hat{H}\,t}\ \hat{\rho}_{\mathrm{ini}}\ e^{+i\,\hat{H}\,t}\,dt. \tag{3.10}$$

For the majority of cases, the hydrogenation period will be much longer than the coherence evolution period, and so this simply gives

$$\hat{\rho}_0 = \begin{array}{c} \\ \langle\alpha\beta| \\ \langle\alpha\alpha| \\ \langle\beta\alpha| \\ \langle\beta\beta| \end{array} \begin{array}{c} \begin{array}{cccc} |\alpha\beta\rangle & |\alpha\alpha\rangle & |\beta\alpha\rangle & |\beta\beta\rangle \end{array} \\ \begin{pmatrix} \frac{1}{2} & 0 & 0 & 0 \\ 0 & 0 & 0 & 0 \\ 0 & 0 & \frac{1}{2} & 0 \\ 0 & 0 & 0 & 0 \end{pmatrix} \end{array}. \tag{3.11}$$

In Figure. 3.13 a comparison is shown between the energy level populations and spectra for a PASADENA experiment and a thermal equilibrium experiment.

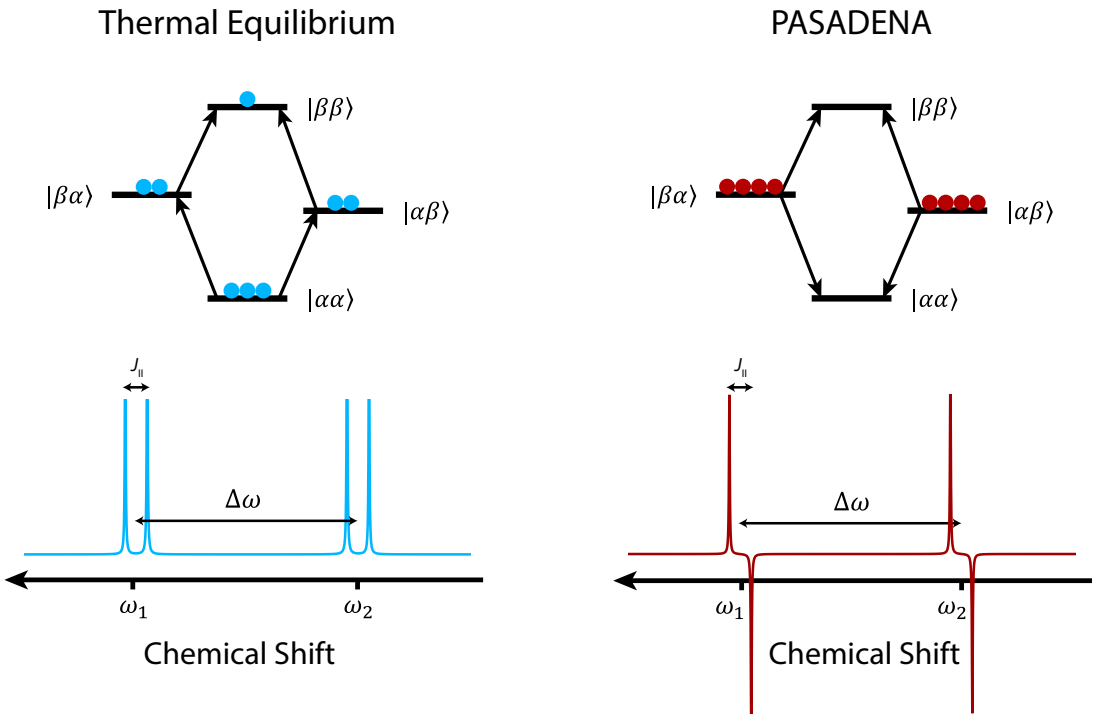

FIGURE 3.13: Balls represent populations of the Zeeman energy levels (not in proportion) for the cases of thermal equilibrium ^{1}H polarization, and ^{1}H polarization after parahydrogen addition in a PASADENA experiment. Simulations of the resulting spectra after applying a $\pi/4$ pulse are shown beneath. Arrows represent the phase of the coherences between states following the $\pi/4$ pulse.

In an NMR experiment on a sample at thermal equilibrium, we have seen that a $\pi/2$ pulse can be used to excite observable single quantum coherences (recall Equations 2.49 and 2.50). For a PASADENA signal to be observed, a $\pi/4$ NMR pulse must be used. The reason for this becomes clear by writing $\hat{\rho}_0$ in terms of spin operators:

$$\hat{\rho}_0 = \frac{1}{4}\mathbb{1} - I_{1z}I_{2z}. \tag{3.12}$$

Neglecting the unity operator $\mathbb{1}$, a $\pi/2$ y-pulse has the following effect:

$$\hat{\hat{R}}_y\left(\frac{\pi}{2}\right)\hat{\rho}_0 = -I_{1x}I_{2x}, \tag{3.13}$$

which is an unobservable double quantum coherence. However, a $\pi/4$ y-pulse produces:

$$\hat{\hat{R}}_y\left(\frac{\pi}{4}\right)\hat{\rho}_0 = -\frac{1}{2}(I_{1x}I_{2x} + I_{1x}I_{2z} + I_{1z}I_{2x} + I_{1z}I_{2z}), \tag{3.14}$$

of which the $I_{1x}I_{2z}$ and $I_{1z}I_{2x}$ terms are observable single quantum coherences that give rise to the antiphase spectral lines in Fig. 3.13.

3.3.1.2 ALTADENA

In the case of an ALTADENA (Adiabatic Longitudinal Transport After Dissociation Engenders Net Alignment) experiment [123], the hydrogenation is performed at *low field*, which is the regime in which $|\Delta\omega| \ll |\omega_{\mathrm{II}}^J|$. When a molecule of parahydrogen is added to the substrate, the density operator $\hat{\rho}_{\mathrm{ini}}$ is projected onto the new eigenbasis, which in this regime is close to the singlet-triplet basis. To a good approximation the only term is the population of the state $|S_0\rangle$, and there is therefore no evolution of the system.

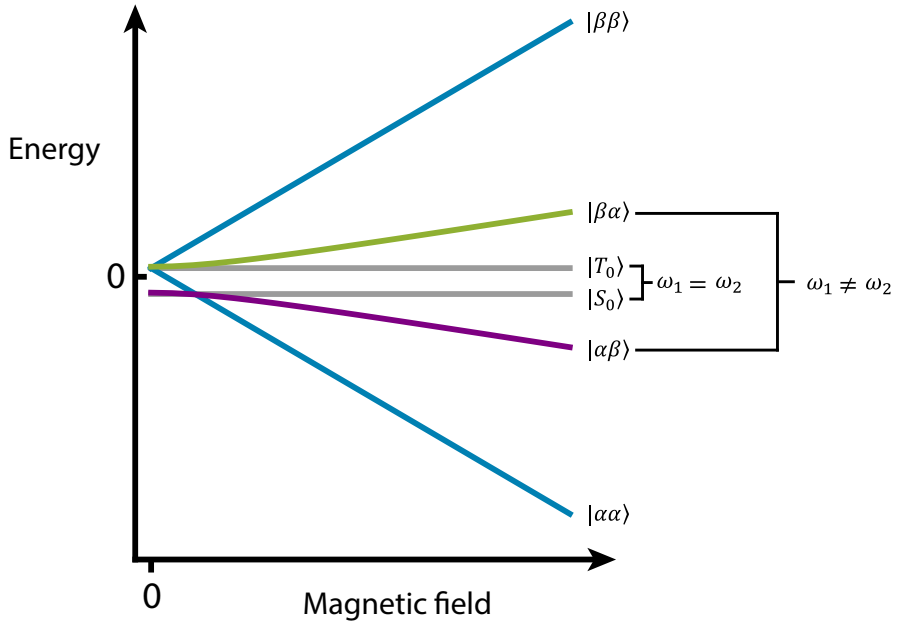

FIGURE 3.14: Eigenvalues of the basis states as a function of magnetic field, for two J-coupled protons with a nonzero chemical shift difference $\Delta\omega$. Arbitrary values of ω_{II}^J and $\Delta\omega$ were chosen for illustration. At zero-field where $\Delta\omega = 0$, the eigenstates are the singlet-triplet states, but as the field is increased such that $\Delta\omega \gg \omega_{\mathrm{II}}^J$, these states smoothly transform into approximately Zeeman states. In grey, the state energies for $|S_0\rangle$ and $|T_0\rangle$ are shown for a system with no chemical shift difference, to illustrate that in this case the singlet-triplet basis remains an exact eigenbasis for any field.

The magnetic field is then increased to *high field*, the regime in which $|\Delta\omega| \gg |\omega_{\mathrm{II}}^J|$, and the eigenbasis will be close to the Zeeman basis. The smooth evolution of the eigenstates from approximately singlet-triplet states, to approximately Zeeman states, is given in Eq. 3.7, and shown in Fig. 3.14.

If this process is performed adiabatically, i.e. the rate of change of magnetic field (where the relevant quantity is $\partial\Delta\omega/\partial t$) is small with respect to $(\omega_{\mathrm{II}}^J)^2$, the population of $|S_0\rangle$ will remain in an eigenstate at all fields, and evolve into population of the approximate state $|\alpha\beta\rangle$. The correspondence between $|S_0\rangle$ and either $|\alpha\beta\rangle$ or $|\beta\alpha\rangle$ is determined by the signs of ω_{II}^J and $\Delta\omega$.

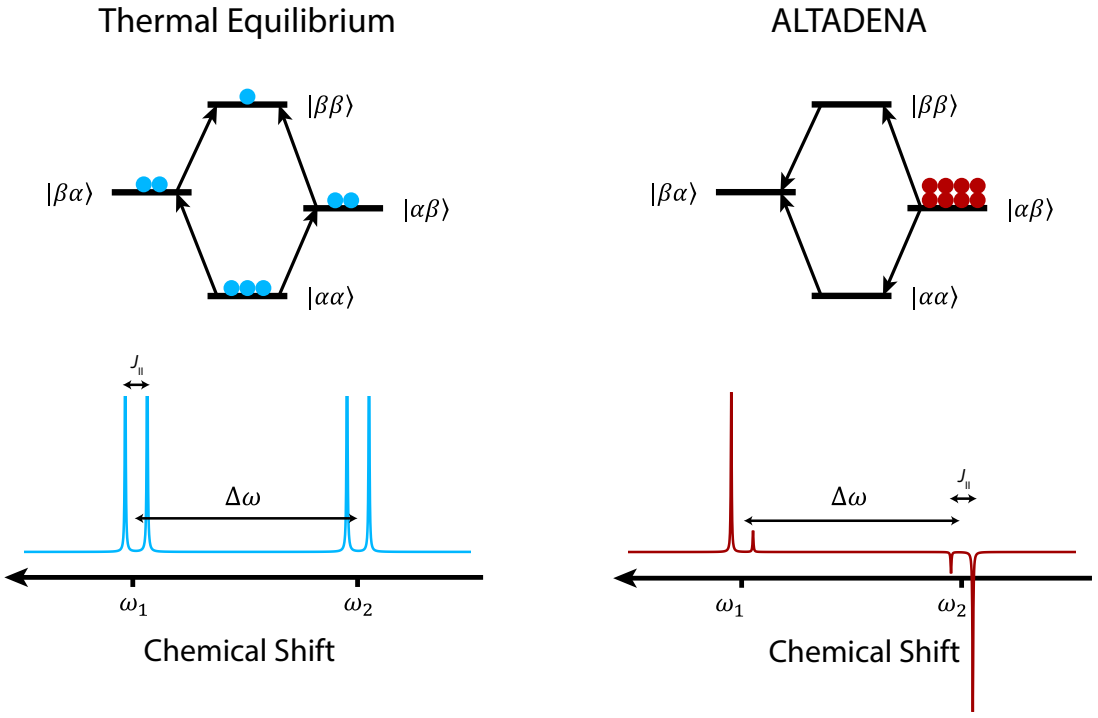

FIGURE 3.15: Balls represent populations of the Zeeman energy levels (not in proportion) for the cases of thermal equilibrium ^{1}H polarization, and ^{1}H polarization after the ALTADENA experiment described in the text. Simulations of the resulting spectra after applying a $\pi/4$ pulse are shown beneath. Arrows represent the phase of the coherences between states following the $\pi/4$ pulse.

In Figure. 3.15 a comparison is shown between the energy level populations and spectra for an ALTADENA experiment and a thermal equilibrium experiment.

3.3.2 Inequivalent J-couplings to a third spin

If the parahydrogen protons (I_1 and I_2) are added to *chemically equivalent* positions on a product molecule, but with different J-couplings to a third spin (S_3), the spin

Hamiltonian is

$$\hat{H} = \omega_{\mathrm{I}} \left(I_{1z} + I_{2z}\right) + \omega_{\mathrm{S}}\, S_{3z} + \omega^{J}_{\mathrm{II}}\, \mathbf{I}_1.\mathbf{I}_2 + \omega^{J}_{13}\, \mathbf{I}_1.\mathbf{S}_3 + \omega^{J}_{23}\, \mathbf{I}_2.\mathbf{S}_3. \tag{3.15}$$

A graphical representation of this molecular system is shown in Fig. 3.16. The spin

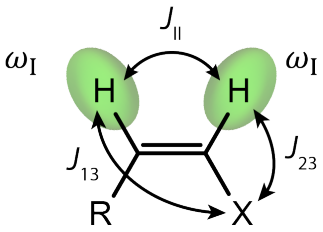

FIGURE 3.16: A graphical representation of a molecule in which a pair of J-coupled parahydrogen protons have identical chemical shifts (ω_1), but different J-couplings to an X nucleus, referred to in the text as the S-spin.

Hamiltonian can be decomposed into two parts:

$$\hat{H}_0 = \omega_{\mathrm{I}} \left(I_{1z} + I_{2z}\right) + \omega_{\mathrm{S}}\, S_{3z} + \omega^{J}_{\mathrm{II}}\, \mathbf{I}_1.\mathbf{I}_2 + \omega^{J}_{13}\, I_{1z} S_{3z} + \omega^{J}_{23}\, I_{2z} S_{3z}, \tag{3.16}$$

and

$$\hat{H}_1 = \omega^{J}_{13} \left(I_{1x} S_{3x} + I_{1y} S_{3y}\right) + \omega^{J}_{23} \left(I_{2x} S_{3x} + I_{2y} S_{3y}\right). \tag{3.17}$$

This will be discussed in more detail in section 4.2. For now it is sufficient to say that when $|\omega_{\mathrm{I}} - \omega_{\mathrm{S}}| \gg \omega^{J}_{13}$ and $|\omega_{\mathrm{I}} - \omega_{\mathrm{S}}| \gg \omega^{J}_{23}$, $\hat{H}_1$ can be neglected. This is the same secular approximation discussed in Eq. 2.67.

The eigenbasis of $\hat{H}_0$ is given by

$$\begin{aligned}
|1\rangle &= \cos\left(\frac{\theta_{\mathrm{G}}}{2}\right)|\beta\alpha\alpha\rangle - \sin\left(\frac{\theta_{\mathrm{G}}}{2}\right)|\alpha\beta\alpha\rangle\,, \\
|2\rangle &= |\alpha\alpha\alpha\rangle\,, \\
|3\rangle &= \cos\left(\frac{\theta_{\mathrm{G}}}{2}\right)|\alpha\beta\alpha\rangle + \sin\left(\frac{\theta_{\mathrm{G}}}{2}\right)|\beta\alpha\alpha\rangle\,, \\
|4\rangle &= |\beta\beta\alpha\rangle\,, \\
|5\rangle &= \cos\left(\frac{\theta_{\mathrm{G}}}{2}\right)|\alpha\beta\beta\rangle - \sin\left(\frac{\theta_{\mathrm{G}}}{2}\right)|\beta\alpha\beta\rangle\,, \\
|6\rangle &= |\alpha\alpha\beta\rangle\,, \\
|7\rangle &= \cos\left(\frac{\theta_{\mathrm{G}}}{2}\right)|\beta\alpha\beta\rangle + \sin\left(\frac{\theta_{\mathrm{G}}}{2}\right)|\alpha\beta\beta\rangle\,, \\
|8\rangle &= |\beta\beta\beta\rangle\,,
\end{aligned} \tag{3.18}$$

where the 'Goldman angle' [124] is given by $\theta_{\mathrm{G}} = \arctan(2\omega^{J}_{\mathrm{II}}/\omega^{\Delta}_{\mathrm{IS}})$, and $\omega^{\Delta}_{\mathrm{IS}} = \omega^{J}_{13} - \omega^{J}_{23}$.

3.3.2.1 Far from equivalence regime

When the protons spins are described as *far from equivalence*, this indicates $|\omega_{\mathrm{II}}^{J}| \ll |\omega_{\mathrm{IS}}^{\Delta}|$. To describe the spin dynamics of the parahydrogen proton pair in this regime, we will take a model system (shown in Fig. 3.17). For this system, the eigenbasis of $\hat{H}_0$ is given by the following kets:

$$\begin{aligned}
|1\rangle &= 0.998\,|\beta\alpha\alpha\rangle - 0.066\,|\alpha\beta\alpha\rangle\,,\\
|2\rangle &= |\alpha\alpha\alpha\rangle\,,\\
|3\rangle &= 0.998\,|\alpha\beta\alpha\rangle + 0.066\,|\beta\alpha\alpha\rangle\,,\\
|4\rangle &= |\beta\beta\alpha\rangle\,,\\
|5\rangle &= 0.998\,|\alpha\beta\beta\rangle - 0.066\,|\beta\alpha\beta\rangle\,,\\
|6\rangle &= |\alpha\alpha\beta\rangle\,,\\
|7\rangle &= 0.998\,|\beta\alpha\beta\rangle + 0.066\,|\alpha\beta\beta\rangle\,,\\
|8\rangle &= |\beta\beta\beta\rangle\,.
\end{aligned} \tag{3.19}$$

These basis states are close to the Zeeman basis states, which is a similar case to the PASADENA experiment described above.

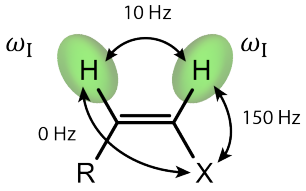

FIGURE 3.17: A model spin system for a proton pair far from equivalence, due to the large asymmetry in J-couplings to a third spin.

When a molecule of parahydrogen is added to the substrate, the density operator $\hat{\rho}_{\mathrm{ini}}$ is projected onto the new eigenbasis. For simplicity this will be taken as the Zeeman basis:

$$\hat{\rho}_{ini} = \begin{array}{c} \\ \langle\beta\alpha\alpha| \\ \langle\alpha\alpha\alpha| \\ \langle\alpha\beta\alpha| \\ \langle\beta\beta\alpha| \\ \langle\alpha\beta\beta| \\ \langle\alpha\alpha\beta| \\ \langle\beta\alpha\beta| \\ \langle\beta\beta\beta| \end{array} \begin{array}{c} \begin{array}{cccccccc} |\beta\alpha\alpha\rangle & |\alpha\alpha\alpha\rangle & |\alpha\beta\alpha\rangle & |\beta\beta\alpha\rangle & |\alpha\beta\beta\rangle & |\alpha\alpha\beta\rangle & |\beta\alpha\beta\rangle & |\beta\beta\beta\rangle \end{array} \\ \begin{pmatrix} \frac{1}{4} & 0 & -\frac{1}{4} & 0 & 0 & 0 & 0 & 0 \\ 0 & 0 & 0 & 0 & 0 & 0 & 0 & 0 \\ -\frac{1}{4} & 0 & \frac{1}{4} & 0 & 0 & 0 & 0 & 0 \\ 0 & 0 & 0 & 0 & 0 & 0 & 0 & 0 \\ 0 & 0 & 0 & 0 & \frac{1}{4} & 0 & -\frac{1}{4} & 0 \\ 0 & 0 & 0 & 0 & 0 & 0 & 0 & 0 \\ 0 & 0 & 0 & 0 & -\frac{1}{4} & 0 & \frac{1}{4} & 0 \\ 0 & 0 & 0 & 0 & 0 & 0 & 0 & 0 \end{pmatrix} \end{array}. \tag{3.20}$$

Similar to the PASADENA case, the hydrogenation period is usually much longer than the coherence evolution period, and so the resulting density operator is

$$\hat{\rho}_0 = \begin{array}{c} \\ \langle\beta\alpha\alpha| \\ \langle\alpha\alpha\alpha| \\ \langle\alpha\beta\alpha| \\ \langle\beta\beta\alpha| \\ \langle\alpha\beta\beta| \\ \langle\alpha\alpha\beta| \\ \langle\beta\alpha\beta| \\ \langle\beta\beta\beta| \end{array} \begin{array}{c} \begin{array}{cccccccc} |\beta\alpha\alpha\rangle & |\alpha\alpha\alpha\rangle & |\alpha\beta\alpha\rangle & |\beta\beta\alpha\rangle & |\alpha\beta\beta\rangle & |\alpha\alpha\beta\rangle & |\beta\alpha\beta\rangle & |\beta\beta\beta\rangle \end{array} \\ \begin{pmatrix} \frac{1}{4} & 0 & 0 & 0 & 0 & 0 & 0 & 0 \\ 0 & 0 & 0 & 0 & 0 & 0 & 0 & 0 \\ 0 & 0 & \frac{1}{4} & 0 & 0 & 0 & 0 & 0 \\ 0 & 0 & 0 & 0 & 0 & 0 & 0 & 0 \\ 0 & 0 & 0 & 0 & \frac{1}{4} & 0 & 0 & 0 \\ 0 & 0 & 0 & 0 & 0 & 0 & 0 & 0 \\ 0 & 0 & 0 & 0 & 0 & 0 & \frac{1}{4} & 0 \\ 0 & 0 & 0 & 0 & 0 & 0 & 0 & 0 \end{pmatrix} \end{array}. \tag{3.21}$$

In Figure. 3.18 simulated proton spectra (only the I-spins) for the model system are shown. A comparison is made between the I-spins originating from parahydrogen addition, and a spin system at thermal equilibrium.

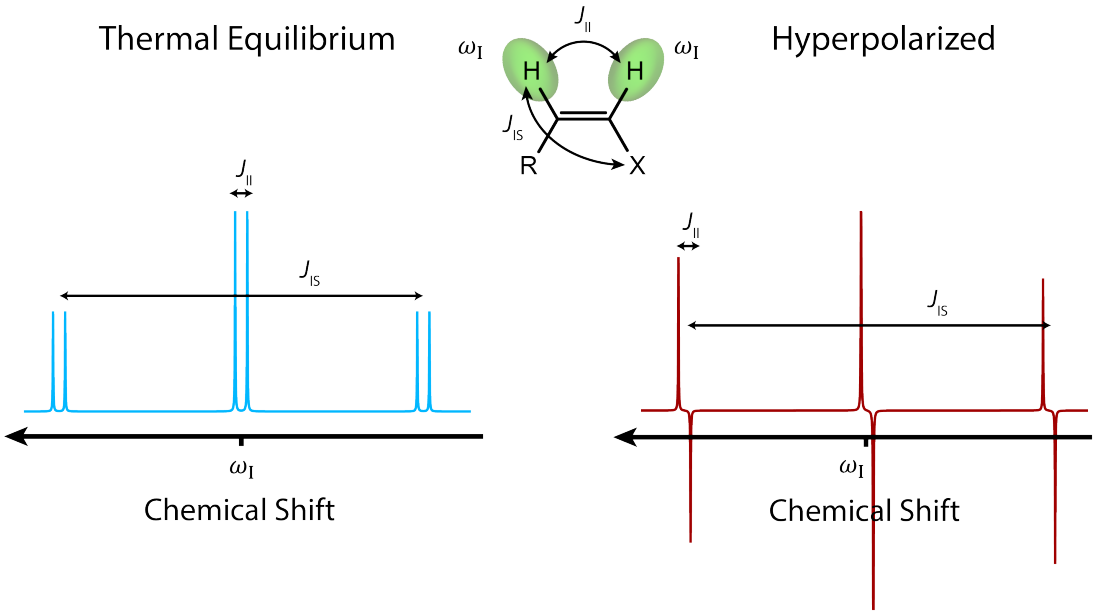

FIGURE 3.18: Simulations of the I-spin spectra of the far from equivalence spin system, assuming after applying a $\pi/4$ pulse for the hyperpolarized (left) and thermal equilibrium (right) cases. The parameters used were $J_{\mathrm{II}} = 10\,\mathrm{Hz}$, $J_{\mathrm{IS}} = 150\,\mathrm{Hz}$, as in the model spin system shown in Fig. 3.17.

Note that since the eigenbasis is approximately the Zeeman basis for this system, the populations that result from parahydrogen addition will relax with T_1, and are not long-lived. If the proton-proton J-coupling is the dominant interaction, and the proton

singlet state is close to being an eigenstate, the parahydrogen singlet order can be long-lived, and this is the case for the *near-equivalence regime*.

3.3.2.2 Near-equivalence regime

When the protons spins are described as *near-equivalence*, this indicates $|\omega_{\mathrm{II}}^{J}| \gg |\omega_{\mathrm{IS}}^{\Delta}|$. To describe the spin dynamics of the parahydrogen proton pair in this regime, we will take a model system (shown in Fig. 3.19). For this system, the eigenbasis of $\hat{H}_0$ is given by the following kets:

$$\begin{aligned}
|1\rangle &= -0.725\,|\beta\alpha\alpha\rangle + 0.689\,|\alpha\beta\alpha\rangle\,,\\
|2\rangle &= |\alpha\alpha\alpha\rangle\,,\\
|3\rangle &= 0.725\,|\alpha\beta\alpha\rangle + 0.689\,|\beta\alpha\alpha\rangle\,,\\
|4\rangle &= |\beta\beta\alpha\rangle\,,\\
|5\rangle &= 0.725\,|\alpha\beta\beta\rangle - 0.689\,|\beta\alpha\beta\rangle\,,\\
|6\rangle &= |\alpha\alpha\beta\rangle\,,\\
|7\rangle &= 0.725\,|\beta\alpha\beta\rangle + 0.689\,|\alpha\beta\beta\rangle\,,\\
|8\rangle &= |\beta\beta\beta\rangle\,.
\end{aligned} \tag{3.22}$$

In this regime, the eigenbasis of $\hat{H}_0$ is close to the Singlet-Triplet-Zeeman ($\mathbb{STZ}$) basis, which is a product basis between the singlet and triplet states for the I-spins, and the Zeeman states for the S-spin. This basis will be discussed in much greater detail in Sections 4.2 and 5.2, but for now it is sufficient to simply understand that the proton singlet state is close to an eigenstate. The nomenclature $|S_0\alpha\rangle$ indicates a proton singlet state and an S-spin $|\alpha\rangle$ state.

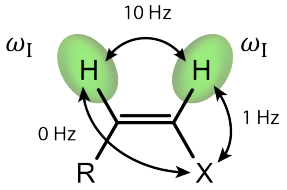

FIGURE 3.19: A model spin system for a near-equivalence proton pair.

When a molecule of parahydrogen is chemically attached to the substrate, $\hat{\rho}_{\mathrm{ini}}$ is projected onto the new eigenbasis. The proton singlet state is close to an eigenstate, and so to a good approximation there is no evolution of the density operator. This is similar to the ALTADENA starting condition, but unlike an ALTADENA experiment the nonmagnetic proton singlet order cannot be automatically transformed into observable Zeeman order by simply increasing the magnetic field, because the term that breaks the proton symmetry, $\omega_{\mathrm{IS}}^{\Delta}$, is not field-dependent.

A number of techniques have therefore been developed for the transfer of singlet population into other states, to produce hyperpolarized I- and S-spin signals.

Case 1: Magnetic field manipulations

Many polarization transfer techniques utilize manipulations of the external B_0 field. This is because at certain values of B_0, avoided crossings arise between the basis states, and these can be exploited.

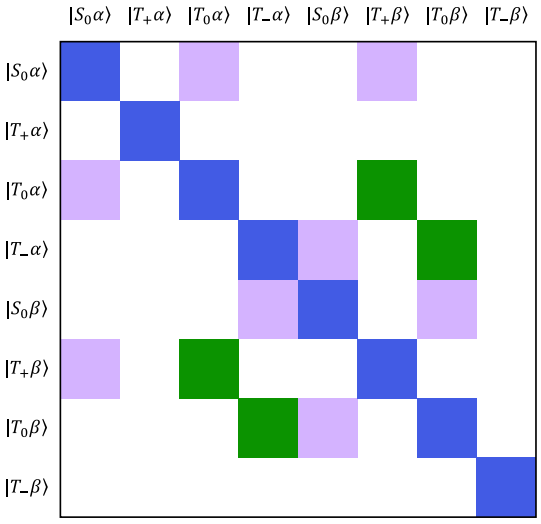

FIGURE 3.20: A matrix plot of $\hat{H}$, which shows off-diagonal coupling elements between states of the $\mathbb{STZ}$ basis. Green represents terms proportional to $\omega_{\mathrm{IS}}^{\Sigma}$, and lilac represents terms proportional to $\omega_{\mathrm{IS}}^{\Delta}$.

A matrix representation of $\hat{H}$ in the $\mathbb{STZ}$ basis is shown in Fig. 3.20. The green and lilac off-diagonal components represent terms proportional to $\omega_{\mathrm{IS}}^{\Sigma}$ and $\omega_{\mathrm{IS}}^{\Delta}$, respectively. The presence of these components causes state mixing, and can lead to an avoided crossing instead of a degeneracy between the connected diagonal components. This is illustrated in Fig. 3.21. The eigenvalues of the eigenstates of $\hat{H}$ (see Eq. 3.15) are plotted against external magnetic field for the J-couplings of the near-equivalence model system from Fig 3.19, and ω_{I} and ω_{S} are ^{1}H and ^{13}C precession frequencies. An avoided crossing appears between the states which most closely correspond to $|S_0\alpha\rangle$ and $|T_{+1}\beta\rangle$ at the field B_0^{match}.

The exact value of B_0^{match} is calculated in section 4.2 for specific spin systems, but for the general discussion here, this is not necessary. For simplicity this is a helpful omission, because real molecules can have many spins in the J-coupling network that dramatically complicate both the number, and positions, of the avoided crossings between states. For the moment it is sufficient to know that the avoided crossing(s) appear at values of B_0 for which matching conditions that have a form not dissimilar to $|\omega_{\mathrm{I}} - \omega_{\mathrm{S}}| \approx J_{\mathrm{II}}$ are satisfied.

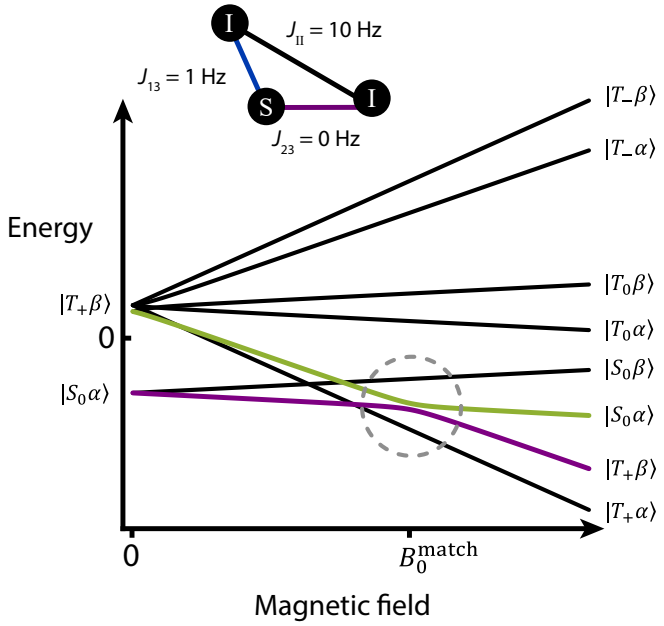

FIGURE 3.21: Eigenvalues of the Hamiltonian $\hat{H}$ basis states as a function of applied field, with the spin system parameters shown by the inset molecule, and ^{1}H and ^{13}C Larmor precession frequencies for the I and S spins, respectively. The solid lines indicate eigenstates that transform smoothly into each other as the magnetic field changes. The lines are labelled with the $\hat{H}_0$ basis state that most closely corresponds to the eigenstate. The eigenvalues of states $|S_0\alpha\rangle$ and $|T_{+1}\beta\rangle$ are shown in green and purple, and the avoided crossing between these states is highlighted by the dashed circle. These two states are labelled on both sides of the Figure to show that they transform into each other.

The J-couplings are typically in the order of 1-10 Hz. If the I and S spins belong to different isotopes, $|\omega_I - \omega_S|$ corresponds to a Larmor frequency difference and B_0^{match} is often in the order of 0.1 - 1 μT. If the I and S spins belong to the same isotope, $|\omega_I - \omega_S|$ corresponds to a chemical shift difference, and B_0^{match} is typically in the order of 10 - 100 mT.

Three techniques for converting I-spin singlet order into observable magnetization by manipulating the B_0 field are given below.

1. Technique 1 is a field-cycling experiment, and is depicted in Fig. 3.22. At $t = t_0$, the sample is parahydrogenated at high-field, and since the singlet state is approximately an eigenstate of $\hat{H}$, the populated states of $\hat{\rho}_0$ are $|S_0\alpha\rangle$ and $|S_0\beta\rangle$. At $t = t_1$, the field is diabatically (rapidly) dropped to near-zero field (i.e. $B_0 < B_0^{match}$). This has the effect of projecting the density operator onto the Hamiltonian eigenbasis at the new field. Since $|S_0\alpha\rangle$ and $|S_0\beta\rangle$ are still approximately eigenstates, the field drop has no effect, so $\hat{\rho}_1 = \hat{\rho}_0$. At $t = t_2$, the field is then adiabatically (slowly) increased to high-field, and the state populations evolve along with the Hamiltonian eigenstates. For the case shown in Fig. 3.21, this means the populated

states of $\hat{\rho}_2$ at the end of the adiabatic sweep are $|T_{+1}\beta\rangle$ and $|S_0\beta\rangle$. In this manner, the proton singlet order has been completely converted into S-spin polarization.

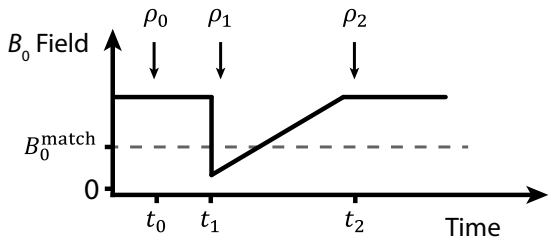

FIGURE 3.22: Technique 1; the B_0 field manipulations for the simple field cycling experiment described in the text.

2. Technique 2 is depicted in Fig. 3.23. At $t = t_0$, the sample is parahydrogenated at high-field, and since the singlet state is approximately an eigenstate of $\hat{H}$, the populated states of $\hat{\rho}_0$ are $|S_0\alpha\rangle$ and $|S_0\beta\rangle$. At $t = t_1$, the field is diabatically (rapidly) dropped to B_0^{match}, and this has the effect of projecting the density operator onto the Hamiltonian eigenbasis at the new field. At B_0^{match} the off-diagonal elements in the Hamiltonian will drive oscillatory transitions between states $|S_0\alpha\rangle$ and $|T_{+1}\beta\rangle$, with frequency $(J_{13} - J_{23})/\sqrt{2}$. At $t = t_2$, which is half an oscillation period after t_1, the system is diabatically returned to high-field, and the populated states of $\hat{\rho}_2$ are $|T_{+1}\beta\rangle$ and $|S_0\beta\rangle$. In this manner, the proton singlet order has been completely converted into S-spin polarization.

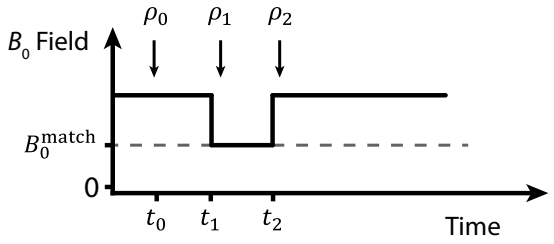

FIGURE 3.23: Technique 2; the B_0 field manipulations for the experiment described in the text.

3. Technique 3 is depicted in Fig. 3.24. This method simply requires parahydrogenation of the sample at the field B_0^{match}. At this field, $|S_0\beta\rangle$ is approximately an eigenstate, so 50% of the spin population will occupy this state. However, at B_0^{match} the off-diagonal elements in the Hamiltonian will drive oscillatory transitions between states $|S_0\alpha\rangle$ and $|T_{+1}\beta\rangle$, and if the hydrogenation period is long with respect to the oscillation period $\sqrt{2}/(J_{13} - J_{23})$, these states will both be 25% populated. The result is 50% S-spin polarization.

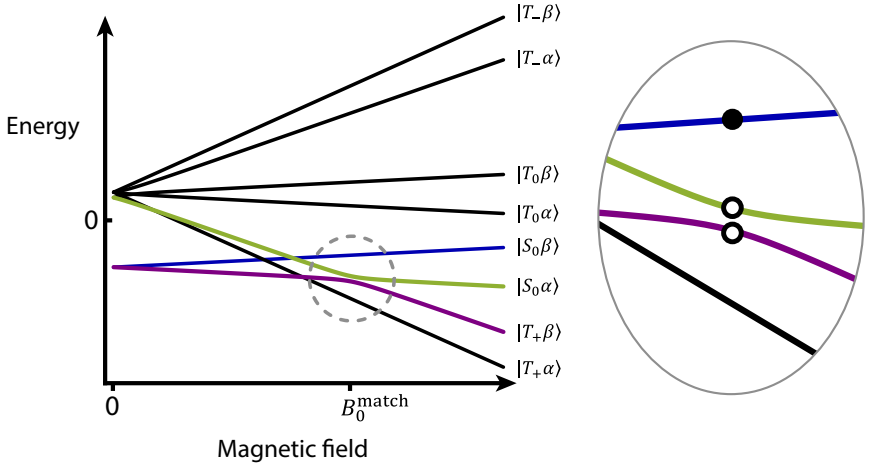

FIGURE 3.24: Technique 3; on the left are the eigenvalues of the $\mathbb{STZ}$ states as a function of B_0 field. On the right a zoom of the avoided crossing region is shown. The balls represent state populations achieved after parahydrogenating the sample at B_0^{match}, with filled representing 50% and empty representing 25%.

To summarise: avoided crossings between states exist at specific magnetic fields, and these can be exploited to transfer spin population between states.

Case 2: Rf irradiation

If the sample is at high-field (i.e. $B_0 \gg B_0^{\text{match}}$), it is possible to create avoided crossings between the states by the application of an electromagnetic field. For the case of high-field NMR this usually means rf irradiation.

The spin Hamiltonian for the system in the presence of on-resonance S-spin rf irradiation (with phase x), is given by

$$\hat{H}_{\text{drf}} = \omega_{\text{I}}^{J}\,\mathbf{I}_1.\mathbf{I}_2 + \omega_{13}^{J}\,I_{1z}S_{3z} + \omega_{23}^{J}\,I_{2z}S_{3z} + \omega_{\text{S}}^{\text{nut}}\,S_{3x}, \tag{3.23}$$

where the rf field amplitude is expressed as a nutation frequency $\omega_{\text{S}}^{\text{nut}}$. The Hamiltonian is written in the doubly rotating frame, which means the I- and S-spin precession terms around z are no longer present. The x and y components of the heteronuclear J-couplings have been neglected under the secular approximation.

Fig. 3.25 shows the eigenvalues of the Hamiltonian eigenstates as a function of $\omega_{\text{S}}^{\text{nut}}$, and spin system parameters are stated in the caption. The S-spin states are now quantized along the rf field axis, and the labels α and β describe the spins being aligned along and against the x-axis, respectively.

There is an avoided crossing between the states which most closely correspond to $|T_0\alpha\rangle$ and $|S_0\beta\rangle$ at a specific matching condition ($\omega_{\text{nut}}^{\text{match}}$) of the S-spin nutation frequency. By manipulating $\omega_{\text{S}}^{\text{nut}}$ this avoided crossing can be exploited to induce state transitions between the approximate states $|T_0\alpha\rangle$ and $|S_0\beta\rangle$. For this spin system, the

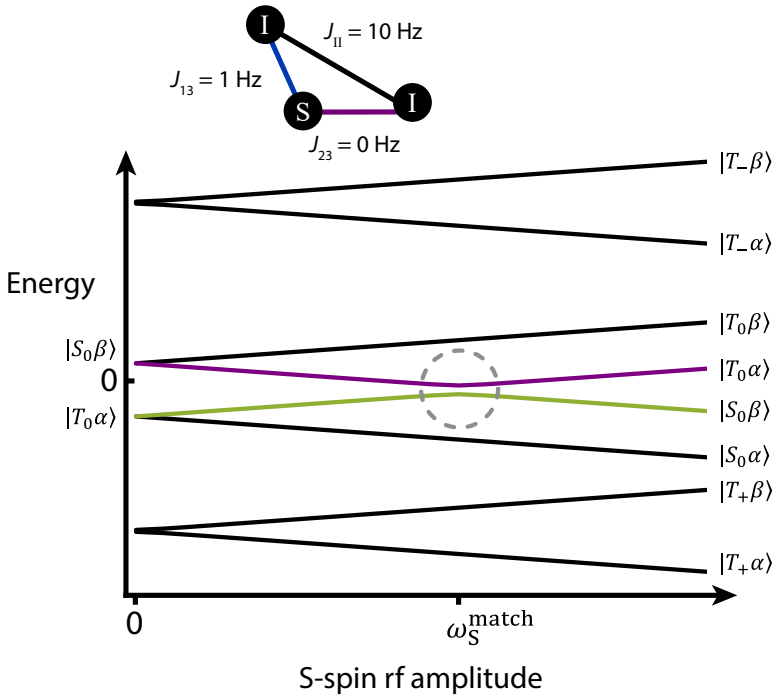

FIGURE 3.25: Eigenvalues of the Hamiltonian $\hat{H}_{drf}$ as a function of rf field amplitude, for the spin system shown, with an additional I-spin precession frequency of $\omega_I(I_{1z}+I_{2z})$, with $\omega_I = 2\pi \times 10\,\text{rad}\,\text{s}^{-1}$ to lift state degeneracies and make the illustration clearer. The solid lines indicate eigenstates that transform smoothly into each other as the rf field changes. The eigenvalues of the states which correspond most closely to $|S_0\beta\rangle$ and $|T_0\alpha\rangle$ are shown in green and purple, and the avoided crossing between these states is highlighted by the dashed circle. These two states are labelled on both sides of the Figure to show that they transform into each other.

exact value of ω_S^{match} turns out to be equal to ω_{II}^J, and this is discussed further in section 5.2.2.

This is similar to the previously described cases of manipulating B_0 to exploit the avoided crossing at B_0^{match} to convert I-spin singlet order into I- and S-spin polarization, although the states involved are different so the final density operator will be different. All three cases described previously can be used in this new high-field rf irradiation context, and will not be described again.

There are other rf transfer techniques that are outside the scope of this discussion, which involve irradiation of multiple spins, or sweeping the offset frequency of ω_S^{nut} (rather than the nutation frequency).

Other high-field rf transfer methods utilise 'hard' pulses, where $|\omega_S^{nut}| \gg |\omega_{II}^J|$, and these will be discussed in more detail in section 5.2.3.

Chapter 4

Singlet Order Manipulation at Ultra-Low Field

The work in this chapter is based on material presented in Ref. [125].

4.1 Introduction

In this chapter, a method for converting proton singlet order into ^{13}C magnetization using zero and ultra-low field manipulations is described. Specifically, this is done by adiabatically sweeping an applied magnetic field from a negative value to a positive value, passing through zero. The molecules studied are the 2% natural abundance [1-^{13}C]maleic acid formed after hydrogenating acetylene dicarboxylic acid (see Fig. 4.1). The method is depicted in Fig. 4.2: (1) react [1-^{13}C]acetylene dicarboxylic acid with para-enriched hydrogen in the presence of a magnetic field (magnetic field = $+2\,\mu$T); (2) perform a non-adiabatic (rapid) field reversal to -2 μT; (3) adiabatically (slowly) reverse the sign of the magnetic field, passing through zero; (4) shuttle the sample to a high-field benchtop NMR (nuclear magnetic resonance) magnet, and (5) observe the ^{13}C NMR signals. To perform the field sweeps, a ZULF (zero and ultra-low field) NMR setup [126] was used, which allows for precise control over the magnetic fields required for polarization transfer. The apparatus is described in more detail in section 4.3.

[1-^{13}C]maleic acid is a three spin-1/2, AA'X system. The J-coupling network is shown in Fig. 4.3a, along with experimental (Fig. 4.3b) and simulated (Fig. 4.3c) ^{13}C NMR spectra for a system at thermal equilibrium. The proton-proton J-coupling is of the same order of magnitude as the difference in proton-carbon J-couplings. An energy level diagram with the single-quantum ^{13}C transitions highlighted is shown in Fig. 4.3d, to illustrate the origin of the spectral lines. The finite amplitude of the outer transitions (5) and (6) is due to singlet-triplet mixing, induced by the heteronuclear J-couplings.

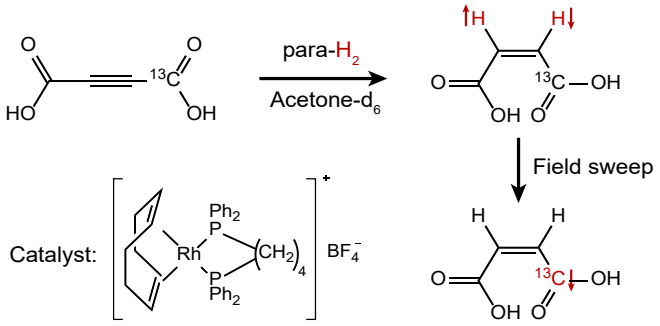

FIGURE 4.1: Para-enriched hydrogen gas undergoes pairwise addition to [1-^{13}C]acetylene dicarboxylic acid to form [1-^{13}C]maleic acid. The reaction catalyst is [1,4-bis(diphenylphosphino)butane](1,5-cyclooctadiene)rhodium(I) tetrafluoroborate. The proton singlet order is transformed into ^{13}C magnetization by applying a field sweep, passing through zero field.

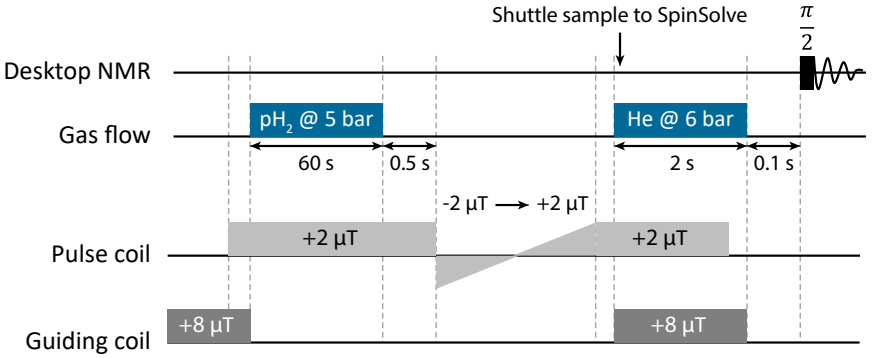

FIGURE 4.2: Event sequence for the experiments performed, unless stated otherwise in the text. Further details are given in the Materials and Methods section.

4.2 Theoretical Description of the Field Sweep

4.2.1 State Bases and the Spin Hamiltonian

Maleic acid is a three spin-1/2 system, with two protons, I_1 and I_2, from the parahydrogen pair, and a heteronuclear ^{13}C spin, S_3. It is convenient to discuss the dynamics of this spin system using the $\mathbb{STZ}$ basis, defined as the tensor product of the singlet-triplet states for spins 1 and 2, and the Zeeman states for spin 3:

$$\mathbb{STZ} = \{|S_0^{12}\rangle, |T_{+1}^{12}\rangle, |T_0^{12}\rangle, |T_{-1}^{12}\rangle\} \otimes \{|\alpha^3\rangle, |\beta^3\rangle\}, \tag{4.1}$$

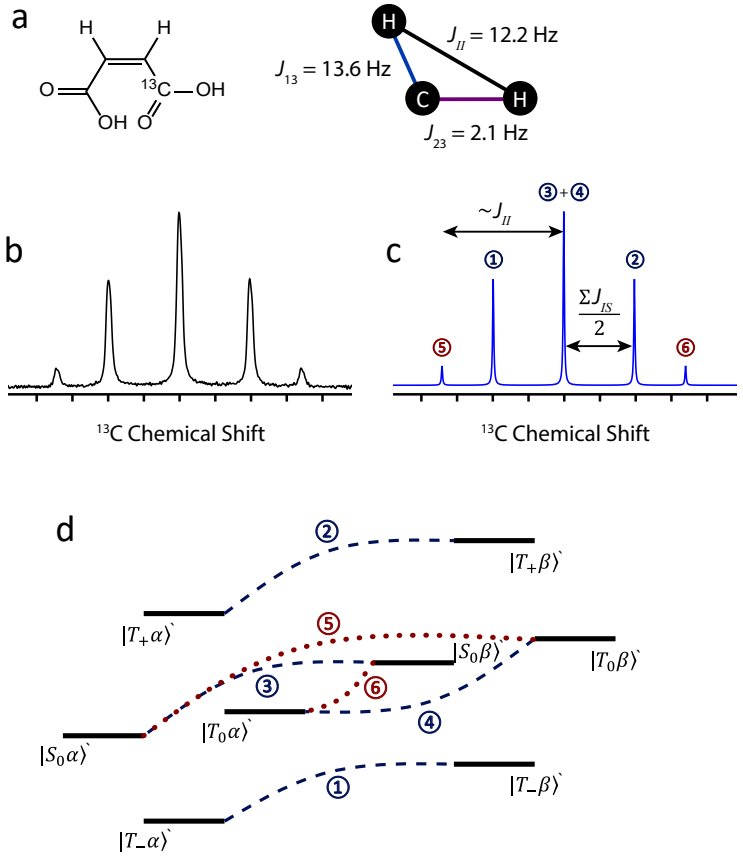

FIGURE 4.3: a) The product of the hydrogenation reaction, [1-^{13}C]maleic acid, alongside a schematic showing the J-coupling network. b) An experimental ^{13}C NMR spectrum without proton decoupling acquired with 16 transients on a sample of 1 M maleic acid in methanol-d_4, showing just the carbonyl ^{13}C peak. c) A simulation of the thermal polarization ^{13}C NMR spectrum of the carbonyl peak in [1-^{13}C]maleic acid. d) The nuclear spin energy levels of [1-^{13}C]maleic acid with the ^{13}C single quantum transitions labelled. The label on each state indicates the $\mathbb{STZ}$ (Singlet-Triplet-Zeeman) basis state which corresponds most closely to the energy eigenstate. The dotted red lines labelled (5)+(6) show weak transitions which would be rigorously forbidden if the singlet and triplet states were exact Hamiltonian eigenstates, but become weakly allowed through singlet-triplet mixing by the heteronuclear J-couplings.

where the singlet and triplet states of the proton pair are defined as follows:

$$\begin{aligned} |S_0^{12}\rangle &= \frac{1}{\sqrt{2}}(|\alpha^1\beta^2\rangle - |\beta^1\alpha^2\rangle) \\ |T_{+1}^{12}\rangle &= |\alpha^1\alpha^2\rangle \\ |T_0^{12}\rangle &= \frac{1}{\sqrt{2}}(|\alpha^1\beta^2\rangle + |\beta^1\alpha^2\rangle) \\ |T_{-1}^{12}\rangle &= |\beta^1\beta^2\rangle\,. \end{aligned} \tag{4.2}$$

The indices indicate the spin label, and will be dropped henceforth.

The spin Hamiltonian for a solution-state sample is

$$\hat{H} = \hat{H}_0 + \hat{H}_1, \tag{4.3}$$

which is split into two parts for convenience, with

$$\begin{aligned}\hat{H}_0 = 2\pi J_{\mathrm{II}}\mathbf{I}_1.\mathbf{I}_2 + 2\pi J_{13}I_{1z}S_{3z} + 2\pi J_{23}I_{2z}S_{3z} \\ +\omega_{\mathrm{I}}^0(I_{1z} + I_{2z}) + \omega_{\mathrm{S}}^0 S_{3z},\end{aligned} \tag{4.4}$$

and

$$\begin{aligned}\hat{H}_1 = 2\pi J_{13}\,\tfrac{1}{2}(I_1^+S_3^- + I_1^-S_3^+) \\ +2\pi J_{23}\,\tfrac{1}{2}(I_2^+S_3^- + I_2^-S_3^+),\end{aligned} \tag{4.5}$$

where $\omega_j^0 = -\gamma_j B_0$, with j a spin label that corresponds to a specific nuclear isotope, and J_{13} is the J-coupling between spins I_1 and S_3. The following symbols are introduced now for brevity in later discussions:

$$\begin{aligned}\omega_{\mathrm{II}} &= 2\pi J_{\mathrm{II}} \\ \omega_{\mathrm{IS}}^{\Delta} &= 2\pi(J_{13} - J_{23}) \\ \omega_{\mathrm{IS}}^{\Sigma} &= 2\pi(J_{13} + J_{23}) \\ \Omega &= \sqrt{4(\omega_{\mathrm{II}})^2 + (\omega_{\mathrm{IS}}^{\Delta})^2}.\end{aligned}$$

The eigenbasis of $\hat{H}_0$ is termed here the $\mathbb{STZ}'$ basis, and consists of the following states:

$$\begin{aligned}|1\rangle &= |S_0\alpha\rangle' = \cos\left(\frac{\theta_{\mathrm{G}}}{2}\right)|\beta\alpha\alpha\rangle - \sin\left(\frac{\theta_{\mathrm{G}}}{2}\right)|\alpha\beta\alpha\rangle \\ |2\rangle &= |T_{+1}\alpha\rangle' = |\alpha\alpha\alpha\rangle \\ |3\rangle &= |T_0\alpha\rangle' = \cos\left(\frac{\theta_{\mathrm{G}}}{2}\right)|\alpha\beta\alpha\rangle + \sin\left(\frac{\theta_{\mathrm{G}}}{2}\right)|\beta\alpha\alpha\rangle \\ |4\rangle &= |T_{-1}\alpha\rangle' = |\beta\beta\alpha\rangle \\ |5\rangle &= |S_0\beta\rangle' = \cos\left(\frac{\theta_{\mathrm{G}}}{2}\right)|\alpha\beta\beta\rangle - \sin\left(\frac{\theta_{\mathrm{G}}}{2}\right)|\beta\alpha\beta\rangle \\ |6\rangle &= |T_{+1}\beta\rangle' = |\alpha\alpha\beta\rangle \\ |7\rangle &= |T_0\beta\rangle' = \cos\left(\frac{\theta_{\mathrm{G}}}{2}\right)|\beta\alpha\beta\rangle + \sin\left(\frac{\theta_{\mathrm{G}}}{2}\right)|\alpha\beta\beta\rangle \\ |8\rangle &= |T_{-1}\beta\rangle' = |\beta\beta\beta\rangle\,,\end{aligned} \tag{4.6}$$

where the 'Goldman angle' [124] is given by $\theta_{\mathrm{G}} = \arctan(2\omega_{\mathrm{II}}/\omega_{\mathrm{IS}}^{\Delta})$. In the case of magnetic equivalence, $\theta_{\mathrm{G}} = \pi/2$, while for strong inequivalence, $\theta_{\mathrm{G}} \to 0$. Note: in chapter 5 of this thesis the term $\theta = \pi/2 - \theta_{\mathrm{G}}$ will be used instead.

The heteronuclear J-coupling terms in $\hat{H}_0$ mix the $|S_0\rangle$ and $|T_0\rangle$ states. The eigenvalues for $\hat{H}_0$ are given in Table 4.1, along with the corresponding $\mathbb{STZ}'$ eigenstate. Note that although the eigenvalues of $\hat{H}_0$ depend on the applied field, the eigenstates do not.

Eigenstate of H_0	**$4 *$ State Energy / rad s^{-1}**
$\|1\rangle = \|S_0\alpha\rangle'$	$-\omega_{\mathrm{II}} - \Omega + 2\omega_{\mathrm{S}}^0$
$\|2\rangle = \|T_{+1}\alpha\rangle'$	$\omega_{\mathrm{II}} + \omega_{\mathrm{IS}}^{\Sigma} + 4\omega_{\mathrm{I}}^0 + 2\omega_{\mathrm{S}}^0$
$\|3\rangle = \|T_0\alpha\rangle'$	$-\omega_{\mathrm{II}} + \Omega + 2\omega_{\mathrm{S}}^0$
$\|4\rangle = \|T_{-1}\alpha\rangle'$	$\omega_{\mathrm{II}} - \omega_{\mathrm{IS}}^{\Sigma} - 4\omega_{\mathrm{I}}^0 + 2\omega_{\mathrm{S}}^0$
$\|5\rangle = \|S_0\beta\rangle'$	$-\omega_{\mathrm{II}} - \Omega - 2\omega_{\mathrm{S}}^0$
$\|6\rangle = \|T_{+1}\beta\rangle'$	$\omega_{\mathrm{II}} - \omega_{\mathrm{IS}}^{\Sigma} + 4\omega_{\mathrm{I}}^0 - 2\omega_{\mathrm{S}}^0$
$\|7\rangle = \|T_0\beta\rangle'$	$-\omega_{\mathrm{II}} + \Omega - 2\omega_{\mathrm{S}}^0$
$\|8\rangle = \|T_{-1}\beta\rangle'$	$\omega_{\mathrm{II}} + \omega_{\mathrm{IS}}^{\Sigma} - 4\omega_{\mathrm{I}}^0 - 2\omega_{\mathrm{S}}^0$

TABLE 4.1: The symbols are defined as follows: $\omega_j^0 = -\gamma_j B_0$, and $\Omega = \sqrt{4(\omega_{\mathrm{II}})^2 + (\omega_{\mathrm{IS}}^{\Delta})^2}$.

4.2.2 Avoided Crossings

At specific matching conditions of the external field B_0, eigenvalues of $\hat{H}_0$ can become degenerate. The flip-flop components of the heteronuclear J-couplings, contained in $\hat{H}_1$, mix the basis states of the full Hamiltonian $\hat{H}$, which leads to avoided crossings between the mixed states at the positions of the $\hat{H}_0$ degeneracies. The B_0 field positions of these avoided crossings are given (in units of tesla) by:

$$B_{\mathrm{AC}}^{(1)} \rightarrow \frac{2\omega_{\mathrm{II}} + \Omega - \omega_{\mathrm{IS}}^{\Sigma}}{4(\gamma_{\mathrm{I}} - \gamma_{\mathrm{S}})}, \tag{4.7}$$

and

$$B_{\mathrm{AC}}^{(2)} \rightarrow \frac{2\omega_{\mathrm{II}} - \Omega - \omega_{\mathrm{IS}}^{\Sigma})}{4(\gamma_{\mathrm{I}} - \gamma_{\mathrm{S}})}. \tag{4.8}$$

When $|\omega_{\mathrm{II}}| \gg |\omega_{\mathrm{IS}}^{\Delta}|$ these equations simplify to:

$$B_{\mathrm{AC}}^{(1)} \rightarrow \frac{4\omega_{\mathrm{II}} - \omega_{\mathrm{IS}}^{\Sigma}}{4(\gamma_{\mathrm{I}} - \gamma_{\mathrm{S}})}, \tag{4.9}$$

and

$$B_{\mathrm{AC}}^{(2)} \rightarrow \frac{-\omega_{\mathrm{IS}}^{\Sigma}}{4(\gamma_{\mathrm{I}} - \gamma_{\mathrm{S}})}. \tag{4.10}$$

Table 4.2 shows the states which have an avoided crossing at the field values given, and gives the mixing terms in the Hamiltonian $\hat{H}_1$ that cause these avoided crossings.

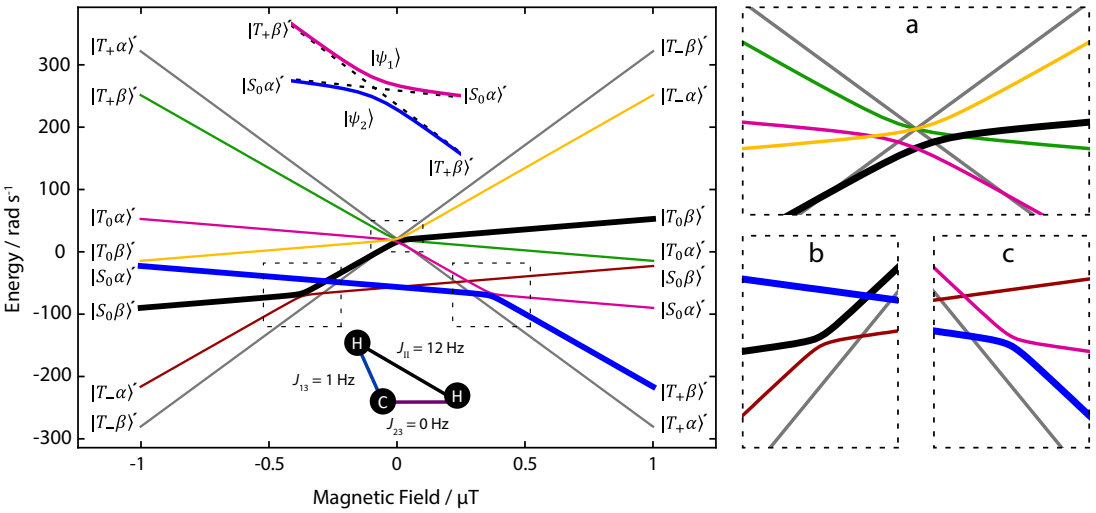

FIGURE 4.4: Eigenvalues of the Hamiltonian $\hat{H}$ for the model three-spin-1/2 system shown in the inset, as a function of applied field. There are four avoided crossings at -369 nT, -8 nT, +8 nT, and +369 nT (shown enlarged in panels a, b, and c). The line colours label eigenvalues corresponding to eigenstates that transform smoothly into each other as the magnetic field changes. The thick black and blue lines indicate the evolution of singlet order during a (fully) adiabatic -1 $\rightarrow$ +1 μT field sweep from proton S_0 polarization at -1 μT into ^{13}C β polarization at +1 μT. The avoided crossing of a pair of Hamiltonian eigenvalues is shown in the inset. The corresponding eigenvalues of $\hat{H}_0$ are shown by the dashed lines; the corresponding eigenstates of $\hat{H}_0$ are termed the *diabatic* states and belong to the $\mathbb{STZ}'$ basis (Eq. 4.6). The $\hat{H}$ eigenstates are denoted $|\psi_1\rangle$ and $|\psi_2\rangle$. Further details are given in the text.

The energy separation between the two states at the position of the avoided crossing is given by twice the magnitude of the mixing term.

Crossing states	**Field**	**Mixing term**
$\|S_0\beta\rangle' \leftrightarrow \|T_{-1}\alpha\rangle'$	$-B_{\mathrm{AC}}^{(1)}$	$\pi(J_{13}\cos\left(\frac{\theta_{\mathrm{G}}}{2}\right) - J_{23}\sin\left(\frac{\theta_{\mathrm{G}}}{2}\right))$
$\|S_0\alpha\rangle' \leftrightarrow \|T_{+1}\beta\rangle'$	$B_{\mathrm{AC}}^{(1)}$	$\pi(J_{13}\cos\left(\frac{\theta_{\mathrm{G}}}{2}\right) - J_{23}\sin\left(\frac{\theta_{\mathrm{G}}}{2}\right))$
$\|T_0\beta\rangle' \leftrightarrow \|T_{-1}\alpha\rangle'$	$-B_{\mathrm{AC}}^{(2)}$	$\pi(J_{13}\sin\left(\frac{\theta_{\mathrm{G}}}{2}\right) + J_{23}\cos\left(\frac{\theta_{\mathrm{G}}}{2}\right))$
$\|T_0\alpha\rangle' \leftrightarrow \|T_{+1}\beta\rangle'$	$B_{\mathrm{AC}}^{(2)}$	$\pi(J_{13}\sin\left(\frac{\theta_{\mathrm{G}}}{2}\right) + J_{23}\cos\left(\frac{\theta_{\mathrm{G}}}{2}\right))$

TABLE 4.2: Mixing terms at avoided crossings.

The 8 eigenvalues of $\hat{H}_0$ are plotted against the field strength B_0 in Fig. 4.4, for the case of a model spin system with $J_{\mathrm{II}} = 12$ Hz, $J_{13} = 1$ Hz, and $J_{23} = 0$ Hz. These values were chosen for clarity. 12 Hz is a typical J-coupling for two protons in a *cis* conformation across a double bond (as is often the case for parahydrogen products). The four avoided crossings in this system, connecting the states in Table 4.2, are visible.

To understand the role of the avoided crossings, consider the inset in Fig. 4.4, which shows the avoided crossing between the $\hat{H}_0$ eigenvalues corresponding to the *diabatic* states $|S_0\alpha\rangle'$ and $|T_{+1}\beta\rangle'$. The eigenvalues of the *diabatic* states (i.e. the eigenstates of $\hat{H}_0$) are shown by dotted black lines, and the corresponding eigenvalues of $\hat{H}$ as thick coloured lines. If the system is prepared in the state ψ_1, and the magnetic field is varied adiabatically (slowly) to take the system through the avoided crossing, the system will remain in the same eigenstate (i.e. follow the thick pink line), assuming the absence of incoherent effects such as relaxation.

4.2.3 The Field-Sweep Experiment

Now consider the density operator evolution for the procedure sketched in Fig. 4.2; (1) sample hydrogenation at a static field strength of $+2\,\mu$T, (2) an instantaneous (diabatic) field reversal to -2 μT, (3) a field sweep from -2 μT to $+2\,\mu$T under the adiabatic approximation.

1. Sample hydrogenation

Immediately after hydrogenation of the precursor with para-enriched hydrogen, the spin density operator $\hat{\rho}_0$ is given by expressing the density operator

$$\hat{\rho}_{\text{singlet}} = \frac{1}{2}(|S_0\alpha\rangle\langle S_0\alpha| + |S_0\beta\rangle\langle S_0\beta|) \tag{4.11}$$

in the Hamiltonian eigenbasis, and removing off-diagonal elements between non-degenerate eigenvalues. The off-diagonal elements are coherences, which are assumed to be averaged to zero during the long hydrogenation period (long in comparison to the inverse of the coherences). The result is of the form

$$\hat{\rho}_0 = \sum_{\psi} p_{\psi}^{\text{ini}} |\psi\rangle\langle\psi|\,, \tag{4.12}$$

where $|\psi\rangle$ is a Hamiltonian eigenstate, and p_{ψ}^{ini} is the population of state ψ.

Since the hydrogenation field is not at an avoided crossing, the eigenstates of $\hat{H}_0$ are close to the eigenstates of $\hat{H}$. The initial populations of the $\hat{H}_0$ eigenstates, assuming

pure pH_2, are

$$\begin{aligned}
p_1^{\text{ini}} &= |\langle S_0|S_0\alpha\rangle'|^2 = \frac{(1+\sin(\theta_G))}{4} \\
p_2^{\text{ini}} &= |\langle S_0|T_{+1}\alpha\rangle'|^2 = 0 \\
p_3^{\text{ini}} &= |\langle S_0|T_0\alpha\rangle'|^2 = \frac{(1-\sin(\theta_G))}{4} \\
p_4^{\text{ini}} &= |\langle S_0|T_{-1}\alpha\rangle'|^2 = 0 \\
p_5^{\text{ini}} &= |\langle S_0|S_0\beta\rangle'|^2 = \frac{(1+\sin(\theta_G))}{4} \\
p_6^{\text{ini}} &= |\langle S_0|T_{+1}\beta\rangle'|^2 = 0 \\
p_7^{\text{ini}} &= |\langle S_0|T_0\beta\rangle'|^2 = \frac{(1-\sin(\theta_G))}{4} \\
p_8^{\text{ini}} &= |\langle S_0|T_{-1}\beta\rangle'|^2 = 0,
\end{aligned} \tag{4.13}$$

where $\langle S_0|$ is shorthand for $(\langle S_0\alpha| + \langle S_0\beta|)/2$.

2. Diabatic field reversal

Diabatic field reversal from $+2\,\mu$T to -2 μT projects the density operator $\hat{\rho}_0$ onto the Hamiltonian eigenbasis at this new field, and this operation has no effect on the density operator. The states $|S_0\alpha\rangle'$ and $|S_0\beta\rangle'$ retain their populations.

3. Adiabatic field sweep

Applying a perfectly adiabatic field sweep from -2 μT to $+2\,\mu$T causes the state populations to evolve along with the Hamiltonian eigenstates. Hence, the populations of states $|S_0\alpha\rangle'$ and $|S_0\beta\rangle'$ are transferred into populations of states $|T_{+1}\beta\rangle'$ and $|T_0\beta\rangle'$, respectively, corresponding to ^{13}C $|\beta\rangle$ polarization. This can be seen visually by following the thick eigenvalue lines in Fig. 4.4. The state populations during the field sweep are shown in Fig. 4.5 for two differently J-coupled spin systems.

In cases for which the proton singlet state is an exact Hamiltonian eigenstate, this process can give rise, in principle, to unity ^{13}C polarization. However, for [1-^{13}C] maleic acid, the incomplete magnetic equivalence of the two protons means that the proton singlet state is not an exact eigenstate of the initial spin Hamiltonian, leading to a limit of 90% ^{13}C polarization, neglecting relaxation and instrumental imperfections.

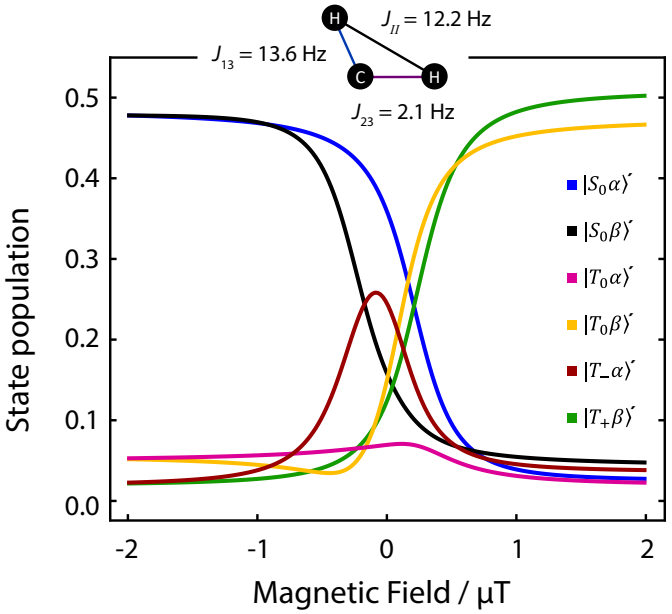

FIGURE 4.5: State populations during an adiabatic -2 to $+2\,\mu$T field sweep for the three spin-1/2 system of maleic acid. The J-couplings are shown in the inset figure.

4.3 Materials and Methods

For ultralow-field experiments, a magnetic shield (MS-1F, Twinleaf LLC, Princeton, U.S.) was used to provide a 10^6 shielding factor against external magnetic fields. Static internal magnetic fields for shimming were produced using built-in B_x, B_y, and B_z coils, powered with computer-controlled DC (Direct Current) calibrators (Krohn-Hite, model 523, Brockton, U.S.), providing three-axis field control. Time-dependent "pulse" fields were generated with three nested Helmholtz coils wound on a 3D-printed former, where each coil was driven with a separate isolated power amplifier (AE Techron 7224-P, Elkhart, U.S.), with waveforms produced with the gradient controller of a low-field NMR spectrometer (Kea II, Magritek GmbH, Aachen, Germany).

NMR tubes held in the ZULF chamber and 1.4 T SpinSolve were connected with PEEK (PolyEther Ether Ketone) tubing (1/16 inch O.D., 0.02 inch I.D.), as shown in Fig. 4.6. Gas and liquid flow were controlled by pneumatically actuated valves (Swagelok, Solon, U.S.); the pneumatic valves were controlled via TTL (Transistor-Transistor Logic) outputs of the Magritek spectrometer. Sample hydrogenation was followed by shuttling into the SpinSolve by reversing the gas flow. The sample transport was performed with helium gas (any unreactive gas could be used), and took 1 s. In order to prevent the sample from passing through any fields that could lead to undesired state-mixing during sample transport, a penetrating solenoid was used to provide a guiding field during transit out of the magnetic shield.

To generate parahydrogen gas at 92% para enrichment, regular hydrogen gas (purity 99.995%) was passed through a Bruker parahydrogen generator operating at

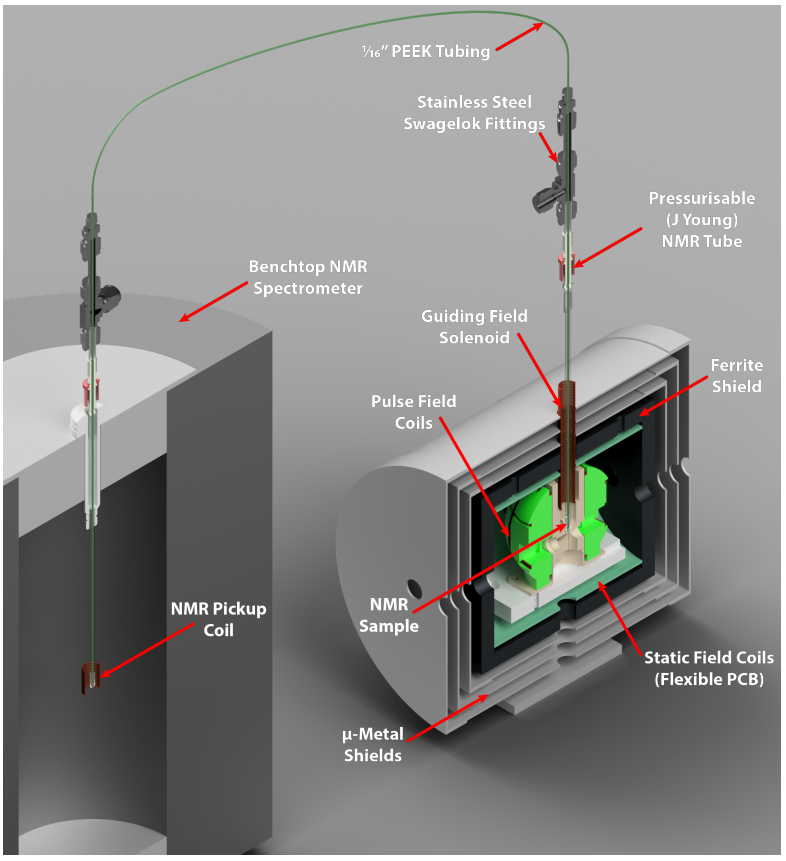

FIGURE 4.6: Schematic of the experimental apparatus. The sample was hydrogenated in the magnetically shielded chamber, and field manipulations were performed using the pulse field coils. The sample was then pneumatically shuttled into the SpinSolve for signal acquisition.

36 K. Unless stated otherwise in the text, the solution prior to hydrogenation was 5 mM 1,4-bis(diphenylphosphino)butane(1,5-cyclooctadiene)rhodium tetrafluoroborate and 100 mM acetylene dicarboxylic acid in 300 μl acetone.

The events sequence is shown in Fig. 4.2. Initially the sample is in the ZULF chamber in a 5 mm NMR tube, in a +10 μT field provided by the pulse and guiding coils. The field was stepped down to +2 μT by turning off the guiding field, and parahydrogen gas was bubbled in at 5 bar for 60 s. After a 0.5 s delay to allow the sample to settle, a field manipulation was applied using the pulse coils. The field manipulation shown in Fig. 4.2 is a sudden step to -2 μT (in $\sim$ 10 μs), followed by a linear sweep to +2 μT in 1 s. The field was then stepped to +2 μT (or in the case shown, kept there). The guiding field was switched back on to provide a +10 μT total field, and helium gas at 6 bar was used to shuttle the sample into the SpinSolve. A $\pi/2$ pulse was applied followed by data acquisition triggered by a TTL signal from the Kea II.

4.4 Results

To evaluate the field sweep methodology the hydrogenation, field sweep, and shuttling to high field procedure was performed, and the ^{13}C NMR signals were detected. In this Section, the effect of performing the sweep is examined, followed by studying the effects of sweep direction (i.e. sweeping from -2 to +2 μT vs sweeping from +2 to -2 μT), sweep rate, and finally estimating the polarization enhancement.

4.4.1 Field-Sweep Hyperpolarization of ^{13}C NMR Signals

To see the effect of the field sweep, a sample of acetylene dicarboxylic acid was hyperpolarized as described in the Materials and Methods section, a linear field sweep from -2 to +2 μT was performed with a duration of 1 s, and the sample was shuttled into the SpinSolve for ^{13}C detection. For comparison, the experiment was repeated, but instead of performing the field sweep, the field was kept static at +2 μT for 1 s. The NMR signal of the hyperpolarized sample was allowed to relax, and a thermal equilibrium spectrum was acquired. The ^{13}C NMR spectra are shown in Fig. 4.7. The field sweep spectrum shows a dramatic ^{13}C signal enhancement compared with thermal equilibrium where no signal is observed.

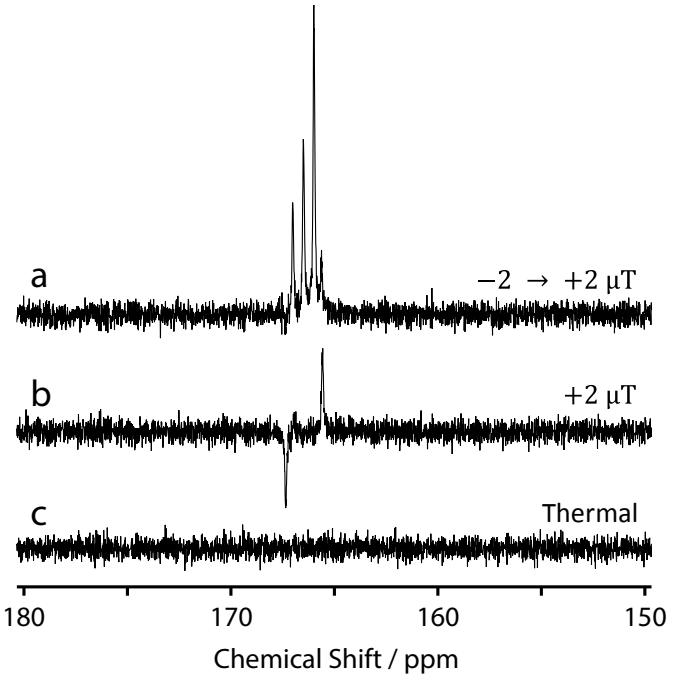

FIGURE 4.7: Single-scan ^{13}C NMR spectra of the reaction mixture acquired without proton decoupling showing a) the signal after performing a -2 to +2 μT field sweep, b) the signal after keeping the sample in a static +2 μT field, c) the thermal equilibrium signal. The outermost spectral lines in (a) and the only visible spectral lines in (b) are caused by $S_0 \leftrightarrow T_0$ state mixing (see Fig. 4.3).

When a field sweep is not used, two relatively weak ^{13}C signals of opposite phase are observed (Fig. 4.7b). These signals derive from the initial singlet polarization of the protons which leads to weakly allowed transitions through singlet-triplet state mixing (see Fig. 4.3).

4.4.2 Reversal of the Field-Sweep Direction

To study the influence of the field-sweep direction, the hyperpolarization procedure was repeated and the field sweep was performed in the positive direction (-2 to +2 μT) to polarize the ^{13}C spins in the $|\beta\rangle$ state, and the negative direction (+2 to -2 μT) to polarize the ^{13}C spins in the $|\alpha\rangle$ state. The results are shown in Fig. 4.8. Note that helium bubbling for excess parahydrogen removal was not performed in this experiment, so the signal-to-noise is higher than in Fig. 4.7a.

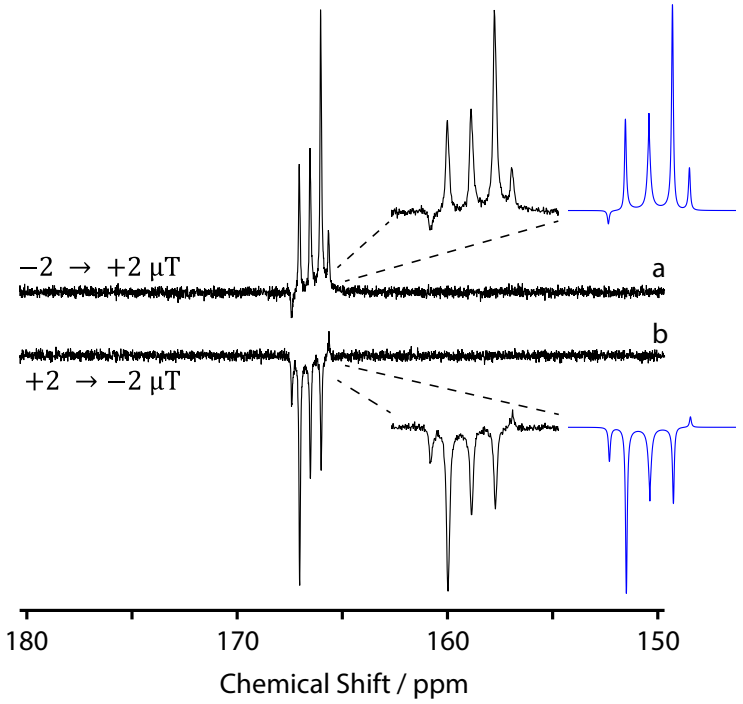

FIGURE 4.8: Single-scan ^{13}C NMR spectra without proton decoupling showing a) the hyperpolarized [1-^{13}C]maleic acid signal acquired after performing a -2 to +2 μT field sweep, b) the hyperpolarized sample signal acquired after performing a +2 to -2μT field sweep. Simulations of the spectra are shown in blue.

Reversal of the sweep direction manifests as an inverted peak phase for the two spectra, and a reflection about the central resonance. This is because, in the ideal case, a positive field sweep polarizes states $|T_0\beta\rangle'$ and $|T_{+1}\beta\rangle'$, whereas a negative field sweep polarizes states $|T_0\alpha\rangle'$ and $|T_{-1}\alpha\rangle'$.

Simulations of the spectral lineshape were performed by using SpinDynamica, a package for Mathematica [28], and the code is given in Appendix II. For the simulations,

the density operator at the start of the field sweep was taken as $\hat{\rho}_0$ from Eq. 4.12. $\hat{\rho}_0$ is then propagated under the time-dependent Hamiltonian as the field is swept. Proton relaxation from fluctuating external random fields (as described in Ref. [127]) is included. The relaxation of populations between the states in the ^{13}C $|\alpha\rangle$ and $|\beta\rangle$ manifolds (but not between these two manifolds) gives rise to the specific lineshapes observed. The correlation between the random field fluctuations at the two spin-sites was set to 0.9. The best-fit estimates of the correlation time τ_c and root-mean-square amplitude of the fluctuating external random fields were given by $(B_{\text{ran}}^{\text{rms}})^2\tau_c = 6 \times 10^{-16}\,\text{T}^2\,\text{s}$.

Although the sample is in precisely zero field at the centre of the sweep, it still matters whether the field is increased from zero in the positive or negative sense. This is because the quantum state in zero field depends on its preparation history, and in particular whether the zero-field state was prepared by an approach from the positive or negative field direction.

4.4.3 Effect of Field-Sweep Duration on Polarization Transfer Efficiency

To understand the effect of the field sweep duration on the degree of polarization transfer to the ^{13}C spin, the hyperpolarization step was performed on a series of reaction mixtures, and a field sweep from -2 to $+2\mu$T was applied with a different duration for each. In Fig. 4.9 the ^{13}C signal intensities (as measured by peak integration) are shown, along with a SpinDynamica simulation of the ^{13}C polarization. The SpinDynamica simulations were performed with the same parameters as used for Fig. 4.8, but with the fluctuating external random field characterised by the parameters $(B_{\text{ran}}^{\text{rms}})^2\tau_c = 2 \times 10^{-16}\,\text{T}^2\,\text{s}$, which represents a weaker random field than that used in the simulations in Fig. 4.8. The reason for the discrepancy is unknown, but might reflect a variation in the oxygen content of the solutions.

For efficient polarization transfer, the adiabatic condition needs to be met. Therefore, for longer sweep durations the ^{13}C signal is larger, as the process becomes more adiabatic. This is true up to a point, but for the longest sweep durations (2 s and 5 s), the signal is notably attenuated by relaxation.

4.4.4 Polarization Enhancement

To estimate the polarization level, a sample of 1 mM [1-^{13}C]acetylene dicarboxylic acid (^{13}C-enriched) and 5 mM rhodium catalyst in acetone was hydrogenated for 10 s at 1 bar parahydrogen pressure, before performing a -2 to $+2\,\mu$T field sweep in 1 s and shuttling to the SpinSolve for detection. After letting the polarized signal decay, a 32 scan thermal spectrum was acquired on the same sample. These results are shown in

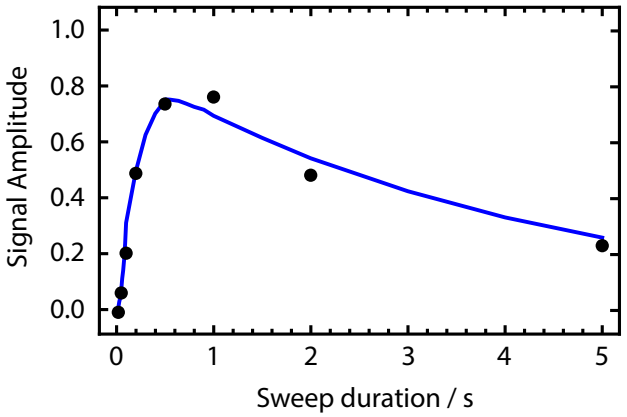

FIGURE 4.9: Signal intensity measured for the ^{13}C spins after applying a -2 to +2 μT field sweep of variable duration, shown by black circles. A SpinDynamica simulation of the transfer efficiency is shown by the blue line, and the code is given in Appendix II. Details of the simulation are given in the text. The signal intensity is normalized to the maximum conversion amplitude of ~0.9 in the *absence* of relaxation.

Fig. 4.10. The [1-^{13}C]maleic acid peak is not visible in the thermal spectrum, so the polarization was estimated by comparison to the 13.5 M natural abundance acetone solvent peak at 207 ppm. The signal enhancement on the product [1-^{13}C]maleic acid was estimated to be by a factor of 10,500, corresponding to a polarization level of >1% in the 1.4 T field. The measured signal enhancement is limited by relaxation of the spins between sample hydrogenation and signal detection.

The conditions used to achieve this polarization enhancement differ from those used in previous experiments. A lower concentration of starting material is used, because it is desirable to achieve complete hydrogenation before the application of the field sweep. If the reaction does not go to completion before the field sweep, additional product is formed which does not contribute to the hyperpolarized ^{13}C NMR signal, but does contribute to the thermally polarized ^{13}C NMR signal. This leads to an underestimation in the signal enhancement. Since the concentration of starting material is reduced, the pressure of parahydrogen gas, and bubbling time, are reduced to avoid overreduction to succinate.

4.5 Conclusions

A method to polarize the ^{13}C spin in [1-^{13}C]maleic acid by transferring the proton singlet order, originating from the parahydrogen proton pair, using a field sweep, has been presented. The field sweeps used are typically -2 to +2 μT and performed in 1 s, although variations of this were used to evaluate the technique. This method can in theory lead to up to 100% ^{13}C polarization, although this depends on the singlet order

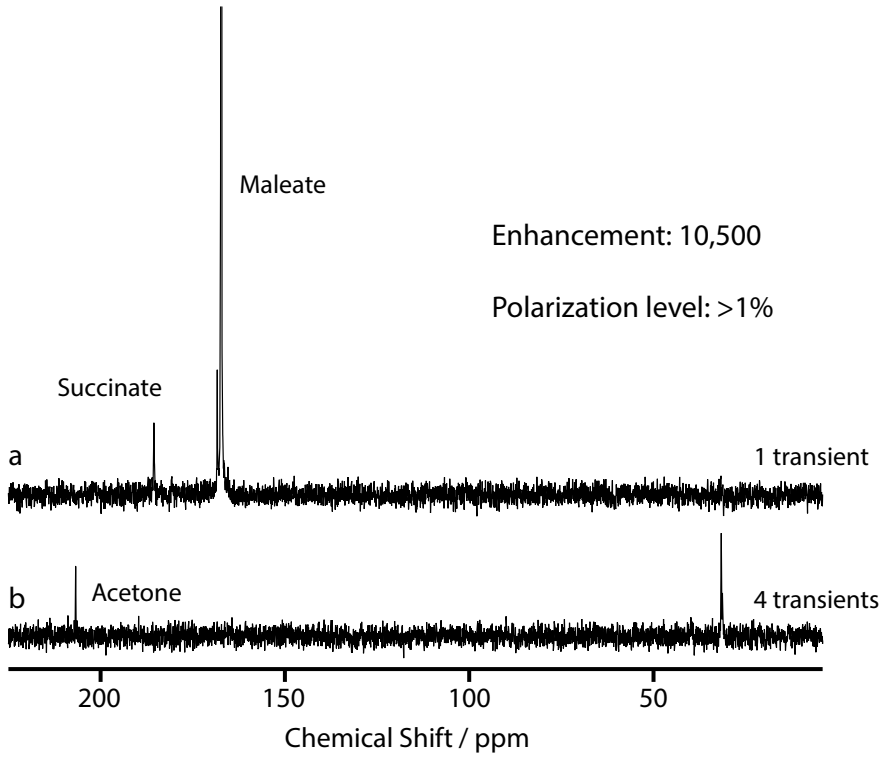

FIGURE 4.10: Proton decoupled ^{13}C NMR spectra with 2 Hz line broadening showing a) hyperpolarized [1-^{13}C]maleic acid after performing a 1 s -2 to +2 μT field sweep, b) thermal-equilibrium signal acquired with 32 transients. The product peak is not visible in the thermal equilibrium spectrum, so the signal enhancement was estimated by integral comparison to the acetone peak at 207 ppm.

polarization level of the hydrogenated molecule prior to the sweep, and the degree of adiabaticity of the sweep used.

In contrast to the three field-manipulation techniques described in section 3.3.2.2, this method can produce up to 100% ^{13}C polarization without the need for diabatic field changes. This might be useful for producing ^{13}C-polarized solution under continuous flow, where rapid field changes can be difficult to achieve.

Chapter 5

Singlet Order Manipulation at High Field

The work in this chapter is based on material presented in Ref. [128], and the S2hM theory is based on work by Stevanato and Pileio in Refs. [129, 130].

5.1 Introduction

When PHIP is used for ^{13}C magnetization enhancement, it is necessary to convert hyperpolarized proton singlet order into nuclear magnetization of a different spin species. One promising concept involves *side-arm hydrogenation*, in which a desired substrate is chemically bonded to a side arm able to react with parahydrogen; the enhanced polarization transferred via para hydrogenation is then converted to spin polarization at one (or more) site of the substrate before chemical cleavage of the side arm to liberate the hyperpolarized agent [87, 88, 107, 131]. A series of techniques have been developed for the transformation of singlet order into heteronuclear magnetization. These include field cycling [131–135] and resonant rf (radio frequency) pulse sequences [21, 90, 118, 124, 128, 129, 136–147]. Most pulse sequence methods are not well-suited to the important near-equivalence regime relevant to the promising side-arm hydrogenation procedures. Kadlecek and co-workers proposed a set of more general solutions [139].

In this chapter, it is demonstrated that the techniques developed in the field of long-lived states [148, 149] may be applied to the problem of converting singlet order into heteronuclear magnetization. The SLIC (Spin-Lock-Induced Crossing) method may be applied almost directly, while the S2M (Singlet-to-Magnetization) sequence may be adapted by changing the pulse sequence loop numbers and definition of the echo delay. These sequences are relatively short, only involve radiation on a single radio frequency channel, and provide an efficient transfer of nuclear singlet order into heteronuclear

magnetization, in the near-equivalence regime. Furthermore, the S2hM (Singlet-to-Heteronuclear-Magnetization) method is well-compensated for resonance offset, without the addition of extra 180° pulses.

The pulse sequences were optimized on thermally polarized nuclear spin systems, using singlet-NMR techniques [148, 149] to generate nuclear singlet order. The amount of singlet polarization generated this way is many orders of magnitude smaller than when parahydrogen is used. However, the thermal procedures are fully reproducible and allow a robust characterisation of the conversion process from proton singlet order to ^{13}C magnetization by removing chemical reaction rates from the dynamics. A simple test system (natural abundance carbon-13 in the carbonyl position in fumaric acid) was used to explore the behaviour of the SLIC and S2hM sequences, and compare these methods to some previously-described procedures in the near-equivalence context.

Additionally, a pulse sequence to perform relayed polarization transfer to a ^{13}C nucleus not J-coupled to the proton pair, using a 'bridging' ^{13}C site, is described. By alleviating the requirement for the target ^{13}C nucleus to have a direct J-coupling to the parahydrogen protons, the range of possible target compounds for *side-arm hydrogenation* is greatly increased.

5.2 Theoretical Description of SLIC and S2hM

The principles of the SLIC method have been extensively discussed in the case of a homonuclear spin-1/2 pair, where a chemical shift difference induces singlet-to-magnetization polarization transfer, and vice versa [149, 150], and also for heteronuclear 4-spin systems [119, 151, 152]. Here the theory of SLIC is presented for a pair of chemically equivalent protons experiencing differential J-couplings to a third spin of different isotopic type, examining the result of using a SLIC matching condition to polarize the heteronuclear third spin.

The S2M pulse sequence is used to convert singlet order into magnetization in homonuclear spin-1/2 pairs, and has been described for the cases of symmetry breaking through chemical shift inequivalence [148, 153], and asymmetric J-couplings in heteronuclear 4-spin systems [154]. Here the theory of the S2hM pulse sequence is presented for a pair of chemically equivalent protons experiencing differential J-couplings to a third spin of different isotopic type, examining the result of using optimized pulse sequence parameters to polarize the heteronuclear third spin.

5.2.1 State Bases and the Spin Hamiltonian

In this chapter the spin dynamics of a three spin-1/2 system are considered, with two proton spins, I_1 and I_2, from the parahydrogen pair, and a heteronuclear ^{13}C spin, S_3. The $\mathbb{STZ}$ basis was defined in Eq. 4.1 in chapter 4. To represent the spin dynamics in the following, it is convenient to rotate the S-spin basis states from the $\mathbb{STZ}$ basis by the angle $\pi/2$ about the y-axis. The resulting basis will be termed $\mathbb{STX}$, and is given by

$$\mathbb{STX} = \{|S_0^{12}\rangle, |T_{+1}^{12}\rangle, |T_0^{12}\rangle, |T_{-1}^{12}\rangle\} \otimes \{R_{\mathrm{y}}^3(\pi/2)\,|\alpha^3\rangle, R_{\mathrm{y}}^3(\pi/2)\,|\beta^3\rangle\}, \tag{5.1}$$

where $R_{\mathrm{y}}^3(\theta) = \exp\{-i\theta S_{3y}\}$. The spin labels will be dropped henceforth. For convenience, state labels 1-8 are introduced:

$$\begin{aligned}\mathbb{STX} &= R_{\mathrm{y}}^3(\pi/2)\{|S_0\alpha\rangle, |T_{+1}\alpha\rangle, |T_0\alpha\rangle, |T_{-1}\alpha\rangle, |S_0\beta\rangle, |T_{+1}\beta\rangle, |T_0\beta\rangle, |T_{-1}\beta\rangle\} \\ &= \{|1\rangle, |2\rangle, .. |8\rangle\}. \end{aligned} \tag{5.2}$$

The spin Hamiltonian for a system of two I-spins-1/2 and one S-spin-1/2 under the "secular" approximation is

$$\hat{H} = 2\pi J_{12}\mathbf{I}_1.\mathbf{I}_2 + 2\pi J_{13} I_{1z} S_{3z} + 2\pi J_{23} I_{2z} S_{3z}. \tag{5.3}$$

The Hamiltonian is written in the doubly rotating frame, which means the I- and S-spin precession frequencies about B_0 are no longer present. Under the secular approximation, the nonsecular (i.e. I_xS_x and I_yS_y) components of the heteronuclear J-couplings are

removed. This approximation is valid when the Larmor frequency difference between two spin species is dramatically larger than the J-coupling frequency.

The following terms are introduced for clarity:

$$\begin{aligned} \omega_{\mathrm{II}} &= 2\pi J_{12}, \\ \omega_{\mathrm{IS}}^{\Delta} &= 2\pi(J_{13} - J_{23}), \\ \omega_{\mathrm{IS}}^{\Sigma} &= 2\pi(J_{13} + J_{23}). \end{aligned} \tag{5.4}$$

The spin Hamiltonian can be written using the terms from Eq. 5.4:

$$\hat{H} = \omega_{\mathrm{II}}\mathbf{I}_1.\mathbf{I}_2 + \frac{1}{2}\omega_{\mathrm{IS}}^{\Delta}(I_{1z}S_{3z} - I_{2z}S_{3z}) + \frac{1}{2}\omega_{\mathrm{IS}}^{\Sigma}(I_{1z}S_{3z} + I_{2z}S_{3z}). \tag{5.5}$$

This Hamiltonian is shown below in matrix form in the $\mathbb{STX}$ basis.

$$\hat{H} = \frac{1}{4}\begin{array}{c} \begin{matrix} |1\rangle & |2\rangle & |3\rangle & |4\rangle & |5\rangle & |6\rangle & |7\rangle & |8\rangle \end{matrix} \\ \begin{pmatrix} -3\omega_{\mathrm{II}} & 0 & 0 & 0 & 0 & 0 & -\omega_{\mathrm{IS}}^{\Delta} & 0 \\ 0 & \omega_{\mathrm{II}} & 0 & 0 & 0 & -\omega_{\mathrm{IS}}^{\Sigma} & 0 & 0 \\ 0 & 0 & \omega_{\mathrm{II}} & 0 & -\omega_{\mathrm{IS}}^{\Delta} & 0 & 0 & 0 \\ 0 & 0 & 0 & \omega_{\mathrm{II}} & 0 & 0 & 0 & \omega_{\mathrm{IS}}^{\Sigma} \\ 0 & 0 & -\omega_{\mathrm{IS}}^{\Delta} & 0 & -3\omega_{\mathrm{II}} & 0 & 0 & 0 \\ 0 & -\omega_{\mathrm{IS}}^{\Sigma} & 0 & 0 & 0 & \omega_{\mathrm{II}} & 0 & 0 \\ -\omega_{\mathrm{IS}}^{\Delta} & 0 & 0 & 0 & 0 & 0 & \omega_{\mathrm{II}} & 0 \\ 0 & 0 & 0 & \omega_{\mathrm{IS}}^{\Sigma} & 0 & 0 & 0 & \omega_{\mathrm{II}} \end{pmatrix} \end{array}. \tag{5.6}$$

5.2.2 S-Spin SLIC

The result of applying the S-spin SLIC to the 3-spin system is now presented. For the case of S-spin SLIC irradiation, which is simply an rf field applied to the S-spins along the x-axis, the Hamiltonian is

$$\hat{H}_{\mathrm{SLIC}} = \omega_{\mathrm{II}}\mathbf{I}_1.\mathbf{I}_2 + \frac{1}{2}\omega_{\mathrm{IS}}^{\Delta}(I_{1z}S_{3z} - I_{2z}S_{3z}) + \frac{1}{2}\omega_{\mathrm{IS}}^{\Sigma}(I_{1z}S_{3z} + I_{2z}S_{3z}) + \omega_{\mathrm{nut}}^{\mathrm{S}}S_{3x}. \tag{5.7}$$

The rf field amplitude is expressed as a nutation frequency $\omega_{\mathrm{nut}}^{\mathrm{S}}$. The rf irradiation is assumed to be exactly on resonance.

This Hamiltonian is shown below in matrix form in the $\mathbb{STX}$ basis.

$$\hat{H}_{\mathrm{SLIC}} = \frac{1}{4}$$

$$\begin{array}{c} \begin{matrix} |1\rangle & |2\rangle & |3\rangle & |4\rangle & |5\rangle & |6\rangle & |7\rangle & |8\rangle \end{matrix} \\ \begin{pmatrix} -3\omega_{\mathrm{II}}+2\omega_{\mathrm{nut}}^{\mathrm{S}} & 0 & 0 & 0 & 0 & 0 & -\omega_{\mathrm{IS}}^{\Delta} & 0 \\ 0 & \omega_{\mathrm{II}}+2\omega_{\mathrm{nut}}^{\mathrm{S}} & 0 & 0 & 0 & -\omega_{\mathrm{IS}}^{\Sigma} & 0 & 0 \\ 0 & 0 & \omega_{\mathrm{II}}+2\omega_{\mathrm{nut}}^{\mathrm{S}} & 0 & -\omega_{\mathrm{IS}}^{\Delta} & 0 & 0 & 0 \\ 0 & 0 & 0 & \omega_{\mathrm{II}}+2\omega_{\mathrm{nut}}^{\mathrm{S}} & 0 & 0 & 0 & \omega_{\mathrm{IS}}^{\Sigma} \\ 0 & 0 & -\omega_{\mathrm{IS}}^{\Delta} & 0 & -3\omega_{\mathrm{II}}-2\omega_{\mathrm{nut}}^{\mathrm{S}} & 0 & 0 & 0 \\ 0 & -\omega_{\mathrm{IS}}^{\Sigma} & 0 & 0 & 0 & \omega_{\mathrm{II}}-2\omega_{\mathrm{nut}}^{\mathrm{S}} & 0 & 0 \\ -\omega_{\mathrm{IS}}^{\Delta} & 0 & 0 & 0 & 0 & 0 & \omega_{\mathrm{II}}-2\omega_{\mathrm{nut}}^{\mathrm{S}} & 0 \\ 0 & 0 & 0 & \omega_{\mathrm{IS}}^{\Sigma} & 0 & 0 & 0 & \omega_{\mathrm{II}}-2\omega_{\mathrm{nut}}^{\mathrm{S}} \end{pmatrix} \end{array} \tag{5.8}$$

By setting $\omega_{\mathrm{nut}}^{\mathrm{S}} = \omega_{\mathrm{II}}$, and removing off-diagonal terms between nondegenerate diagonal elements (to give an approximate "secular" form of the Hamiltonian) this matrix becomes

$$\hat{H}_{\mathrm{SLIC}}^{\mathrm{sec}} = \frac{1}{4} \begin{array}{c} \begin{matrix} |1\rangle & |2\rangle & |3\rangle & |4\rangle & |5\rangle & |6\rangle & |7\rangle & |8\rangle \end{matrix} \\ \begin{pmatrix} -\omega_{\mathrm{II}} & 0 & 0 & 0 & 0 & 0 & -\omega_{\mathrm{IS}}^{\Delta} & 0 \\ 0 & 3\omega_{\mathrm{II}} & 0 & 0 & 0 & 0 & 0 & 0 \\ 0 & 0 & 3\omega_{\mathrm{II}} & 0 & 0 & 0 & 0 & 0 \\ 0 & 0 & 0 & 3\omega_{\mathrm{II}} & 0 & 0 & 0 & 0 \\ 0 & 0 & 0 & 0 & -5\omega_{\mathrm{II}} & 0 & 0 & 0 \\ 0 & 0 & 0 & 0 & 0 & -\omega_{\mathrm{II}} & 0 & 0 \\ -\omega_{\mathrm{IS}}^{\Delta} & 0 & 0 & 0 & 0 & 0 & -\omega_{\mathrm{II}} & 0 \\ 0 & 0 & 0 & 0 & 0 & 0 & 0 & -\omega_{\mathrm{II}} \end{pmatrix} \end{array}. \tag{5.9}$$

This approximation is justified if $|\omega_{\mathrm{IS}}^{\Delta}| \ll |\omega_{\mathrm{II}}|$ and $|\omega_{\mathrm{IS}}^{\Sigma}| \ll |\omega_{\mathrm{II}}|$, i.e. the near-equivalence regime.

When $\omega_{\mathrm{nut}}^{\mathrm{S}} = \omega_{\mathrm{II}}$, states $|1\rangle$ and $|7\rangle$ become degenerate. The off-diagonal coupling term $-\omega_{\mathrm{IS}}^{\Delta}$ causes oscillatory state transitions between the two degenerate states.

The action of the S-spin SLIC pulse is now examined on a state of pure proton singlet order between spins I_1 and I_2 in a 3-spin system. The corresponding density operator is

$$\hat{\rho}_{\mathrm{singlet}} = \frac{1}{8}\mathbb{1} - \frac{1}{2}\mathbf{I}_1.\mathbf{I}_2. \tag{5.10}$$

The unity operator is dropped from the following calculations, as it does not participate in the evolution.

During SLIC irradiation on the S-spin with rf amplitude $\omega_{\mathrm{nut}}^{\mathrm{S}} = \omega_{\mathrm{II}}$, the evolution of the system from the initial state in Eq. 5.10 is given by

$$\hat{\rho}(t) = e^{-i\,\hat{H}_{\mathrm{SLIC}}^{\mathrm{sec}}\,t}\ \hat{\rho}_{\mathrm{singlet}}\ e^{+i\,\hat{H}_{\mathrm{SLIC}}^{\mathrm{sec}}\,t}. \tag{5.11}$$

A *SpinDynamica* simulation shows this is given by

$$\begin{aligned}\hat{\rho}(t) = \quad & -\tfrac{1}{2}I_{1z}I_{2z} - \tfrac{1}{2}\cos^2(\tfrac{\omega_{\mathrm{IS}}^{\Delta}\, t}{4})(I_{1x}I_{2x} + I_{1y}I_{2y}) \\ & +\tfrac{1}{8}(\cos(\tfrac{\omega_{\mathrm{IS}}^{\Delta}\, t}{2}) - 1)S_{3x} \\ & +\sin^2(\tfrac{\omega_{\mathrm{IS}}^{\Delta}\, t}{4}))I_{1z}I_{2z}S_{3x} \\ & +\tfrac{1}{4}\sin(\tfrac{\omega_{\mathrm{IS}}^{\Delta}\, t}{2})(I_{1z} - I_{2z})S_{3y} \\ & +\tfrac{1}{2}\sin(\tfrac{\omega_{\mathrm{IS}}^{\Delta}\, t}{2})(I_{1x}I_{2y} - I_{1y}I_{2x})S_{3z}. \end{aligned} \tag{5.12}$$

When $t = 2\pi/\omega_{\mathrm{IS}}^{\Delta}$, this simplifies to

$$\hat{\rho}(2\pi/\omega_{\mathrm{IS}}^{\Delta}) = \quad -\tfrac{1}{2}I_{1z}I_{2z} + \tfrac{1}{4}(4I_{1z}I_{2z} - 1)S_{3x}, \tag{5.13}$$

which corresponds to negative S-spin polarization along the x-axis.

State polarization levels during the application of an on-resonance S-spin SLIC pulse are shown in Fig. 5.1. The terms plotted are $\langle \rho \rightarrow P_{\mathrm{S}}^{\mathrm{I}} \rangle$ in orange, and $\langle \rho \rightarrow P_{\mathrm{x}}^{\mathrm{S}} \rangle$ in blue, where $P_{\mathrm{S}}^{\mathrm{I}}$ is the I-spin singlet polarization level operator and $P_{\mathrm{x}}^{\mathrm{S}}$ is the S-spin Zeeman polarization level operator along the x-axis [128]. The *operator amplitude* is defined as $\langle A \rightarrow B \rangle = \frac{\langle B|A \rangle}{\langle B|B \rangle}$, where the Liouville bracket is $\langle B|A \rangle = \mathrm{Tr}\{B^{\dagger}A\}$.

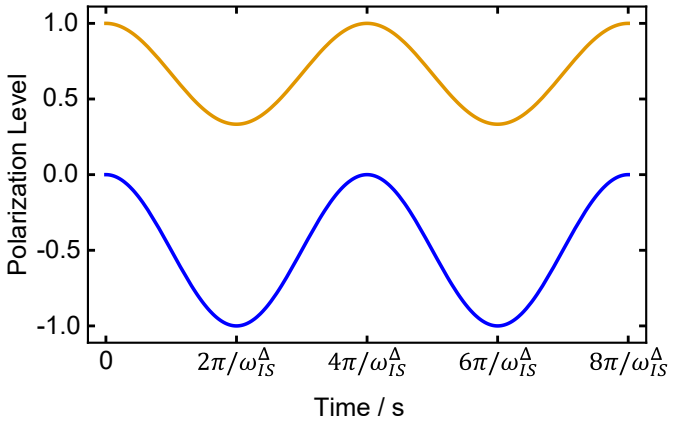

FIGURE 5.1: Polarization level of the I-spin singlet state (orange) and S-spin along the x-axis (blue) during an S-spin SLIC pulse, assuming an initial state of pure I-spin singlet order. The image was generated using the SpinDynamica package for Mathematica [28], and the code is given in Appendix II.

5.2.3 S-Spin S2hM

The Hamiltonian from Eq. 5.6 is shown again below in the $\mathbb{STX}$ basis, with the same state labels 1-8, as defined in Eq. 5.2.

$$\hat{H} = \frac{1}{4}\begin{array}{c} \begin{matrix} |1\rangle & |2\rangle & |3\rangle & |4\rangle & |5\rangle & |6\rangle & |7\rangle & |8\rangle \end{matrix} \\ \begin{pmatrix} -3\omega_{\mathrm{II}} & 0 & 0 & 0 & 0 & 0 & -\omega_{\mathrm{IS}}^{\Delta} & 0 \\ 0 & \omega_{\mathrm{II}} & 0 & 0 & 0 & -\omega_{\mathrm{IS}}^{\Sigma} & 0 & 0 \\ 0 & 0 & \omega_{\mathrm{II}} & 0 & -\omega_{\mathrm{IS}}^{\Delta} & 0 & 0 & 0 \\ 0 & 0 & 0 & \omega_{\mathrm{II}} & 0 & 0 & 0 & \omega_{\mathrm{IS}}^{\Sigma} \\ 0 & 0 & -\omega_{\mathrm{IS}}^{\Delta} & 0 & -3\omega_{\mathrm{II}} & 0 & 0 & 0 \\ 0 & -\omega_{\mathrm{IS}}^{\Sigma} & 0 & 0 & 0 & \omega_{\mathrm{II}} & 0 & 0 \\ -\omega_{\mathrm{IS}}^{\Delta} & 0 & 0 & 0 & 0 & 0 & \omega_{\mathrm{II}} & 0 \\ 0 & 0 & 0 & \omega_{\mathrm{IS}}^{\Sigma} & 0 & 0 & 0 & \omega_{\mathrm{II}} \end{pmatrix} \end{array} \tag{5.14}$$

This Hamiltonian is the direct sum of 4 orthogonal 2×2 subspaces

$$\hat{H} = \hat{H}^{17} \oplus \hat{H}^{26} \oplus \hat{H}^{35} \oplus \hat{H}^{48}, \tag{5.15}$$

with

$$\begin{aligned} \hat{H}^{17} &= -\omega_{\mathrm{II}}\mathbf{I}_z^{17} - \frac{\omega_{\mathrm{IS}}^{\Delta}}{2}\mathbf{I}_x^{17} - \frac{\omega_{\mathrm{II}}}{4}\mathbf{1}^{17}, \\ \hat{H}^{26} &= -\frac{\omega_{\mathrm{IS}}^{\Sigma}}{2}\mathbf{I}_x^{26} + \frac{\omega_{\mathrm{II}}}{4}\mathbf{1}^{26}, \\ \hat{H}^{35} &= +\omega_{\mathrm{II}}\mathbf{I}_z^{35} - \frac{\omega_{\mathrm{IS}}^{\Delta}}{2}\mathbf{I}_x^{35} - \frac{\omega_{\mathrm{II}}}{4}\mathbf{1}^{35}, \\ \hat{H}^{48} &= +\frac{\omega_{\mathrm{IS}}^{\Sigma}}{2}\mathbf{I}_x^{48} + \frac{\omega_{\mathrm{II}}}{4}\mathbf{1}^{48}. \end{aligned} \tag{5.16}$$

The superscript rs indicates the subspace spanned by the r-th and s-th functions in the $\mathbb{STX}$ basis, and $\mathbf{I}_k^{\mathrm{rs}}$ is the single-transition spin operator along the k-axis for the rs subspace defined as:

$$\begin{aligned} \mathbf{I}_x^{\mathrm{rs}} &= \frac{1}{2}(|\mathrm{r}\rangle\langle\mathrm{s}| + |\mathrm{s}\rangle\langle\mathrm{r}|), \\ \mathbf{I}_y^{\mathrm{rs}} &= \frac{1}{2i}(|\mathrm{r}\rangle\langle\mathrm{s}| - |\mathrm{s}\rangle\langle\mathrm{r}|), \\ \mathbf{I}_z^{\mathrm{rs}} &= \frac{1}{2}(|\mathrm{r}\rangle\langle\mathrm{r}| - |\mathrm{s}\rangle\langle\mathrm{s}|), \\ \mathbf{1}^{\mathrm{rs}} &= (|\mathrm{r}\rangle\langle\mathrm{r}| + |\mathrm{s}\rangle\langle\mathrm{s}|). \end{aligned} \tag{5.17}$$

$\hat{\hat{U}}^{\mathrm{rs}}(t)$ is a propagator that acts on the spin system, defined as

$$\hat{\hat{U}}^{\mathrm{rs}}(t)\hat{\rho} = e^{-i\,\hat{H}^{\mathrm{rs}}\,t}\;\hat{\rho}\;e^{+i\,\hat{H}^{\mathrm{rs}}\,t}. \tag{5.18}$$

$\hat{\hat{R}}_k^{\mathrm{rs}}(\theta)$ is a rotation superoperator which rotates an operator by the angle θ about the k-axis of the subspace spanned by kets r and s. For example:

$$\hat{\hat{R}}_y^{\mathrm{rs}}\Big(\frac{\pi}{2}\Big)\mathbf{I}_z^{\mathrm{rs}} = e^{-i\,(\frac{\pi}{2})\,\mathbf{I}_y^{\mathrm{rs}}}\ \mathbf{I}_z^{\mathrm{rs}}\ e^{+i\,(\frac{\pi}{2})\,\mathbf{I}_y^{\mathrm{rs}}} = \mathbf{I}_x^{\mathrm{rs}}. \tag{5.19}$$

The result of using the S2hM pulse sequence to polarize the S-spin is now examined. The pulse sequence is shown in Fig. 5.2.

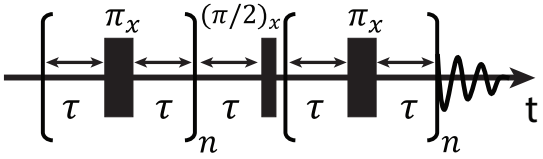

FIGURE 5.2: The S2hM pulse sequence. π_x represents a hard π pulse about the x-axis in the lab frame (note: *not* the x-axis in the coordinate system of the single-transition spin operators.)

The values θ and ω_{e} are introduced:

$$\begin{aligned}\theta &= \arctan\left(\omega_{\mathrm{IS}}^{\Delta}/2\omega_{\mathrm{II}}\right),\\ \omega_{\mathrm{e}} &= \sqrt{\omega_{\mathrm{II}}^2 + (\omega_{\mathrm{IS}}^{\Delta}/2)^2}.\end{aligned} \tag{5.20}$$

The optimal delay, τ, and loop number, n, values for maximum transfer of I-spin singlet order into S-spin polarization, are given by

$$\begin{aligned}\tau &= \frac{\pi}{2\omega_{\mathrm{e}}},\\ n &= \mathrm{round}\Big\{\frac{\pi}{4\theta}\Big\}.\end{aligned} \tag{5.21}$$

The evolution of the system under the Hamiltonian (given in Eq. 5.16) is approximately given by

$$\hat{\hat{U}}_{\mathrm{free}}^{\mathrm{S2hM}}(t) \approx \hat{\hat{R}}_y^{17}(\theta)\hat{\hat{R}}_z^{17}(-\omega_{\mathrm{e}}t)\hat{\hat{R}}_y^{17}(-\theta)\hat{\hat{R}}_y^{35}(-\theta)\hat{\hat{R}}_z^{35}(\omega_{\mathrm{e}}t)\hat{\hat{R}}_y^{35}(\theta). \tag{5.22}$$

This is only valid in the near-equivalence limit ($\theta \ll 1$), and neglects propagators in the 2, 6, and 4, 8 subspaces, since I-spin singlet order is not present there. If t is set to $t = \tau\,(= \pi/(2\omega_{\mathrm{e}}))$, this becomes

$$\hat{\hat{U}}_{\mathrm{free}}^{\mathrm{S2hM}}(\tau) \approx \hat{\hat{R}}_y^{17}(\theta)\hat{\hat{R}}_z^{17}\Big(-\frac{\pi}{2}\Big)\hat{\hat{R}}_y^{17}(-\theta)\hat{\hat{R}}_y^{35}(-\theta)\hat{\hat{R}}_z^{35}\Big(\frac{\pi}{2}\Big)\hat{\hat{R}}_y^{35}(\theta), \tag{5.23}$$

i.e. components of the density operator in the 1, 7 subspace experience a $\pi/2$ rotation about an axis tilted by an angle θ_y from the z-axis, and components of the density operator in the 3, 5 subspace experience a $-\pi/2$ rotation about an axis tilted by an angle $-\theta_y$ from the z-axis. This is shown in Fig. 5.3.

The propagator for a spin echo of the form $\tau - \pi_x - \tau$ is approximately

$$\hat{\hat{U}}_{\text{echo}}^{\text{S2hM}}(\tau) \approx \hat{\hat{R}}_x^{17}(-2\theta)\hat{\hat{R}}_x^{35}(-2\theta), \tag{5.24}$$

corresponding to a rotation of components in the 1, 7, and 3, 5 subspaces by an angle of -2θ about the x-axis. For a train of $n\,(=\text{round}\{\pi/4\theta\})$ spin echoes, the propagator becomes

$$\left[\hat{\hat{U}}_{\text{echo}}^{\text{S2hM}}(\tau)\right]^n \approx \hat{\hat{R}}_x^{17}\Big(-\frac{\pi}{2}\Big)\hat{\hat{R}}_x^{35}\Big(-\frac{\pi}{2}\Big). \tag{5.25}$$

The trajectory of the density operator in the 1, 7 subspace during the S2hM pulse sequence is shown in Fig. 5.3, with the x, y, and z-axes given by the corresponding single-transition spin operators $\mathbf{I}_x^{17}$, $\mathbf{I}_y^{17}$, and $\mathbf{I}_z^{17}$. The red arrow indicates the effective field about which the spins precess during the free evolution period τ, which is tilted by an angle θ about the y-axis from z (see Eq. 5.22).

The initial density operator is assumed to be pure proton singlet order between spins I_1 and I_2, which was previously written as

$$\hat{\rho}_{\text{singlet}} = \hat{\rho}_1 = \frac{1}{8}\mathbb{1} - \frac{1}{2}\mathbf{I}_1.\mathbf{I}_2. \tag{5.26}$$

To describe the evolution of the system during the S2hM pulse sequence, it is more clear to use the spin operators defined in Eq. 5.17, which produces

$$\hat{\rho}_{\text{singlet}} = \frac{1}{2}(+\mathbf{I}_z^{17} - \mathbf{I}_z^{35} + \frac{1}{2}\mathbf{1}^{17} + \frac{1}{2}\mathbf{1}^{35}). \tag{5.27}$$

The unity operators $\mathbf{1}^{17}$ and $\mathbf{1}^{35}$ are dropped from the following calculations, as they do not participate in the evolution. This finally gives

$$\hat{\rho}_0 = \frac{1}{2}(+\mathbf{I}_z^{17} - \mathbf{I}_z^{35}). \tag{5.28}$$

Applying n spin echoes to the S-spin, with the value of n given in Eq. 5.21, causes a $-\pi/2$ rotation about the x-axis, i.e. $\hat{\hat{R}}_x^{17}(-\pi/2)\hat{\hat{R}}_x^{35}(-\pi/2)$, which gives

$$\hat{\rho}_1 = \frac{1}{2}(+\mathbf{I}_y^{17} - \mathbf{I}_y^{35}). \tag{5.29}$$

During the delay τ, $\hat{\rho}_1$ evolves into $\hat{\rho}_2$.

$$\hat{\rho}_2 = \frac{1}{2}(+\mathbf{I}_x^{17} + \mathbf{I}_x^{35}). \tag{5.30}$$

The $(\pi/2)_x$ pulse is written in this basis, using the single-transition spin operators, as $\hat{\hat{R}}_z^{17}(\pi/2)\hat{\hat{R}}_z^{35}(\pi/2)$, and transforms $\hat{\rho}_2$ into $\hat{\rho}_3$.

$$\hat{\rho}_3 = \frac{1}{2}(+\mathbf{I}_y^{17} + \mathbf{I}_y^{35}). \tag{5.31}$$

Finally, the second spin echo train causes a $-\pi/2$ rotation about the x-axes of the 1, 7, and 3, 5 subspaces, i.e. $\hat{\hat{R}}_x^{17}(-\pi/2)\hat{\hat{R}}_x^{35}(-\pi/2)$, which gives

$$\hat{\rho}_4 = \frac{1}{2}(-\mathbf{I}_z^{17} - \mathbf{I}_z^{35}). \tag{5.32}$$

This can be written as

$$\hat{\rho}_4 = -\frac{1}{2}I_{1z}I_{2z} + \frac{1}{4}(4I_{1z}I_{2z} - \mathbb{1})S_{3x}, \tag{5.33}$$

which corresponds to negative S-spin polarization along the x-axis.

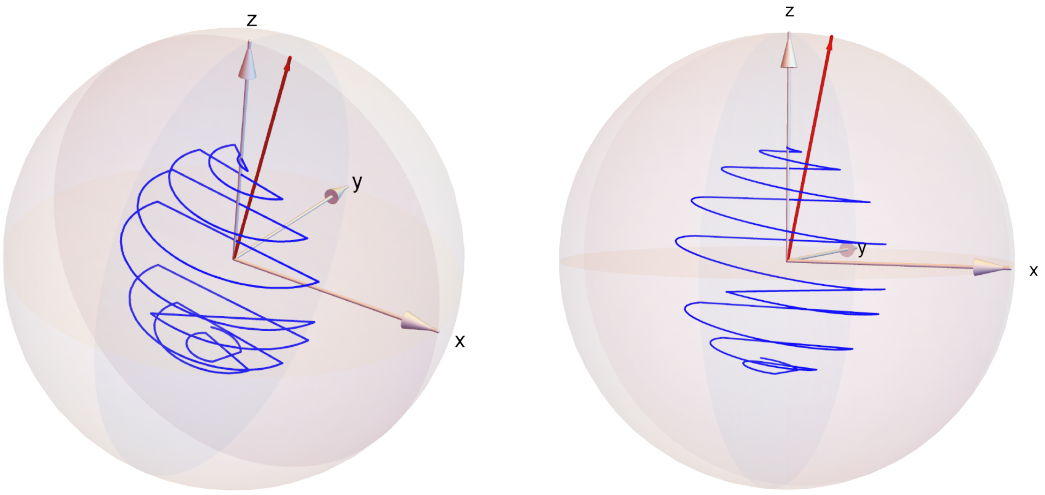

FIGURE 5.3: Evolution of the density operator during the S2hM pulse sequence in the 1, 7 subspace, in the coordinate system of the single-transition spin operators $\mathbf{I}_x^{17}$, $\mathbf{I}_y^{17}$, and $\mathbf{I}_z^{17}$. The parameters chosen were $\omega_{\mathrm{II}} = 2\pi \times 10$, $\omega_{\mathrm{IS}}^{\Delta} = 2\pi \times 4$, and hence $\tau = 24.5\,\mathrm{ms}$ and $n = 4$. The red line indicates an axis tilted by an angle θ_y from the z-axis. The two images show the same picture, from different angles. The image was generated using the SpinDynamica package for Mathematica [28], and the code is given in Appendix II.

5.3 Materials and Methods

All NMR experiments were performed at 11.7 T in a 5 mm BBO probe using a Bruker AVANCE III (Billerica, U.S.) console.

Thermal polarization experiments were performed on an unlabelled sample of 0.86 M fumaric acid in degassed DMSO-d_6, sealed in an airtight 5 mm NMR tube.

To generate hydrogen gas at 50% para enrichment, hydrogen gas (purity 99.995%) was passed through a home-built parahydrogen generator containing a charcoal catalyst cooled to 77 K. The solution prior to hydrogenation reactions was ~20 mM 1,4-bis(diphenylphosphino)butane(1,5-cyclooctadiene)rhodium tetrafluoroborate and 5 mM dimethyl acetylene dicarboxylate-d_6 in acetone-d_6. For sample hydrogenation, parahydrogen gas was bubbled at atmospheric pressure and 25°C for 15 s through 1/16 inch PEEK tubing that extended to the bottom of a 5 mm NMR tube. The bubbling was performed inside the magnet and was controlled manually by hand-operated valves (Swagelok, Solon, U.S.).

5.4 Results

All experiments studied the ^{13}C NMR signals from the naturally occurring ~2% of fumaric acid molecules with a ^{13}C nucleus at the carboxylic acid site (1-^{13}C). The spin system and J-couplings are shown in Fig. 5.4a. The ordinary ^{13}C NMR spectrum without ^{1}H decoupling, shown in Fig. 5.4b, displays a 1:2:1 triplet structure, with the peak splitting given by the mean of the two ^{1}H-^{13}C J-couplings, $(^{2}J_{IS} + {}^{3}J_{IS})/2 = 4.9 \pm 0.3$ Hz.

The near-equivalence regime, as discussed in section 3.3.2.2, is defined as $\theta \leq 30°$, where $\theta = \arctan(\omega_{IS}^{\Delta}/2\omega_{II})$. This means $\omega_{II} > \omega_{IS}^{\Delta}$, which is often the case if the S-spin is many bonds from the I-spin pair. The couplings in fumaric acid give $\theta = 6.5°$, which makes it a convenient test system for evaluating pulse sequences to mimic polarization transfer across a large number of bonds. In this regime, it is not possible to determine the $^{2}J_{IS}$ and $^{3}J_{IS}$ couplings individually from the NMR spectrum. The difference between the heteronuclear couplings $\Delta J_{IS} = 3.4 \pm 0.3$ Hz was estimated by data from the singlet NMR experiments (see below). The estimates of the individual heteronuclear couplings are therefore $^{2}J_{IS} = 3.2 \pm 0.2$ Hz and $^{3}J_{IS} = 6.6 \pm 0.2$ Hz. It should be noted that the methods described here provide a useful way of estimating J-couplings in the near-equivalence regime.

Experimental work on the conversion of proton singlet order into heteronuclear magnetization often employs parahydrogen reactions to generate singlet order, which makes quantification difficult. In this work, proton singlet order was generated in a

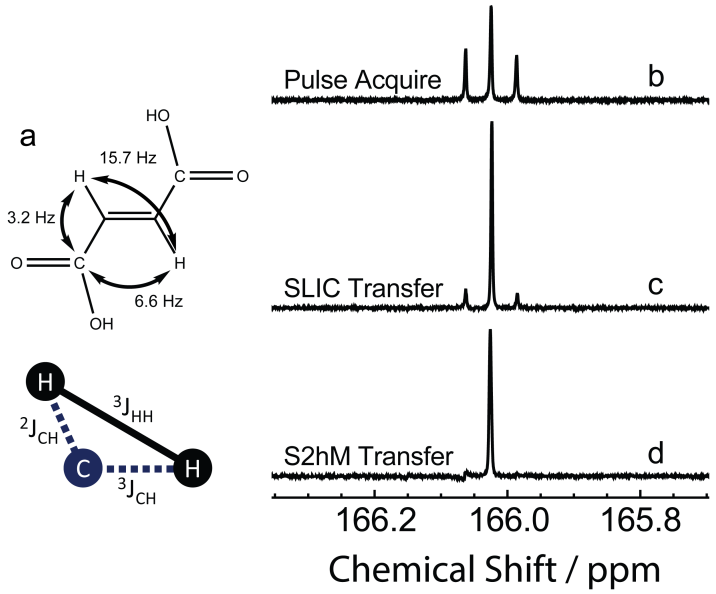

FIGURE 5.4: a) Molecular structure of fumaric acid showing the J-couplings in the 1-^{13}C isotopomer. b) ^{13}C spectrum obtained by a single $(\pi/2)_x$ ^{13}C pulse, showing the 1:2:1 triplet associated with a near-equivalent AA'X system. c) ^{13}C spectrum obtained using the pulse sequence in Fig. 5.5a, with proton singlet order converted into ^{13}C magnetization by the SLIC pulse. d) ^{13}C spectrum obtained using the pulse sequence in Fig. 5.5b, with proton singlet order converted into ^{13}C magnetization by the S2hM pulse sequence. All spectra show the carbonyl spectral region and were obtained with 64 transients, acquired at a magnetic field of 11.7 T. No ^{1}H decoupling was used during data acquisition. A phase shift of $\pi/2$ was applied to spectra (b) and (c) relative to spectrum (d).

reproducible manner from thermal equilibrium proton magnetization, using techniques developed in the context of long-lived states [149].

The pulse sequences are shown in Fig. 5.5. Singlet order is generated on the protons by applying a SLIC pulse sequence at the proton resonance frequency. The radio frequency field amplitude is set to match the proton nutation frequency with the proton-proton J-coupling $\omega^{\mathrm{I}}_{\mathrm{SLIC}} = 2\pi J_{\mathrm{II}}$. This condition establishes a resonance, in which the difference between the two ^{1}H-^{13}C J-couplings drives oscillations from proton magnetization into proton singlet order. As shown in Ref. [128], the amplitude of the proton singlet order is proportional to $\sin^2((\pi\ \Delta J_{\mathrm{IS}}\ \tau^{\mathrm{I}}_{\mathrm{SLIC}})/(2\sqrt{2}))$, in the absence of relaxation and other imperfections, and is maximised at $\tau^{\mathrm{I}}_{\mathrm{SLIC}} = \sqrt{2}/\Delta J_{\mathrm{IS}}$. The ^{1}H SLIC sequence is followed by a "T_{00} filter", used to suppress NMR signals not passing through proton singlet order [153]. This is the sequence $[G_1]-90_{54.7°}-[G_2]-90_{54.7°}-90_{180°}-[G_3]$. G_1, G_2 and G_3 are z pulsed-field-gradients with a sine-bell shape. The relative strengths were 10, -10 and -15 G cm^{-1}, and the durations were 8.8, 4.8 and 4.0 ms. The complete T_{00} filter sequence is shown in Appendix I. 9.2.6.

The two different methods discussed in this work for converting proton singlet

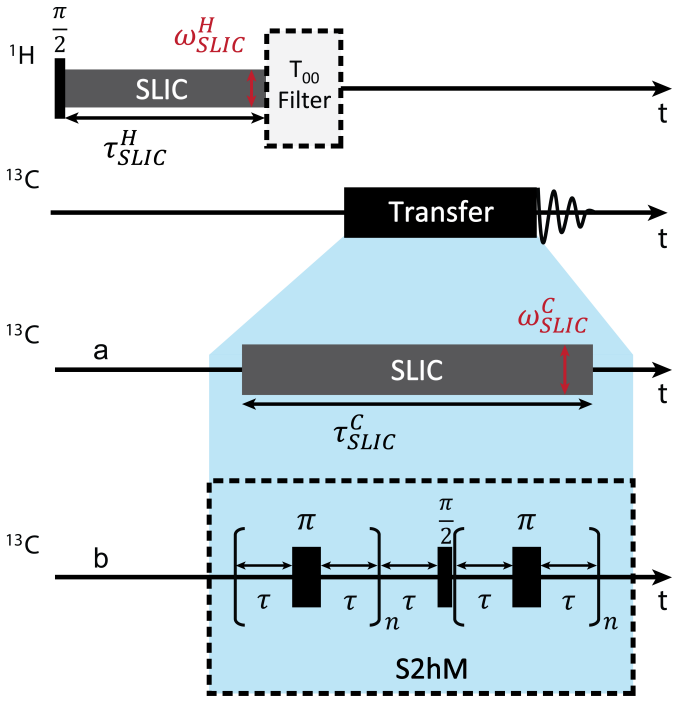

FIGURE 5.5: Pulse sequence for characterising the transformation of ^{1}H singlet order into ^{13}C magnetization. A SLIC sequence on the proton channel generates singlet order, followed by a "T$_{00}$" filter to remove any signals not passing through singlet order. The transformation of proton singlet order into ^{13}C magnetization is achieved by: a) A SLIC pulse on the ^{13}C channel applied on resonance with the target ^{13}C site. b) An S2hM pulse sequence using strong, non-selective, pulses on the ^{13}C channel, separated by delays. In practice, composite π pulses are used.

order into ^{13}C magnetization are SLIC and S2hM, both of which operate in the near-equivalence regime and only employ radio frequency irradiation on the ^{13}C channel.

5.4.1 SLIC Method

A weak unmodulated rf field is applied at the resonance frequency of the "target" ^{13}C site. If the amplitude of the ^{13}C field is such that the ^{13}C nutation frequency matches the ^{1}H-^{1}H J-coupling $\omega^{\mathrm{S}}_{\mathrm{SLIC}} = 2\pi J_{\mathrm{II}}$, proton singlet order oscillates into transverse ^{13}C magnetization, locked in the opposite direction to the rf field. In the absence of relaxation and other imperfections, as shown in section 5.2.2, the amplitude of transverse ^{13}C magnetization is proportional to $\sin^2((\pi\ \Delta J_{\mathrm{IS}}\ \tau^{\mathrm{S}}_{\mathrm{SLIC}})/2)$, so that the ^{13}C magnetization yield is optimized after an interval $\tau^{\mathrm{S}}_{\mathrm{SLIC}} = 1/\Delta J_{\mathrm{IS}}$.

Experimental results showing the oscillatory transfer of proton singlet order into transverse ^{13}C magnetization under the ^{13}C SLIC sequence are shown in Fig. 5.6a. The data points were obtained by repeating the pulse sequence in Fig. 5.5a for different ^{13}C SLIC durations. The experimental data points were normalised by calibration experiments, such that a value of 1 would correspond to 100% conversion of proton singlet

polarization into ^{13}C Zeeman polarization, as described in Appendix I. 9.1. An optimal transfer amplitude of 54.0% is obtained at a SLIC duration $\tau^{S}_{SLIC} = 280\,ms$.

The experimental polarization conversion amplitude for SLIC, as derived from the spectral integral, is plotted against ^{13}C rf amplitude (expressed as a nutation frequency) in Fig. 5.6b. This shows a distinct peak at 15.7 Hz, corresponding to the match of ω^{S}_{SLIC} with $2\pi J_{II}$.

The ^{13}C NMR spectrum, obtained by the pulse sequence in Fig. 5.5a using a ^{13}C SLIC pulse of duration 280 ms, is shown in Fig. 5.4c. The weak outer components of the ^{1}H-coupled ^{13}C multiplet are in agreement with the theory of the SLIC singlet-to-magnetization transfer process. The singlet order between the protons is converted predominantly into ^{13}C coherences involving the ^{1}H singlet state and the central ^{1}H triplet state, both of which make up the central peak of the ^{13}C multiplet.

Numerical simulations of the conversion amplitudes, using the SpinDynamica package for Mathematica [28], are shown by solid blue lines in Fig. 5.6, and the code is given in Appendix II.

5.4.2 S2hM Method

The *homonuclear* S2M sequence [148, 153] comprises a strong $\pi/2$ pulse and a delay, on either side of two π pulse echo trains, with the second echo train being twice as long as the first. The S2M sequence is adapted to perform *heteronuclear* singlet-to-magnetization transfer by making the two echo trains equal in repetition number, as depicted in Fig. 5.5b. The theoretical values of the intervals τ and loop numbers n are given in Eq. 5.21.

The S2hM sequence converts proton singlet order into heteronuclear magnetization in a near-equivalent 3-spin-1/2 system, with a near-100% theoretical conversion amplitude. Although the S2hM sequence is a factor of $\sim \pi/2$ longer than SLIC, it is more robust with respect to resonance offset and magnetic field homogeneity, especially when composite π pulses are used [155]. Fig. 5.6c and d show experimental conversion amplitudes for proton singlet order into transverse ^{13}C magnetization using the S2hM sequence, as a function of the echo interval τ and loop number n. The experimental data points were normalised by calibration experiments, such that a value of 1 would correspond to 100% conversion of proton singlet polarization into ^{13}C Zeeman polarization, as described in Appendix I. 9.1. An optimal transfer amplitude of the conversion step of 59.3% was obtained for echo interval $\tau = 15.8\,ms$ and loop number $n = 7$. The ^{13}C NMR spectrum, obtained by the pulse sequence in Fig. 5.5b using an S2hM sequence on the ^{13}C channel, is shown in Fig. 5.4b. The spectrum has a similar appearance to that obtained using SLIC.

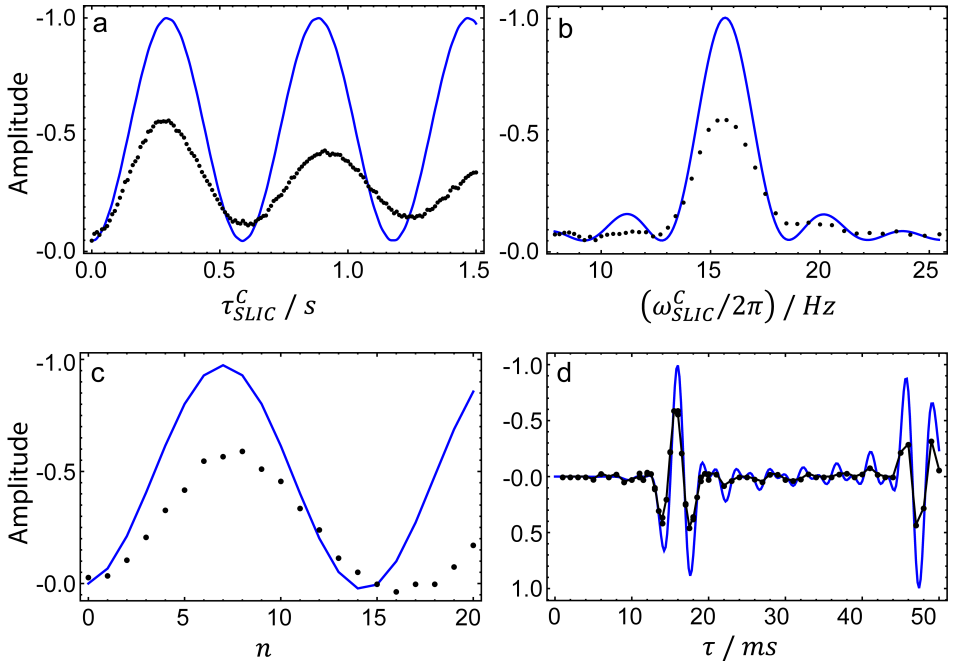

FIGURE 5.6: Amplitudes for the conversion of proton singlet polarization into ^{13}C Zeeman polarization in [1-^{13}C]fumaric acid: simulations (solid blue lines) and experimental results (black points). The vertical scale in all plots is normalised such that 1 corresponds to 100% conversion from proton singlet order into ^{13}C polarization. A conversion amplitude of 1 indicates that pure parahydrogen, if reacted without loss, would give rise to fully polarized ^{13}C nuclei. All amplitudes are negative to indicate magnetization generated opposite to the pulse phase. The best-case transfer amplitude was 54.0% for SLIC and 59.3% for S2hM. a) SLIC pulse sequence as a function of SLIC duration $\tau^{\mathrm{S}}_{\mathrm{SLIC}}$ with a fixed amplitude $\omega^{\mathrm{S}}_{\mathrm{SLIC}}/2\pi = 15.7\,\mathrm{Hz}$. b) SLIC pulse sequence as a function of ^{13}C nutation frequency with a fixed duration $\tau^{\mathrm{S}}_{\mathrm{SLIC}} = 280\,\mathrm{ms}$. c) S2hM pulse sequence as a function of loop number n, with delay τ fixed at 15.8 ms. d) S2hM pulse sequence as a function of delay τ, with loop number $n = 7$. Each experimental point is a result of 4 transients, using a delay between transients of 60 s.

The SLIC and S2hM sequences are both efficient in converting proton singlet order into heteronuclear magnetization, in the near-equivalence regime. Two other sequences are known to work well in this regime: Kadlecek Case 2b [139], called here 'K2b', and a modified 'Goldman' sequence which incorporates a number of "pumping pulses" to build up magnetization on the target nucleus [140]. These hard-pulse sequences work similarly to S2hM, but have more adjustable delay periods, which is advantageous when θ is near 30°. For comparison, these two hard-pulse sequences were also applied to fumaric acid in the same way as S2hM and SLIC, and give transfer amplitudes of 50.2% (Goldman) and 54.5% (K2b). For all four sequences explored here, the correspondence of experimental results with simulations is acceptable, except for an additional loss in experimental signal strength observed, presumably associated with relaxation and rf inhomogeneity.

A favourable feature of SLIC is its high rate of transfer. In the near-equivalence limit, the duration of the SLIC method required to provide complete transfer is a factor of $2/\pi$ shorter than S2hM, K2b and modified Goldman schemes. SLIC performs the

transfer on fumaric acid in 280 ms, compared to the 460 ms required for the hard-pulse methods.

Some applications of these pulse sequences involve manipulations of the spins in a low magnetic field, in order to minimize proton chemical shift. Low-field electromagnets often have a limited field homogeneity and suffer from instability and drift. The performance of these methods in the presence of a frequency mismatch between the applied rf frequency and the Larmor frequency of the spins (resonance offset) is therefore an important characteristic. Fig. 5.7 shows the performance of the singlet-to-magnetization procedures as a function of resonance offset. Although these data were obtained on fumaric acid in high field, they provide valuable information on the performance of the same pulse sequences in the low-field context.

Fig. 5.7a shows the resonance offset performance of the SLIC sequence. The method is highly sensitive to resonance offset, as expected for a weak rf field. Fig. 5.7b shows that S2hM, on the other hand, is highly robust with respect to resonance offset. The K2b and Goldman sequences display a strongly oscillatory transfer with respect to resonance offset (Fig. 5.7c and d). For example, the conversion amplitude of the K2b sequence changes sign every ∼21 Hz, which corresponds to a field difference of ∼2 μT. These sequences may be offset-compensated by including two pairs of 180° pulses on both the ^{13}C and ^{1}H channels in every pulse sequence delay [132, 140], but this adds much complexity and presumably gives rise to additional losses due to pulse imperfections.

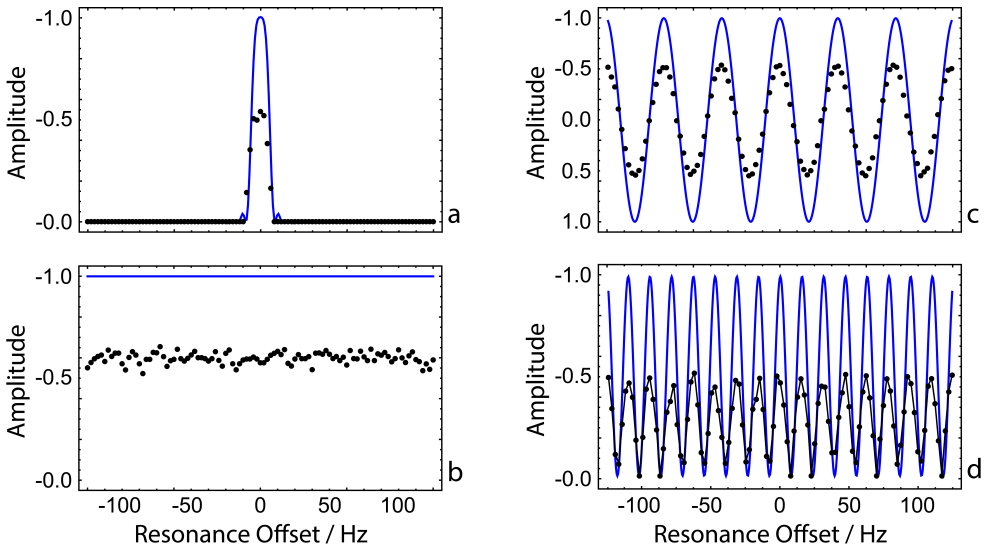

FIGURE 5.7: Conversion amplitudes as a function of resonance offset from the target carbon resonance in [1-^{13}C]fumaric acid: simulations (solid blue lines) and experimental results (black points). The vertical scale is the same as in Fig. 5.6. a) SLIC pulse sequence using amplitude $\omega^{S}_{SLIC}/2\pi = 15.7$ Hz and duration $\tau^{S}_{SLIC} = 280$ ms. b) S2hM pulse sequence using delay $\tau = 15.8$ ms and loop number $n = 7$. c) K2b pulse sequence using delays $\tau_{1,2,3} = 31.6$ and $\tau_4 = 7.9$ ms, with loop number $n = 5$. d) Goldman pulse sequence using delays $\tau_{0,1,3,4} = 31.6$ and $\tau_2 = 15.8$ ms, with loop numbers $n_1 = 5$ and $n_2 = 7$. The full pulse sequences are shown in Appendix I. 9.2.

5.4.3 SLIC Parahydrogen Demonstration

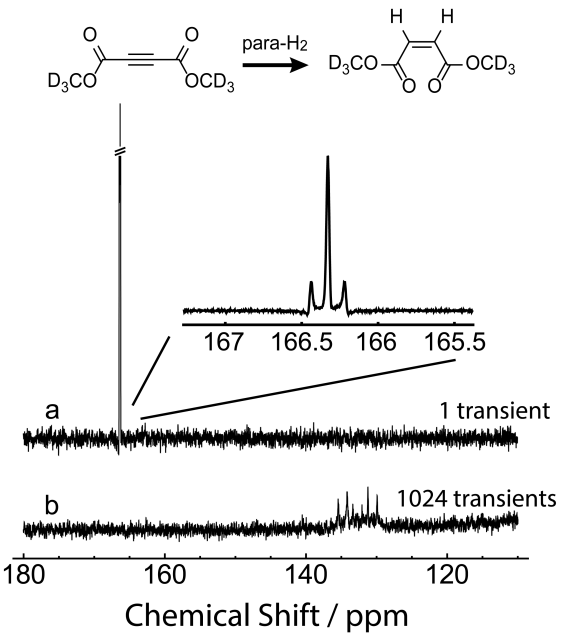

FIGURE 5.8: ^{13}C NMR spectra of the PHIP reaction mixture, obtained after catalytic reaction of dimethyl acetylene dicarboxylate-d_6 with para-enriched hydrogen, in the NMR magnet. a) A ^{13}C spectrum acquired after bubbling the para-enriched hydrogen gas for 15 s and applying a ^{13}C SLIC pulse with duration 95 ms, at the frequency of the carbonyl ^{13}C resonance. No proton decoupling was used during signal acquisition. b) An attempt to acquire the ^{13}C NMR spectrum after completion of the reaction by acquiring 1024 single-pulse transients separated by a delay of 60 s. The catalyst gives rise to the structure around 133 ppm. The vertical scale in (b) has been reduced by 32 so as to equalize the noise. Both (a) and (b) have line broadening of 2.3 Hz applied, but the inset spectrum does not. The NMR signal enhancement factor is approximately 9000.

The S-spin SLIC sequence was demonstrated on the molecule dimethyl maleate to hyperpolarize the carbonyl ^{13}C spin. The results are shown in Fig. 5.8. The J-couplings were assumed to be the same as for maleic acid: $J_{\mathrm{II}} = 12.2$ Hz, $\Delta J_{\mathrm{IS}} = 11.5$ Hz. The sample (5 mM dimethyl acetylene dicarboxylate-d_6 and ~20 mM rhodium catalyst in acetone-d_6) was hydrogenated as described in section 5.3. Immediately after parahydrogen bubbling, a ^{13}C SLIC pulse of duration 95 ms was applied. The Fourier transform of one ^{13}C signal transient is shown in Fig. 5.8a.

After the reaction had completed, an attempt was made to acquire the unenhanced ^{13}C spectrum by acquiring 1024 single-pulse transients using 90° pulses separated by a relaxation interval of 60 s. The signal could not be detected, as shown in Fig. 5.8b. Independent experiments determined the ^{13}C T_1 of the carbonyl site to be 44 s. The parahydrogen-induced signal enhancement in Fig. 5.8a was estimated to be at least 9000, corresponding to a ^{13}C polarization level of more than 9%. This estimate takes into account a signal loss of ~23% in the unenhanced spectrum due to partial saturation by the 90° pulses, and was later confirmed by comparing the hyperpolarized peak intensity to

that of a ^{13}C-labelled standard ([1-^{13}C]boc-gly-OH). A further enhancement by a factor of ∼3 would be available by enriching the H_2 gas with parahydrogen at a temperature of 25 K instead of 77 K. The demonstration in Fig. 5.8 was performed on a molecular system in which the relevant isotopomer of the reaction product contains only three spins-1/2 (neglecting the deuterons), with identical proton chemical shifts. The same procedure could be performed on more general molecules in low magnetic field, so that any chemical shift difference between the protons becomes unimportant.

5.5 Relayed Polarization Transfer in an AA'MX System

It is possible to polarize ^{13}C spins not directly J-coupled to the spin-singlet proton pair, by relaying the spin polarization through a 'bridge' nucleus. In this section, a demonstration of this is performed on the molecule [1-^{13}C-O-^{13}C$_2$]dimethyl maleate where the carbonyl ^{13}C acts as the bridge nucleus and the methyl ^{13}C is the target nucleus. The S2hM sequence was used to polarize the carbonyl ^{13}C followed by additional rf pulses to achieve homonuclear polarization transfer to the methyl ^{13}C, as shown in Fig. 5.9. This pulse sequence will be referred to henceforth as S2B2M (Singlet to Bridge to Magnetization).

In the same style as the SLIC and S2hM optimizations, thermal polarization experiments were initially performed to optimize the S2B2M pulse sequence parameters. These were followed by a hyperpolarized demonstration using para-H_2 gas.

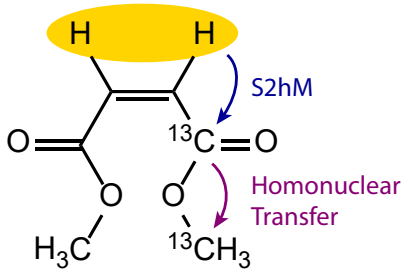

FIGURE 5.9: The molecule [1-^{13}C-O-^{13}C]dimethyl maleate, with the spin-singlet proton pair highlighted in yellow, and the transfer steps labelled.

5.5.1 Materials and Methods

All NMR experiments were performed at 11.7 T in a 5 mm BBO probe using a Bruker AVANCE III console (Billerica, U.S.).

Thermal polarization experiments were performed on a sample of 200 mM [1-^{13}C-O-^{13}C$_2$]dimethyl maleate in $CDCl_3$, sealed in an airtight 5 mm NMR tube.

To generate hydrogen gas at 50% para enrichment, hydrogen gas (purity 99.995%) was passed through a home-built parahydrogen generator containing an iron(III) oxide catalyst cooled to 77 K. The solution prior to hydrogenation reactions was 5 mM 1,4-bis(diphenylphosphino)butane(1,5-cyclooctadiene)rhodium tetrafluoroborate and 10 mM dimethyl acetylene dicarboxylate in acetone-d_6. For sample hydrogenation, parahydrogen gas was bubbled at 5 bar and 25°C for 30 s through 1/16 inch PEEK tubing that extended to the bottom of a pressurizable 5 mm NMR tube. The bubbling was performed inside the magnet and was controlled manually by hand-operated valves (Swagelok, Solon, U.S.).

5.5.2 Results and Analysis

A ^{13}C spectrum of [1-^{13}C-O-^{13}C$_2$]dimethyl maleate is shown in Fig. 5.10, along with an image of the molecular J-couplings.

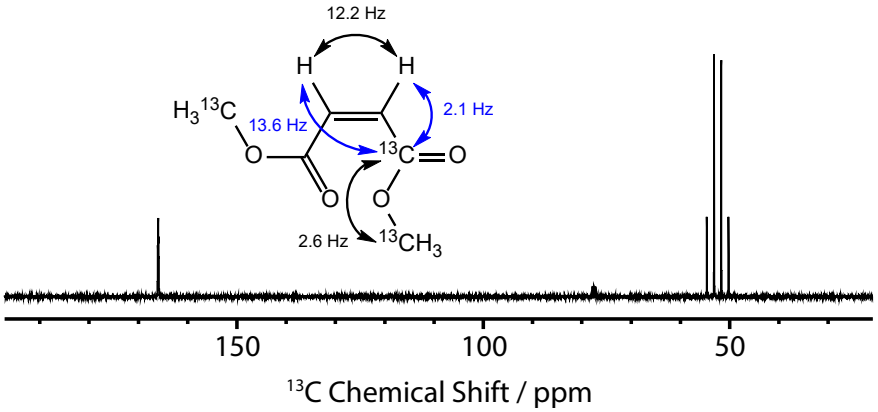

FIGURE 5.10: ^{13}C NMR spectrum acquired with one transient on a sample of 200 mM [1-^{13}C-O-^{13}C$_2$]dimethyl maleate in $CDCl_3$. The peak at 165.5 ppm is from the carbonyl ^{13}C, and the peak at 51 ppm is from the methyl ^{13}C and shows a quartet structure from J-coupling to the directly bound protons. The J-coupling network in [1-^{13}C-O-^{13}C$_2$]dimethyl maleate is shown in the inset.

The S2B2M pulse sequence is shown in Fig. 5.12. The initial part is identical to the pulse sequence used in section 5.4, except the SLIC and S2hM pulse parameters were adapted for the J-couplings in [1-^{13}C-O-^{13}C$_2$]dimethyl maleate. The intensity and duration of the ^{1}H SLIC pulse are given by: $\omega^{\mathrm{I}}_{\mathrm{SLIC}} = 2\pi J_{\mathrm{II}}$ and $\tau^{\mathrm{I}}_{\mathrm{SLIC}} = \sqrt{2}/\Delta J_{\mathrm{IS}}$. The delay and loop number chosen for the S2hM sequence are given in Eq. 5.21.

The homonuclear transfer step in the ^{13}C sequence is made more complicated by the large resonance frequency offset ($\Delta\delta$ = 14278 Hz) between the two ^{13}C spins. Conventional 'hard' pulses cannot provide excitation of uniform phase over a spectral width of tens of kHz, because this would require a short pulse of unfeasibly high power. For this reason, the pulses used were cosine modulated to split the excitation profile in the frequency domain into two components, split by twice the modulation frequency. The

effect of modulating the pulse profile with a cosine function can be seen by considering the Fourier transform of such a function. Recall from section 2.1.4 the Fourier transform is defined as:

$$f(s) = \int_{-\infty}^{\infty} f(t) e^{-2\pi i s t} dt, \tag{5.34}$$

where $s = \omega/2\pi$, which can be written more concisely as

$$f(s) = \mathcal{F}\{f(t)\}(s),$$

where $f(t)$ is a signal in the time domain (which in this case could be the NMR pulse), and $f(s)$ is the same signal represented in the frequency domain.

If the NMR pulse in the rotating frame is assumed to have a box function profile with amplitude 1 and total duration τ i.e.

$$\Pi(t) = \begin{cases} 0 & \text{for } t < 0 \\ \frac{1}{2} & \text{for } t = 0 \\ 1 & \text{for } 0 < t < \tau \\ \frac{1}{2} & \text{for } t = \tau \\ 0 & \text{for } t > \tau \end{cases}. \tag{5.35}$$

this will Fourier transform as follows:

$$f(s) = \mathcal{F}\{\Pi(t)\}(s) = \frac{\sin(2\pi s\tau)}{\sqrt{2\pi}\,(2\pi\, s)}. \tag{5.36}$$

Note: only the real component is kept. The result is a sinc function in s (where s is in units of hertz), centred around 0. This is illustrated graphically in Fig. 5.11.

If $\Pi(t)$ is multiplied by a cosine modulation of frequency Ω (in hertz), the result is:

$$f(s) = \mathcal{F}_t\{\Pi(t)\cos(2\pi\Omega t)\}(s) = \frac{s\sin(2\pi s\tau)}{2\pi(\sqrt{2\pi}s^2 - \Omega^2)}. \tag{5.37}$$

This has the effect of splitting the excitation profile into two equal intensity sinc functions, with a frequency difference of 2Ω Hz, centred around 0. This is illustrated graphically in Fig. 5.11.

Therefore, to excite the two ^{13}C resonances with a frequency difference of 14,278 Hz, a cosine modulated square pulse with a modulation frequency of 7139 Hz was used. The pulse duration was 10 ms, which corresponds to an excitation bandwidth in the order of 100 Hz. This ensured the two excitation regions in the frequency domain did not interfere to affect the pulse phase/intensity. Due to this narrow excitation bandwidth,

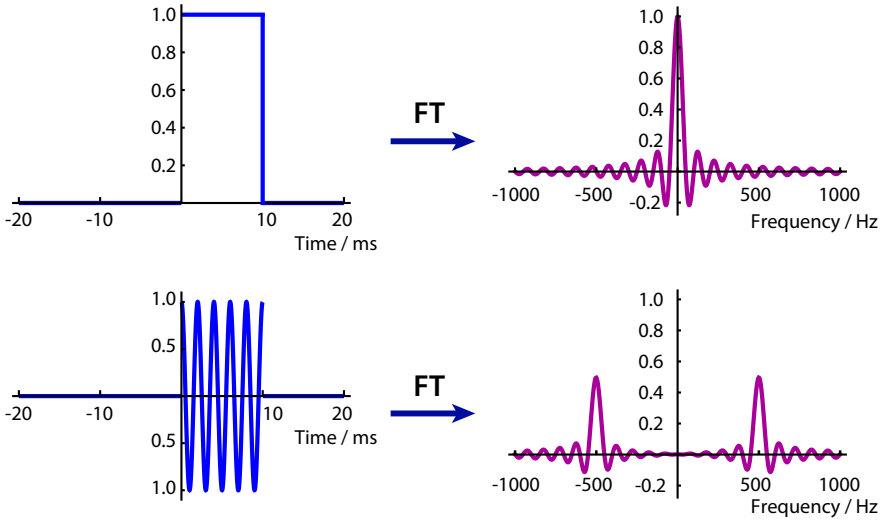

FIGURE 5.11: Graphical representation of the frequency-domain excitation profile of time-domain NMR pulses. Top: A square pulse, which produces a sinc function excitation profile. Bottom: A cosine modulated square pulse, which produces a sinc function excitation profile split by twice the modulation frequency. The pulse duration was chosen to be 10 ms, the modulation frequency was 500 Hz, and intensities have been normalized to 1.

it was necessary to ^{1}H decouple during the ^{13}C pulses to collapse the $^{1}J_{CH}$ couplings, and allow for excitation of the full ^{13}C resonance.

Experimental results showing the oscillatory transfer of ^{13}C magnetization (deriving from ^{1}H singlet order) between the carbonyl and methyl ^{13}C spins are given in Fig. 5.12. The carbonyl ^{13}C spin is polarized after the S2hM sequence, and by varying the x delay in the second part of the sequence, this polarization oscillates between the two J-coupled ^{13}C spins with period $1/2J_{CC}$.

Experimental results showing the hyperpolarized ^{13}C NMR signals deriving from parahydrogenation of dimethyl acetylene dicarboxylate followed by the S2B2M transfer sequence optimized for polarization of the methyl ^{13}C (i.e. x = 96 ms) are shown in Fig. 5.13. The precursor was at full natural abundance of the ^{13}C spins, so only ∼0.02% of the molecules had ^{13}C spins in adjacent carbonyl and methyl sites to allow for polarization transfer. This explains why the carbonyl peak at 165.5 ppm is dramatically larger than the methyl peak at 51 ppm; 99% of the molecules with a ^{13}C in the carbonyl position lack a ^{13}C in the methyl position, so the carbonyl spin remains polarized after the S2B2M sequence.

After the hyperpolarization experiment, the signals were allowed to relax. A thermal equilibrium spectrum was acquired with 47 transients, and from this the signal enhancement on the methyl ^{13}C was estimated to be by a factor of 300.

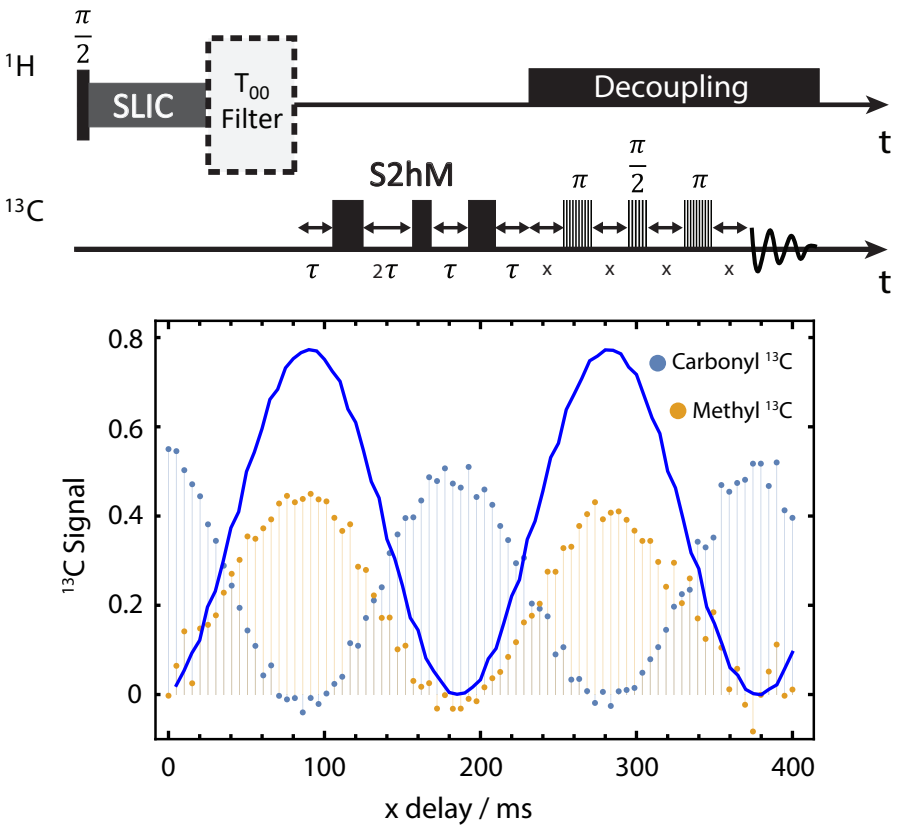

FIGURE 5.12: Top: The complete pulse sequence used for experiments on thermally polarized [1-^{13}C-O-^{13}C$_2$]dimethyl maleate, with the ^{13}C-channel pulses collectively representing the S2B2M sequence. The ^{1}H $\pi/2$ and SLIC pulses converted proton magnetization into singlet order. The S2hM sequence was then applied, optimized for the J-couplings in maleate ($\tau = 18.5$ ms, $n = 1$). Finally, the homonuclear transfer sequence was applied using cosine modulated rf pulses (shown by striped boxes). Bottom: Amplitudes for the conversion of proton singlet polarization into ^{13}C Zeeman polarization in [1-^{13}C-O-^{13}C$_2$]dimethyl maleate. The solid blue line shows a SpinDynamica simulation of the ^{13}C methyl signal, and experimental results are shown by blue and orange points. Simulation code is given in Appendix II. The vertical scale is normalised such that 1 corresponds to 100% conversion from proton singlet order into ^{13}C polarization.

5.6 Summary

Two pulse sequences, SLIC and S2hM, have been presented for the purpose of converting proton singlet order into heteronuclear magnetization. These pulse sequences are designed to work in the important near-equivalence limit, which is characterised by $\omega_{\mathrm{II}} > \omega_{\mathrm{IS}}^{\Delta}$. The SLIC method achieves the transfer faster than any of the hard-pulse sequences described so far, and is extraordinarily simple and requires minimal rf power. However, the SLIC method is sensitive to resonance offset, although it might be made more robust with respect to resonance offsets and field inhomogeneity by modulating the amplitude and/or the frequency [150]. The S2hM scheme is a factor $\sim \pi/2$ longer than SLIC, but is much less sensitive to resonance offset than SLIC, and also the other single-channel hard-pulse sequences described in the literature. The power requirements of S2hM may be minimized by employing moderately weak rf pulses. These sequences

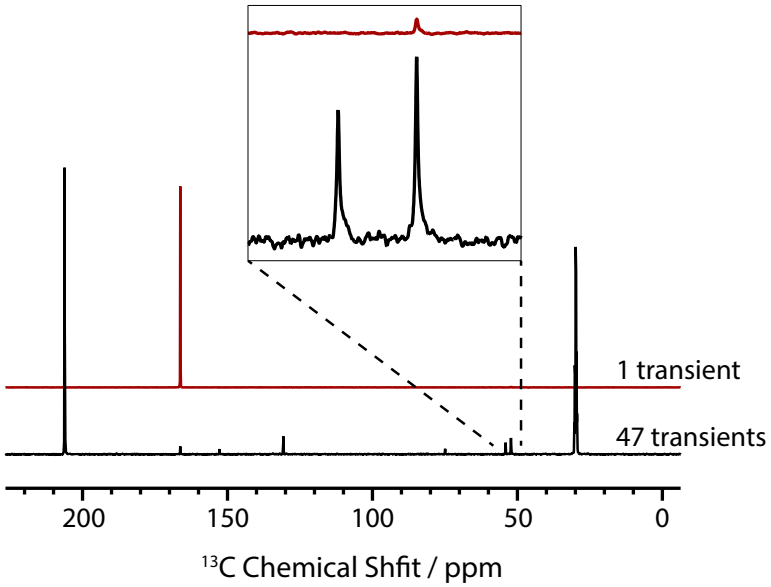

FIGURE 5.13: ^{13}C NMR spectra obtained after parahydrogenation of dimethyl acetylene dicarboxylate in the NMR magnet. A ^{13}C spectrum acquired after bubbling the para-enriched hydrogen gas into the reaction mixture for 30 s and applying the S2B2M pulse sequence is shown in red. No proton decoupling was used during signal acquisition. After the hyperpolarized signal has fully relaxed, a thermal equilibrium pulse-acquire spectrum was acquired using 47 transients, with a relaxation delay of 120 s between acquisitions. Both spectra have line broadening of 5 Hz applied. The NMR signal enhancement factor is approximately 300.

are likely to be useful at low field, in which case the proton pair may be chemically asymmetric, as is the case for most side-arm hydrogenation molecular targets.

Additionally, the S2B2M pulse sequence has been presented, which includes additional pulses to transfer the proton singlet order through a bridging nucleus to a heteronuclear spin not directly J-coupled to the parahydrogen proton pair.

This work shows it is possible to quantitate the processes underlying parahydrogen-induced polarization experiments by using singlet NMR techniques on thermally polarized samples. This allows the reproducible characterisation and optimization of the relevant pulse sequences.

Chapter 6

Hyperpolarized [1-^{13}C]fumarate via Parahydrogen

The work in this chapter is based on material presented in Ref. [85].

6.1 Introduction

To produce hyperpolarized [1-^{13}C]fumarate for *in vivo* applications, dissolution dynamic nuclear polarization (dDNP) [2, 7] is the preferred hyperpolarization technique [14, 15, 17, 18]. Despite significant advances in this field over the last decade, dDNP still has some limitations: expensive equipment is required, the hyperpolarized material is delivered in batch mode, and the polarization build-up time per batch is in the order of one hour. In this chapter, PHIP is shown to be a viable alternative.

Hyperpolarized fumarate can be prepared by pairwise hydrogenation of an acetylene dicarboxylate precursor in water (Fig. 6.1), using a commercially available ruthenium-based catalyst to achieve *trans*-hydrogenation [114–117, 156]. This is in contrast to the vast majority of parahydrogenation reactions reported in the literature, which lead to the para-H_2 protons occupying *cis*-positions on the product molecule. For example, maleate, the *cis* isomer of butenedioic acid, is readily formed after hydrogenation of acetylene dicarboxylate with parahydrogen using the most widely used hydrogenative PHIP catalyst, i.e. [1,4-bis(diphenylphosphino)butane](1,5-cyclooctadiene)rhodium(I) tetrafluoroborate [21, 128, 157]. Maleate itself is a toxic compound, so for *in vivo* application a second hydrogenative step is used to produce the metabolite succinate [21].

If ^{13}C nuclei are absent, the protons in fumarate are chemically and magnetically equivalent, so the hyperpolarized proton singlet order remains in an NMR-silent form, and enhanced NMR signals cannot be directly observed. The hyperpolarized ^{1}H NMR

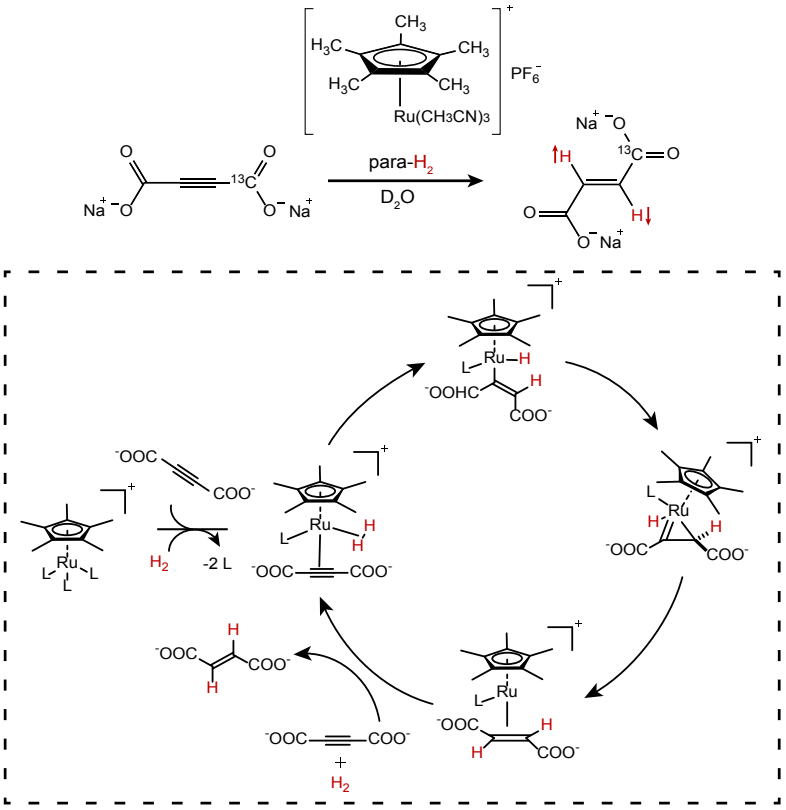

FIGURE 6.1: [1-^{13}C]acetylene dicarboxylate reacts with parahydrogen in the presence of [Cp*Ru(CH_3CN)$_3$]PF_6 to form [1-^{13}C]fumarate. The proton nuclear spin singlet state is indicated by opposing red arrows. The expected catalyst mechanism, modified from reference [116], is shown in the box.

signals can be released by enzymatic conversion to malate [158], or chemical desymmetrization [159]. In the cases of maleate and succinate, magnetic inequivalence caused by a difference in J_{CH} couplings to a ^{13}C spin has be used to convert the ^{1}H singlet order into observable ^{13}C magnetization [21, 128]. Here the same principle is used: ^{13}C labelling of one of the carboxylate moieties breaks the magnetic equivalence of the protons, which have different ^{1}H-^{13}C J-couplings to the ^{13}C label. Since the protons remain close to magnetic equivalence, the application of a simple $\pi/2$ pulse on ^{13}C leads to relatively weak hyperpolarized ^{13}C NMR signals, which are due to singlet-triplet mixing. A specific pulse sequence such as S2hM (Singlet-to-Heteronuclear-Magnetization) (as described in section 5.2.3 and Refs [128, 129]), on the other hand, leads to full conversion of proton singlet order into ^{13}C magnetization, producing strongly enhanced ^{13}C NMR signals.

The S2hM pulse sequence, shown in Fig. 6.2, exploits the molecular J-couplings (and not chemical shifts) to achieve polarization transfer, and is optimized for the case of small heteronuclear coupling to the parahydrogen proton pair. The sequence is designed to work independent of magnetic field homogeneity [128, 129], which is an improvement on similar sequences [124, 139]. It can additionally be made robust to radio frequency

field inhomogeneity by the use of composite pulses, and can therefore be readily implemented on large sample volumes at low magnetic field, as is commonly the case in a clinical setting.

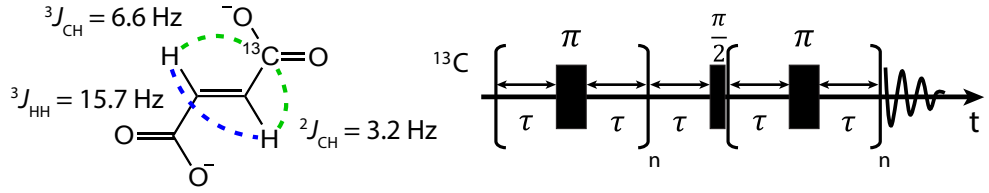

FIGURE 6.2: The S2hM pulse sequence used to convert proton singlet order into ^{13}C magnetization. As stated in section 5.2.3, the delay is given by $\tau = 1/(4\sqrt{J_{HH}^2 + (\Delta J_{CH}/2)^2})$ and the number of loops is $n = \text{round}(\pi/(4\arctan(\Delta J_{CH}/2J_{HH})))$. The fumarate J-couplings are shown. The values of τ and n used in experiments were $\tau = 15.8$ ms and $n = 7$.

It should be noted that although *trans*-hydrogenation has been used before in combination with parahydrogen [114–117], the product molecules formed in those cases have chemically inequivalent proton pairs, giving rise to so-called PASADENA-enhanced NMR signals. This approach is ineffective for releasing the proton singlet order as observable magnetization for the chemically equivalent protons of fumarate.

6.2 Reaction Chemistry

6.3 Materials and Methods

To generate hydrogen gas at 50% para enrichment, hydrogen gas (purity 99.995%) was passed through a home-built parahydrogen generator containing an iron(III) oxide catalyst cooled to 77 K. The solution prior to hydrogenation reactions was 6 mM [Cp*Ru(CH_3CN)$_3$]PF_6, 100 mM disodium [1-^{13}C]acetylene dicarboxylate and 100 mM sodium sulphite in D_2O. For sample hydrogenation, parahydrogen gas was bubbled at 5 bar and 50°C for 30 s through 1/16 inch PEEK tubing that extended to the bottom of a pressurizable 5 mm NMR tube. The bubbling was performed inside the magnet and was controlled manually by hand-operated valves (Swagelok, Solon, U.S.). NMR experiments were performed at 11.7 T in a 5 mm BBO probe using a Bruker AVANCE III console (Billerica, U.S.).

6.4 Results and Analysis

To determine whether the para-H_2 protons remain in a singlet-state after catalytic addition to the precursor, the S2M (Singlet-to-Magnetization) pulse sequence was used

to convert proton singlet order into observable proton magnetization. This is achieved through the asymmetry in ^{1}H-^{13}C couplings (similar to the S2hM sequence), and a complete description of the S2M pulse sequence can be found in Ref [148]. The sample was hydrogenated as described above, and the S2M pulse sequence was applied, followed by signal detection. For comparison, the experiment was repeated on a fresh sample, and the signal was acquired with a $\pi/4$ pulse. The hyperpolarized signal was then allowed to relax, and a thermal equilibrium spectrum was acquired with a $\pi/2$ pulse.

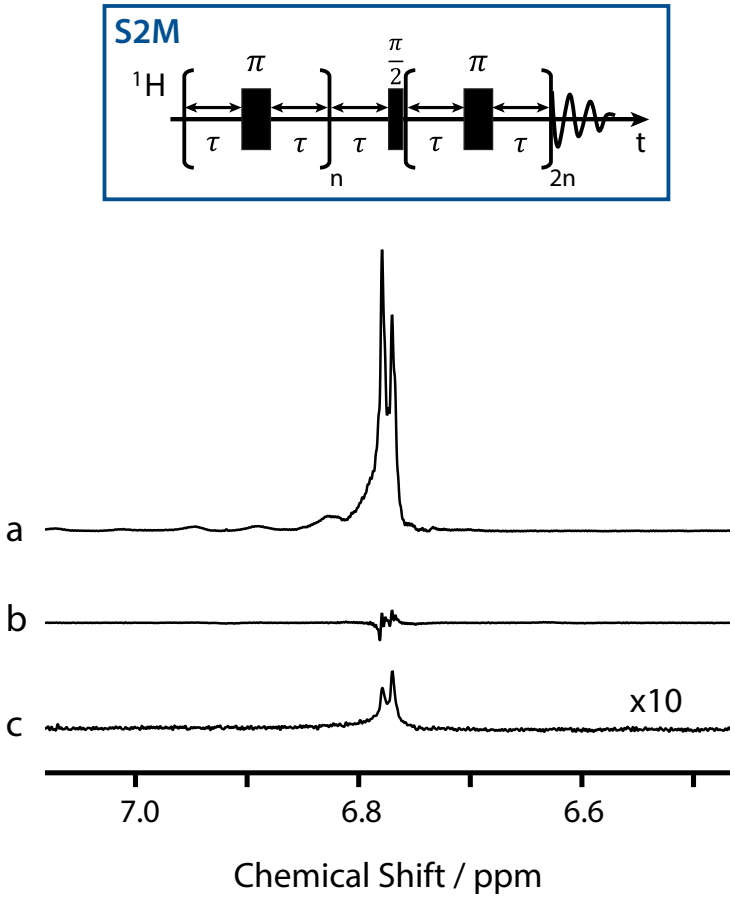

FIGURE 6.3: ^{1}H NMR spectra, each acquired with a single scan. a) Hyperpolarized signal acquired after applying the S2M pulse sequence, b) direct acquisition of the hyperpolarized signal with a $\pi/4$ pulse, c) thermal equilibrium signal, expanded by a factor of 10 for clarity. The 4.2 Hz splitting is the average of the two J_{CH} couplings in fumarate. Lineshape distortions are due to poor sample shimming. The values used in the S2M pulse sequences were $\tau = 15.8$ ms and $n = 7$.

The PHIP [1-^{13}C]fumarate NMR signal by direct detection with a $\pi/4$ pulse is small, and shows almost no net proton polarization (i.e. the integral is close to zero). In contrast, the signal appears dramatically enhanced and in phase after applying the S2M sequence. The parahydrogen singlet order is therefore thought to be preserved during the catalytic addition step, and is released after application of the S2M sequence.

To demonstrate hyperpolarization of the ^{13}C spins, the sample was hydrogenated as described above and the S2hM pulse sequence was applied, optimized for the *J*-couplings in fumarate on the ^{13}C channel before ^{13}C detection. For comparison, the hyperpolarized NMR signal was allowed to decay, and a thermal equilibrium spectrum was acquired with a $\pi/2$ pulse. The results are shown in Fig. 6.4. A typical ^{13}C spectrum of [1-^{13}C]fumarate shows a triplet peak structure from *J*-coupling to the strongly coupled proton pair. However, the S2hM sequence enhances only the central peak of the expected triplet [128], and this observation is supported by a SpinDynamica [28] simulation of the spectrum. The out-of-phase outer peaks are given by weakly allowed proton singlet-triplet state mixing, as described in section 4.2. There is no evidence of formation of the *cis*-product maleate in the ^{13}C NMR spectra, which would appear at 167.3 ppm.

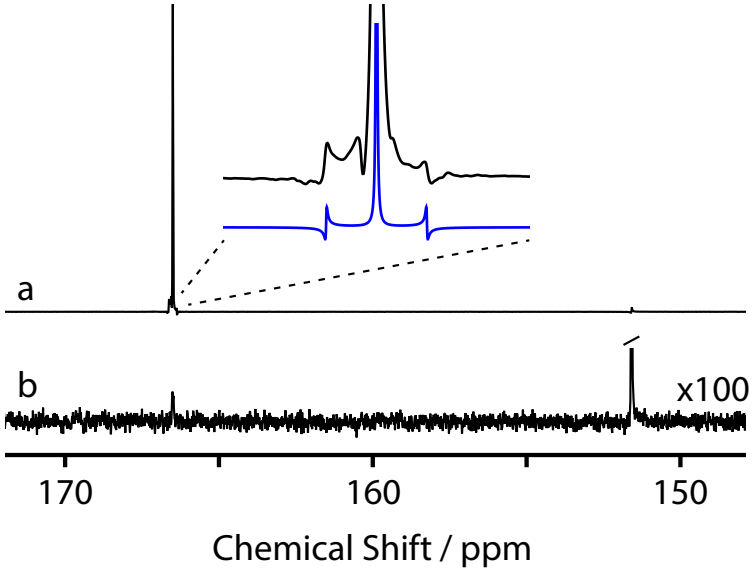

FIGURE 6.4: ^{13}C NMR spectra shown with 1 Hz line broadening, acquired without proton decoupling. a) Hyperpolarized signal acquired after applying the S2hM pulse sequence. An expansion of the signal is shown and compared to a SpinDynamica simulation in blue. The simulation code is given in Appendix II. b) Thermal equilibrium signal acquired in one scan, expanded by a factor of 100 for clarity. The peak assignments are as follows: acetylene [1-^{13}C]dicarboxylate precursor (151.6 ppm), [1-^{13}C]fumarate (166.5 ppm). The [1-^{13}C]fumarate hyperpolarization is revealed when an S2hM sequence is used to convert the ^{1}H singlet order into ^{13}C magnetization, and the signal enhancement achieved here is over 1000.

To quantify the catalyst selectivity for *trans*-hydrogenation over *cis*-hydrogenation, a ^{1}H NMR spectrum was acquired after sample hydrogenation for 300 s, and is shown in Fig. 6.5. There was no detectable maleate signal in a 32 transient ^{1}H spectrum, and the ratio of *trans*:*cis* product was therefore over 500:1. Additionally, succinate was produced as a side-product in 9% yield compared to fumarate. Succinate is a metabolite safe for injection *in vivo*, so this is less concerning than the formation of maleate, which is toxic. It has previously been shown that succinate forms through a Ru-carbene intermediate in a separate catalytic pathway, and not from the over-reduction of fumarate [116, 117].

Importantly, this means that once fumarate is formed, it is not over-hydrogenated to succinate or isomerised to maleate.

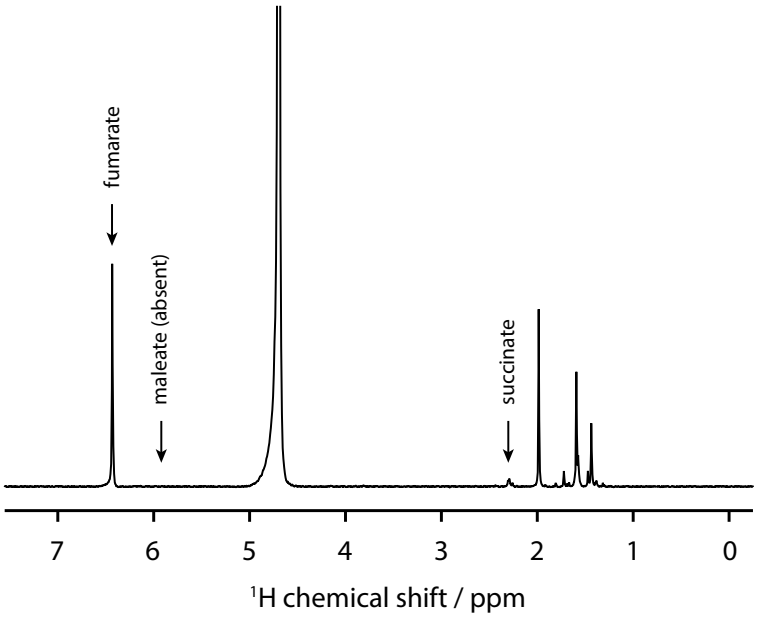

FIGURE 6.5: Thermal ^{1}H NMR spectrum after hydrogenating a solution of 100 mM acetylenedicarboxylic acid disodium salt, 6mM [Cp*Ru(CH_3CN)$_3$]PF_6 and 100 mM ammonium sulphite in D_2O.

The signal enhancement after the S2hM sequence was measured to be over 1000 at a field of 11.7 T, corresponding to a polarization level of over 1%. The enhancement factor and reaction yield could be improved by optimizing the reaction conditions, i.e. parahydrogen pressure, temperature, increasing the catalyst concentration, reducing the reaction time to limit losses due to relaxation, and reducing the precursor concentration to achieve complete hydrogenation. The proton singlet order generated from parahydrogen can also be increased by a factor of 3 by equilibrating the hydrogen gas over a catalyst at 25 K, instead of the 77 K used here.

Spin relaxation times were measured on a sample of 20 mM [1-^{13}C]fumarate in a 40 mM phosphate buffer (pH 7) in water. The results and pulse sequences used are shown in Fig. 6.6 for a sample with and without removal of dissolved O_2 by 15 minutes of N_2 degassing. The data are summarized in Table 6.1.

	^{1}H T_1 / s	^{1}H T_S / s	^{13}C T_1 / s
N_2 degassed	22.6 ± 0.3	46 ± 7	28 ± 2
Not degassed	15.3 ± 0.2	24 ± 5	26 ± 2

TABLE 6.1: Spin relaxation data.

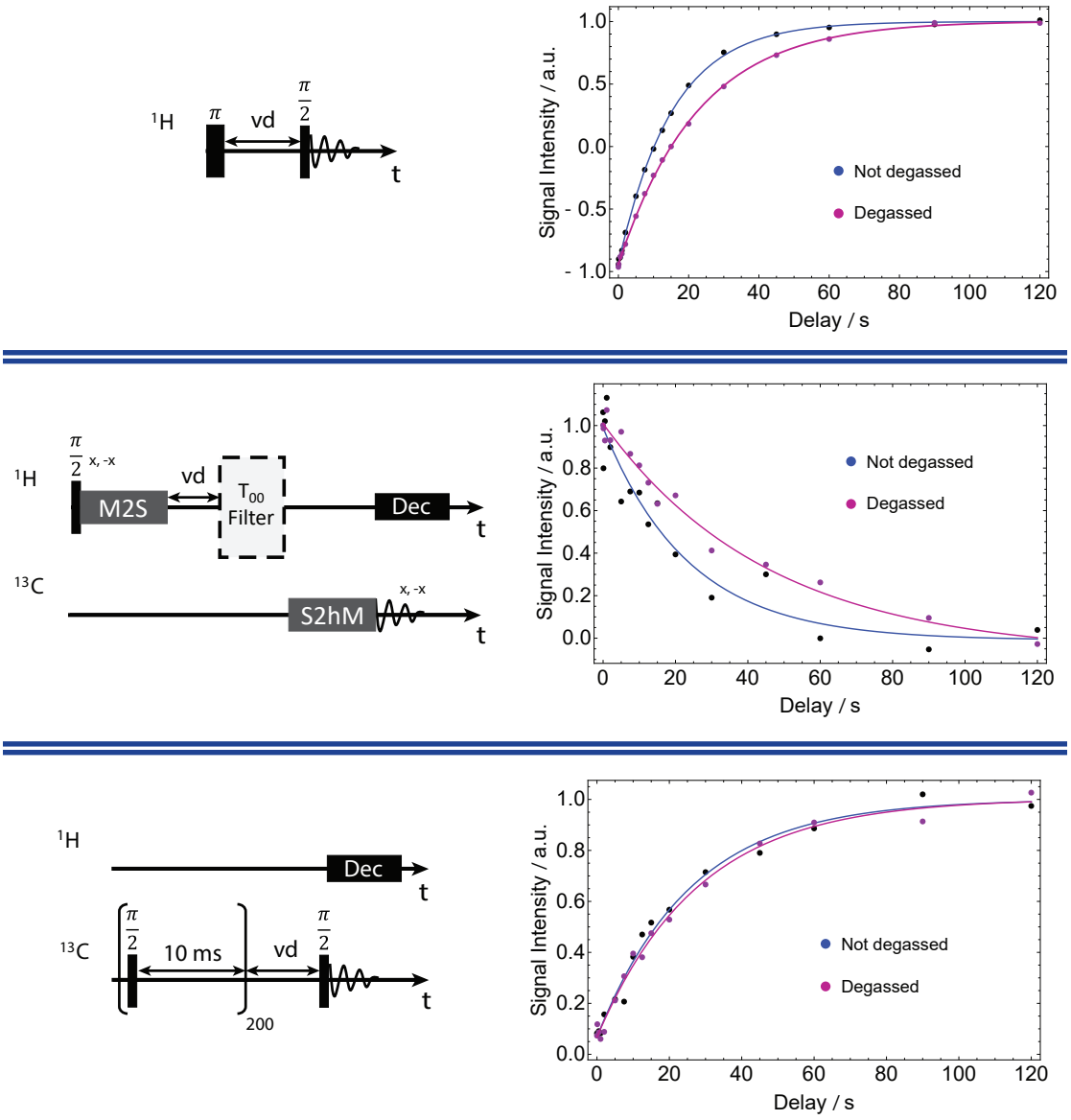

FIGURE 6.6: Top: inversion-recovery pulse sequence used to measure the ^{1}H T_1, and data. Middle: pulse sequence used to measure the ^{1}H T_S, and data. The first pulse and acquisiton are phase cycled as shown, to ensure that the signal acquired came through the proton channel. Bottom: saturation-recovery pulse sequence used to measure the ^{13}C T_1, and data.

The ^{1}H singlet relaxation time T_S is longer than the spin-lattice relaxation time T_1 because the singlet state is immune to intra-pair ^{1}H-^{1}H dipolar relaxation [160]. Nevertheless, it is clear that oxygen significantly impacts both T_1 and T_S. The ^{1}H T_S in the degassed solution is relatively long, which is appealing because time is needed during the parahydrogenation step to build up significant quantities of hyperpolarized material, for catalyst removal and sample transport. The ^{13}C T_1 is probably limited by the large chemical shift anisotropy, and is almost independent of oxygen concentration at 11.7 T; this means the ^{13}C T_1 is probably longer at lower field strengths.

Given the relatively long-lived nature of the proton singlet state, this might provide a means to perform metabolic imaging using hyperpolarized ^{1}H NMR, which is more sensitive than ^{13}C detection. The presence of a ^{13}C label allows the hyperpolarized singlet order in fumarate to be converted into ^{1}H magnetization by a S2M sequence. Even in the absence of a ^{13}C label, the hyperpolarized proton singlet order of fumarate may be liberated by enzymatic conversion to malate [158]. The proton singlet lifetime is expected to be much longer (many minutes) [157–159] in the non ^{13}C-labelled molecule, because the ^{1}H-^{13}C dipolar coupling relaxation contribution is removed. This is appealing for the production of hyperpolarized fumarate, but the oxygen sensitivity should still limit the T_S for in vivo application.

6.5 Summary

In summary, this is a promising method for producing hyperpolarized fumarate from parahydrogen using a ruthenium-based catalyst in water. With radio frequency pulse sequences the hyperpolarized singlet order was transformed into magnetization on the ^{13}C spin in [1-^{13}C]fumarate. There is much room for improvement of the ^{13}C polarization level by optimization of the catalyst, the parahydrogen preparation, and the reaction conditions. If these important issues are addressed, this might lead to a practical route for the convenient and inexpensive preparation of hyperpolarized fumarate for magnetic resonance spectroscopy and imaging experiments.

Chapter 7

Preservation of [1-^{13}C]fumarate Spin Order

The work in this chapter is based on material presented in Ref. [161].

7.1 Introduction

As mentioned in section 1, hyperpolarization methods are limited by an intrinsic longitudinal relaxation time (T_1) that governs the return of non-equilibrium magnetization to thermal equilibrium. If metabolites are prepared in a hyperpolarized nuclear spin state [1, 7, 11, 17, 64, 68, 162–165] for *in vivo* application, the T_1 of the hyperpolarized nuclear spin(s) limits how they can be used. In the case of dDNP (Dissolution Dynamic Nuclear Polarization), the time for extracting the sample from the hyperpolarization equipment, purification, transport, delivery, and signal acquisition is often similar to the nuclear T_1, meaning that the polarizer needs to be located close to the point of use.

Efforts have been made towards the goal of storing hyperpolarized magnetization in the solid state [166, 167]. This is difficult in the case of dynamic nuclear polarization where radicals are used for the polarization step, because they can induce rapid nuclear spin relaxation, especially in the solid state [168]. One approach employs heterogeneous materials, in which the hyperpolarized spin order is transported by spin diffusion to regions distant from the unpaired electron sites [162]. Another approach is to induce radical formation at low temperature by ultraviolet irradiation. The UV-induced radicals are quenched when the sample is warmed [163]. It is also possible to immobilize the radicals by attachment to a matrix, so that they remain behind when the polarized material is flushed out [164, 165].

In this chapter, a new possibility is demonstrated, in which a polarized solution of [1-^{13}C]fumarate is prepared, and the sample precipitated to form a suspension of

microcrystals. It is shown that non-equilibrium magnetization can be substantially preserved by this process, because under the experimental conditions used, the solid-state T_1 is significantly longer than the solution-state T_1. The polarized substance can be liberated into solution by redissolving the solid at a later time. Additionally, the precipitation procedure effectively excludes DNP radicals (which would induce rapid relaxation in the solid state) from the sample.

A crucial aspect of this experiment is the nontrivial demonstration that nuclear spin polarization is not lost during the phase transitions. Other cases in which spin magnetization is known to be preserved through phase transitions include dissolution DNP [7, 68] and the freezing and sublimation of hyperpolarized ^{129}Xe gas [64] or molecules dissolved within [169, 170].

In section 7.2, the ^{13}C T_1 is studied for [1-^{13}C]fumarate in both the solution-state and solid-state, at variable temperature and static field strength. Additionally, PXRD (Powder X-Ray Diffraction) and EPR (Electron Paramagnetic Resonance) results are shown.

In section 7.3, the concept of T_1 extension by precipitation as a solid is demonstrated on thermally polarized samples.

In section 7.4, the precipitation procedure is used together with the novel bullet-DNP technique [171] and sample cooling with liquid nitrogen to dramatically extend the ^{13}C T_1 for a hyperpolarized sample of [1-^{13}C]fumarate.

7.2 Physicochemical Properties of [1-^{13}C]fumarate

7.2.1 Relaxation Properties of [1-^{13}C]Fumarate - Field and Temperature Dependence

Solution-state relaxation experiments at fields of 7.0 and 11.7 T were performed on samples of 1.2 M [1-^{13}C-2,3-D_2]sodium fumarate and [2,3-D_2]sodium fumarate in a 1:9 ratio, in H_2O. Inversion-recovery experiments (as described in section 2.1.6) were used to determine T_1. The results are shown in Table 7.1.

The decrease in T_1 with increasing field strength indicates chemical shift anisotropy (CSA) is the dominant relaxation mechanism for this nuclear spin, as indicated by the B_0^2 dependence in Eq. 7.1 [172]:

$$R_1^{\mathrm{CSA}} = \frac{1}{T_1^{\mathrm{CSA}}} = \frac{2}{15}\gamma^2\Delta\sigma^2 B_0^2\tau_c \tag{7.1}$$

where $\Delta\sigma = \sigma_{\parallel} - \sigma_{\perp}$ is the difference in chemical shielding perpendicular to, and along, the axis of the chemical shift tensor. This mechanism often dominates the relaxation

Magnetic Field / T	T_1 / s
7.0	31.9 ± 0.7
11.7	19.4 ± 1.6

TABLE 7.1: Carbonyl ^{13}C solution-state relaxation times of 1.2 M sodium fumarate in H_2O.

of carbonyl ^{13}C spins, due to the significant gradient of electron density around the sp^2 hybridised carbon producing a large $\Delta\sigma$.

Solid-state relaxation experiments at fields of 2.3, 7.0, 14.1 and 20.0 T were performed on a dry sample of [1-^{13}C-2,3-D_2]fumaric acid and [2,3-D_2]fumaric acid (mixed polycrystalline solids) in a 1:9 ratio, under 12 kHz MAS (Magic Angle Spinning) packed in a 4 mm zirconia rotor. Saturation recovery pulse sequences (as described in section 2.1.6) were used to measure the T_1 without an initial ^{1}H-^{13}C cross polarization step. Measurements were also performed at a field strength of 7.0 T on a wet precipitated sample of [1-^{13}C-2,3-D_2]fumaric acid and [2,3-D_2]fumaric acid in a 1:9 ratio, to mimic the solid formed in the precipitation experiments. 5 ml of 12 M HCl was added to a 5 ml sample of 1.2 M [1-^{13}C-2,3-D_2]sodium fumarate (10% ^{13}C labeling) in water. The resulting precipitate was partially dried with filter paper and this wet solid was packed into a 4 mm zirconia rotor. A saturation recovery sequence was used to measure the T_1 under 12 kHz MAS. The saturation recovery results are shown in Fig. 7.1.

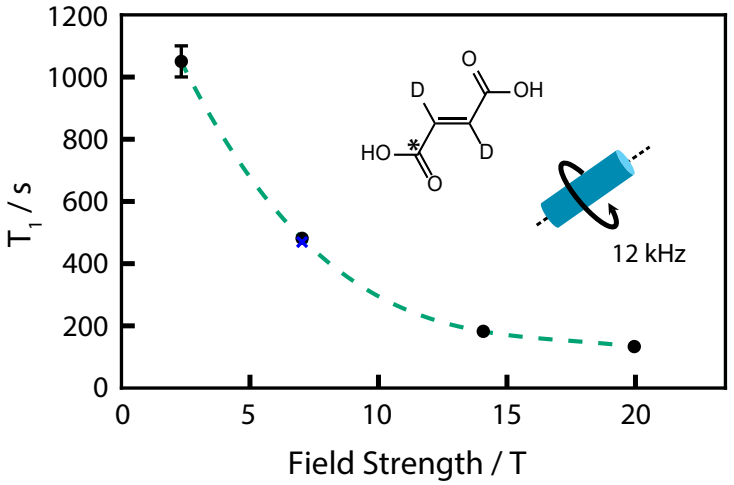

FIGURE 7.1: The T_1 of the carbonyl ^{13}C in dry [1-^{13}C-2,3-D_2]fumaric acid (black points) as a function of static field strength. Measurements were performed on samples packed into 4 mm zirconia rotors under 12 kHz MAS. The dashed line is an interpolation to guide the eye. The T_1 of a wet sample of [1-^{13}C-2,3-D_2]fumaric acid is shown by the blue cross. Within the error, the solid-state T_1 at 7.0 T is the same for a wet or dry sample.

Solid-state relaxation measurements were also performed at variable temperature. These experiments were performed on a dry sample of [1-^{13}C-2,3-D_2]fumaric acid at a static field strength of 2.1 T, without sample spinning. These results are shown in Fig. 7.2.

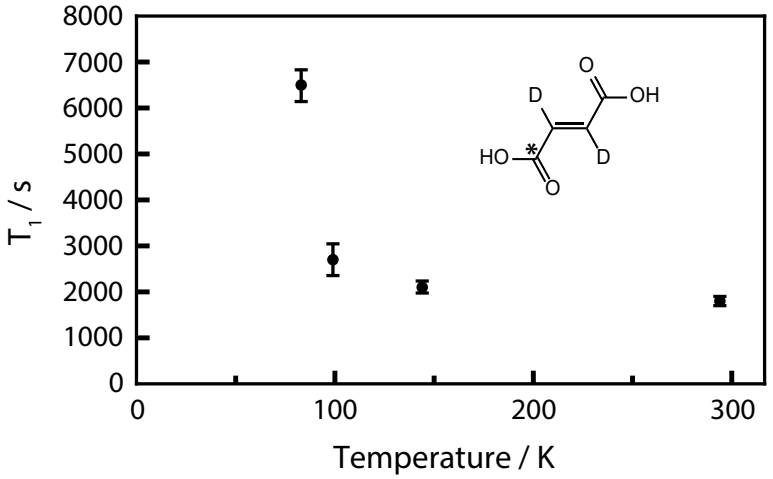

FIGURE 7.2: The T_1 of the carbonyl ^{13}C in dry [1-^{13}C-2,3-D_2]fumaric acid (black points) as a function of temperature at a static field strength of 2.1 T. Measurements were performed on a static (i.e. not spinning) sample packed into 5 mm NMR tube.

These measurements collectively show the solid state T_1 can be dramatically increased by storing the sample at low field, and low temperature.

Fumaric acid crystallizes as long chains of hydrogen-bonded molecules [173], which are rigid and possess no flexible moieties. If we recall from section 2.1.6 that nuclear spin relaxation is induced by fluctuating magnetic fields, this lack of molecular motion in the crystal structure is key to explaining the long T_1 times observed for solid-state fumaric acid. The dominant relaxation mechanism here is thought to be ^{1}H-^{13}C dipolar coupling which is modulated by the carboxylic acid protons tunneling ('hopping') between adjacent fumarate molecules [174].

7.2.2 EPR Measurements on Precipitated Fumarate

Synthetic chemists use crystallization as a purification technique to exclude impurities from a desired compound. This is not dissimilar to the precipitation of fumaric acid from a dissolution-DNP solution containing free radical impurities. The free radicals, which are necessary for the polarization process, can induce rapid nuclear spin relaxation in [1-^{13}C]fumarate due to dipolar coupling between the nuclei and unpaired radical electrons [175, 176]. For this reason, it was important to determine to what degree this precipitation procedure would exclude the free radicals from the hyperpolarized product.

To determine this, EPR experiments were performed as described in the following sections.

7.2.2.1 Materials and Methods

To a solution of 1.2 M sodium fumarate and 2 mM TEMPO in water, HCl was added to precipitate out fumaric acid. The crystals were washed with 25 ml water to remove residual TEMPO from the crystal surfaces, and dried by filtering off the water using a Hirsch funnel. Fumaric acid crystals (139 mg) were redissolved with 1 ml 2.4 M sodium hydroxide in water. Solution-state EPR measurements were taken using an EMX Micro EPR spectrometer (Bruker BioSpin, Billerica, U.S.) with 16 scans of 100 G sweep width lasting 10 s each. The microwave frequency was 9.82 GHz at a power of 6 mW.

7.2.2.2 Results and Analysis

Electron paramagnetic resonance measurements quantifying the concentration of TEMPO contamination in the precipitated crystals are shown in (Fig. 7.3). Additional spectra were taken of 10 μM TEMPO and 1.2 M sodium fumarate in water. TEMPO radicals in solution produce a characteristic three line EPR profile from the electron hyperfine coupling to the spin-1 nitrogen-14 nucleus [177]. After correcting for the background signal from residual TEMPO in the sample region, this pattern was observed in the 10 μM TEMPO solution, but not in the solution of washed precipitate. An upper bound on the radical concentration was set at 1 μM as this was the detection limit.

These results show that to a good approximation the radical molecules are excluded from the precipitate, suggesting that the precipitation step acts as an effective purification method for removing contaminants from the hyperpolarized substance.

7.2.3 Crystallinity of Precipitated Fumarate

To grow large crystals from a solution, the slower the crystal growth the better [178]. In this procedure, the fumaric acid crystal formation after the addition of HCl to the sodium fumarate takes less than 1 s. To verify the solid formed was crystalline, and not largely amorphous, PXRD measurements were performed as described in the following sections.

7.2.3.1 Materials and Methods

To prepare the precipitated solid for PXRD and SEM (scanning electron microscopy) characterisation, 2.2 ml 12 M HCl was added to 10 ml 1.2 M sodium fumarate. The resulting solid suspension was filtered and dried under vacuum for 2 h. The stock fumaric acid used for PXRD comparison was purchased from Sigma Aldrich (Gillingham, U.K.) and used directly.

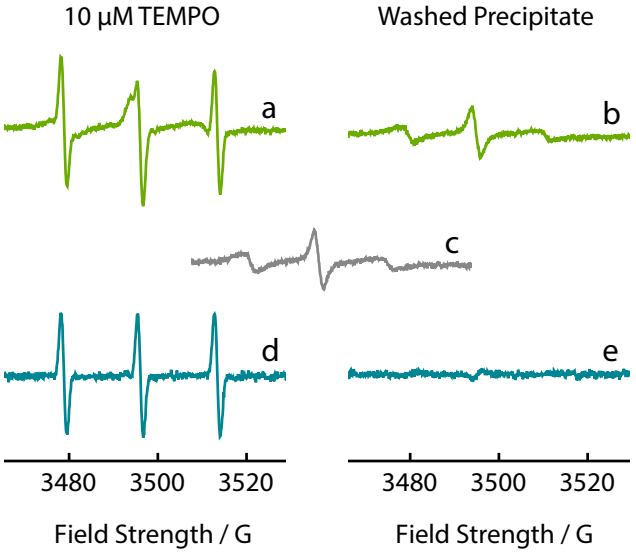

FIGURE 7.3: A comparison of solution-state EPR spectra for a co-solution of 1.2 M sodium fumarate and 10 μM TEMPO in water, and the precipitate from our experiment. The precipitate solution was prepared as described in the Methods. a) Spectrum of 1.2 M sodium fumarate and 10 μM TEMPO solution. b) Spectrum after precipitation of a 1.2 M sodium fumarate and 2 mM TEMPO solution, washing, and dissolving in NaOH solution. c) The background signal of pure sodium fumarate solution. d) Residual spectrum after subtracting the background signal from (a). e) Residual spectrum after subtracting the background signal from (b).

For the PXRD experiments, the x-ray source was swept from 5° to 80° (2θ) over 200 s. Cu Kα x-rays at a wavelength of 1.54 Å were used.

7.2.3.2 Results and Analysis

A comparison between the powder x-ray diffraction patterns for the precipitated particles and a stock sample of fumaric acid is shown in Fig. 7.4. The sample preparation is given in section 7.3.1. The sharp peaks indicate the particles in both cases are largely crystalline, and the overlap between the patterns suggests the crystal structures are nearly identical. There appears to be a small degree of amorphicity, as indicated by the broad feature centred at $2\theta = 14°$. Importantly, this feature is of equal intensity for the precipitate and stock fumaric acid.

An SEM image is shown in the inset of Fig. 7.4. From this the average particle diameter is estimated to be approximately 1 μm, but the variance is clearly large.

7.3 Thermal Polarization Demonstration

In the following section, the ^{13}C lifetime extension by precipitation is demonstrated on thermally polarized samples of [1-^{13}C]fumarate. A π pulse can be used to disturb

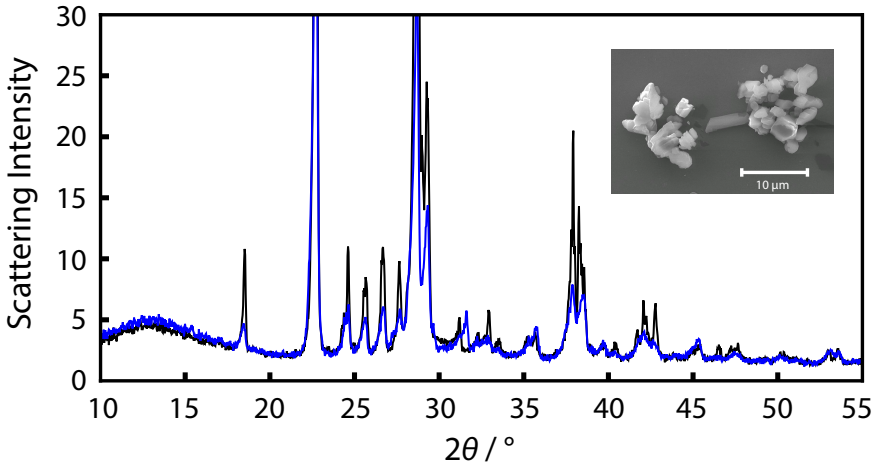

FIGURE 7.4: Powder x-ray diffraction scattering patterns for stock fumaric acid (black), and precipitated fumaric acid (blue). The scattering intensity has been normalized to 100 for the maximum scattering in stock fumaric acid in both spectra. An inset shows an SEM image of the precipitated fumaric acid.

the nuclear spin polarization, and the signal recovery to thermal equilibrium is observed. Precipitation is realized through the pH-dependent solubility of fumarate, as illustrated in Fig. 7.5. Disodium fumarate readily dissolves in water as sodium cations and the fumarate dianion, while the protonated form, fumaric acid, is relatively insoluble (7 mg ml^{-1}) [179].

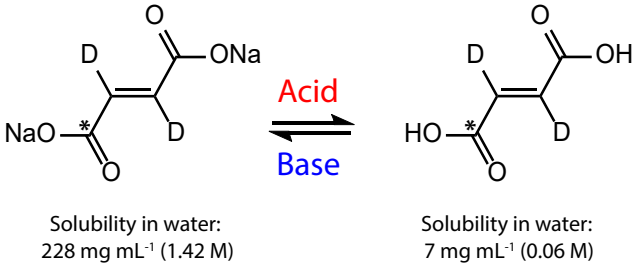

FIGURE 7.5: Solubility of the labelled fumarate. The solution-state T_1 is for a 1.2 M sample at 298 K. The solid-state T_1 is for the 1-^{13}C site in a pure, dry sample at 298 K.

7.3.1 Materials and Methods

All precipitation experiments were performed with 1.2 M samples of [1-^{13}C-2,3-D_2]disodium fumarate, mixed with [2,3-D_2]disodium fumarate in a 1:9 ratio, and dissolved in 1 ml of water, and loaded into 10 mm NMR tubes. Deuteration was used to extend the solution-state carbonyl ^{13}C T_1. The experiments were performed at a magnetic field of 7.0 T (300 MHz ^{1}H frequency) using a Bruker Avance III spectrometer (Billerica, U.S.). The experimental apparatus is shown in Fig. 7.6.

The precipitation and redissolution steps were performed separately using 0.22 ml 12 M HCl and 0.33 ml 9 M NaOH. These two solutions were loaded into separate 1/16

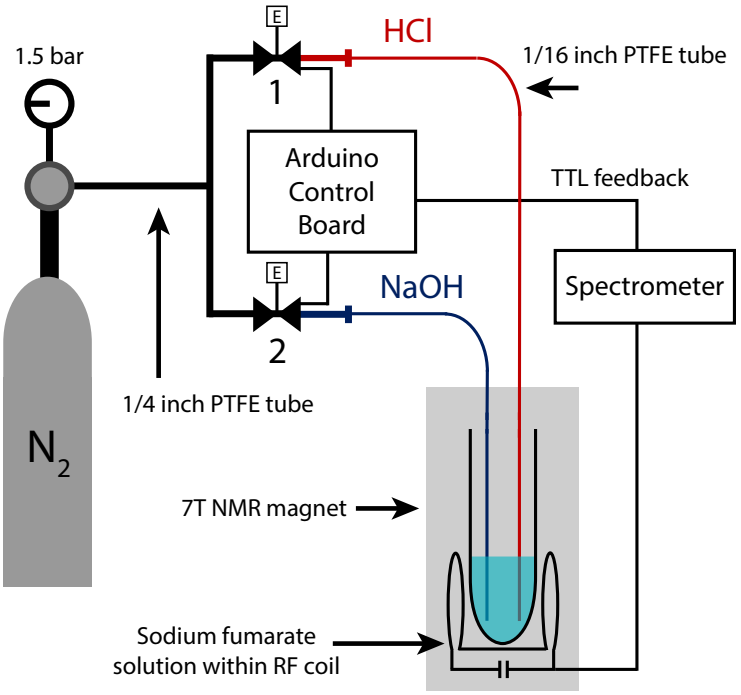

FIGURE 7.6: Sketch of the apparatus. The acid and base were loaded individually in 1/16 inch PTFE tubes, which were placed in a 10 mm NMR tube in the spectrometer. The N_2 flow to inject acid/base was controlled by opening the electrovalves, interfaced with the spectrometer through an Arduino board.

inch PTFE (polytetrafluoroethylene) tubes which terminated just below the surface of the sample. The 1 ml sodium fumarate sample was placed inside the probe's radio frequency (rf) coil, with the PTFE tubes penetrating by ~5 mm. The small initial sample volume ensures that all ^{13}C spins experience a strong radio frequency field (see below).

For the data in Fig. 7.7, the following procedure was used: (1) the ^{13}C spins were inverted by a π pulse, (2) after a delay of 0.1 s, the HCl solution was added over 2 s by flowing N_2 gas at a pressure of 1.5 bar from behind, (3) after a further 2 s delay, the NaOH solution was injected over 4 s. Throughout this procedure, a spectrum was acquired every 2.2 s with an 8° flip angle pulse. Using small flip angle pulses means the nuclear spin order is not significantly disturbed.

The NMR experiments in Fig. 7.8 were performed using inversion recovery sequences (recall from section 2.1.6), with precipitation by addition of acid, and dissolution by addition of base, during the variable wait time. A π pulse was applied to invert all carbon spins, followed by a delay of 0.1 s. The HCl solution was added over 3 s by flowing N_2 gas at a pressure of 1.5 bar from behind, and fumaric acid precipitated out of the solution. After a variable delay τ, the NaOH solution was injected over 4.5 s,

followed by a 2 s wait time for the solution to settle, and the signal acquired with a $\pi/2$ pulse.

The small initial sample volume (1 ml) was to ensure that the sample was contained entirely within the rf coil, to ensure that the π pulse inverted the ^{13}C magnetization of the entire sample, to a good approximation. This avoids problems associated with the physical mixing of sample regions, some of which contain ^{13}C nuclei that experienced a near-ideal π pulse, and some of which were only partially affected.

Adding the acid and base increased the sample volume by 55%, introduced a high concentration of ions, increased the temperature by 17 K and altered the shims. The introduction of ions reduced the total rf power that perturbed the nuclei, but in a reproducible manner between experiments, so the final $(\pi/2)_y$ pulse length could be calibrated accordingly. The shim and temperature alteration was ignored, because the peak integrals should be independent of this.

7.3.2 Results and Analysis

The results in Fig. 7.7 demonstrate the ^{13}C spin order is preserved through the precipitation procedure. Immediately after the π pulse, the first acquired signal is large and has inverted phase. Before the next acquisition, HCl is added which causes fumaric acid to precipitate out of solution as a solid. The dipolar couplings and chemical shift anisotropy interactions are not isotropically averaged in a static solid, and the signal is broadened to the point of being unobservable. NaOH is then added to the solution to redissolve the fumaric acid, and the ^{13}C signal reappears. Importantly, the signal retains its inverted phase, which proves the spin order was not lost during the two phase transitions. After some time, the signal recovers to a steady-state value.

The steady-state spectra have integrals approximately 4.4 times lower than the first spectrum, and three contributing factors have been identified:

1. After adding the acid and base, the concentration of sodium fumarate fell by ∼55%, and the extra sample volume was not inside the rf coil. Also, a moderate concentration of Na^+ and Cl^- ions were introduced, which reduced the detection sensitivity. By comparing the signal acquired from a 90° pulse on the sample before and after addition of acid and base, the reduction in signal was measured to be by a factor of 2.1.

2. All small flip angle pulses applied were 5 μs pulses. Before the acid and base were added, this corresponded to a flip angle of 11° . After introducing the Na^+ and Cl^- ions, the flip angle was 8°, because the ions absorbed a fraction of the rf power. This afforded a drop in signal by a factor of 1.4.

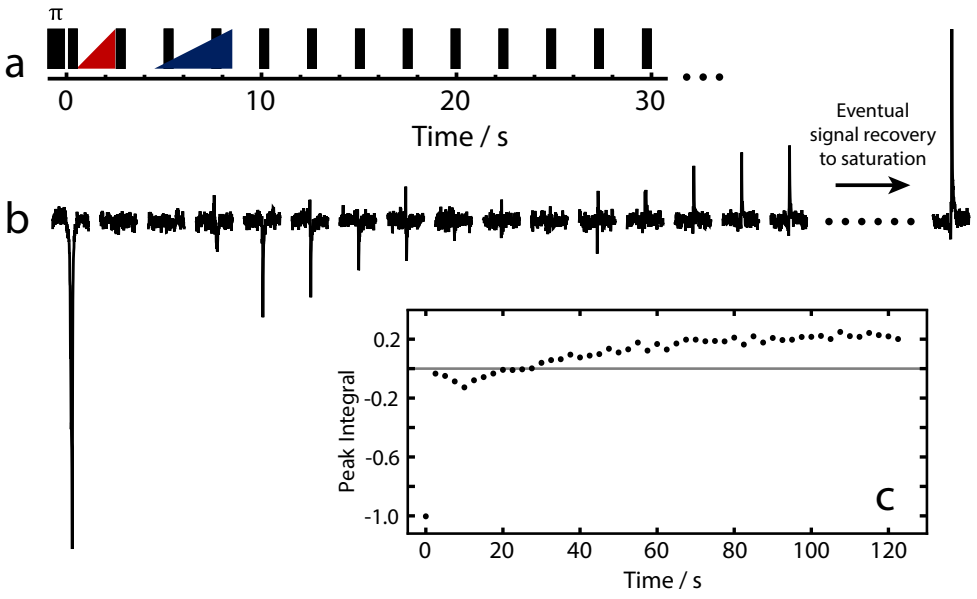

FIGURE 7.7: a) Events sequence, with 8° flip angle pulses shown by black boxes, and acid and base additions shown in red and blue, respectively. b) Images of the carbonyl ^{13}C resonance detected in each acquisition. c) A plot showing the carbonyl ^{13}C peak integral in each spectrum acquired in the experiment, normalized to the first integral.

3. The carbonyl ^{13}C T_1 was 32 s, and pulses with a 7.8° flip angle were applied every 2.5 s. This caused partial saturation of the signal, and a steady state of ~90% of the equilibrium magnetization was reached. This reduced the signal by a factor of 1.1.

From these factors, a drop in signal by a factor of 3.2 was estimated. A factor of 1.4 is unaccounted for in this estimate. This might be due to sample splashing during the acid and base bubbling to leave undissolved sample around the sides of the NMR tube.

The inversion recovery experiment shown in Fig. 7.8a was performed on six samples, using a different τ delay for each, and the results are shown in Fig. 7.8b. The green and blue relaxation curves were acquired by performing experiments on a sample of 1.2 M [1-^{13}C-2,3-D_2]disodium fumarate in water before and after the acid/base addition, respectively. This data allows comparison with a sample that wasn't precipitated during the experiment, and relaxed with the solution-state T_1. Using the procedure in Fig. 7.8a, an effective relaxation time for the microcrystalline suspension, T_1^{susp}, of 190±31 s was estimated, a factor of ~6 times longer than the solution-state T_1 of ~32 s. For each dataset, the signal was normalized and fit to an exponential of the form $1 - Ae^{-t/T_1}$, where A and T_1 are variables.

The effect of including TEMPO ((2,2,6,6-tetramethylpiperidin-1-yl)oxyl) radicals at a concentration of 2 mM in the solution was investigated. The radicals are paramagnetic and can provide an efficient source of nuclear spin relaxation, especially in the

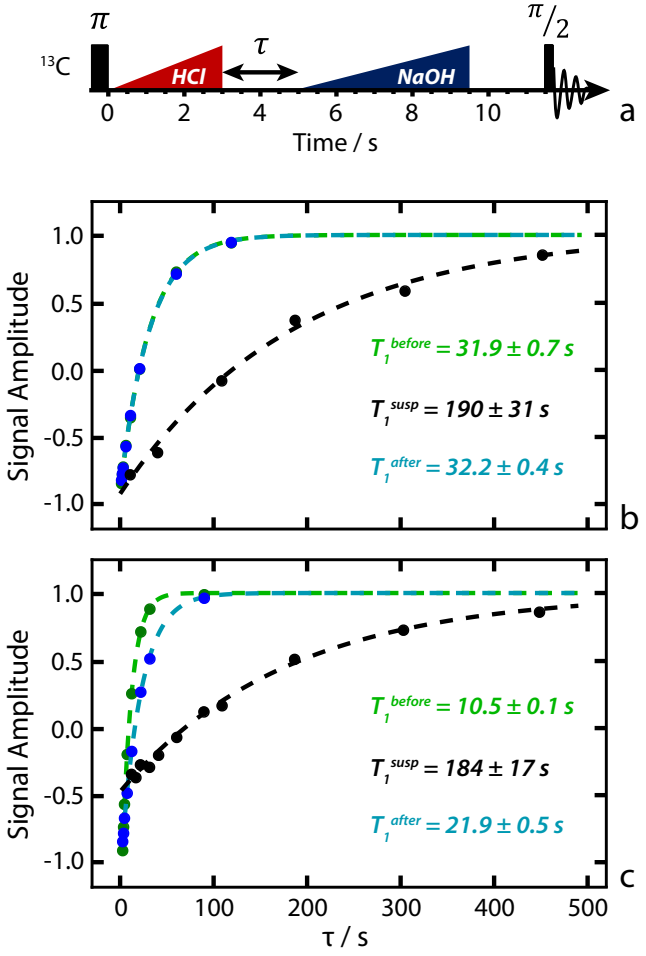

FIGURE 7.8: a) Inversion-recovery pulse sequence, including the acid and base additions. The addition of HCl causes fumaric acid to precipitate out of solution, and the addition of NaOH causes redissolution. b) A relaxation plot of the [1-^{13}C-2,3-D_2]fumarate carbonyl ^{13}C NMR signals. Black points correspond to the experiment in (a). Green and blue points are from a conventional solution-state inversion-recovery relaxation measurement on a 1.2 M sample at 298 K before and after the acid/base additions, respectively. Dashed lines are the monoexponential best-fit curve for each dataset. The three data sets have been normalized to recover to a signal amplitude of 1. c) A relaxation plot acquired in the same manner as that shown in (b), but with TEMPO radical present in the sample at an initial concentration of 2 mM.

solid state. For the precipitation measurements, shown in Fig. 7.8c, the same experimental procedure was used as before. A T_1^{susp} of 184±17 s was measured, compared to solution-state T_1 values of 10.5 and 22 s before and after addition of the acid and base, respectively. The slower ^{13}C relaxation in solution after the acid and base additions is attributed to the dilution of the radicals by the additional liquids.

The solution-state T_1 values are shorter in the presence of radicals, and strongly depend on the TEMPO concentration [175, 176]. However, within experimental error, the measured T_1^{susp} values of the particle suspension are the same with and without radicals.

7.4 Dynamic Nuclear Polarization Demonstration

After a proof-of-principle demonstration using thermally polarized samples, the precipitation procedure was used in combination with DNP to prolong the ^{13}C lifetime in samples of [1-^{13}C-2,3-D_2]fumaric acid. The [1-^{13}C-2,3-D_2]fumaric acid was hyperpolarized, and then rapidly transferred into a 0.45 T Halbach where the precipitation occurred. The sample was held as a solid in this field for a variable delay to allow solid-state ^{13}C relaxation, and then dissolved and shuttled into a high-field magnet for signal detection.

7.4.1 Materials and Methods

The sample for DNP polarization was 2 M [1-^{13}C-2,3-D_2]fumaric acid and 20 mM OX63 (tris-(8-carboxyl-2,2,6,6-tetrakis(2-hydroxyethyl)-1,3,5,7-tetrathia-2,6-dihydro-s-indacene-4-yl)methyl sodium salt) in 45 μl DMSO. The sample was loaded into a PTFE case, and rapidly cooled in a liquid nitrogen bath to form a glassy solid. DMSO was chosen as a solvent for two reasons; (1) it is a solvent for fumaric acid, and (2) it is self-glassing, which is important for radical dispersion in the solid and hence efficient polarization build-up. Full details of the DNP apparatus can be found in Ref. [171].

The sample was loaded into a liquid helium cryostat in a 6.7 T magnet, and was cooled to 1.45 K with vacuum pumping. The sample was irradiated with 188 GHz, 50 mW microwaves from a microwave source (ELVA-1, Sweden) for 1 h, and the ^{13}C polarization build-up was monitored with small flip angle pulses using an rf coil in the cryostat tuned to the ^{13}C resonance frequency.

The sample in the PTFE case was shuttled from the cryostat through a solenoid tunnel providing a 60 mT field, using 8 bar helium gas. After reaching a 3D-printed 'receiver' which caught the PTFE case, inertia carried the sample through, into a solution of 1 ml 12 M HCl in H_2O on a glass sinter. The HCl solution was held in a Halbach permanent magnet array providing a magnetic field of 0.45 T. The fumaric acid precipitated out as a solid, but the DMSO dissolved into the HCl solution. The liquid was filtered off, and the solid fumaric acid precipitate was washed with 2 ml H_2O to remove residual OX63 radical from the surface of the crystals. After waiting for a variable delay to allow spin relaxation, the sample was dissolved in 1 ml 2 M NaOH and shuttled using 5 bar nitrogen gas into a 5 mm NMR tube in an 11.7 T magnet for ^{13}C signal detection. The signal was acquired every 5 s with a 10° flip angle pulse.

Images showing the sample precipitation in HCl, followed by washing with H_2O are shown in Fig. 7.9.

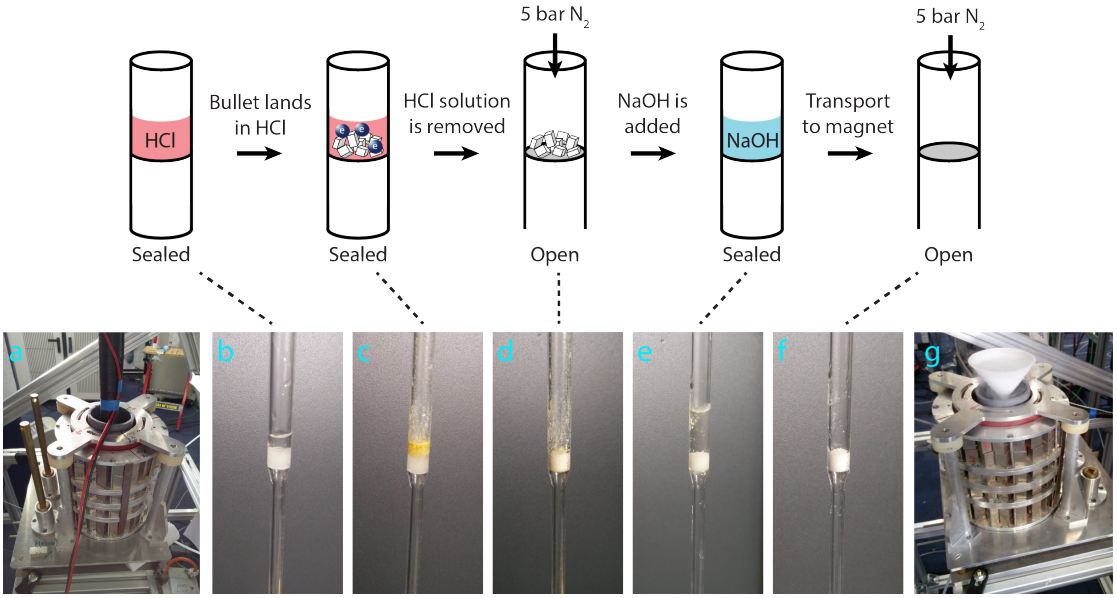

FIGURE 7.9: a) The glass tube was held in the 0.45 T Halbach, with a solenoid tunnel attached to the top. b) 1 ml 12 M HCl on the glass sinter. c) The DNP sample landed in the HCl and the fumarate precipitated out, while the DMSO and radical dissolved. The yellow colour is due to dissolved OX63 radical. d) The liquid was filtered off to leave just crystals of the hyperpolarized [1-^{13}C-2,3-D_2]fumaric acid. e) After a variable delay to allow for relaxation, 1 ml of 2 M NaOH was added to dissolve the precipitate. f) The hyperpolarized solution was shuttled to the 11.7 T magnet for signal acquisition. g) An image of the sample being cooled by liquid nitrogen, which was provided via a glass funnel. The cooling was implemented during the relaxation delay, between steps (d) and (e) in the sequence.

7.4.2 Results and Analysis

The experimental procedure described in section 7.4.1 was used to study the solid-state relaxation of the precipitated [1-^{13}C-2,3-D_2]fumaric acid in the 0.45 T Halbach magnet. Two additional experiments were performed for comparison; (1) the hyperpolarized sample was shuttled directly from the polarizer into a 2 M NaOH solution in the 11.7 T magnet for signal detection (i.e. without precipitation), and (2) the previously described precipitation procedure was used, but during the relaxation delay the sample was cooled to 77 K with liquid nitrogen for 75 min, to allow the DNP-team time to catch the 2nd half of a FIFA World Cup game between Nigeria and Iceland. The results are shown in Fig. 7.10.

The polarization level of the sample shuttled directly into the detection magnet was 7.4%, which is dramatically higher than the polarization levels achieved on the precipitated samples (<100). The polarization loss observed when the precipitation procedure was performed is not currently understood. A contributing factor is slow sample transport in the solution-state from the Halbach to the detection tube (∼10 s), in which time solution-state relaxation occurs.

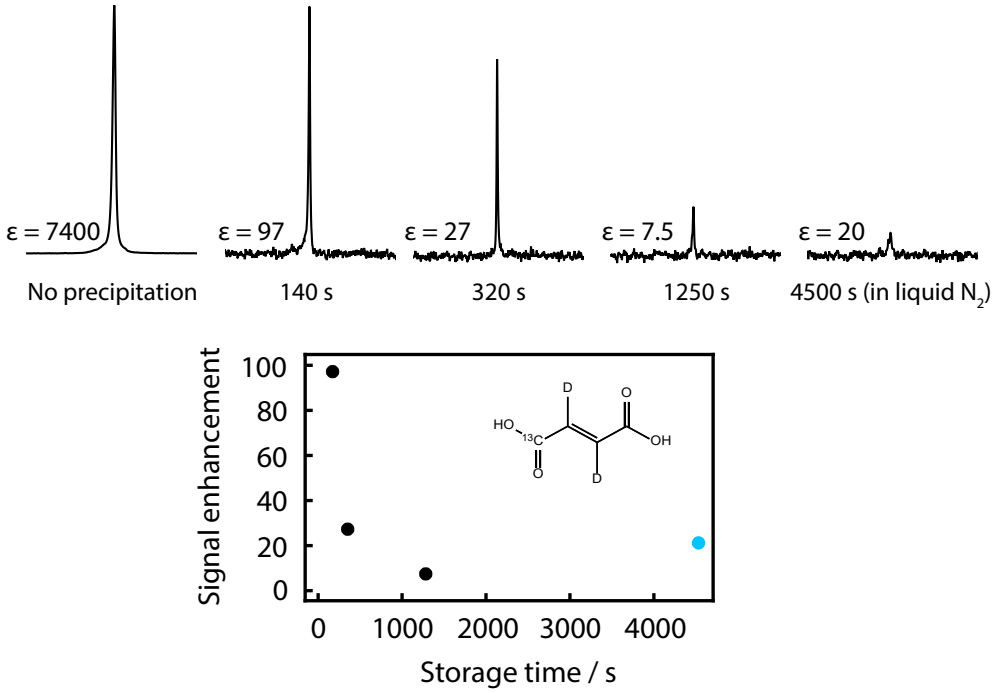

FIGURE 7.10: Top: Hyperpolarized carbonyl ^{13}C peaks from [1-^{13}C-2,3-d$_2$]fumarate. The stated signal enhancements were determined for each sample individually by comparison with a thermal equilibrium ^{13}C spectrum after the hyperpolarized NMR signal had decayed. Bottom: The results from the precipitation experiments (i.e. omitting the direct-acquisition experiment without precipitation), with the blue point indicating the sample that was stored in liquid nitrogen for the relaxation delay. Discrepancies between the stated signal enhancement and the signal intensity in the spectra are thought to be caused by a difference in the amount of fumarate that ends up in the NMR tube. This is probably due to the fumarate dissolving to different degrees in H_2O washing step, and part of the hyperpolarized material being lost.

By cooling the precipitate to 77 K with liquid nitrogen, the ^{13}C T_1 is dramatically enhanced. After 75 min of storage time as a precipitate at 0.45 T, the hyperpolarization persists. However, the observed signal enhancement is too low to be useful for the proposed *in vivo* applications. It will be important to understand where polarization is lost during the precipitation procedure to increase the signal enhancements to a level relevant for *in vivo* application.

7.5 Summary

By precipitating the metabolite fumarate out of solution, non-equilibrium nuclear spin order can persist for times much longer than the solution-state T_1. This has been demonstrated on both thermally polarized and hyperpolarized samples. The precipitation step purifies the sample of undesired contaminants, such as free radicals, which were present in the dDNP experiments. For the current case of isotopically enriched fumarate, the relaxation times observed in the solid state are found to be considerably longer at low

magnetic field, which holds promise for the low-field transport of hyperpolarized substances from the point of polarization to the point of use. Additionally, cooling the solid samples to liquid nitrogen temperature increased the T_1. Although this method is likely to be limited in scope to substances with suitable physicochemical characteristics, some suitable cases do exist and are known to be important. Hyperpolarized fumarate is already used for investigations of cancer [17].

At this point the different relaxation behaviour of the suspended particles and the solid precipitate is not understood. One possibility is that amorphous or surface regions of the suspended microcrystals act as relaxation sinks which are brought into contact with the bulk through ^{13}C-^{13}C spin diffusion, driven by the slow tumbling motion of the suspended particles, as in rotational resonance phenomena [180, 181]. This mechanism requires dipole-dipole coupling between nearby ^{13}C nuclei, and would be effectively suppressed in the MAS relaxation experiments. Another possibility is that crystallite molecules are in exchange with the surrounding solution, so that the relaxation rate constant corresponds to a weighted average of the solid and liquid values. However, this mechanism appears to be inconsistent with observations for the wet precipitate, for which the ^{13}C relaxation time is much longer than in the particle suspension and is indistinguishable from that of the dry solid (see above). This provides an intriguing direction for further study.

Chapter 8

Conclusions and Outlook

In this thesis, developments are presented in the field of generating ^{13}C-hyperpolarized metabolites, and extending the lifetime of the hyperpolarization.

Parahydrogen-induced hyperpolarization is an inexpensive method for producing hyperpolarized molecules, and the mild reaction conditions and fast polarization build-up times means hyperpolarized material can be produced under continuous-flow conditions (as opposed to batch-mode). These contrasts to the currently preferred method (dissolution dynamic nuclear polarization) for producing hyperpolarized metabolites for *in vivo* imaging make PHIP an exciting method for future application.

In hydrogenative PHIP reactions, metabolites are formed through direct hydrogenation (i.e. [^{13}C]succinate [21, 24]), and in side-arm hydrogenation procedures (i.e. pyruvate [87, 88]). In both methods, after hydrogenation of the precursor, the proton singlet order needs to be converted into ^{13}C magnetization, which is a more suitable nucleus for *in vivo* imaging.

In chapters 4 and 5, techniques to transform parahydrogen singlet order into ^{13}C magnetization are presented. Chapter 4 describes a method that requires an ultralow magnetic field sweep from a negative value to a positive value. The simplicity of this method holds promise for application to continuous-flow systems for producing hyperpolarized material [182]. Chapter 5 describes the SLIC (Spin-Lock Induced Crossing) and S2hM (Singlet-to-Heteronuclear-Magnetization) rf pulse techniques that are designed to work in high or low magnetic field. The SLIC method induces the polarization transfer faster than S2hM and other 'hard pulse' techniques, which is appealing if the ^{1}H or ^{13}C spins relax rapidly. The S2hM method is robust to pulse offset and B_0 inhomogeneity, which is particularly useful for polarizing large-volume samples, or samples in poorly shimmed magnetic fields.

In chapter 6, the metabolite [^{13}C]fumarate is produced via a PHIP-reaction using a ruthenium catalyst for *trans*-hydrogenation (in contrast to the more common rhodium

cis-addition catalysts). The S2hM sequence was applied to generate hyperpolarized ^{13}C magnetization on [^{13}C]fumarate. This is an important step forward for the production of PHIP-polarized metabolites, because hyperpolarized [^{13}C]fumarate (generated via dDNP) is already being applied clinically [14, 15, 17].

Whether generated via PHIP or dDNP, the application of hyperpolarized [^{13}C]fumarate is limited by the T_1 relaxation time of the ^{13}C spins. In chapter 7, a method is presented for extending the ^{13}C T_1 by temporary precipitation of the sample as a solid. This method is applied to samples hyperpolarized via DNP, and weakly hyperpolarized signals can be observed after more than an hour of precipitate storage time at liquid nitrogen temperature.

Hyperpolarized-NMR is a rapidly growing field of research that has many applications beyond the *in vivo* imaging experiments that have been discussed at length in this thesis. The challenges are to produce hyperpolarized materials cheaply, with ease, and preserve the hyperpolarization beyond typical nonequilibrium nuclear spin lifetimes.

Chapter 9

Appendix I

9.1 Transformation Efficiency

The solid blue lines in Figures 5.6 and 5.7 represent the simulated conversion amplitudes from I-spin (^{1}H) singlet order to S-spin (^{13}C) x-polarization, i.e.

$$a = \langle P_{\mathrm{S}}^{\mathrm{I}} \xrightarrow{U} P_{\mathrm{x}}^{\mathrm{S}} \rangle, \tag{9.1}$$

where $P_{\mathrm{S}}^{\mathrm{I}}$ is the I-spin singlet polarization level operator, $P_{\mathrm{x}}^{\mathrm{S}}$ is the S-spin Zeeman polarization level operator along the x-axis [128], and the transformation amplitude under a unitary propagator U is defined

$$\langle A \xrightarrow{U} B \rangle = \langle U A U^{\dagger} \rightarrow B \rangle. \tag{9.2}$$

In Figures 5.6 and 5.7, the numerically simulated conversion amplitudes a are plotted against parameters such as time, pulse sequence intervals, rf amplitude, and resonance offset, for various procedures. In all cases, $a = 1$ represents complete conversion of I-spin singlet polarization into S-spin x-polarization.

Comparison of these curves with experimental measurements is not straightforward. Although the degree of S-spin x-polarization has a direct correspondence with the integrated amplitude of the S-spin NMR signal, no direct NMR measurement of proton singlet polarization is available.

The results of the four different experiments shown in Fig. 9.1 were used to obtain a calibrated measurement of the conversion amplitudes from I-spin singlet order to S-spin x-polarization. All experiments conclude with detection of the S-spin (^{13}C) NMR signal, so that their amplitudes are directly comparable.

Experiment ① involves direct excitation of thermal equilibrium S-spin magnetization and detection of the S-spin signal under I-spin decoupled conditions. The integrated

signal amplitude is given by

$$a_{①} = f p^{\mathrm{eq}}_{\mathrm{S_z}}, \tag{9.3}$$

assuming that enough time is left between transients for full thermal equilibration, as was the case here. $p^{\mathrm{eq}}_{\mathrm{S_z}}$ is the thermal equilibrium S-spin polarization level (defined in Eq. 2.2). The instrumental factor f is common to all four experiments.

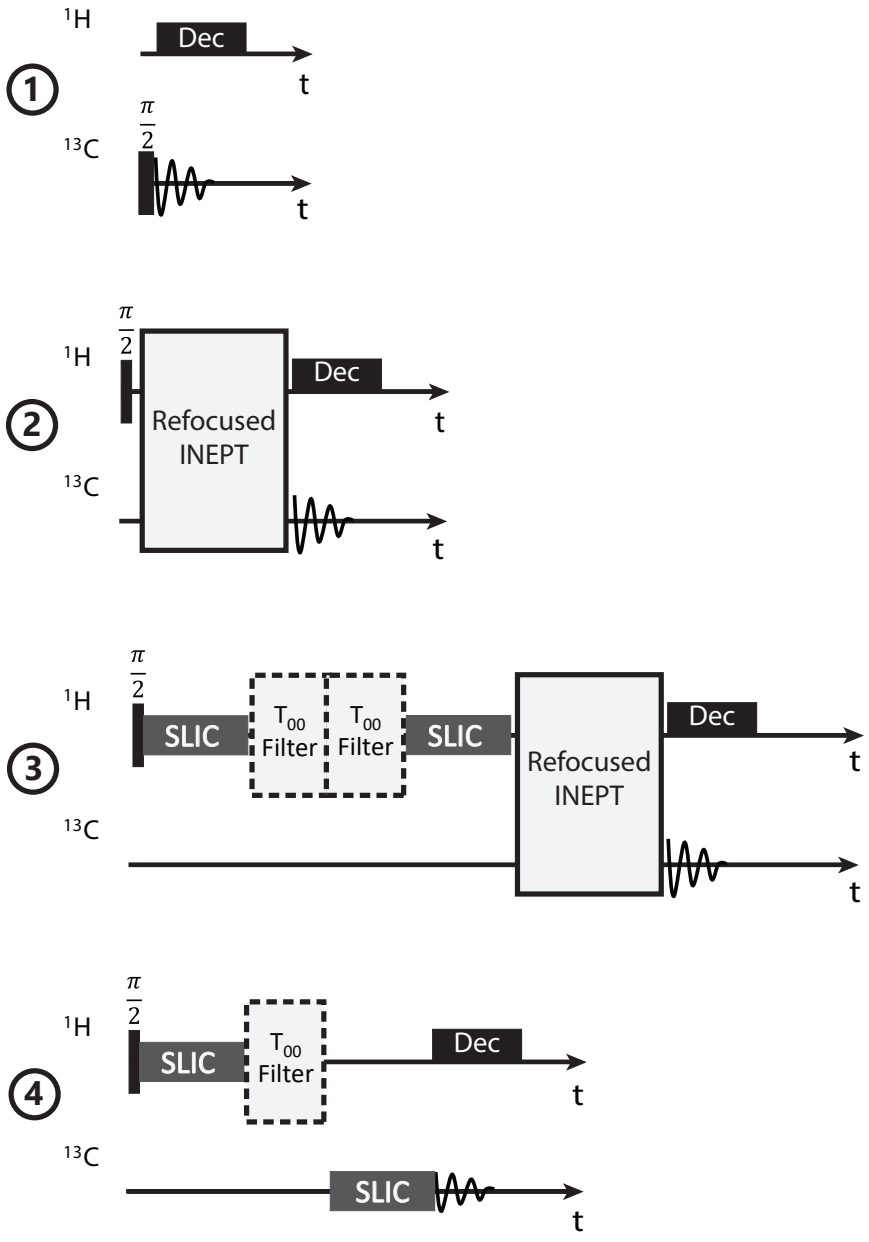

FIGURE 9.1: Pulse sequences used to calibrate the conversion amplitude of the ^{13}C SLIC pulse. Details of the INEPT (Insensitive Nuclei Enhanced by Polarization Transfer) pulse scheme are included in Appendix I. 9.2.5.

Experiment ② involves conversion of thermal equilibrium I-spin magnetization into S-spin magnetization by a refocused INEPT method, followed by S-spin detection.

The INEPT pulse sequence and relevant parameters are given in Appendix I. 9.2.5. The integrated signal amplitude is given by

$$a_{②} = f p_{\mathrm{I_z}}^{\mathrm{eq}} \langle P_{\mathrm{z}}^{\mathrm{I}} \xrightarrow{\mathrm{INEPT}} P_{\mathrm{z}}^{\mathrm{S}} \rangle, \tag{9.4}$$

where the INEPT transformation of I-spin polarization into S-spin polarization has a maximal amplitude of 1. The experimental INEPT conversion amplitude may be determined by comparing the signal amplitudes in these two experiments:

$$\langle P_{\mathrm{z}}^{\mathrm{I}} \xrightarrow{\mathrm{INEPT}} P_{\mathrm{z}}^{\mathrm{S}} \rangle_{\mathrm{exp}} = \frac{p_{\mathrm{S_z}}^{\mathrm{eq}}}{p_{\mathrm{I_z}}^{\mathrm{eq}}} \times \frac{a_{②}}{a_{①}} = \frac{\gamma_{\mathrm{S}}}{\gamma_{\mathrm{I}}} \frac{a_{②}}{a_{①}}. \tag{9.5}$$

The experimental INEPT conversion amplitude was found to be ∼0.67 in these experiments.

Experiment ③ involves generation of I-spin singlet order from thermal I-spin z-polarization using a SLIC scheme, followed by suppression of other density operator components using a T_{00} filter (see Appendix I. 9.2.6 for the implementation), followed by another filtration step and reconversion to I-spin z-polarization, INEPT transfer to S-spin polarization, and detection. The integrated signal amplitude is given by

$$a_{③} = f p_{\mathrm{I_z}}^{\mathrm{eq}} \langle P_{\mathrm{z}}^{\mathrm{I}} \xrightarrow{\mathrm{SLIC^I}} P_{\mathrm{S}}^{\mathrm{I}} \rangle \langle P_{\mathrm{S}}^{\mathrm{I}} \xrightarrow{\mathrm{SLIC^I}} P_{\mathrm{z}}^{\mathrm{I}} \rangle \langle P_{\mathrm{z}}^{\mathrm{I}} \xrightarrow{\mathrm{INEPT}} P_{\mathrm{z}}^{\mathrm{S}} \rangle, \tag{9.6}$$

where the T_{00} filters have been implicitly included in $\mathrm{SLIC^I}$, for the sake of brevity.

It has been shown by Levitt that the maximum transformation amplitude $\langle P_{\mathrm{S}}^{\mathrm{I}} \rightarrow P_{\mathrm{z}}^{\mathrm{I}} \rangle$ is 2/3 [183], and hence

$$a_{③} = \frac{3}{2} f p_{\mathrm{I_z}}^{\mathrm{eq}} \left| \langle P_{\mathrm{z}}^{\mathrm{I}} \xrightarrow{\mathrm{SLIC^I}} P_{\mathrm{S}}^{\mathrm{I}} \rangle \right|^2 \langle P_{\mathrm{z}}^{\mathrm{I}} \xrightarrow{\mathrm{INEPT}} P_{\mathrm{z}}^{\mathrm{S}} \rangle. \tag{9.7}$$

This leads to

$$\frac{a_{③}}{a_{②}} = \frac{3}{2} \left| \langle P_{\mathrm{z}}^{\mathrm{I}} \xrightarrow{\mathrm{SLIC^I}} P_{\mathrm{S}}^{\mathrm{I}} \rangle \right|^2. \tag{9.8}$$

The experimental amplitude ratio was found to be ③/② = 0.24 which gives an experimental transformation amplitude $\langle P_{\mathrm{z}}^{\mathrm{I}} \rightarrow P_{\mathrm{S}}^{\mathrm{I}} \rangle = 0.4$ for the conversion of thermal I-spin z-polarization into I-spin singlet order by the I-spin SLIC sequence, followed by T_{00} filtering. This should be compared with the theoretical maximum of 2/3.

Experiment ④ involves generation of I-spin singlet order from thermal I-spin z-polarization using a I-spin SLIC scheme, followed by a T_{00} filter and conversion into S-spin polarization using a S-spin SLIC scheme. The integrated signal amplitude is given by

$$a_{④} = f p_{\mathrm{I_z}}^{\mathrm{eq}} \langle P_{\mathrm{z}}^{\mathrm{I}} \xrightarrow{\mathrm{SLIC^I}} P_{\mathrm{S}}^{\mathrm{I}} \rangle \langle P_{\mathrm{S}}^{\mathrm{I}} \xrightarrow{\mathrm{SLIC^S}} P_{\mathrm{z}}^{\mathrm{S}} \rangle. \tag{9.9}$$

The transformation amplitude for the S-spin SLIC sequence may therefore be derived from the experimental amplitudes as follows:

$$\langle P_S^I \xrightarrow{\text{SLIC}^S} P_z^S \rangle = \sqrt{\frac{3}{2}} \frac{\gamma_S}{\gamma_I} \frac{a④}{a①} \sqrt{\frac{a②}{a③}}. \tag{9.10}$$

These are the experimental points plotted in Figures 5.6 and 5.7.

9.2 Pulse Sequences

9.2.1 SLIC Transfer Sequence

^{13}C SLIC duration and amplitude optimizations were performed with the pulse sequence detailed in Fig. 9.2. Pulse phases are denoted by letters, and specified in Table 9.1.

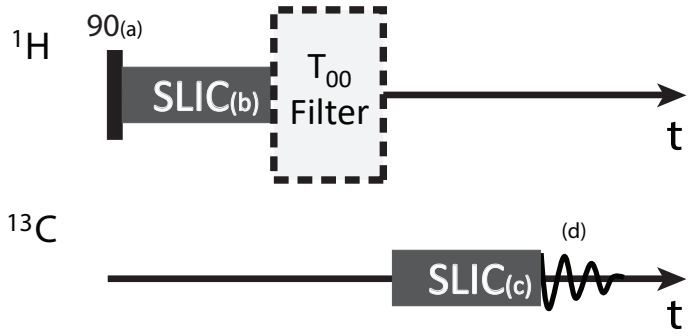

FIGURE 9.2: Pulse sequence used for SLIC optimization. Events a-d are indicated in parentheses.

Event	Event Description	Phase
a	^{1}H 90	0, 180
b	^{1}H SLIC	90
c	^{13}C SLIC	90
d	Acquire	0, 180

TABLE 9.1: Phase cycle used to ensure the observed signal came through the proton channel.

9.2.2 S2hM Transfer Sequence

S2hM delay and loop optimizations were performed with the pulse sequence in Fig. 9.3. The pulse phases are given by letters, and specified in Table 9.2.

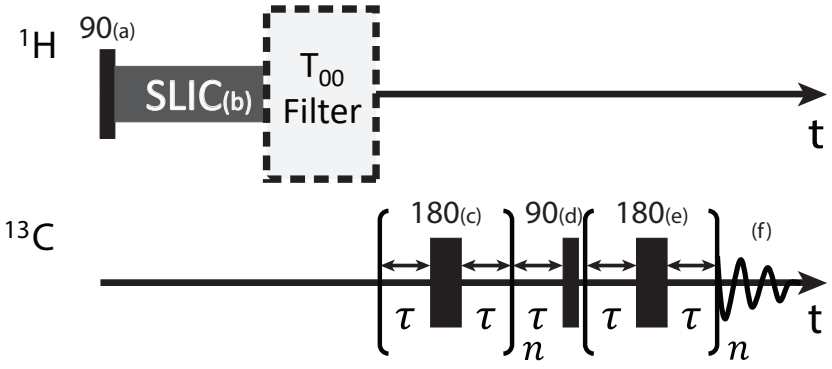

FIGURE 9.3: Pulse sequence used for S2hM optimization. Events a-f are indicated in parentheses.

Event	Event Description	Phase
a	^{1}H 90	0, 180
b	^{1}H SLIC	90
c	^{13}C Composite 180 (90, 180, 90)	(0, 90, 0)
d	^{13}C 90	90
e	^{13}C Composite 180 (90, 180, 90)	(0, 90, 0)
f	Acquire	0, 180

TABLE 9.2: Phase cycle used to ensure the observed signal came through the proton channel.

9.2.3 Goldman Transfer Sequence

Goldman sequence offset dependence experiments were performed with the pulse sequence in Fig. 9.4. The pulse phases are given by letters, and specified in Table 9.3.

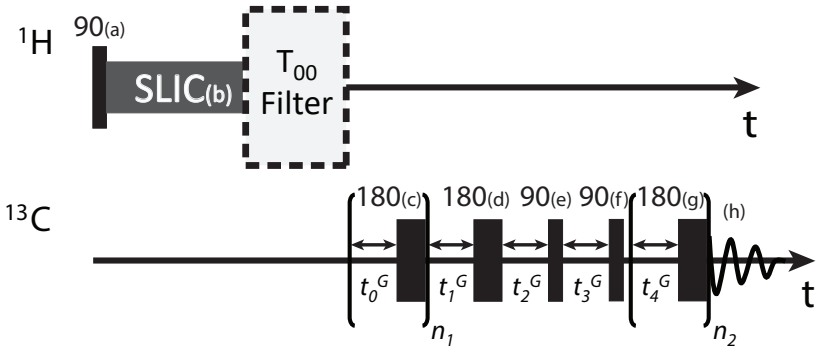

FIGURE 9.4: Pulse sequence used for Goldman sequence optimization. Events a-h are indicated in parentheses. Delays used were $t_0^G = t_1^G = t_3^G = t_4^G = 31.6\,\text{ms}$, $t_2^G = 15.8\,\text{ms}$. $n_1 = 5$, $n_2 = 7$.

Event	Event Description	Phase
a	^{1}H 90	0, 180
b	^{1}H SLIC	90
c	^{13}C Composite 180 (90, 180, 90)	(0, 90, 0)
d	^{13}C Composite 180 (90, 180, 90)	(0, 90, 0)
e	^{13}C 90	0
f	^{13}C 90	90
g	^{13}C Composite 180 (90, 180, 90)	(0, 90, 0)
h	Acquire	0, 180

TABLE 9.3: Phase cycle used to ensure the observed signal came through the proton channel.

9.2.4 Kadlecek 2b Transfer Sequence

Kadlecek 2b sequence offset dependence experiments were performed with the pulse sequence in Fig. 9.5. The pulse phases are given by letters, and specified in Table 9.4.

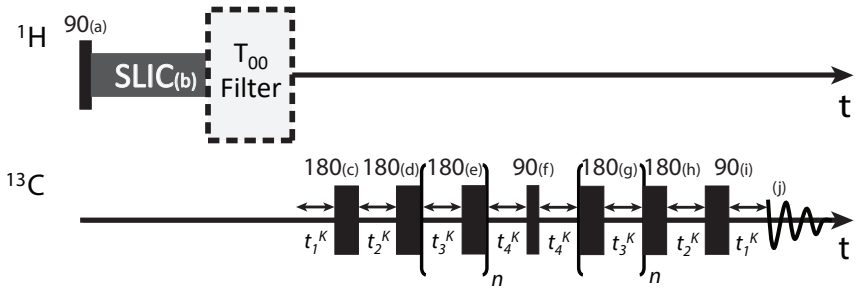

FIGURE 9.5: Pulse sequence used for Kadlecek 2b sequence optimization. Events a-j are indicated in parentheses. Delays used were $t_1^K = t_2^K = t_3^K = 31.6\,\text{ms}$, $t_4^K = 7.9\,\text{ms}$. $n = 5$.

Event	Event Description	Phase
a	^{1}H 90	0, 180
b	^{1}H SLIC	90
c	^{13}C Composite 180 (90, 180, 90)	(0, 90, 0)
d	^{13}C Composite 180 (90, 180, 90)	(0, 90, 0)
e	^{13}C Composite 180 (90, 180, 90)	(0, 90, 0)
f	^{13}C 90	90
g	^{13}C Composite 180 (90, 180, 90)	(0, 90, 0)
h	^{13}C Composite 180 (90, 180, 90)	(0, 90, 0)
i	^{13}C Composite 180 (90, 180, 90)	(0, 90, 0)
j	Acquire	0, 180

TABLE 9.4: Phase cycle used to ensure the observed signal came through the proton channel.

9.2.5 Refocused INEPT

The refocused INEPT sequence is shown in Fig. 9.6.

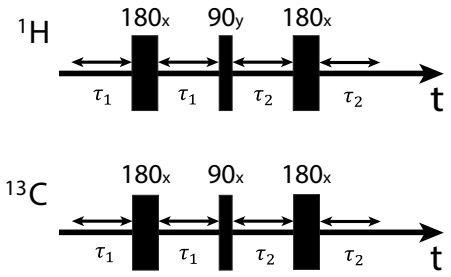

FIGURE 9.6: The refocused INEPT block used in the Fig. 9.1 pulse sequences. The pulse phases assume the initial 90 pulse on the proton channel has phase x. The evolution delays used were $\tau_1 = 51\,\text{ms}$ and $\tau_2 = 34\,\text{ms}$. The values were determined by the formulae $\tau_1 = 1/4J_{\text{CH}}$ and $\tau_2 = 1/6J_{\text{CH}}$, where the average proton-carbon J coupling of 4.9 Hz was used. Using a refocused INEPT allows us to decouple on the proton channel during acquisition.

9.2.6 T_{00} Filter

The T_{00} gradient filter used in experiments only allows NMR signals passing through singlet order to be observed. The T_{00} filter sequence is shown in full in Fig. 9.7. The relevant paraneters are summarized in Table 9.5.

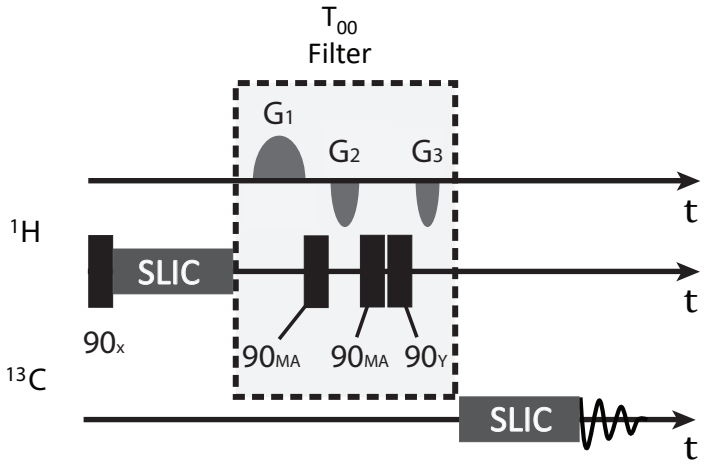

FIGURE 9.7: Graphical depiction of the T_{00} filter used to remove proton magnetization. MA indicates a phase at the *magic angle*, 54.7°.

PFG	Shape	Strength / G cm^{-1}	Duration / ms
G1	SINE.100	10	8.8
G2	SINE.100	-10	4.8
G3	SINE.100	-15	4.0

TABLE 9.5: Parameters used for the T_{00} filter.

Chapter 10

Appendix II

This Appendix contains the SpinDynamica code used to generate many of the figures in this thesis. The following documents are included:

- Introduction trajectory simulations
- Field sweep simulations
- S-spin SLIC polarization levels
- S2hM 3D representation
- Fumarate S2hM and SLIC simulations
- S2B2M methyl ^{13}C polarization
- Trans-hydrogenative PHIP spectrum

Introduction trajectory simulations

```
In[•]:= Needs["SpinDynamica`"]
```

```
SpinDynamica version 3.3.2 loaded
```

SetUserLevel: The user level is being initialized to 2. The user level may be set to an integer between 1 and 3 by using SetUserLevel[level]. Low user levels provide strong syntax trapping at the expense of slow execution for some routines. High user levels relax the syntax trapping in order to provide better execution speeds.

SetUserLevel: The user level has been set to 2.

SetUserLevel: Additional definitions have been given to the following symbols:
{Dot, Exp, Expand, Plus, Power, Simplify, Times, WignerD}

```
In[•]:= SetSpinSystem[1]
```

SetSpinSystem: the spin system has been set to $\left\{\left\{1, \frac{1}{2}\right\}\right\}$

SetBasis: the state basis has been set to ZeemanBasis$\left[\left\{\left\{1, \frac{1}{2}\right\}\right\}, \text{BasisLabels} \to \text{Automatic}\right]$.

```
In[•]:= ρeq = ThermalEquilibriumDensityOperator[LarmorFrequency[1, 11.7] opI[1, "z"], 300]
Out[•]= Operator[ << .. >> , OperatorType → Hermitian ]
```

Rotations

```
In[•]:= {trajx, trajy, trajz} =
 Trajectory[10 000 ρeq → {opI[1, "x"] / 2, opI[1, "y"] / 2, opI[1, "z"] / 2}, {{None, 10}},
  BackgroundGenerator → CombineGenerators[2 π 3 opI[1, "z"], ThermalizeSuperoperator[
     PhenomenologicalRelaxationSuperoperator[{1, 1, 0.7}], opI[1, "z"], 300]]]
```

SetOperatorBasis: the operator basis has been set to ShiftAndZOperatorBasis$\left[\left\{\left\{1, \frac{1}{2}\right\}\right\}, \text{Sorted} \to \text{CoherenceOrder}\right]$.

```
Out[•]= {TrajectoryFunction[ {{0, 10.}} , <>],
 TrajectoryFunction[ {{0, 10.}} , <>], TrajectoryFunction[ {{0, 10.}} , <>]}
```

In[•]:=
```
Show[SphereAndAxes[], ParametricPlot3D[{trajx[t], trajy[t], trajz[t]},
  {t, 0, 12}, PlotRange → {{-0.6, 0.6}, {-0.6, 0.6}, {-0.6, 0.6}},
  PlotStyle → {Blue, Thickness[0.015]}],
 Arrow3D[{0, 0, 0}, Directive → {Blue, Thickness[0.006]}], Boxed → False, ImageSize → 200]
```

Out[•]=

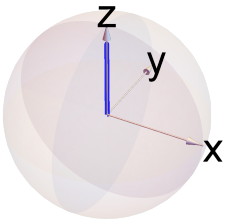

In[•]:=
```
{trajx, trajy, trajz} =
 Trajectory[10000 ρeq → {opI[1, "x"] / 2, opI[1, "y"] / 2, opI[1, "z"] / 2},
  {RotationSuperoperator[1, {π / 2, "y"}], {None, 1}},
  BackgroundGenerator → CombineGenerators[2 π 0 opI[1, "z"], ThermalizeSuperoperator[
     PhenomenologicalRelaxationSuperoperator[{1, 1, 0.7}], opI[1, "z"], 300]]]
```

Out[•]=
```
{TrajectoryFunction[ {{0, 1.}} , <>],
 TrajectoryFunction[ {{0, 1.}} , <>], TrajectoryFunction[ {{0, 1.}} , <>]}
```

In[•]:=
```
Show[SphereAndAxes[], ParametricPlot3D[{trajx[t], trajy[t], trajz[t]},
  {t, 0, 12}, PlotRange → {{-0.6, 0.6}, {-0.6, 0.6}, {-0.6, 0.6}},
  PlotStyle → {Blue, Thickness[0.015]}],
 Arrow3D[{0, 0, 0}, Directive → {Blue, Thickness[0.006]}], Boxed → False, ImageSize → 200]
```

Out[•]=

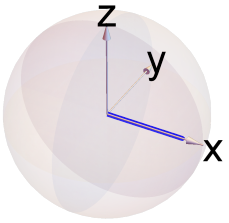

```
In[•]:= {trajx, trajy, trajz} =
         Trajectory[10 000 ρeq → {opI[1, "x"] / 2, opI[1, "y"] / 2, opI[1, "z"] / 2},
          {RotationSuperoperator[1, {π / 2, "y"}],
           RotationSuperoperator[1, {π / 3, "z"}], {None, 1}},
          BackgroundGenerator → CombineGenerators[2 π 0 opI[1, "z"], ThermalizeSuperoperator[
             PhenomenologicalRelaxationSuperoperator[{1, 1, 0.7}], opI[1, "z"], 300]]]

Out[•]= {TrajectoryFunction[ {{0, 1.}} , <>],
         TrajectoryFunction[ {{0, 1.}} , <>], TrajectoryFunction[ {{0, 1.}} , <>]}
```

```
In[•]:= Show[SphereAndAxes[], ParametricPlot3D[{trajx[t], trajy[t], trajz[t]},
          {t, 0, 12}, PlotRange → {{-0.6, 0.6}, {-0.6, 0.6}, {-0.6, 0.6}},
          PlotStyle → {Blue, Thickness[0.015]}],
         Arrow3D[{0, 0, 0}, Directive → {Blue, Thickness[0.006]}], Boxed → False, ImageSize → 200]
```

Out[•]=

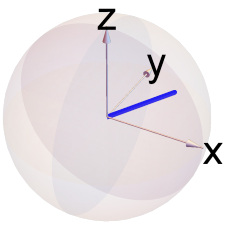

Pulse acquire

```
In[•]:= {trajx, trajy, trajz} =
         Trajectory[10 000 ρeq → {opI[1, "x"] / 2, opI[1, "y"] / 2, opI[1, "z"] / 2}, {{None, 10}},
          BackgroundGenerator → CombineGenerators[2 π 3 opI[1, "z"], ThermalizeSuperoperator[
             PhenomenologicalRelaxationSuperoperator[{1, 1, 0.7}], opI[1, "z"], 300]]]

Out[•]= {TrajectoryFunction[ {{0, 10.}} , <>],
         TrajectoryFunction[ {{0, 10.}} , <>], TrajectoryFunction[ {{0, 10.}} , <>]}
```

```
In[•]:= Show[SphereAndAxes[], ParametricPlot3D[{trajx[t], trajy[t], trajz[t]},
          {t, 0, 12}, PlotRange → {{-0.6, 0.6}, {-0.6, 0.6}, {-0.6, 0.6}},
          PlotStyle → {Blue, Thickness[0.005]}],
         Arrow3D[{0, 0, 0}, Directive → {Blue, Thickness[0.006]}], Boxed → False, ImageSize → 200]
```

Out[•]=

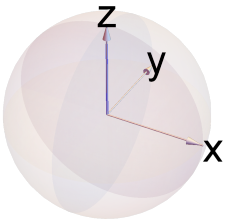


```
In[•]:= {trajx, trajy, trajz} =
         Trajectory[10000 ρeq → {opI[1, "x"] / 2, opI[1, "y"] / 2, opI[1, "z"] / 2},
          {{2 π 0.25 opI[1, "y"], 1}}, BackgroundGenerator → 0]
Out[•]= {TrajectoryFunction[ {{0, 1.}} , <>],
         TrajectoryFunction[ {{0, 1.}} , <>], TrajectoryFunction[ {{0, 1.}} , <>]}

In[•]:= Show[SphereAndAxes[], ParametricPlot3D[{trajx[t], trajy[t], trajz[t]},
          {t, 0, 12}, PlotRange → {{-0.6, 0.6}, {-0.6, 0.6}, {-0.6, 0.6}},
          PlotStyle → {Blue, Thickness[0.005]}], Boxed → False, ImageSize → 200]
```

Out[•]=

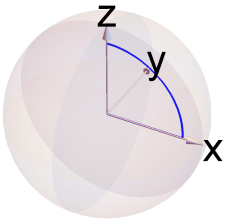


```
In[•]:= {trajx, trajy, trajz} =
         Trajectory[10000 ρeq → {opI[1, "x"] / 2, opI[1, "y"] / 2, opI[1, "z"] / 2},
          {RotationSuperoperator[1, {π / 2, "y"}], {None, 12}},
          BackgroundGenerator → CombineGenerators[2 π 3 opI[1, "z"],
            ThermalizeSuperoperator[PhenomenologicalRelaxationSuperoperator[{1, 1, 0.6}],
             LarmorFrequency[1, 11.7] opI[1, "z"], 300]]]
Out[•]= {TrajectoryFunction[ {{0, 12.}} , <>],
         TrajectoryFunction[ {{0, 12.}} , <>], TrajectoryFunction[ {{0, 12.}} , <>]}
```

```
In[•]:= Plot[{trajx[t] / trajx[0], trajz[t] / trajz[12]},
          {t, 0, 5}, PlotRange → {{0, 5}, {-1.1, 1.1}}, ImageSize → 200]
```

Out[•]=

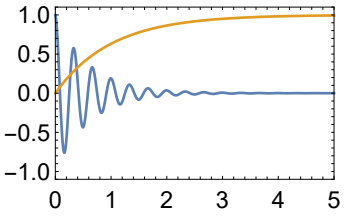


```
In[•]:= Plot[trajz[t] / trajz[12], {t, 0, 5}, PlotRange → {{0, 5}, {-1.1, 1.1}}, ImageSize → 200]
```

Out[•]=

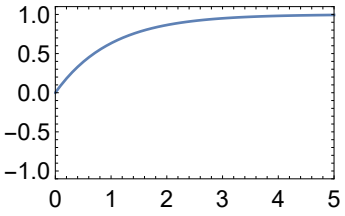

Inversion recovery

Stage 1

```
In[•]:= {trajx1, trajy1, trajz1} =
         Trajectory[10 000 ρeq → {opI[1, "x"] / 2, opI[1, "y"] / 2, opI[1, "z"] / 2},
          {RotationSuperoperator[1, {π, "y"}], {None, 10}},
          BackgroundGenerator → CombineGenerators[2 π 3 opI[1, "z"], ThermalizeSuperoperator[
             PhenomenologicalRelaxationSuperoperator[{1, 1, 0.7}], opI[1, "z"], 300]]]
```

```
Out[•]= {TrajectoryFunction[ {{0, 10.}} , <>],
         TrajectoryFunction[ {{0, 10.}} , <>], TrajectoryFunction[ {{0, 10.}} , <>]}
```

```
In[•]:= Show[SphereAndAxes[], ParametricPlot3D[{trajx1[t], trajy1[t], trajz1[t]},
          {t, 0, 10}, PlotRange → {{-0.6, 0.6}, {-0.6, 0.6}, {-0.6, 0.6}},
          PlotStyle → {Blue, Thickness[0.015]}],
         Arrow3D[{0, 0, 0}, Directive → {Blue, Thickness[0.006]}], Boxed → False, ImageSize → 200]
```

Out[•]=

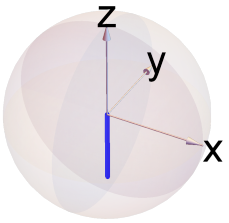

Stage 2

```
In[•]:= {trajx2, trajy2, trajz2} =
         Trajectory[3000 ρeq → {opI[1, "x"] / 2, opI[1, "y"] / 2, opI[1, "z"] / 2},
          {RotationSuperoperator[1, {π, "y"}], {None, 10}},
          BackgroundGenerator → CombineGenerators[2 π 3 opI[1, "z"], ThermalizeSuperoperator[
             PhenomenologicalRelaxationSuperoperator[{1, 1, 0.7}], opI[1, "z"], 300]]]
```

Out[•]= {TrajectoryFunction[{{0, 10.}} , <>],
TrajectoryFunction[{{0, 10.}} , <>], TrajectoryFunction[{{0, 10.}} , <>]}

```
In[•]:= Show[SphereAndAxes[], ParametricPlot3D[{trajx2[t], trajy2[t], trajz2[t]},
          {t, 0, 10}, PlotRange → {{-0.6, 0.6}, {-0.6, 0.6}, {-0.6, 0.6}},
          PlotStyle → {Blue, Thickness[0.015]}],
         Arrow3D[{0, 0, 0}, Directive → {Blue, Thickness[0.006]}], Boxed → False, ImageSize → 200]
```

Out[•]=

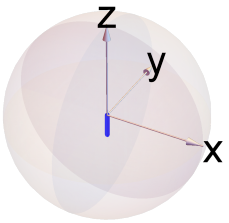

Stage 3

```
In[•]:= {trajx3, trajy3, trajz3} =
         Trajectory[3000 ρeq → {opI[1, "x"] / 2, opI[1, "y"] / 2, opI[1, "z"] / (10 / 1.5)},
          {RotationSuperoperator[1, {-π / 2, "y"}], {None, 12}},
          BackgroundGenerator → CombineGenerators[2 π 3 opI[1, "z"],
            ThermalizeSuperoperator[PhenomenologicalRelaxationSuperoperator[{1, 1, 0.6}],
             LarmorFrequency[1, 11.7] opI[1, "z"], 300]]]

Out[•]= {TrajectoryFunction[ {{0, 12.}} , <>],
         TrajectoryFunction[ {{0, 12.}} , <>], TrajectoryFunction[ {{0, 12.}} , <>]}
```

```
In[•]:= Show[SphereAndAxes[], ParametricPlot3D[{trajx3[t], trajy3[t], trajz3[t]},
          {t, 0, 12}, PlotRange → {{-0.6, 0.6}, {-0.6, 0.6}, {-0.6, 0.6}},
          PlotStyle → {Blue, Thickness[0.005]}], Boxed → False, ImageSize → 200]
```

Out[•]=

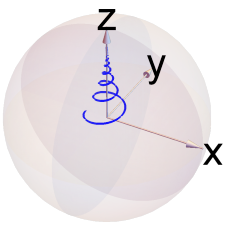

Saturation recovery

Stage 1

```
In[•]:= {trajx1, trajy1, trajz1} =
         Trajectory[1 ρeq → {opI[1, "x"] / 2, opI[1, "y"] / 2, opI[1, "z"] / 2},
          {RotationSuperoperator[1, {π, "y"}], {None, 10}},
          BackgroundGenerator → CombineGenerators[2 π 3 opI[1, "z"], ThermalizeSuperoperator[
             PhenomenologicalRelaxationSuperoperator[{1, 1, 0.7}], opI[1, "z"], 300]]]

Out[•]= {TrajectoryFunction[ {{0, 10.}} , <>],
         TrajectoryFunction[ {{0, 10.}} , <>], TrajectoryFunction[ {{0, 10.}} , <>]}
```

```
In[•]:= Show[SphereAndAxes[], ParametricPlot3D[{trajx1[t], trajy1[t], trajz1[t]},
          {t, 0, 10}, PlotRange → {{-0.6, 0.6}, {-0.6, 0.6}, {-0.6, 0.6}},
          PlotStyle → {Blue, Thickness[0.015]}],
         Arrow3D[{0, 0, 0}, Directive → {Blue, Thickness[0.006]}], Boxed → False, ImageSize → 200]
```

Out[•]=

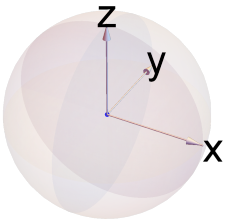

Stage 2

```
In[•]:= {trajx2, trajy2, trajz2} =
         Trajectory[5000 ρeq → {opI[1, "x"] / 2, opI[1, "y"] / 2, opI[1, "z"] / 2}, {{None, 10}},
          BackgroundGenerator → CombineGenerators[2 π 3 opI[1, "z"], ThermalizeSuperoperator[
             PhenomenologicalRelaxationSuperoperator[{1, 1, 0.7}], opI[1, "z"], 300]]]
```

```
Out[•]= {TrajectoryFunction[ {{0, 10.}} , <>],
         TrajectoryFunction[ {{0, 10.}} , <>], TrajectoryFunction[ {{0, 10.}} , <>]}
```

```
In[•]:= Show[SphereAndAxes[], ParametricPlot3D[{trajx2[t], trajy2[t], trajz2[t]},
          {t, 0, 10}, PlotRange → {{-0.6, 0.6}, {-0.6, 0.6}, {-0.6, 0.6}},
          PlotStyle → {Blue, Thickness[0.015]}],
         Arrow3D[{0, 0, 0}, Directive → {Blue, Thickness[0.006]}], Boxed → False, ImageSize → 200]
```

Out[•]=

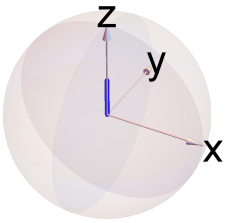

Stage 3

```
In[•]:= {trajx3, trajy3, trajz3} =
         Trajectory[5000 ρeq → {opI[1, "x"] / 2, opI[1, "y"] / 2, opI[1, "z"] / 4},
          {RotationSuperoperator[1, {π / 2, "y"}], {None, 12}},
          BackgroundGenerator → CombineGenerators[2 π 3 opI[1, "z"],
            ThermalizeSuperoperator[PhenomenologicalRelaxationSuperoperator[{1, 1, 0.6}],
             LarmorFrequency[1, 11.7] opI[1, "z"], 300]]]

Out[•]= {TrajectoryFunction[ {{0, 12.}} , <>],
         TrajectoryFunction[ {{0, 12.}} , <>], TrajectoryFunction[ {{0, 12.}} , <>]}

In[•]:= Show[SphereAndAxes[], ParametricPlot3D[{trajx3[t], trajy3[t], trajz3[t]},
          {t, 0, 12}, PlotRange → {{-0.6, 0.6}, {-0.6, 0.6}, {-0.6, 0.6}},
          PlotStyle → {Blue, Thickness[0.005]}], Boxed → False, ImageSize → 200]
```

Out[•]=

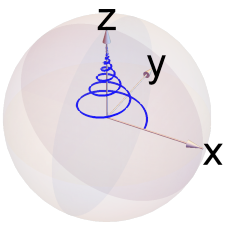

Field sweep simulations

Setup

```
In[•]:= Needs["SpinDynamica`"]
```

```
SpinDynamica version 3.3.2 loaded
```

SetUserLevel: The user level is being initialized to 2. The user level may be set to an integer between 1 and 3 by using SetUserLevel[level]. Low user levels provide strong syntax trapping at the expense of slow execution for some routines. High user levels relax the syntax trapping in order to provide better execution speeds.

SetUserLevel: The user level has been set to 2.

SetUserLevel: Additional definitions have been given to the following symbols:
{Dot, Exp, Expand, Plus, Power, Simplify, Times, WignerD}

```
In[•]:= SetSpinSystem[3]
```

SetSpinSystem: the spin system has been set to $\left\{\left\{1, \frac{1}{2}\right\}, \left\{2, \frac{1}{2}\right\}, \left\{3, \frac{1}{2}\right\}\right\}$

SetBasis: the state basis has been set to ZeemanBasis$\left[\left\{\left\{1, \frac{1}{2}\right\}, \left\{2, \frac{1}{2}\right\}, \left\{3, \frac{1}{2}\right\}\right\}, \text{BasisLabels} \to \text{Automatic}\right]$.

```
In[•]:= H[B_] := 2 π J12 opI[1].opI[2] + 2 π J13 opI[1].opI[3] + 2 π J23 opI[2].opI[3] +
          LarmorFrequency[1, B] opI[{1, 2}, "z"] + LarmorFrequency[13, B] opI[{3}, "z"]
```

Thermal equilibrium 13C spectrum

```
In[•]:= sig1 = Signal1D[{{2 π 100, "2k"}},
          Preparation → RotationSuperoperator[3, {π / 2, "x"}], InitialDensityOperator →
           ThermalEquilibriumDensityOperator[H[1] /. {J12 → 12.2, J13 → 13.6, J23 → 2.1}, 298],
          Observable → {3}, BackgroundGenerator → 2 π 12.2 opI[1].opI[2] +
            2 π 13.6 opI[1, "z"].opI[3, "z"] + 2 π 2.1 opI[2, "z"].opI[3, "z"]];
```

Signal1D: Using SignalCalculationMethod → Diagonalization

Signal1D: Using LineBroadening → $2\pi \times 71.6457 \times 10^{-3}$ rad s^{-1}.

```
In[•]:= ListPlot[Re@FT[sig1], PlotRange → {All, All}, PlotStyle → Blue]
```

Out[•]=

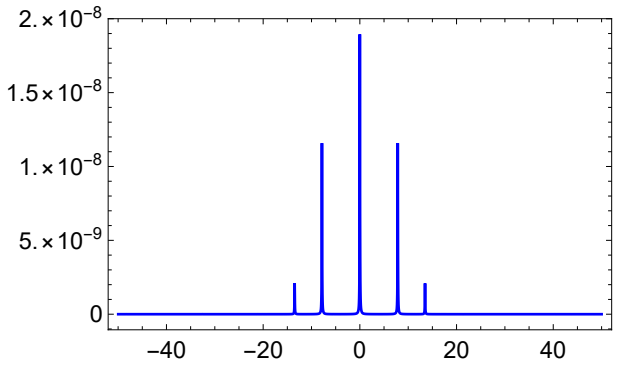

Eigenvalues plot

```
In[•]:= {evalset, evecset} =
  CorrelatedEigensystems[H[B] /. {J12 → 12, J13 → 1, J23 → 0}, {B, -1 * 10^-6, 1 * 10^-6, 10^-8}];
```

```
In[•]:= ListPlot[evalset, PlotLegends → Automatic]
```

Out[•]=

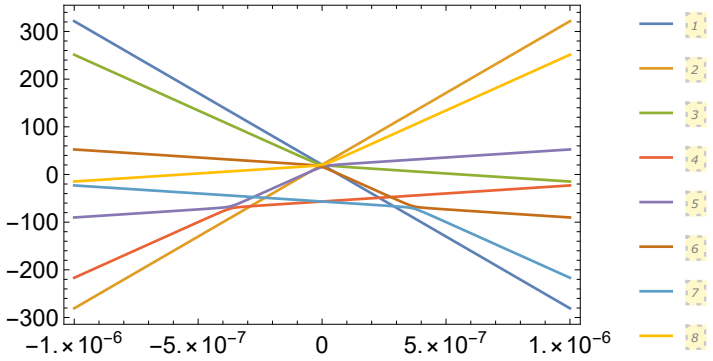

13C spectrum after sweep

```
In[•]:= ρini = Secularize[SingletPolarizedDensityOperator[{1, 2}],
    H[2 * 10^-6] /. {J12 → 12.2, J13 → 13.6, J23 → 2.1}];
```

SetOperatorBasis: the operator basis has been set to ShiftAndZOperatorBasis[{{1, 1/2}, {2, 1/2}, {3, 1/2}}, Sorted → CoherenceOrder].

```
In[•]:= OperatorAmplitude[ρini → SingletPolarizedDensityOperator[{1, 2}]]
```

```
Out[•]= 0.899204
```

```
In[•]:= Γrandterm[i_, j_] := -κ[i, j] τΘ
  Sum[DoubleCommutationSuperoperator[Adjoint[opT[i, {1, m}]], opT[j, {1, m}]], {m, -1, 1}]
```

```
In[•]:= κ[i_, i_] := 1;
  κ[i_, j_] := .9;
```

```
In[•]:= Γrand = Sum[Γrandterm[i, j], {i, 1, 2}, {j, 1, 2}];

In[•]:= Γnum = Γrand /. {τC → 10^-11, τθ → 1.05} // N // Superoperator
Out[•]= Superoperator[<<..>>, SuperoperatorType→ Undefined ]

In[•]:= sweep = Function[{B0a, B0b, T, t}, B0a + t / T (B0b - B0a)];

In[•]:= Lsweep = Function[t, Evaluate[Superoperator[
          Γnum - I * (CommutationSuperoperator@H[sweep[-2 * 10^-6, 2 * 10^-6, Tsweep, t]] /.
              {J12 → 12.2, J13 → 13.6, J23 → 2.1})]]]
Out[•]= Function[t, Superoperator[<<..>>, SuperoperatorType→ Undefined ]]

In[•]:= matfunc = Function[t, Evaluate@SuperoperatorMatrixRepresentation[Lsweep[t]]]
Out[•]= Function[t, SparseArray[ 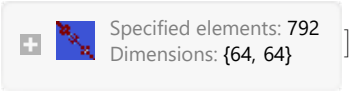
                                 Specified elements: 792
                                 Dimensions: {64, 64} ]]

In[•]:= Tsweep = 1000 * 10^-3;
        ρfunc = ρ /. First@NDSolve[{ρ'[t] == matfunc[t].ρ[t],
              ρ[0] == Normal@OperatorVectorRepresentation[ρini]}, ρ, {t, 0, Tsweep}]
Out[•]= InterpolatingFunction[ 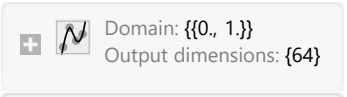
                               Domain: {{0., 1.}}
                               Output dimensions: {64}
                                ]

In[•]:= ρ1 = Operator[SparseArray@ρfunc[Tsweep], OperatorBasis[], ZeemanBasis[]]
        ρfinal = Secularize[ρ1 + 0.4 SingletPolarizedDensityOperator[{1, 2}],
          H[50 * 10^-6] /. {J12 → 12.2, J13 → 13.6, J23 → 2.1}]
Out[•]= Operator[SparseArray[ 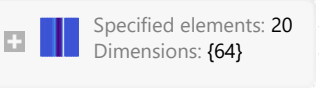
                              Specified elements: 20
                              Dimensions: {64} ],

        ShiftAndZOperatorBasis[{{1, 1/2}, {2, 1/2}, {3, 1/2}}, Sorted → CoherenceOrder],

        ZeemanBasis[{{1, 1/2}, {2, 1/2}, {3, 1/2}}, BasisLabels → Automatic]]

Out[•]= -0.0648951 (I1⁻•I2⁺) - 0.0005031 (I1⁻•I3⁺) - 0.0648951 (I1⁺•I2⁻) - 0.0005031 (I1⁺•I3⁻) -
        0.174427 (I1z•I2z) - 0.112274 (I1z•I3z) - 0.00023107 (I2⁻•I3⁺) - 0.00023107 (I2⁺•I3⁻) +
        0.00972757 (I2z•I3z) - 0.0635342 (I1⁻•I2⁺•I3z) + 0.000698928 (I1⁻•I2z•I3⁺) - 0.0635342 (I1⁺•I2⁻•I3z) +
        0.000698928 (I1⁺•I2z•I3⁻) - 0.000508864 (I1z•I2⁻•I3⁺) - 0.000508864 (I1z•I2⁺•I3⁻) -
        0.116146 (I1z•I2z•I3z) + 0.0102117 I1z + 0.0398123 I2z - 0.103263 I3z + 0.175 𝕀
```

```
In[•]:= sig2 = Signal1D[{{2 π 100, "8k"}}, Preparation → RotationSuperoperator[3, {π/2, "-x"}],
           InitialDensityOperator → 28 ρfinal, Observable → {3},
           BackgroundGenerator → CombineGenerators[2 π 12.2 opI[1].opI[2] +
              2 π 13.6 opI[1, "z"].opI[3, "z"] + 2 π 2.1 opI[2, "z"].opI[3, "z"], Γnum]];
```

Signal1D: Using SignalCalculationMethod → Diagonalization

Signal1D: Using LineBroadening → $2\pi \times 17.8983 \times 10^{-3}$ rad s^{-1}.

```
In[•]:= ListPlot[Re@FT[sig2], PlotRange → {All, All}, PlotStyle → Blue]
```

Out[•]=

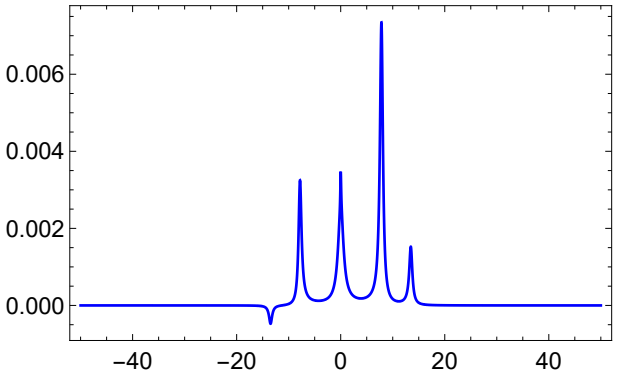

Sweep rate simulation

```
In[•]:= Γrandterm[i_, j_] := -κ[i, j] τθ
          Sum[DoubleCommutationSuperoperator[Adjoint[opT[i, {1, m}]], opT[j, {1, m}]], {m, -1, 1}]

In[•]:= κ[i_, i_] := 1;
        κ[i_, j_] := .9;

In[•]:= Γrand = Sum[Γrandterm[i, j], {i, 1, 2}, {j, 1, 2}];

In[•]:= Γnum = Γrand /. {τC → 10^-11, τθ → 0.35} // N // Superoperator

Out[•]= Superoperator[<<..>>, SuperoperatorType→Undefined ]

In[•]:= ρsweep = Table[
          NPropagate[{Function[t, CombineGenerators[Γnum, H[sweep[-2 * 10^-6, 2 * 10^-6, τ, t]] /.
                {J12 → 12.2, J13 → 13.6, J23 → 2.1}]], τ}][ρini], {τ, {0.01, 0.02, 0.03,
            0.04, 0.05, 0.06, 0.07, 0.08, 0.09, 0.1, 0.2, 0.3, 0.4, 0.5, 0.75, 1, 2, 5}}];

In[•]:= sweepratesim =
         Flatten[{{0.01, 0.02, 0.03, 0.04, 0.05, 0.06, 0.07, 0.08, 0.09, 0.1, 0.2, 0.3, 0.4,
            0.5, 0.75, 1, 2, 5}, Abs@Re@Table[OperatorAmplitude[
              ρsweep[[x]] → PolarizationLevelOperator[3, "z"]], {x, 1, 18, 1}]}, {{2}, {1}}]

Out[•]= {{0.01, 0.0206444}, {0.02, 0.0186365}, {0.03, 0.00994833}, {0.04, 0.0229264},
         {0.05, 0.0711719}, {0.06, 0.20354}, {0.07, 0.222626}, {0.08, 0.184227},
         {0.09, 0.200378}, {0.1, 0.315944}, {0.2, 0.524928}, {0.3, 0.601769}, {0.4, 0.67001},
         {0.5, 0.73032}, {0.75, 0.717395}, {1, 0.671888}, {2, 0.524315}, {5, 0.253423}}
```

```
In[•]:= ListPlot[sweepratesim, Joined → True, PlotStyle → {Blue, Thickness[0.005]}]
```

Out[•]=

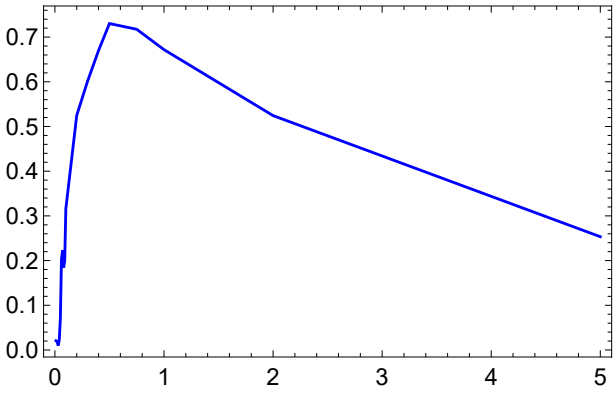

State populations during sweep

```
In[•]:= DefineBasis[STZbasis, ProductBasis[{SingletTripletBasis[{1, 2}], ZeemanBasis[{3}]}]]
```

CheckBasis: State basis is orthonormal.

DefineBasis: The state basis STZbasis has been defined. To use this basis, execute SetBasis[STZbasis].

```
In[•]:= SetBasis[STZbasis]
```

SetBasis: the state basis has been set to STZbasis.

```
In[•]:= ρfinal = Table[NPropagate[{Function[t,
          H[sweep[-2 * 10^-6, B * 10^-6, .001, t]] /. {J12 → 12.2, J13 → 13.6, J23 → 2.1}], .001,
        PropagationMethod → Adiabatic, EventSampling → 50}][ρini], {B, -1.98, 2, 0.02}];

In[•]:= ListPlot[{Table[MatrixRepresentation[ρfinal[[τ]]][[1, 1]], {τ, 1, 200, 1}],
    Table[MatrixRepresentation[ρfinal[[τ]]][[5, 5]], {τ, 1, 200, 1}],
    Table[MatrixRepresentation[ρfinal[[τ]]][[6, 6]], {τ, 1, 200, 1}],
    Table[MatrixRepresentation[ρfinal[[τ]]][[7, 7]], {τ, 1, 200, 1}],
    Table[MatrixRepresentation[ρfinal[[τ]]][[3, 3]], {τ, 1, 200, 1}],
    Table[MatrixRepresentation[ρfinal[[τ]]][[4, 4]], {τ, 1, 200, 1}]}]
```

Out[•]=

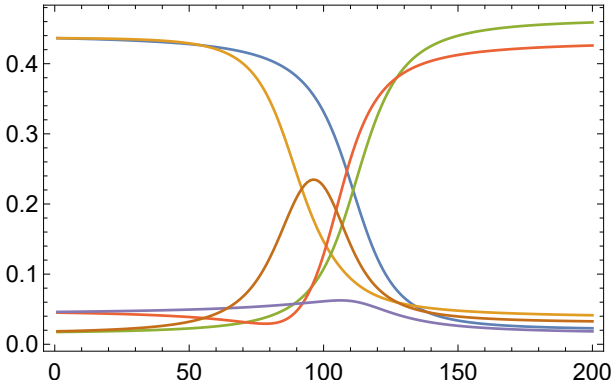

S-spin SLIC polarization levels

In[•]:=
```
Needs["SpinDynamica`"]
```

```
SpinDynamica version 3.0.1 loaded
```

ModifyBuiltIn: The following built–in routines have been modified in SpinDynamica:
{Chop, Dot, Duration, Exp, Expand, ExpandAll, NumericQ, Plus, Power, Simplify, Times, WignerD}.
Evaluate ??*symbol* to generate the additional definitions for *symbol*.

Setup spin system

In[•]:=
```
SetSpinSystem[3];
```

SetSpinSystem: the spin system has been set to $\{\{1, \frac{1}{2}\}, \{2, \frac{1}{2}\}, \{3, \frac{1}{2}\}\}$

SetBasis: the state basis has been set to ZeemanBasis$[\{\{1, \frac{1}{2}\}, \{2, \frac{1}{2}\}, \{3, \frac{1}{2}\}\}$, BasisLabels → Automatic$]$.

In[•]:=
```
DefineBasis[STZbasis,
 ProductBasis[SingletTripletBasis[{{1, 1/2}, {2, 1/2}}], ZeemanBasis[{3}]]]
```

CheckBasis: State basis is orthonormal.

DefineBasis: The state basis STZbasis has been defined. To use this basis, execute SetBasis[STZbasis].

In[•]:=
```
DefineBasis[STXbasis, Map[opR[3, {π/2, "y"}], BasisKets[STZbasis]]]
```

CheckBasis: State basis is orthonormal.

DefineBasis: The state basis STXbasis has been defined. To use this basis, execute SetBasis[STXbasis].

In[•]:=
```
SetBasis[STXbasis]
BasisKets[] // Column
```

SetBasis: the state basis has been set to STXbasis.

Out[•]=
$$-\frac{|\beta\alpha\beta\rangle}{2} - \frac{|\beta\alpha\alpha\rangle}{2} + \frac{|\alpha\beta\beta\rangle}{2} + \frac{|\alpha\beta\alpha\rangle}{2}$$
$$\frac{|\alpha\alpha\beta\rangle}{\sqrt{2}} + \frac{|\alpha\alpha\alpha\rangle}{\sqrt{2}}$$
$$\frac{|\beta\alpha\beta\rangle}{2} + \frac{|\beta\alpha\alpha\rangle}{2} + \frac{|\alpha\beta\beta\rangle}{2} + \frac{|\alpha\beta\alpha\rangle}{2}$$
$$\frac{|\beta\beta\beta\rangle}{\sqrt{2}} + \frac{|\beta\beta\alpha\rangle}{\sqrt{2}}$$
$$-\frac{|\beta\alpha\beta\rangle}{2} + \frac{|\beta\alpha\alpha\rangle}{2} + \frac{|\alpha\beta\beta\rangle}{2} - \frac{|\alpha\beta\alpha\rangle}{2}$$
$$\frac{|\alpha\alpha\beta\rangle}{\sqrt{2}} - \frac{|\alpha\alpha\alpha\rangle}{\sqrt{2}}$$
$$\frac{|\beta\alpha\beta\rangle}{2} - \frac{|\beta\alpha\alpha\rangle}{2} + \frac{|\alpha\beta\beta\rangle}{2} - \frac{|\alpha\beta\alpha\rangle}{2}$$
$$\frac{|\beta\beta\beta\rangle}{\sqrt{2}} - \frac{|\beta\beta\alpha\rangle}{\sqrt{2}}$$

S-spin SLIC operator propagation

In[•]:=
```
H = ω12 opI[1].opI[2] + (Δω/2) (opI[1, "z"].opI[3, "z"] - opI[2, "z"].opI[3, "z"]) +
    (Σω/2) (opI[1, "z"].opI[3, "z"] + opI[2, "z"].opI[3, "z"])
```

Out[•]=
$$\omega 12\ (I_{1x} \bullet I_{2x} + I_{1y} \bullet I_{2y} + I_{1z} \bullet I_{2z}) + \frac{1}{2} \Delta\omega\ (I_{1z} \bullet I_{3z} - I_{2z} \bullet I_{3z}) + \frac{1}{2} \Sigma\omega\ (I_{1z} \bullet I_{3z} + I_{2z} \bullet I_{3z})$$

In[•]:=
```
SLIC = ExpressOperator[
    PopulationOperator[5] / 2 + Exp[-I (t) (H + ω12 opI[3, "x"])].(PopulationOperator[1] / 2).
      Exp[I (t) (H + ω12 opI[3, "x"])], CartesianProductOperatorBasis[]];
```

In[•]:=
```
FullSimplify[ExpToTrig[SLIC]] // ExpToTrig
```

Out[•]=
$$-\frac{1}{2} \text{Cos}\left[\frac{t\,\Delta\omega}{4}\right]^2 (I_{1x} \bullet I_{2x}) - \frac{1}{2} \text{Cos}\left[\frac{t\,\Delta\omega}{4}\right]^2 (I_{1y} \bullet I_{2y}) - \frac{1}{2} (I_{1z} \bullet I_{2z}) -$$
$$\frac{I_{3x}}{8} + \frac{1}{8} \text{Cos}\left[\frac{t\,\Delta\omega}{2}\right] I_{3x} + (I_{1z} \bullet I_{2z} \bullet I_{3x}) \text{Sin}\left[\frac{t\,\Delta\omega}{4}\right]^2 + \frac{1}{4} (I_{1z} \bullet I_{3y}) \text{Sin}\left[\frac{t\,\Delta\omega}{2}\right] -$$
$$\frac{1}{4} (I_{2z} \bullet I_{3y}) \text{Sin}\left[\frac{t\,\Delta\omega}{2}\right] + \frac{1}{2} (I_{1x} \bullet I_{2y} \bullet I_{3z}) \text{Sin}\left[\frac{t\,\Delta\omega}{2}\right] - \frac{1}{2} (I_{1y} \bullet I_{2x} \bullet I_{3z}) \text{Sin}\left[\frac{t\,\Delta\omega}{2}\right] + \frac{\mathbb{1}}{8}$$

In[•]:=
```
SLICpropagation = SLIC /. {Δω → 2 π} // ExpToTrig // FullSimplify
```

Out[•]=
$$\frac{1}{8} \Big(-2 \left(1 + \text{Cos}[\pi t]\right) (I_{1x} \bullet I_{2x}) - 2 \left(1 + \text{Cos}[\pi t]\right) (I_{1y} \bullet I_{2y}) -$$
$$4 (I_{1z} \bullet I_{2z}) - 4 \left(-1 + \text{Cos}[\pi t]\right) (I_{1z} \bullet I_{2z} \bullet I_{3x}) - I_{3x} + \text{Cos}[\pi t]\, I_{3x} +$$
$$2 \left(I_{1z} \bullet I_{3y} - I_{2z} \bullet I_{3y} + 2 (I_{1x} \bullet I_{2y} \bullet I_{3z}) - 2 (I_{1y} \bullet I_{2x} \bullet I_{3z})\right) \text{Sin}[\pi t] + \mathbb{1}\Big)$$

In[•]:=
```
Plot[{OperatorAmplitude[SLICpropagation → PolarizationLevelOperator[3, "x"]],
  OperatorAmplitude[SLICpropagation → SingletPolarizationLevelOperator[{1, 2}]]},
 {t, 0, 4}, ImageSize → 400]
```

Out[•]=

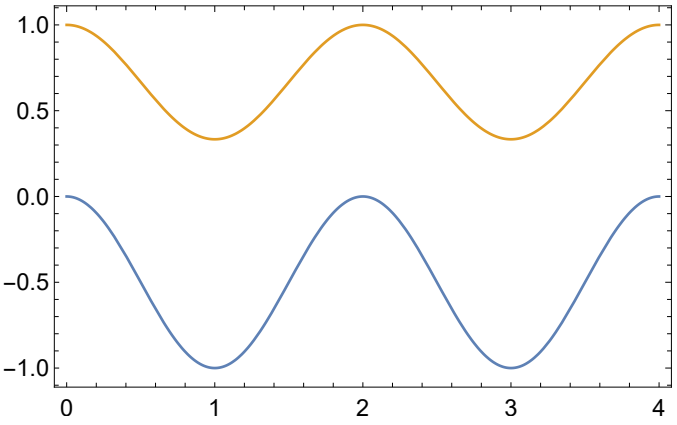

S2hM 3D representation

```
In[•]:= Needs["SpinDynamica`"]
```

```
SpinDynamica version 3.0.1 loaded
```

ModifyBuiltIn: The following built–in routines have been modified in SpinDynamica:
{Chop, Dot, Duration, Exp, Expand, ExpandAll, NumericQ, Plus, Power, Simplify, Times, WignerD}.
Evaluate ??*symbol* to generate the additional definitions for *symbol*.

Setup Spin System

```
In[•]:= SetSpinSystem[3];
```

SetSpinSystem: the spin system has been set to $\{\{1, \frac{1}{2}\}, \{2, \frac{1}{2}\}, \{3, \frac{1}{2}\}\}$

SetBasis: the state basis has been set to ZeemanBasis$\left[\{\{1, \frac{1}{2}\}, \{2, \frac{1}{2}\}, \{3, \frac{1}{2}\}\}, \text{BasisLabels} \to \text{Automatic}\right]$.

STZ

```
In[•]:= DefineBasis[STZbasis,
         ProductBasis[SingletTripletBasis[{{1, 1/2}, {2, 1/2}}], ZeemanBasis[{3}]]]
```

CheckBasis: State basis is orthonormal.

DefineBasis: The state basis STZbasis has been defined. To use this basis, execute SetBasis[STZbasis].

```
In[•]:= SetBasis[STZbasis]
        BasisKets[]
```

SetBasis: the state basis has been set to STZbasis.

$$\text{Out}[•]= \left\{\frac{-|\beta\alpha\alpha\rangle + |\alpha\beta\alpha\rangle}{\sqrt{2}}, |\alpha\alpha\alpha\rangle, \frac{|\beta\alpha\alpha\rangle + |\alpha\beta\alpha\rangle}{\sqrt{2}}, |\beta\beta\alpha\rangle, \frac{-|\beta\alpha\beta\rangle + |\alpha\beta\beta\rangle}{\sqrt{2}}, |\alpha\alpha\beta\rangle, \frac{|\beta\alpha\beta\rangle + |\alpha\beta\beta\rangle}{\sqrt{2}}, |\beta\beta\beta\rangle\right\}$$

STX

```
In[•]:= BasisKets[ProductBasis[SingletTripletBasis[{{1, 1/2}, {2, 1/2}}], ZeemanBasis[{3}]]]
```

$$\text{Out}[•]= \left\{\frac{-|\beta\alpha\alpha\rangle + |\alpha\beta\alpha\rangle}{\sqrt{2}}, |\alpha\alpha\alpha\rangle, \frac{|\beta\alpha\alpha\rangle + |\alpha\beta\alpha\rangle}{\sqrt{2}}, |\beta\beta\alpha\rangle, \frac{-|\beta\alpha\beta\rangle + |\alpha\beta\beta\rangle}{\sqrt{2}}, |\alpha\alpha\beta\rangle, \frac{|\beta\alpha\beta\rangle + |\alpha\beta\beta\rangle}{\sqrt{2}}, |\beta\beta\beta\rangle\right\}$$

```
In[•]:= DefineBasis[STXbasis, Map[opR[3, {π/2, "y"}], BasisKets[
           ProductBasis[SingletTripletBasis[{{1, 1/2}, {2, 1/2}}], ZeemanBasis[{3}]]]]]
```

CheckBasis: State basis is orthonormal.

DefineBasis: The state basis STXbasis has been defined. To use this basis, execute SetBasis[STXbasis].

```
In[•]:= SetBasis[STXbasis]
        BasisKets[] // Column
```

SetBasis: the state basis has been set to STXbasis.

$$\begin{pmatrix} -\frac{|\beta\alpha\beta\rangle}{2} - \frac{|\beta\alpha\alpha\rangle}{2} + \frac{|\alpha\beta\beta\rangle}{2} + \frac{|\alpha\beta\alpha\rangle}{2} \\ \frac{|\alpha\alpha\beta\rangle}{\sqrt{2}} + \frac{|\alpha\alpha\alpha\rangle}{\sqrt{2}} \\ \frac{|\beta\alpha\beta\rangle}{2} + \frac{|\beta\alpha\alpha\rangle}{2} + \frac{|\alpha\beta\beta\rangle}{2} + \frac{|\alpha\beta\alpha\rangle}{2} \\ \frac{|\beta\beta\beta\rangle}{\sqrt{2}} + \frac{|\beta\beta\alpha\rangle}{\sqrt{2}} \\ -\frac{|\beta\alpha\beta\rangle}{2} + \frac{|\beta\alpha\alpha\rangle}{2} + \frac{|\alpha\beta\beta\rangle}{2} - \frac{|\alpha\beta\alpha\rangle}{2} \\ \frac{|\alpha\alpha\beta\rangle}{\sqrt{2}} - \frac{|\alpha\alpha\alpha\rangle}{\sqrt{2}} \\ \frac{|\beta\alpha\beta\rangle}{2} - \frac{|\beta\alpha\alpha\rangle}{2} + \frac{|\alpha\beta\beta\rangle}{2} - \frac{|\alpha\beta\alpha\rangle}{2} \\ \frac{|\beta\beta\beta\rangle}{\sqrt{2}} - \frac{|\beta\beta\alpha\rangle}{\sqrt{2}} \end{pmatrix}$$

3D Representation

```
In[•]:= opI17x = (1/2) (BasisKets[][[1]].BasisBras[][[7]] + BasisKets[][[7]].BasisBras[][[1]]);
        opI17y = (1/2 I) (BasisKets[][[1]].BasisBras[][[7]] - BasisKets[][[7]].BasisBras[][[1]]);
        opI17z = (1/2) (BasisKets[][[1]].BasisBras[][[1]] - BasisKets[][[7]].BasisBras[][[7]]);

In[•]:= ω12 = 2 π 10;
        Δω = 2 π 4;

In[•]:= H = ω12 opI[1].opI[2] + (Δω/2) (opI[1, "z"].opI[3, "z"] - opI[2, "z"].opI[3, "z"])
Out[•]= 20 π (I1x•I2x + I1y•I2y + I1z•I2z) + 4 π (I1z•I3z - I2z•I3z)

In[•]:= Θ = ArcTan[Δω / (2 ω12)]
Out[•]= ArcTan[1/5]

In[•]:= ωe = Sqrt[ω12^2 + (Δω/2)^2]
Out[•]= 4 √26 π

In[•]:= τ = π/(2 ωe) // N
Out[•]= 0.0245145

In[•]:= n = π / (4 Θ) // N
Out[•]= 3.9788
```

```
In[•]:= {trajx, trajy, trajz} =
 Trajectory[SingletPolarizedDensityOperator[{1, 2}] → {opI17x, opI17y, opI17z},
  {Repeat[{{None, τ}, RotationSuperoperator[3, {π, "x"}], {None, τ}}, 4],
   {None, τ}, RotationSuperoperator[3, {π / 2, "x"}], Repeat[{{None, τ},
     RotationSuperoperator[3, {π, "x"}], {None, τ}}, 4]}, BackgroundGenerator → H]
```

```
Out[•]= {TrajectoryFunction[ {{0, 416.747 × 10^-3}} , <>],
 TrajectoryFunction[ {{0, 416.747 × 10^-3}} , <>],
 TrajectoryFunction[ {{0, 416.747 × 10^-3}} , <>]}
```

```
In[•]:= Show[SphereAndAxes[], ParametricPlot3D[{trajx[t], trajy[t], trajz[t]},
   {t, 0, 17 τ}, PlotRange → All, PlotStyle → {Blue, Thickness[0.003]}],
 Arrow3D[{Sin[θ], 0, Cos[θ]}, Directive → Red], Boxed → False, ImageSize → 300]
```

Out[•]=

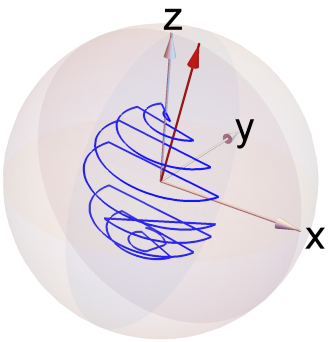

Fumarate S2hM and SLIC simulations

```
In[•]:= Needs["SpinDynamica`"]
```

```
SpinDynamica version 3.3.2 loaded
```

SetUserLevel: The user level is being initialized to 2. The user level may be set to an integer between 1 and 3 by using SetUserLevel[level]. Low user levels provide strong syntax trapping at the expense of slow execution for some routines. High user levels relax the syntax trapping in order to provide better execution speeds.

SetUserLevel: The user level has been set to 2.

SetUserLevel: Additional definitions have been given to the following symbols:
{Dot, Exp, Expand, Plus, Power, Simplify, Times, WignerD}

```
In[•]:= SetSpinSystem[3]
```

SetSpinSystem: the spin system has been set to $\{\{1, \frac{1}{2}\}, \{2, \frac{1}{2}\}, \{3, \frac{1}{2}\}\}$

SetBasis: the state basis has been set to ZeemanBasis$[\{\{1, \frac{1}{2}\}, \{2, \frac{1}{2}\}, \{3, \frac{1}{2}\}\}$, BasisLabels → Automatic$]$.

```
In[•]:= H = 2 π 15.7 opI[1].opI[2] + 2 π 6.6 opI[1, "z"].opI[3, "z"] + 2 π 3.2 opI[2, "z"].opI[3, "z"];
```

S2hM

```
In[•]:= S2hMτ = TransformationAmplitudeTable[
    SingletPolarizedDensityOperator[{1, 2}] → PolarizationLevelOperator[3, "x"],
    {Repeat[{{None, t}, RotationSuperoperator[3, {π, "x"}], {None, t}}, 7],
     {None, t}, RotationSuperoperator[3, {π / 2, "-x"}],
     Repeat[{{None, t}, RotationSuperoperator[3, {π, "x"}], {None, t}}, 7]},
    {t, 0, 0.05, 0.0002}, BackgroundGenerator → H, TableCoordinates → t];
```

```
In[•]:= ListPlot[S2hMτ]
```

Out[•]=

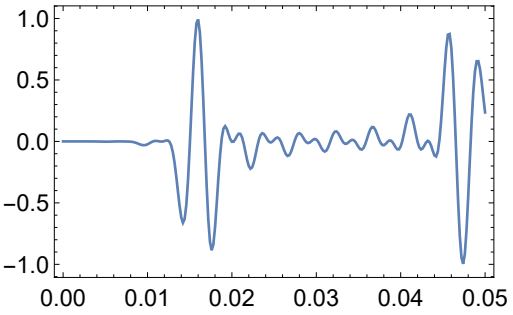

```
In[•]:= S2hMn = TransformationAmplitudeTable[
          SingletPolarizedDensityOperator[{1, 2}] → PolarizationLevelOperator[3, "x"],
          {Repeat[{{None, 0.0158}, RotationSuperoperator[3, {π, "x"}], {None, 0.0158}}, n],
           {None, 0.0158}, RotationSuperoperator[3, {π / 2, "-x"}],
           Repeat[{{None, 0.0158}, RotationSuperoperator[3, {π, "x"}], {None, 0.0158}}, n]},
          {n, 1, 20, 1}, BackgroundGenerator → H, TableCoordinates → n];

In[•]:= ListPlot[S2hMn, ImageSize → 300]
```

Out[•]=

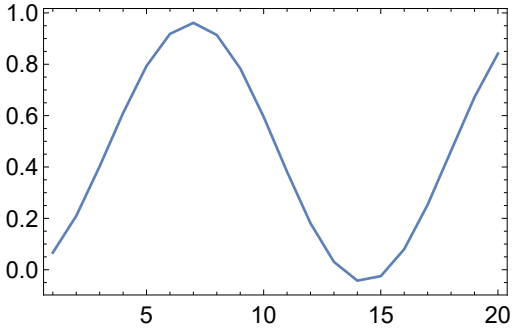

SLIC

```
In[•]:= SLICτ = TransformationAmplitudeTable[SingletPolarizedDensityOperator[{1, 2}] →
           PolarizationLevelOperator[3, "x"], {2 π 15.7 opI[3, "-x"], t},
          {t, 0, 1.5, 0.01}, BackgroundGenerator → H, TableCoordinates → t];

In[•]:= ListPlot[SLICτ, ImageSize → 300]
```

Out[•]=

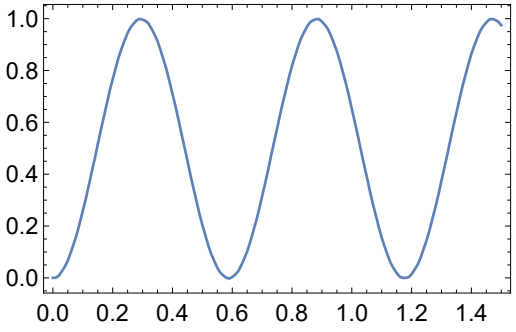


```
In[•]:= SLICω = TransformationAmplitudeTable[SingletPolarizedDensityOperator[{1, 2}] →
           PolarizationLevelOperator[3, "x"], {2 π ω opI[3, "-x"], 0.28},
          {ω, 8, 26, 0.1}, BackgroundGenerator → H, TableCoordinates → ω];
```

In[ ]:= **ListPlot[SLICω, ImageSize → 300]**

Out[ ]=

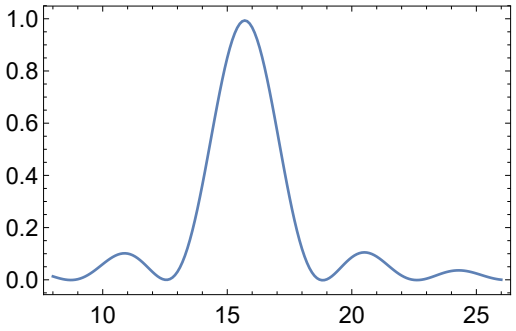

S2B2M methyl 13C polarization

```
In[•]:= Needs["SpinDynamica`"]
```

```
SpinDynamica version 3.3.2 loaded
```

SetUserLevel: The user level is being initialized to 2. The user level may be set to an integer between 1 and 3 by using SetUserLevel[level]. Low user levels provide strong syntax trapping at the expense of slow execution for some routines. High user levels relax the syntax trapping in order to provide better execution speeds.

SetUserLevel: The user level has been set to 2.

SetUserLevel: Additional definitions have been given to the following symbols:
{Dot, Exp, Expand, Plus, Power, Simplify, Times, WignerD}

```
In[•]:= SetSpinSystem[4]
```

SetSpinSystem: the spin system has been set to $\left\{\left\{1, \frac{1}{2}\right\}, \left\{2, \frac{1}{2}\right\}, \left\{3, \frac{1}{2}\right\}, \left\{4, \frac{1}{2}\right\}\right\}$

SetBasis: the state basis has been set to ZeemanBasis$\left[\left\{\left\{1, \frac{1}{2}\right\}, \left\{2, \frac{1}{2}\right\}, \left\{3, \frac{1}{2}\right\}, \left\{4, \frac{1}{2}\right\}\right\}, \text{BasisLabels} \to \text{Automatic}\right]$.

```
In[•]:= JHH = 12.2;
JH1C = 7.9 + 5.3;
JH2C = 7.9 - 5.3;
JCC = 2.6;
```

```
In[•]:= H = 2 π JHH opI[1].opI[2] + 2 π JH1C opI[1, "z"].opI[3, "z"] +
  2 π JH2C opI[2, "z"].opI[3, "z"] + 2 π JCC opI[3, "z"].opI[4, "z"]
```

```
Out[•]= 76.6549 (I1x•I2x + I1y•I2y + I1z•I2z) + 82.938 (I1z•I3z) + 16.3363 (I2z•I3z) + 16.3363 (I3z•I4z)
```

```
In[•]:= sim = TransformationAmplitudeTable[
    SingletPolarizedDensityOperator[{1, 2}] → PolarizationLevelOperator[4, "x"],
    {{None, .0185}, RotationSuperoperator[3, {π, "x"}], {None, 2 * .0185},
     RotationSuperoperator[3, {π/2, "-x"}], {None, .0185},
     RotationSuperoperator[3, {π, "x"}], {None, .0185},
     {2 π 10 000 opI[{1, 2}, "x"], τ}, RotationSuperoperator[{3, 4}, {π, "x"}],
     {2 π 10 000 opI[{1, 2}, "x"], τ}, RotationSuperoperator[{3, 4}, {π/2, "x"}],
     {2 π 10 000 opI[{1, 2}, "x"], τ}, RotationSuperoperator[{3, 4}, {π, "x"}],
     {2 π 10 000 opI[{1, 2}, "x"], τ}},
    {τ, 0.01, 0.41, 0.01}, BackgroundGenerator → H, TableCoordinates → τ];
```

In[•]:= **ListPlot[sim, PlotRange → All]**

Out[•]=

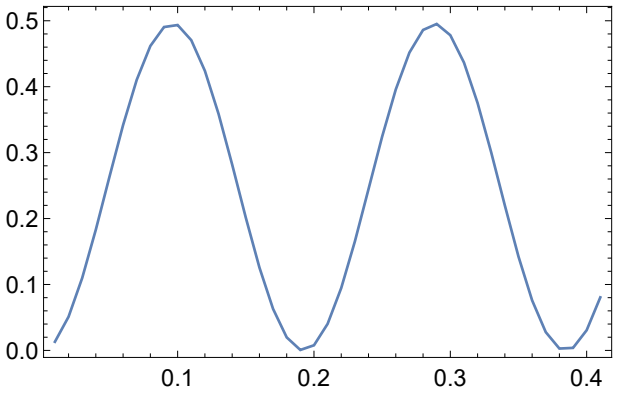

Trans-hydrogenative PHIP spectrum

```
In[•]:= Needs["SpinDynamica`"]
```

```
SpinDynamica version 3.3.2 loaded
```

SetUserLevel: The user level is being initialized to 2. The user level may be set to an integer between 1 and 3 by using SetUserLevel[level]. Low user levels provide strong syntax trapping at the expense of slow execution for some routines. High user levels relax the syntax trapping in order to provide better execution speeds.

SetUserLevel: The user level has been set to 2.

SetUserLevel: Additional definitions have been given to the following symbols:
{Dot, Exp, Expand, Plus, Power, Simplify, Times, WignerD}

```
In[•]:= SetSpinSystem[3]
```

SetSpinSystem: the spin system has been set to $\{\{1, \frac{1}{2}\}, \{2, \frac{1}{2}\}, \{3, \frac{1}{2}\}\}$

SetBasis: the state basis has been set to ZeemanBasis$[\{\{1, \frac{1}{2}\}, \{2, \frac{1}{2}\}, \{3, \frac{1}{2}\}\}$, BasisLabels → Automatic$]$.

```
In[•]:= H = 2 π 15.7 opI[1].opI[2] + 2 π 6.6 opI[1, "z"].opI[3, "z"] + 2 π 3.2 opI[2, "z"].opI[3, "z"];
```

```
In[•]:= ρini = Secularize[SingletPolarizedDensityOperator[{1, 2}], H];
```

SetOperatorBasis: the operator basis has been set to ShiftAndZOperatorBasis$[\{\{1, \frac{1}{2}\}, \{2, \frac{1}{2}\}, \{3, \frac{1}{2}\}\}$, Sorted → CoherenceOrder$]$.

```
In[•]:= ρ =
  NPropagate[{Repeat[{{None, 0.0158}, RotationSuperoperator[3, {π, "x"}], {None, 0.0158}},
      7], {None, 0.0158}, RotationSuperoperator[3, {π/2, "-x"}],
    Repeat[{{None, 0.0158}, RotationSuperoperator[3, {π, "x"}], {None, 0.0158}}, 7]},
   BackgroundGenerator → H][ρini]
```

```
Out[•]= Operator[<< .. >> , OperatorType → Hermitian ]
```

S2hM 13C spectrum

```
In[•]:= sig = Signal1D[{{2 π 60, "1k"}}, Preparation → {None, 0.01},
    InitialDensityOperator → ρ, Observable → opI[3, "x"], BackgroundGenerator → H];
```

Signal1D: Using SignalCalculationMethod → Diagonalization

Signal1D: Using LineBroadening → $2\pi \times 86.059 \times 10^{-3}$ rad s^{-1}.

In[ ]:=
```
ListPlot[Re@FT[sig], PlotRange → {All, {-0.0003, 0.0005}},
 PlotStyle → Blue, ImageSize → 400]
```

Out[ ]=

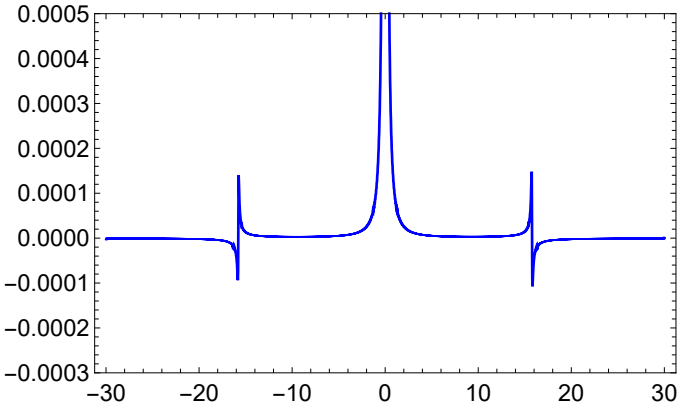

Bibliography

[1] G. Jeschke and L. Frydman. Nuclear hyperpolarization comes of age. *J. Magn. Reson.*, 264:1–2, 2016.

[2] Jan Henrik Ardenkjaer-Larsen. On the present and future of dissolution-DNP. *Journal of Magnetic Resonance*, 264:3–12, 2016.

[3] Panayiotis Nikolaou, Boyd M Goodson, and Eduard Y Chekmenev. NMR hyperpolarization techniques for biomedicine. *Chemistry–A European Journal*, 21(8):3156–3166, 2015.

[4] Richard A Green, Ralph W Adams, Simon B Duckett, Ryan E Mewis, David C Williamson, and Gary GR Green. The theory and practice of hyperpolarization in magnetic resonance using parahydrogen. *Progress in nuclear magnetic resonance spectroscopy*, (67):1–48, 2012.

[5] FA Gallagher, MI Kettunen, and KM Brindle. Biomedical applications of hyperpolarized ^{13}C magnetic resonance imaging. *Progress in Nuclear Magnetic Resonance Spectroscopy*, 4(55):285–295, 2009.

[6] C Russell Bowers and Daniel P Weitekamp. Parahydrogen and synthesis allow dramatically enhanced nuclear alignment. *Journal of the American Chemical Society*, 109(18):5541–5542, 1987.

[7] Jan H Ardenkjær-Larsen, Björn Fridlund, Andreas Gram, Georg Hansson, Lennart Hansson, Mathilde H Lerche, Rolf Servin, Mikkel Thaning, and Klaes Golman. Increase in signal-to-noise ratio of >10,000 times in liquid-state NMR. *Proceedings of the National Academy of Sciences*, 100(18):10158–10163, 2003.

[8] Anatole Abragam and Maurice Goldman. Principles of dynamic nuclear polarisation. *Reports on Progress in Physics*, 41(3):395, 1978.

[9] Klaes Golman, Mikkel Thaning, et al. Real-time metabolic imaging. *Proceedings of the National Academy of Sciences*, 103(30):11270–11275, 2006.

[10] Jan-Bernd Hövener, Andrey N Pravdivtsev, Bryce Kidd, C Russell Bowers, Stefan Glöggler, Kirill V Kovtunov, Markus Plaumann, Rachel Katz-Brull, Kai Buckenmaier, Alexej Jerschow, et al. Parahydrogen-based hyperpolarization for

biomedicine. *Angewandte Chemie International Edition*, 57(35):11140–11162, 2018.

[11] Sarah J Nelson, John Kurhanewicz, Daniel B Vigneron, Peder EZ Larson, Andrea L Harzstark, Marcus Ferrone, Mark van Criekinge, Jose W Chang, Robert Bok, Ilwoo Park, et al. Metabolic imaging of patients with prostate cancer using hyperpolarized [1-^{13}C] pyruvate. *Science translational medicine*, 5(198):198ra108–198ra108, 2013.

[12] Klaes Golman, Mathilde Lerche, Rikard Pehrson, Jan Henrik Ardenkjaer-Larsen, et al. Metabolic imaging by hyperpolarized ^{13}C magnetic resonance imaging for *in vivo* tumor diagnosis. *Cancer research*, 66(22):10855–10860, 2006.

[13] Albert P Chen, Mark J Albers, Charles H Cunningham, Susan J Kohler, Yi-Fen Yen, Ralph E Hurd, James Tropp, Robert Bok, John M Pauly, Sarah J Nelson, et al. Hyperpolarized C-13 spectroscopic imaging of the TRAMP mouse at 3T—initial experience. *Magnetic Resonance in Medicine: An Official Journal of the International Society for Magnetic Resonance in Medicine*, 58(6):1099–1106, 2007.

[14] Ferdia A Gallagher, Mikko I Kettunen, De-En Hu, Pernille R Jensen, Magnus Karlsson, Anna Gisselsson, Sarah K Nelson, Timothy H Witney, Sarah E Bohndiek, Georg Hansson, et al. Production of hyperpolarized [1, 4-$^{13}C_2$] malate from [1, 4-$^{13}C_2$] fumarate is a marker of cell necrosis and treatment response in tumors. *Proceedings of the National Academy of Sciences*, pages pnas–0911447106, 2009.

[15] TH Witney, MI Kettunen, DE Hu, FA Gallagher, SE Bohndiek, R Napolitano, and KM Brindle. Detecting treatment response in a model of human breast adenocarcinoma using hyperpolarised [1-^{13}C] pyruvate and [1, 4-$^{13}C_2$] fumarate. *British journal of cancer*, 103(9):1400, 2010.

[16] Sarah E Bohndiek, Mikko I Kettunen, De-en Hu, Timothy H Witney, Brett WC Kennedy, Ferdia A Gallagher, and Kevin M Brindle. Detection of tumor response to a vascular disrupting agent by hyperpolarized ^{13}C magnetic resonance spectroscopy. *Molecular cancer therapeutics*, 9(12):3278–3288, 2010.

[17] Menna R Clatworthy, Mikko I Kettunen, De-En Hu, Rebeccah J Mathews, Timothy H Witney, Brett WC Kennedy, Sarah E Bohndiek, Ferdia A Gallagher, Lorna B Jarvis, Kenneth GC Smith, et al. Magnetic resonance imaging with hyperpolarized [1, 4-$^{13}C_2$] fumarate allows detection of early renal acute tubular necrosis. *Proceedings of the National Academy of Sciences*, 109(33):13374–13379, 2012.

[18] Lionel Mignion, Prasanta Dutta, Gary V Martinez, Parastou Foroutan, Robert J Gillies, and Bénédicte F Jordan. Monitoring chemotherapeutic response by hyperpolarized ^{13}C-fumarate MRS and diffusion MRI. *Cancer research*, 74(3):686–694, 2014.

[19] Ferdia A Gallagher, Mikko I Kettunen, Sam E Day, De-en Hu, Magnus Karlsson, Anna Gisselsson, Mathilde H Lerche, and Kevin M Brindle. Detection of tumor glutamate metabolism in vivo using ^{13}C magnetic resonance spectroscopy and hyperpolarized [1-^{13}C] glutamate. *Magnetic resonance in medicine*, 66(1):18–23, 2011.

[20] Myriam M Chaumeil, Peder EZ Larson, Sarah M Woods, Larry Cai, Pia Eriksson, Aaron E Robinson, Janine M Lupo, Daniel B Vigneron, Sarah J Nelson, Russell O Pieper, et al. Hyperpolarized [1-^{13}C] glutamate: a metabolic imaging biomarker of IDH1 mutational status in glioma. *Cancer research*, pages canres–0680, 2014.

[21] Pratip Bhattacharya, Eduard Y Chekmenev, William H Perman, Kent C Harris, Alexander P Lin, Valerie A Norton, Chou T Tan, Brian D Ross, and Daniel P Weitekamp. Towards hyperpolarized ^{13}C-succinate imaging of brain cancer. *Journal of magnetic resonance*, 186(1):150–155, 2007.

[22] Eduard Y Chekmenev, Jan Hövener, Valerie A Norton, Kent Harris, Lynne S Batchelder, Pratip Bhattacharya, Brian D Ross, and Daniel P Weitekamp. PASADENA hyperpolarization of succinic acid for MRI and NMR spectroscopy. *Journal of the American Chemical Society*, 130(13):4212–4213, 2008.

[23] Niki M Zacharias, Henry R Chan, Napapon Sailasuta, Brian D Ross, and Pratip Bhattacharya. Real-time molecular imaging of tricarboxylic acid cycle metabolism *in vivo* by hyperpolarized 1-^{13}C diethyl succinate. *Journal of the American Chemical Society*, 134(2):934–943, 2011.

[24] Niki M Zacharias, Christopher R McCullough, Shawn Wagner, Napapon Sailasuta, Henry R Chan, Youngbok Lee, Jingzhe Hu, William H Perman, Cameron Henneberg, Brian D Ross, et al. Towards real-time metabolic profiling of cancer with hyperpolarized succinate. *Journal of molecular imaging & dynamics*, 6(1), 2016.

[25] Richard R Ernst, Geoffrey Bodenhausen, Alexander Wokaun, et al. *Principles of nuclear magnetic resonance in one and two dimensions*, volume 14. Clarendon Press Oxford, 1987.

[26] Malcolm H Levitt. *Spin dynamics: basics of nuclear magnetic resonance*. John Wiley & Sons, 2001.

[27] Felix Bloch. Nuclear induction. *Physical review*, 70(7-8):460, 1946.

[28] Christian Bengs and Malcolm H Levitt. SpinDynamica: Symbolic and numerical magnetic resonance in a Mathematica environment. *Magnetic Resonance in Chemistry*, 56(6):374–414, 2018.

[29] Alexej Jerschow. From nuclear structure to the quadrupolar NMR interaction and high-resolution spectroscopy. *Progress in Nuclear Magnetic Resonance Spectroscopy*, 46(1):63–78, 2005.

[30] E. L. Hahn. Spin echoes. *Phys. Rev.*, 80:580–594, Nov 1950.

[31] GM Bydder and IR Young. Mr imaging: clinical use of the inversion recovery sequence. 1985.

[32] GM Bydder and IR Young. Clinical use of the partial saturation and saturation recovery sequences in mr imaging. *Journal of computer assisted tomography*, 9(6):1020–1032, 1985.

[33] Andrei Tokmakoff. Introductory quantum mechanics II. *MIT OpenCourseWare*, 5.74, 2009.

[34] M Ebert, T Grossmann, W Heil, EW Otten, R Surkau, M Thelen, M Leduc, P Bachert, MV Knopp, and LR Schad. Nuclear magnetic resonance imaging with hyperpolarised helium-3. *The Lancet*, 347(9011):1297–1299, 1996.

[35] Sean B Fain, Frank R Korosec, James H Holmes, Rafael O'halloran, Ronald L Sorkness, and Thomas M Grist. Functional lung imaging using hyperpolarized gas MRI. *Journal of Magnetic Resonance Imaging: An Official Journal of the International Society for Magnetic Resonance in Medicine*, 25(5):910–923, 2007.

[36] John P Mugler and Talissa A Altes. Hyperpolarized ^{129}Xe MRI of the human lung. *Journal of Magnetic Resonance Imaging*, 37(2):313–331, 2013.

[37] Leif Schröder, Thomas J Lowery, Christian Hilty, David E Wemmer, and Alexander Pines. Molecular imaging using a targeted magnetic resonance hyperpolarized biosensor. *Science*, 314(5798):446–449, 2006.

[38] Julie A Aaron, Jennifer M Chambers, Kevin M Jude, Luigi Di Costanzo, Ivan J Dmochowski, and David W Christianson. Structure of a ^{129}Xe-cryptophane biosensor complexed with human carbonic anhydrase II. *Journal of the American Chemical Society*, 130(22):6942–6943, 2008.

[39] Mathilde H Lerche, Sebastian Meier, Pernille R Jensen, Herbert Baumann, Bent O Petersen, Magnus Karlsson, Jens Ø Duus, and Jan H Ardenkjær-Larsen. Study of molecular interactions with ^{13}C DNP-NMR. *Journal of Magnetic Resonance*, 203(1):52–56, 2010.

[40] Youngbok Lee, Haifeng Zeng, Simon Ruedisser, Alvar D Gossert, and Christian Hilty. Nuclear magnetic resonance of hyperpolarized fluorine for characterization of protein–ligand interactions. *Journal of the American Chemical Society*, 134(42):17448–17451, 2012.

[41] Roberto Buratto, Daniele Mammoli, Elisabetta Chiarparin, Glyn Williams, and Geoffrey Bodenhausen. Exploring weak ligand–protein interactions by long-lived NMR states: improved contrast in fragment-based drug screening. *Angewandte Chemie International Edition*, 53(42):11376–11380, 2014.

[42] Zackary I Cleveland, Karl F Stupic, Galina E Pavlovskaya, John E Repine, Jan B Wooten, and Thomas Meersmann. Hyperpolarized ^{83}Kr and ^{129}Xe NMR relaxation measurements of hydrated surfaces: implications for materials science and pulmonary diagnostics. *Journal of the American Chemical Society*, 129(6):1784–1792, 2007.

[43] Kirill V Kovtunov, Irene E Beck, Valery I Bukhtiyarov, and Igor V Koptyug. Observation of parahydrogen-induced polarization in heterogeneous hydrogenation on supported metal catalysts. *Angewandte Chemie*, 120(8):1514–1517, 2008.

[44] Anne Lesage, Moreno Lelli, David Gajan, Marc A Caporini, Veronika Vitzthum, Pascal Miéville, Johan Alauzun, Arthur Roussey, Chloé Thieuleux, Ahmad Mehdi, et al. Surface enhanced NMR spectroscopy by dynamic nuclear polarization. *Journal of the American Chemical Society*, 132(44):15459–15461, 2010.

[45] Moreno Lelli, David Gajan, Anne Lesage, Marc A Caporini, Veronika Vitzthum, Pascal Miéville, Florent Héroguel, Fernando Rascón, Arthur Roussey, Chloé Thieuleux, et al. Fast characterization of functionalized silica materials by silicon-29 surface-enhanced NMR spectroscopy using dynamic nuclear polarization. *Journal of the American Chemical Society*, 133(7):2104–2107, 2011.

[46] Kirill V Kovtunov, Irene E Beck, Vladimir V Zhivonitko, Danila A Barskiy, Valery I Bukhtiyarov, and Igor V Koptyug. Heterogeneous addition of h_2 to double and triple bonds over supported Pd catalysts: a parahydrogen-induced polarization technique study. *Physical Chemistry Chemical Physics*, 14(31):11008–11014, 2012.

[47] Aaron J Rossini, Alexandre Zagdoun, Moreno Lelli, Anne Lesage, Christophe Copéret, and Lyndon Emsley. Dynamic nuclear polarization surface enhanced NMR spectroscopy. *Accounts of chemical research*, 46(9):1942–1951, 2013.

[48] Sangmoo Jeong, Roozbeh Eskandari, Sun Mi Park, Julio Alvarez, Sui Seng Tee, Ralph Weissleder, Michael G Kharas, Hakho Lee, and Kayvan R Keshari. Real-time quantitative analysis of metabolic flux in live cells using a hyperpolarized micromagnetic resonance spectrometer. *Science advances*, 3(6):e1700341, 2017.

[49] Melanie Rosay, Jonathan C Lansing, Kristin C Haddad, William W Bachovchin, Judith Herzfeld, Richard J Temkin, and Robert G Griffin. High-frequency dynamic nuclear polarization in MAS spectra of membrane and soluble proteins. *Journal of the American Chemical Society*, 125(45):13626–13627, 2003.

[50] Galia T Debelouchina, Marvin J Bayro, Anthony W Fitzpatrick, Vladimir Ladizhansky, Michael T Colvin, Marc A Caporini, Christopher P Jaroniec, Vikram S Bajaj, Melanie Rosay, Cait E MacPhee, et al. Higher order amyloid fibril structure by MAS NMR and DNP spectroscopy. *Journal of the American Chemical Society*, 135(51):19237–19247, 2013.

[51] Ümit Akbey and Hartmut Oschkinat. Structural biology applications of solid state MAS DNP NMR. *Journal of Magnetic Resonance*, 269:213–224, 2016.

[52] Wing YingáChow et al. Essential but sparse collagen hydroxylysyl post-translational modifications detected by DNP NMR. *Chemical Communications*, 54(89):12570–12573, 2018.

[53] Roberto Buratto, Aurélien Bornet, Jonas Milani, Daniele Mammoli, Basile Vuichoud, Nicola Salvi, Maninder Singh, Aurélien Laguerre, Solène Passemard, Sandrine Gerber-Lemaire, et al. Drug screening boosted by hyperpolarized long-lived states in NMR. *ChemMedChem*, 9(11):2509–2515, 2014.

[54] Hlaing Min, Giridhar Sekar, and Christian Hilty. Polarization transfer from ligands hyperpolarized by dissolution dynamic nuclear polarization for screening in drug discovery. *ChemMedChem*, 10(9):1559–1563, 2015.

[55] Quentin Chappuis, Jonas Milani, Basile Vuichoud, Aurélien Bornet, Alvar D Gossert, Geoffrey Bodenhausen, and Sami Jannin. Hyperpolarized water to study protein–ligand interactions. *The journal of physical chemistry letters*, 6(9):1674–1678, 2015.

[56] Louis-S Bouchard, Scott R Burt, M Sabieh Anwar, Kirill V Kovtunov, Igor V Koptyug, and Alexander Pines. NMR imaging of catalytic hydrogenation in microreactors with the use of para-hydrogen. *Science*, 319(5862):442–445, 2008.

[57] Sean Bowen and Christian Hilty. Temporal chemical shift correlations in reactions studied by hyperpolarized nuclear magnetic resonance. *Analytical chemistry*, 81(11):4543–4547, 2009.

[58] Haifeng Zeng, Youngbok Lee, and Christian Hilty. Quantitative rate determination by dynamic nuclear polarization enhanced NMR of a Diels-Alder reaction. *Analytical chemistry*, 82(21):8897–8902, 2010.

[59] Mathis Duewel, Nicolas Vogel, Clemens K Weiss, Katharina Landfester, Hans-Wolfgang Spiess, and Kerstin Münnemann. Online monitoring of styrene polymerization in miniemulsion by hyperpolarized ^{129}Xe NMR spectroscopy. *Macromolecules*, 45(4):1839–1846, 2012.

[60] Youngbok Lee, Gyu Seong Heo, Haifeng Zeng, Karen L Wooley, and Christian Hilty. Detection of living anionic species in polymerization reactions using hyperpolarized NMR. *Journal of the American Chemical Society*, 135(12):4636–4639, 2013.

[61] Matthew L Hirsch, Neal Kalechofsky, Avrum Belzer, Melanie Rosay, and James G Kempf. Brute-force hyperpolarization for NMR and MRI. *Journal of the American Chemical Society*, 137(26):8428–8434, 2015.

[62] David T Peat, Matthew L Hirsch, David G Gadian, Anthony J Horsewill, John R Owers-Bradley, and James G Kempf. Low-field thermal mixing in [1-^{13}C] pyruvic acid for brute-force hyperpolarization. *Physical Chemistry Chemical Physics*, 18(28):19173–19182, 2016.

[63] Thad G Walker and William Happer. Spin-exchange optical pumping of noble-gas nuclei. *Reviews of Modern Physics*, 69(2):629, 1997.

[64] F. W. Hersman, I. C. Ruset, S. Ketel, I. Muradian, S. D. Covrig, J. Distelbrink, W. Porter, D. Watt, J. Ketel, J. Brackett, et al. Large production system for hyperpolarized ^{129}Xe for human lung imaging studies. *Acad. Radiol.*, 15(6):683–692, 2008.

[65] NR Newbury, AS Barton, P Bogorad, GD Cates, M Gatzke, B Saam, L Han, R Holmes, PA Souder, J Xu, et al. Laser polarized muonic helium. *Physical review letters*, 67(23):3219, 1991.

[66] PL Anthony. Determination of the neutron spin structure function. *Phys. Rev. Lett.*, 71:959, 1993.

[67] Guoquan Liu, Marcel Levien, Niels Karschin, Giacomo Parigi, Claudio Luchinat, and Marina Bennati. One-thousand-fold enhancement of high field liquid nuclear magnetic resonance signals at room temperature. *Nature chemistry*, 9(7):676, 2017.

[68] A. Bornet, R. Melzi, A. J. Perez Linde, P. Hautle, B. van den Brandt, S. Jannin, and G. Bodenhausen. Boosting dissolution dynamic nuclear polarization by cross polarization. *J. Phys. Chem. Lett.*, 4(1):111–114, 2012.

[69] Hunter Middleton, Robert D Black, Brian Saam, Gordon D Cates, Gary P Cofer, Robert Guenther, William Happer, Lawrence W Hedlund, G Alan Johnson, Kim Juvan, et al. MR imaging with hyperpolarized ^{3}He gas. *Magnetic Resonance in Medicine*, 33(2):271–275, 1995.

[70] MS Albert, GD Cates, B Driehuys, W Happer, B Saam, CS Springer Jr, and A Wishnia. Biological magnetic resonance imaging using laser-polarized ^{129}Xe. *Nature*, 370(6486):199, 1994.

[71] John P Mugler III, Bastiaan Driehuys, James R Brookeman, Gordon D Cates, Stuart S Berr, Robert G Bryant, Thomas M Daniel, Eduard E De Lange, J Hunter Downs, Christopher J Erickson, et al. MR imaging and spectroscopy using hyperpolarized ^{129}Xe gas: preliminary human results. *Magnetic Resonance in Medicine*, 37(6):809–815, 1997.

[72] Kuniyoshi Sakai, Anastacia M Bilek, Eduardo Oteiza, Ronald L Walsworth, Dilip Balamore, Ferenc A Jolesz, and Mitchell S Albert. Temporal dynamics of hyperpolarized ^{129}Xe resonances in living rats, 1996.

[73] Mark E Wagshul, Terry M Button, Haifang F Li, Zhengrong Liang, Charles S Springer, Kai Zhong, and Arnold Wishnia. *In vivo* MR imaging and spectroscopy using hyperpolarized ^{129}Xe. *Magnetic resonance in medicine*, 36(2):183–191, 1996.

[74] Patrick Berthault, Gaspard Huber, and Hervé Desvaux. Biosensing using laser-polarized xenon NMR/MRI. *Progress in Nuclear Magnetic Resonance Spectroscopy*, 1(55):35–60, 2009.

[75] Leif Schröder. Xenon for NMR biosensing–inert but alert. *Physica Medica*, 29(1):3–16, 2013.

[76] Hyla Allouche-Arnon, Trevor Wade, Lanette Friesen Waldner, Valentina N Miller, J Moshe Gomori, Rachel Katz-Brull, and Charles A McKenzie. *In vivo* magnetic resonance imaging of glucose–initial experience. *Contrast media & molecular imaging*, 8(1):72–82, 2013.

[77] Tiago B Rodrigues, Eva M Serrao, Brett WC Kennedy, De-En Hu, Mikko I Kettunen, and Kevin M Brindle. Magnetic resonance imaging of tumor glycolysis using hyperpolarized ^{13}C-labeled glucose. *Nature medicine*, 20(1):93, 2014.

[78] Sarah E Bohndiek, Mikko I Kettunen, De-en Hu, Brett WC Kennedy, Joan Boren, Ferdia A Gallagher, and Kevin M Brindle. Hyperpolarized [1-^{13}C]-ascorbic and dehydroascorbic acid: vitamin C as a probe for imaging redox status *in vivo*. *Journal of the American Chemical Society*, 133(30):11795–11801, 2011.

[79] Kayvan R Keshari, John Kurhanewicz, Robert Bok, Peder EZ Larson, Daniel B Vigneron, and David M Wilson. Hyperpolarized ^{13}C dehydroascorbate as an endogenous redox sensor for *in vivo* metabolic imaging. *Proceedings of the National Academy of Sciences*, 2011.

[80] Kayvan R Keshari, Victor Sai, Zhen J Wang, Henry F VanBrocklin, John Kurhanewicz, and David M Wilson. Hyperpolarized [1-^{13}C] dehydroascorbate

MR spectroscopy in a murine model of prostate cancer: comparison with ^{18}F-FDG PET. *Journal of nuclear medicine: official publication, Society of Nuclear Medicine*, 54(6):922, 2013.

[81] K Golman, Oskar Axelsson, Haukur Jóhannesson, S Månsson, C Olofsson, and JS Petersson. Parahydrogen-induced polarization in imaging: Subsecond ^{13}C angiography. *Magnetic resonance in medicine*, 46(1):1–5, 2001.

[82] P Bhattacharya, Kent Harris, AP Lin, M Mansson, Valerie A Norton, WH Perman, Daniel P Weitekamp, and Brian D Ross. Ultra-fast three dimensional imaging of hyperpolarized ^{13}C *in vivo*. *Magnetic Resonance Materials in Physics, Biology and Medicine*, 18(5):245–256, 2005.

[83] Lars E Olsson, Chun-Ming Chai, Oskar Axelsson, Magnus Karlsson, Klaes Golman, and J Stefan Petersson. MR coronary angiography in pigs with intraarterial injections of a hyperpolarized ^{13}C substance. *Magnetic Resonance in Medicine: An Official Journal of the International Society for Magnetic Resonance in Medicine*, 55(4):731–737, 2006.

[84] Edvin Johansson, LE Olsson, S Månsson, JS Petersson, K Golman, Freddy Ståhlberg, and Ronnie Wirestam. Perfusion assessment with bolus differentiation: a technique applicable to hyperpolarized tracers. *Magnetic Resonance in Medicine: An Official Journal of the International Society for Magnetic Resonance in Medicine*, 52(5):1043–1051, 2004.

[85] Barbara Ripka, James Eills, Hana Kouřilová, Markus Leutzsch, Malcolm H Levitt, and Kerstin Münnemann. Hyperpolarized fumarate via parahydrogen. *Chemical Communications*, 2018.

[86] Thomas Trantzschel, Johannes Bernarding, Markus Plaumann, Denise Lego, Torsten Gutmann, Tomasz Ratajczyk, Sonja Dillenberger, Gerd Buntkowsky, Joachim Bargon, and Ute Bommerich. Parahydrogen induced polarization in face of keto–enol tautomerism: proof of concept with hyperpolarized ethanol. *Physical Chemistry Chemical Physics*, 14(16):5601–5604, 2012.

[87] Francesca Reineri, Tommaso Boi, and Silvio Aime. Parahydrogen induced polarization of ^{13}C carboxylate resonance in acetate and pyruvate. *Nature communications*, 6:5858, 2015.

[88] Eleonora Cavallari, Carla Carrera, Matteo Sorge, Gisèle Bonne, Antoine Muchir, Silvio Aime, and Francesca Reineri. The ^{13}C hyperpolarized pyruvate generated by parahydrogen detects the response of the heart to altered metabolism in real time. *Scientific reports*, 8(1):8366, 2018.

[89] Ralph W Adams, Juan A Aguilar, Kevin D Atkinson, Michael J Cowley, Paul IP Elliott, Simon B Duckett, Gary GR Green, Iman G Khazal, Joaquín López-Serrano, and David C Williamson. Reversible interactions with para-hydrogen enhance NMR sensitivity by polarization transfer. *Science*, 323(5922):1708–1711, 2009.

[90] Milton L Truong, Thomas Theis, Aaron M Coffey, Roman V Shchepin, Kevin W Waddell, Fan Shi, Boyd M Goodson, Warren S Warren, and Eduard Y Chekmenev. ^{15}N hyperpolarization by reversible exchange using SABRE-SHEATH. *The journal of physical chemistry C*, 119(16):8786–8797, 2015.

[91] Thomas Theis, Milton L Truong, Aaron M Coffey, Roman V Shchepin, Kevin W Waddell, Fan Shi, Boyd M Goodson, Warren S Warren, and Eduard Y Chekmenev. Microtesla SABRE enables 10% nitrogen-15 nuclear spin polarization. *Journal of the American Chemical Society*, 137(4):1404–1407, 2015.

[92] Giuseppe Pileio. Relaxation theory of nuclear singlet states in two spin-1/2 systems. *Progress in nuclear magnetic resonance spectroscopy*, 56(3):217–231, 2010.

[93] Malcolm H Levitt. Singlet nuclear magnetic resonance. *Annual review of physical chemistry*, 63:89–105, 2012.

[94] RED McClung. Spin–rotation relaxation theory. *eMagRes*, 2007.

[95] Giuseppe Pileio, Marina Carravetta, Eric Hughes, and Malcolm H Levitt. The long-lived nuclear singlet state of ^{15}N-nitrous oxide in solution. *Journal of the American Chemical Society*, 130(38):12582–12583, 2008.

[96] Gabriele Stevanato, Soumya Singha Roy, Joe Hill-Cousins, Ilya Kuprov, Lynda J Brown, Richard CD Brown, Giuseppe Pileio, and Malcolm H Levitt. Long-lived nuclear spin states far from magnetic equivalence. *Physical Chemistry Chemical Physics*, 17(8):5913–5922, 2015.

[97] Shawn Wagner. Conversion rate of para-hydrogen to ortho-hydrogen by oxygen: Implications for PHIP gas storage and utilization. *Magnetic Resonance Materials in Physics, Biology and Medicine*, 27(3):195–199, 2014.

[98] Danila A Barskiy, Aaron M. Coffey, Panayiotis Nikolaou, Dmitry M Mikhaylov, Boyd M Goodson, Rosa T Branca, George J Lu, Mikhail G. Shapiro, Ville-Veikko Telkki, Vladimir V Zhivonitko, Igor V Koptyug, Oleg G Salnikov, Kirill V Kovtunov, Valerii I Bukhtiyarov, Matthew S. Rosen, Michael J Barlow, Shahideh Safavi, Ian P Hall, Leif Schröder, and Eduard Y Chekmenev. NMR hyperpolarization techniques of gases. *Chemistry, a European Journal*, 234:725–751, 2017.

[99] BP Stoicheff. High resolution raman spectroscopy of gases: Ix. spectra of h2, hd, and d2. *Canadian Journal of Physics*, 35(6):730–741, 1957.

[100] Eugene Wigner. *Zeitschrift für Physikalische Chemie*, 4, 1929.

[101] Rein U Kirss and Richard Eisenberg. Para-hydrogen-induced polarization in rhodium complex-catalyzed hydrogenation reactions. *Journal of Organometallic Chemistry*, 359(1):C22–C26, 1989.

[102] Thomas C Eisenschmid, Rein U Kirss, Paul P Deutsch, Sven I Hommeltoft, Richard Eisenberg, Joachim Bargon, Ronald G Lawler, and Alan L Balch. Para hydrogen induced polarization in hydrogenation reactions. *Journal of the American Chemical Society*, 109(26):8089–8091, 1987.

[103] Andreas Harthun, Ralf Giernoth, Cornelis J Elsevier, and Joachim Bargon. Rhodium-and palladium-catalysed proton exchange in styrene detected in situ by para-hydrogen induced polarization. *Chemical Communications*, (21):2483–2484, 1996.

[104] M Emondts, JFP Colell, B Blümich, and PPM Schleker. Polarization transfer efficiency in PHIP experiments. *Physical Chemistry Chemical Physics*, 19(33):21933–21937, 2017.

[105] Stephen Kadlecek, Vahid Vahdat, Takeshi Nakayama, Danny Ng, Kiarash Emami, and Rahim Rizi. A simple and low-cost device for generating hyperpolarized contrast agents using parahydrogen. *NMR in Biomedicine*, 24(8):933–942, 2011.

[106] Roman V Shchepin, Aaron M Coffey, Kevin W Waddell, and Eduard Y Chekmenev. Parahydrogen-induced polarization with a Rh-based monodentate ligand in water. *The journal of physical chemistry letters*, 3(22):3281–3285, 2012.

[107] Francesca Reineri, Alessandra Viale, Silvano Ellena, Tommaso Boi, Valeria Daniele, Roberto Gobetto, and Silvio Aime. Use of labile precursors for the generation of hyperpolarized molecules from hydrogenation with parahydrogen and aqueous-phase extraction. *Angewandte Chemie*, 123(32):7488–7491, 2011.

[108] Igor V Koptyug, Kirill V Kovtunov, Scott R Burt, M Sabieh Anwar, Christian Hilty, Song-I Han, Alexander Pines, and Renad Z Sagdeev. Para-hydrogen-induced polarization in heterogeneous hydrogenation reactions. *Journal of the American Chemical Society*, 129(17):5580–5586, 2007.

[109] Kirill V Kovtunov, Vladimir V Zhivonitko, Avelino Corma, and Igor V Koptyug. Parahydrogen-induced polarization in heterogeneous hydrogenations catalyzed by an immobilized au (iii) complex. *The Journal of Physical Chemistry Letters*, 1(11):1705–1708, 2010.

[110] Igor V Koptyug, Vladimir V Zhivonitko, and Kirill V Kovtunov. New perspectives for parahydrogen-induced polarization in liquid phase heterogeneous hydrogenation: An aqueous phase and altadena study. *ChemPhysChem*, 11(14):3086–3088, 2010.

[111] Kirill V Kovtunov, Danila A Barskiy, Oleg G Salnikov, Alexander K Khudorozhkov, Valery I Bukhtiyarov, Igor P Prosvirin, and Igor V Koptyug. Parahydrogen-induced polarization (phip) in heterogeneous hydrogenation over bulk metals and metal oxides. *Chemical Communications*, 50(7):875–878, 2014.

[112] Stefan Glöggler, Alexander M Grunfeld, Yavuz N Ertas, Jeffrey McCormick, Shawn Wagner, P Philipp M Schleker, and Louis-S Bouchard. A nanoparticle catalyst for heterogeneous phase para-hydrogen-induced polarization in water. *Angewandte Chemie International Edition*, 54(8):2452–2456, 2015.

[113] S Glöggler, AM Grunfeld, YN Ertas, J McCormick, S Wagner, and L-S Bouchard. Surface ligand-directed pair-wise hydrogenation for heterogeneous phase hyperpolarization. *Chemical Communications*, 52(3):605–608, 2016.

[114] Dana Schleyer, Heiko G Niessen, and Joachim Bargon. In situ ^{1}H-PHIP-NMR studies of the stereoselective hydrogenation of alkynes to (E)-alkenes catalyzed by a homogeneous [Cp* Ru]+ catalyst. *New Journal of Chemistry*, 25(3):423–426, 2001.

[115] Karin Radkowski, Basker Sundararaju, and Alois Fürstner. A functional-group-tolerant catalytic trans hydrogenation of alkynes. *Angewandte Chemie*, 125(1):373–378, 2013.

[116] Markus Leutzsch, Larry M Wolf, Puneet Gupta, Michael Fuchs, Walter Thiel, Christophe Farès, and Alois Fürstner. Formation of ruthenium carbenes by gem-hydrogen transfer to internal alkynes: Implications for alkyne trans-hydrogenation. *Angewandte Chemie*, 127(42):12608–12613, 2015.

[117] Alexandre Guthertz, Markus Leutzsch, Lawrence M Wolf, Puneet Gupta, Stephan M Rummelt, Richard Goddard, Christophe Farès, Walter Thiel, and Alois Fürstner. Half-sandwich ruthenium carbene complexes link trans-hydrogenation and gem-hydrogenation of internal alkynes. *Journal of the American Chemical Society*, 140(8):3156–3169, 2018.

[118] Danila A Barskiy, Kirill V Kovtunov, Igor V Koptyug, Ping He, Kirsten A Groome, Quinn A Best, Fan Shi, Boyd M Goodson, Roman V Shchepin, Milton L Truong, et al. In situ and ex situ low-field NMR spectroscopy and MRI endowed by SABRE hyperpolarization. *ChemPhysChem*, 15(18):4100–4107, 2014.

[119] Thomas Theis, Milton Truong, Aaron M Coffey, Eduard Y Chekmenev, and Warren S Warren. LIGHT-SABRE enables efficient in-magnet catalytic hyperpolarization. *Journal of Magnetic Resonance*, 248:23–26, 2014.

[120] Bram JA van Weerdenburg, Stefan Glöggler, Nan Eshuis, AHJ Ton Engwerda, Jan MM Smits, René de Gelder, Stephan Appelt, Sybren S Wymenga, Marco Tessari, Martin C Feiters, et al. Ligand effects of nhc–iridium catalysts for

signal amplification by reversible exchange (sabre). *Chemical Communications*, 49(67):7388–7390, 2013.

[121] Milton L Truong, Fan Shi, Ping He, Bingxin Yuan, Kyle N Plunkett, Aaron M Coffey, Roman V Shchepin, Danila A Barskiy, Kirill V Kovtunov, Igor V Koptyug, et al. Irreversible catalyst activation enables hyperpolarization and water solubility for NMR signal amplification by reversible exchange. *The Journal of Physical Chemistry B*, 118(48):13882–13889, 2014.

[122] M Fekete, C Gibard, GJ Dear, GGR Green, AJJ Hooper, AD Roberts, F Cisnetti, and SB Duckett. Utilisation of water soluble iridium catalysts for signal amplification by reversible exchange. *Dalton Transactions*, 44(17):7870–7880, 2015.

[123] Michael G Pravica and Daniel P Weitekamp. Net NMR alignment by adiabatic transport of parahydrogen addition products to high magnetic field. *Chemical physics letters*, 145(4):255–258, 1988.

[124] Maurice Goldman and Haukur Jóhannesson. Conversion of a proton pair para order into ^{13}C polarization by rf irradiation, for use in MRI. *Comptes Rendus Physique*, 6(4-5):575–581, 2005.

[125] James Eills, John W. Blanchard, Teng Wu, Christian Bengs, Julia Hollenbach, Dmitry Budker, and Malcolm H. Levitt. Polarization transfer via field sweeping in parahydrogen-enhanced nuclear magnetic resonance. *ChemRxiv*, 2019.

[126] Michael CD Tayler, Thomas Theis, Tobias F Sjolander, John W Blanchard, Arne Kentner, Szymon Pustelny, Alexander Pines, and Dmitry Budker. Invited review article: Instrumentation for nuclear magnetic resonance in zero and ultralow magnetic field. *Review of Scientific Instruments*, 88(9):091101, 2017.

[127] Marina Carravetta and Malcolm H Levitt. Theory of long-lived nuclear spin states in solution nuclear magnetic resonance. I. singlet states in low magnetic field. *The Journal of chemical physics*, 122(21):214505, 2005.

[128] James Eills, Gabriele Stevanato, Christian Bengs, Stefan Glöggler, Stuart J Elliott, Javier Alonso-Valdesueiro, Giuseppe Pileio, and Malcolm H Levitt. Singlet order conversion and parahydrogen-induced hyperpolarization of ^{13}C nuclei in near-equivalent spin systems. *Journal of Magnetic Resonance*, 274:163–172, 2017.

[129] Gabriele Stevanato, James Eills, Christian Bengs, and Giuseppe Pileio. A pulse sequence for singlet to heteronuclear magnetization transfer: S2hM. *Journal of Magnetic Resonance*, 277:169–178, 2017.

[130] Gabriele Stevanato. Alternating delays achieve polarization transfer (adapt) to heteronuclei in phip experiments. *Journal of Magnetic Resonance*, 274:148–162, 2017.

[131] Eleonora Cavallari, Carla Carrera, Tommaso Boi, Silvio Aime, and Francesca Reineri. Effects of magnetic field cycle on the polarization transfer from parahydrogen to heteronuclei through long-range j-couplings. *The Journal of Physical Chemistry B*, 119(31):10035–10041, 2015.

[132] Haukur Jóhannesson, Oskar Axelsson, and Magnus Karlsson. Transfer of parahydrogen spin order into polarization by diabatic field cycling. *Comptes Rendus Physique*, 5(3):315–324, 2004.

[133] Maurice Goldman, Haukur Jóhannesson, Oskar Axelsson, and Magnus Karlsson. Hyperpolarization of ^{13}C through order transfer from parahydrogen: a new contrast agent for MRI. *Magnetic resonance imaging*, 23(2):153–157, 2005.

[134] L Buljubasich, MB Franzoni, Hans Wolfgang Spiess, and Kerstin Münnemann. Level anti-crossings in parahydrogen induced polarization experiments with Cs-symmetric molecules. *Journal of Magnetic Resonance*, 219:33–40, 2012.

[135] Alexey S Kiryutin, Alexandra V Yurkovskaya, Robert Kaptein, Hans-Martin Vieth, and Konstantin L Ivanov. Evidence for coherent transfer of para-hydrogen-induced polarization at low magnetic fields. *The journal of physical chemistry letters*, 4(15):2514–2519, 2013.

[136] Jens Barkemeyer, Mathias Haake, and Joachim Bargon. Hetero-NMR enhancement via parahydrogen labeling. *Journal of the American Chemical Society*, 117(10):2927–2928, 1995.

[137] Mathias Haake, Johannes Natterer, and Joachim Bargon. Efficient NMR pulse sequences to transfer the parahydrogen-induced polarization to hetero nuclei. *Journal of the American Chemical Society*, 118(36):8688–8691, 1996.

[138] Eduard Y Chekmenev, Valerie A Norton, Daniel P Weitekamp, and Pratip Bhattacharya. Hyperpolarized ^{1}H NMR employing low γ nucleus for spin polarization storage. *Journal of the American Chemical Society*, 131(9):3164–3165, 2009.

[139] Stephen Kadlecek, Kiarash Emami, Masaru Ishii, and Rahim Rizi. Optimal transfer of spin-order between a singlet nuclear pair and a heteronucleus. *Journal of Magnetic Resonance*, 205(1):9–13, 2010.

[140] Sébastien Bär, Thomas Lange, Dieter Leibfritz, Jürgen Hennig, Dominik von Elverfeldt, and Jan-Bernd Hövener. On the spin order transfer from parahydrogen to another nucleus. *Journal of Magnetic Resonance*, 225:25–35, 2012.

[141] Maria Belen Franzoni, Dirk Graafen, L Buljubasich, LM Schreiber, Hans Wolfgang Spiess, and Kerstin Münnemann. Hyperpolarized ^{1}H long lived states originating from parahydrogen accessed by rf irradiation. *Physical Chemistry Chemical Physics*, 15(40):17233–17239, 2013.

[142] Chong Cai, Aaron M Coffey, Roman V Shchepin, Eduard Y Chekmenev, and Kevin W Waddell. Efficient transformation of parahydrogen spin order into heteronuclear magnetization. *The Journal of Physical Chemistry B*, 117(5):1219–1224, 2013.

[143] Andrey N Pravdivtsev, Alexandra V Yurkovskaya, Hans-Martin Vieth, Konstantin L Ivanov, and Robert Kaptein. Level anti-crossings are a key factor for understanding para-hydrogen-induced hyperpolarization in SABRE experiments. *ChemPhysChem*, 14(14):3327–3331, 2013.

[144] Andrey N Pravdivtsev, Alexandra V Yurkovskaya, Nikita N Lukzen, Konstantin L Ivanov, and Hans-Martin Vieth. Highly efficient polarization of spin-1/2 insensitive NMR nuclei by adiabatic passage through level anticrossings. *The journal of physical chemistry letters*, 5(19):3421–3426, 2014.

[145] Alexey S Kiryutin, Alexandra V Yurkovskaya, Nikita N Lukzen, Hans-Martin Vieth, and Konstantin L Ivanov. Exploiting adiabatically switched rf-field for manipulating spin hyperpolarization induced by para hydrogen. *The Journal of Chemical Physics*, 143(23):234203, 2015.

[146] Andrey N Pravdivtsev, Alexey S Kiryutin, Alexandra V Yurkovskaya, Hans-Martin Vieth, and Konstantin L Ivanov. Robust conversion of singlet spin order in coupled spin-1/2 pairs by adiabatically ramped rf-fields. *Journal of Magnetic Resonance*, 273:56–64, 2016.

[147] Michael CD Tayler, Tobias F Sjolander, Alexander Pines, and Dmitry Budker. Nuclear magnetic resonance at millitesla fields using a zero-field spectrometer. *Journal of Magnetic Resonance*, 270:35–39, 2016.

[148] Giuseppe Pileio, Marina Carravetta, and Malcolm H Levitt. Storage of nuclear magnetization as long-lived singlet order in low magnetic field. *Proceedings of the National Academy of Sciences*, 107(40):17135–17139, 2010.

[149] Stephen J DeVience, Ronald L Walsworth, and Matthew S Rosen. Preparation of nuclear spin singlet states using spin-lock induced crossing. *Physical review letters*, 111(17):173002, 2013.

[150] Thomas Theis, Yesu Feng, T-l Wu, and Warren S Warren. Composite and shaped pulses for efficient and robust pumping of disconnected eigenstates in magnetic resonance. *The Journal of chemical physics*, 140(1):014201, 2014.

[151] Yesu Feng, Thomas Theis, Tung-Lin Wu, Kevin Claytor, and Warren S Warren. Long-lived polarization protected by symmetry. *The Journal of chemical physics*, 141(13):134307, 2014.

[152] Y Zhang, K Basu, JW Canary, and A Jerschow. Singlet lifetime measurements in an all-proton chemically equivalent spin system by hyperpolarization and weak spin lock transfers. *Physical Chemistry Chemical Physics*, 17(37):24370–24375, 2015.

[153] Michael CD Tayler and Malcolm H Levitt. Singlet nuclear magnetic resonance of nearly-equivalent spins. *Physical Chemistry Chemical Physics*, 13(13):5556–5560, 2011.

[154] Yesu Feng, Ryan M Davis, and Warren S Warren. Accessing long-lived nuclear singlet states between chemically equivalent spins without breaking symmetry. *Nature physics*, 8(11):831, 2012.

[155] Malcolm H Levitt and Ray Freeman. Compensation for pulse imperfections in NMR spin-echo experiments. *Journal of Magnetic Resonance (1969)*, 43(1):65–80, 1981.

[156] Dragoş-Adrian Roşca, Karin Radkowski, Larry M Wolf, Minal Wagh, Richard Goddard, Walter Thiel, and Alois Fürstner. Ruthenium-catalyzed alkyne trans-hydrometalation: Mechanistic insights and preparative implications. *Journal of the American Chemical Society*, 139(6):2443–2455, 2017.

[157] María Belén Franzoni, Lisandro Buljubasich, Hans W Spiess, and Kerstin Münnemann. Long-lived ^{1}H singlet spin states originating from para-hydrogen in Cs-symmetric molecules stored for minutes in high magnetic fields. *Journal of the American Chemical Society*, 134(25):10393–10396, 2012.

[158] Aurélien Bornet, Xiao Ji, Daniele Mammoli, Basile Vuichoud, Jonas Milani, Geoffrey Bodenhausen, and Sami Jannin. Long-lived states of magnetically equivalent spins populated by dissolution-DNP and revealed by enzymatic reactions. *Chemistry–A European Journal*, 20(51):17113–17118, 2014.

[159] Yuning Zhang, Xueyou Duan, Pei Che Soon, Vladimír Sychrovskỳ, James W Canary, and Alexej Jerschow. Limits in proton nuclear singlet-state lifetimes measured with para-hydrogen-induced polarization. *ChemPhysChem*, 17(19):2967–2971, 2016.

[160] Marina Carravetta, Ole G Johannessen, and Malcolm H Levitt. Beyond the t_1 limit: singlet nuclear spin states in low magnetic fields. *Physical review letters*, 92(15):153003, 2004.

[161] James Eills, Javier Alonso-Valdesueiro, David E Salazar Marcano, Jesse Ferreira da Silva, Shamim Alom, Gregory J Rees, John V Hanna, Marina Carravetta, and Malcolm H Levitt. Preservation of nuclear spin order by precipitation. *ChemPhysChem*, 19(1):40–44, 2018.

[162] X. Ji, A. Bornet, B. Vuichoud, J. Milani, D. Gajan, A. J. Rossini, L. Emsley, G. Bodenhausen, and S. Jannin. Transportable hyperpolarized metabolites. *Nat. Commun.*, 8:13975, 2017.

[163] A. Capozzi, T. Cheng, G. Boero, C. Roussel, and A. Comment. Thermal annihilation of photo-induced radicals following dynamic nuclear polarization to produce transportable frozen hyperpolarized ^{13}C-substrates. *Nat. Commun.*, 8:15757, 2017.

[164] D. Gajan, A. Bornet, B. Vuichoud, J. Milani, R. Melzi, H. A. van Kalkeren, L. Veyre, C. Thieuleux, M. P. Conley, W. R. Grüning, M. Schwarzwälder, A. Lesage, C. Copéret, G. Bodenhausen, L. Emsley, and S. Jannin. Hybrid polarizing solids for pure hyperpolarized liquids through dissolution dynamic nuclear polarization. *Proc. Natl. Acad. Sci.*, 111(41):14693–14697, 2014.

[165] B. Vuichoud, A. Bornet, F. De Nanteuil, J. Milani, E. Canet, X. Ji, P. Miéville, E. Weber, D. Kurzbach, A. Flamm, and et al. Filterable agents for hyperpolarization of water, metabolites, and proteins. *Chem. Eur. J.*, 22(41):14696–14700, 2016.

[166] M. Gatzke, G. D. Cates, B. Driehuys, D. Fox, W. Happer, and B. Saam. Extraordinarily slow nuclear spin relaxation in frozen laser-polarized ^{129}Xe. *Phys. Rev. Lett.*, 70:690–693, 1993.

[167] H.-U. Kauczor, R. Surkau, and T. Roberts. MRI using hyperpolarized noble gases. *Eur. Radiol.*, 8(5):820–827, 1998.

[168] W. E. Blumberg. Nuclear spin-lattice relaxation caused by paramagnetic impurities. *Phys. Rev.*, 119(1):79, 1960.

[169] N. Lisitza, I. Muradian, E. Frederick, S. Patz, H. Hatabu, and E. Y. Chekmenev. Toward ^{13}C hyperpolarized biomarkers produced by thermal mixing with hyperpolarized ^{129}Xe. *J. Chem. Phys.*, 131(4):044508, 2009.

[170] A. Cherubini, G. S. Payne, M. O. Leach, and A. Bifone. Hyperpolarising ^{13}C for NMR studies using laser-polarised ^{129}Xe: SPINOE vs thermal mixing. *Chem. Phys. Lett.*, 371(5):640–644, 2003.

[171] Karel Kouřil, Hana Kouřilová, Malcolm H Levitt, and Benno Meier. Dissolution-dynamic nuclear polarization with rapid transfer of a polarized solid. *arXiv preprint arXiv:1807.00223*, 2018.

[172] George C Levy and Ulf Edlund. Carbon-13 chemical shift anisotropy relaxation in organic compounds. *Journal of the American Chemical Society*, 97(17):5031–5032, 1975.

[173] AL Bednowitz and B Post. Direct determination of the crystal structure of β-fumaric acid. *Acta Crystallographica*, 21(4):566–571, 1966.

[174] W Wu, DL Noble, JR Owers-Bradley, and AJ Horsewill. A ^{13}C field-cycling NMR relaxometry investigation of proton tunnelling in the hydrogen bond: Dynamic isotope effects, the influence of heteronuclear interactions and coupled relaxation. *Journal of Magnetic Resonance*, 175(2):210–221, 2005.

[175] J. Kowalewski and L. Maler. *Nuclear spin relaxation in liquids: theory, experiments, and applications*. CRC press, 2006.

[176] P. Vallet, Y. Van Haverbeke, P. A. Bonnet, G. Subra, J.-P. Chapat, and R. N. Muller. Relaxivity enhancement of low molecular weight nitroxide stable free radicals: importance of structure and medium. *Magn. Reson. Med.*, 32(1):11–15, 1994.

[177] A. Schweiger and G. Jeschke. *Principles of Pulse Electron Paramagnetic Resonance*. Oxford University Press, 2001.

[178] Ingo H Leubner. Continuous crystallization: Nucleation and size control as a function of crystal solubility. In *Nucleation and Atmospheric Aerosols*, pages 50–51. Springer, 2007.

[179] S. H. Yalkowsky, Y. He, and P. Jain. *Handbook of aqueous solubility data*. CRC press, 2016.

[180] M. G. Colombo, B. H. Meier, and R. R. Ernst. Rotor-driven spin diffusion in natural-abundance ^{13}C spin systems. *Chem. Phys. Lett.*, 146(3):189–196, 1988.

[181] M. H. Levitt, D. P. Raleigh, F. Creuzet, and R. G. Griffin. Theory and simulations of homonuclear spin pair systems in rotating solids. *J. Chem. Phys.*, 92(11):6347–6364, 1990.

[182] James Eills, William Hale, Manvendra Sharma, Matheus Rossetto, Malcolm H Levitt, and Marcel Utz. High-resolution nuclear magnetic resonance spectroscopy with picomole sensitivity by hyperpolarisation on a chip. *arXiv preprint arXiv:1901.07065*, 2019.

[183] Malcolm H Levitt. Symmetry constraints on spin dynamics: Application to hyperpolarized NMR. *Journal of Magnetic Resonance*, 262:91–99, 2016.